THE INFLUENCE OF ENVIRONMENTAL CONDITIONS ON VOLCANIC PROCESSES ON THE TERRESTRIAL PLANETS

A thesis submitted to University College London
for the degree of Doctor of Philosophy
by

Oliver Luke White

Department of Earth Sciences
University College London
Gower Street
London
WC1E 6BT

September 2010

Signed Declaration

I, Oliver Luke White confirm that the work presented in this thesis is my own. Where information has been derived from other sources, I confirm that this has been indicated in the thesis

Abstract

This thesis aims to identify what environmental conditions are most influential on volcanic processes on the terrestrial planets. The research primarily focuses on intermediate-sized volcanoes on Venus and Mars; complete surveys of these planets have been performed in order to compile a new catalogue of all such features that lists morphological and locational information for each one. This has yielded three key findings: evolutionary precursors of large volcanoes and several morphologies of steep-sided domes have been identified on Venus, and low-relief shields with very similar morphologies have been identified on Venus and Mars. In each case, morphological differences and similarities are interpreted with respect to the changing configuration of magma within the edifices, differences in surface environment, and magma properties and supply rate.

The research topic is also approached from two other aspects. Data obtained by the MARSIS radar sounder have been scrutinized in order to identify aquifers in the shallow Martian crust, and from this gauge the potential for crustal water to have influenced past volcanic activity. However, MARSIS has not succeeded in resolving Martian aquifers, leading to an independent estimate of its aquifer detection depth, and the conclusion that this instrument is insufficient to significantly constrain estimates of the crustal water budget.

In addition, ground-penetrating radar surveys have been performed on Icelandic rootless cones, a category of small volcanic feature, in order to determine how their environments have affected their morphologies and interior structures during formation and subsequent modification. Five Icelandic cones have been surveyed, and three classes of cone morphology have been identified. Analogous cone morphologies are observed on Mars, and have been correlated to their interpreted modification environments using the results of the Icelandic surveys as a basis.

Acknowledgements

I offer my utmost thanks to my two supervisors, Prof. Ellen Stofan and Dr. Ian Crawford, whose input, support and advice have been crucial in helping me achieve my goal of completing this thesis. There are many other individuals who are also very much worthy of mention. Prof. John Guest has shared his phenomenal knowledge of planetary volcanology on numerous occasions, and Dr. Peter Grindrod lent much helpful advice during the compilation of the volcano catalogues. Dr. Charlie Bristow of Birkbeck College offered much of his time to train me in the operation of ground-penetrating radar, as well to help interpret the radar profiles. Dr. Bristow, Dr. Crawford, Dr. Katherine Joy, Dr. Claire Cousins and Mr. Anselm Aston are all acknowledged for having helped lug the ground-penetrating radar across several steep, craggy rootless cones in Iceland. Dr. Ólafur Gudmundsson of the University of Iceland provided us with various pieces of equipment necessary for the Iceland surveys that saved us carrying even more bulky luggage from Britain. I must also thank the several members of the MARSIS team who aided me in the interpretation of MARSIS radargrams and were co-authors on the paper I published in Icarus: Dr. Jeffrey Plaut and Dr. Essam Heggy of the Jet Propulsion Laboratory, Dr. Stephen Clifford of the Lunar and Planetary Institute, Dr. William Farrell of the NASA Goddard Space Flight Center, and most importantly Dr. Ali Safaeinili of the Jet Propulsion Laboratory, who tragically died from cancer in 2009 and who will be remembered by all who knew him as an enormously friendly and knowledgeable person.

My parents, Georgina and Robert, have been a lasting source of encouragement for me – thanks for putting up with my moaning during the more strenuous times! I must also acknowledge the people who I have shared the planetary office with for the last three and a half years – Pete, Dom, Katie, Helen, Claire, Ceri, Lottie, Josh, Aidan, and Shoshana, who have made the workspace a very friendly (and often entertaining) place to be.

Contents

Chapter 3: Investigation of Environmental Controls on Volcanic Feature Morphology on Venus and Mars

Chapter 4: Introduction to Space- and Ground-Based Radar Sounding

Chapter 5: Interpretation of Reflections Observed by MARSIS

Chapter 6: The Failure of MARSIS to Detect Aquifers and Associated Implications for the Martian Water Budget

Chapter 7: Fieldwork Investigations of Icelandic Rootless Cone Groups and Implications for the Formation Conditions and Modification Histories of Martian Rootless Cones

Chapter 8: Conclusions

List of Figures

List of Tables

Chapter 1
Introduction to Environmental Effects on Volcanic Processes on the Terrestrial Planets

1.1 Premise and aspects of the research

Planetary science research in the past several decades has established that, as on Earth, volcanism has been an extremely important process in the evolution of Mars and Venus. Volcanism represents a major way by which terrestrial planets lose heat, and involves the ascent of melt from the deep interior to shallower levels (forming intrusive magma bodies), as well as to the surface (forming extrusive volcanic landforms). The manner in which the melts ascend and erupt onto the surface, and the appearance of the landforms that result from these processes, will be strongly influenced by the physical properties of the planet itself as well as the nature of the environmental conditions that exist at the surface. The very different surface conditions displayed by the terrestrial planets (in this case Earth, Mars and Venus) mean that intrusive and extrusive volcanic processes will be affected in quite different ways on each of them. To date, extensive study has been devoted to determining exactly how certain conditions affect volcanic processes by observing and interpreting volcanic morphologies on the different planets.

This thesis aims to develop the present understanding of environmental effects on volcanic processes and morphology, and it will focus on three aspects of this area of research. The primary topic concerns the quantitative characterisation of the morphologies of volcanic landforms on Mars and Venus. The extremely different surface conditions exhibited by these two planets means that they are ideal localities to investigate the effect of environmental conditions on volcanic processes and morphology. Previous research on volcano morphologies on these two planets has tended to focus on large volcanoes (i.e. with basal diameters greater than 100 km), with comparatively less attention having been accorded to smaller features. The general lack of consideration of this size population in the context of larger edifices is regarded to impact significantly on the issues of morphological evolution with edifice size and whether the influence of environmental conditions on volcano morphology behaves consistently over different size ranges. This study will perform global surveys dedicated to cataloguing volcanic landforms with basal diameters between 20 and 100 km on both planets, recording certain statistics for each landform including morphological parameters and coordinates. The aims are to identify controls on

volcano morphology based on the distribution of certain morphologies across and between planets, and to infer how the variation in morphology reflects differences in the magmatic systems feeding the edifices. The conclusions drawn from this study are compared with those from previous studies that have focused on larger volcanoes in order to determine whether the observed environmental effects on volcanic processes are consistent across different size ranges.

An important influence on the style of terrestrial volcanic eruptions is the extent to which the magma interacts with water, an effect that is regarded to have been a common occurrence throughout Martian history as well. This study incorporates the topic of magma-water interaction on Mars into the broader theme of environmental influences on volcanic processes and morphology. Previous studies have inferred the occurrence of magma-water interaction on Mars based primarily on interpretation of volcanic morphologies from spacecraft imagery, as well as theoretical considerations of the volume of water that should have existed on Mars. This study will investigate the topic of magma-water interaction using sounding radar, a technique not previously applied at Mars, and which forms the second aspect of the thesis research. The European Space Agency's Mars Express satellite, launched in June 2003, carried a sounding radar instrument, the primary objective of which was to detect the presence of liquid aquifers and ice layers within the Martian crust. Achieving this task would not only allow the distribution and state of water in the crust to be better characterised, but would also allow estimates of the total volume of water currently present within the crust to be refined. In association with the morphological studies achieved from the catalogue of Martian volcanic edifices, this study aims to determine how magma-water interaction has influenced the formation of volcanic landforms across the planet based on the distribution and volume of crustal water as inferred from the data returned by the instrument.

The third aspect of the research focuses on rootless cones, which form through the interaction of a lava flow with a waterlogged substrate. On Earth, these features most commonly occur in Iceland, where they reach several tens of metres across. Features very similar in appearance and size to rootless cones have also been imaged on Mars, implying that near-surface water/ice has existed at the point in Martian history when the cones formed. Previous research on rootless cones has noted that variation in the ratio of lava mass to water mass during cone formation will strongly influence their resulting

morphology and petrology, although the relation of formation conditions to resulting morphology remains somewhat ambiguous. In addition, the morphologies of the cones will have undergone modification since their formation. This study used a combination of techniques including ground-penetrating radar (which works on the same principle as sounding radar) and stratigraphic logging to investigate the interior structures of rootless cones within various Icelandic cone groups, identify the different rock facies comprising them, and determine the formation conditions and erosional histories of the cones based on the configuration of the cone facies and the environment in which the cone fields are situated. The findings of the Icelandic surveys will be used to make inferences regarding the formation conditions and erosional histories of Martian cones based on comparison of cone morphologies on the two planets. While this research focuses on volcanic landforms that are on a very different scale from those that are the subject of the rest of the thesis, the same principles apply to the interpretation of the volcanic edifice morphologies based on the environmental conditions considered to have prevailed during and after their eruption.

In three sections, the remainder of this chapter will explore previous research that is relevant to each of the three aspects of the thesis research. Outstanding questions in each subject area will be identified, and will be related to the objectives of the thesis research that are described at the end of each section.

1.2 Volcanism on Mars and Venus

1.2.1 Introduction

Current knowledge of volcanism on Mars and Venus has essentially been accumulated over a period of almost four decades, commencing with the Mariner 9 mission in 1971 and 1972 that was the first mission to identify Olympus Mons and the Tharsis Rise volcanoes (see e.g. *McCauley et al.* [1972]; *Masursky* [1973]; *Carr* [1973]). This was followed by the two Viking orbiters, active from 1976 to 1980, that far surpassed Mariner 9 with respect to variety, quality and quantity of remote sensing data, obtaining global photographic coverage of the surface at a maximum resolution of 7.5 m/pixel [*Snyder and Moroz*, 1992]. The Viking orbiters allowed the volcanic features that had already been identified by Mariner 9 to be scrutinized in much greater detail, allowing more confident inferences to be made regarding the ages, morphologies

and evolutionary histories of the edifices based on the identification and interpretation of small-scale features and stratigraphy (see e.g. *Crumpler and Aubele* [1978]; *Greeley and Spudis* [1981]; *Mouginis-Mark et al.* [1992]). Within the past decade four orbiting spacecraft have studied the Martian surface and crust using very high resolution cameras in addition to a host of new instrumentation including laser altimeters, spectrometers, magnetometers and thermal infrared cameras. The HiRISE camera aboard the Mars Reconnaissance Orbiter can provide detail down to 25 cm/pixel [*McEwen et al.*, 2007], allowing the observation of Mars almost at a scale familiar to terrestrial field geologists. The multidisciplinary investigations arising from the variety of high-quality instrumentation available on this recent fleet of spacecraft has permitted reconciliation of both geological and geophysical data, leading to an improved understanding of edifice evolution as well as intrusive processes.

Venusian volcanism was essentially revealed for the first time by the Pioneer Venus Orbiter, launched in 1978, which was the first spacecraft to peer through the opaque high-altitude cloud cover using synthetic aperture radar (SAR), mapping both radar reflectivity and topography with a periapsis resolution of 23 × 7 km [*Masursky et al.*, 1980; *Pettengill et al.*, 1980]; altimetry data were acquired for the area between latitudes 74°N and 63°S, whereas radar imaging covered a narrower band between latitudes 45°N and 15°S. Similar mapping was performed by SAR on board Veneras 15 and 16, which arrived at Venus in 1983, with the SAR having a maximum resolution of 1-2 km, and the altimeter a lateral resolution of 40-50 km and a vertical resolution of 30 m [*Barsukov et al.*, 1986; *Rzhiga*, 1987]; radar images were obtained for 25% of the planet. The data from these missions provided rudimentary and incomplete views of the distribution of large shield volcanoes and smaller volcanic domes across the planet. They were succeeded by the Magellan mission, which operated at Venus from 1990 to 1994, and featured SAR that achieved a maximum resolution of 120 m, with the altimeter producing topographic data with a lateral resolution of ~10 km and a vertical resolution better than 50 m [*Saunders et al.*, 1990]. Magellan obtained radar maps of 98% of the surface of Venus [*Ford and Plaut*, 1993]. The resulting dataset has allowed the documentation of the characteristics, location and dimensions of a wide variety of surface features down to a small scale across nearly the entire planet [*Crumpler et al.*, 1991; *Head et al.*, 1992; *Crumpler et al.*, 1997; *Crumpler & Aubele*, 2000].

The most prominent volcanic features on Mars and Venus are the extremely wide, and in the case of Mars sometimes extremely high, shield volcanoes: Alba Patera on Mars has a basal diameter of ~1200 km, but only 2-5 km of relief, whereas Olympus Mons has a basal diameter of ~600 km and a relief of 24-26 km [*Hodges and Moore*, 1994]. Var Mons and Atanua Mons on Venus have basal diameters reaching ~1000 km [*planetarynames.wr.usgs.gov*] but, in general, large shields on Venus do not rise as high as Martian ones, tending to have vertical reliefs of 2-3 km [*Head et al.*, 1992; *Crumpler et al.*, 1997]. The volumes of such edifices are comparable to volcanic volumes produced at terrestrial hotspot island chains [*Stofan et al.*, 1995]. Volcanoes on Mars and Venus attain such large sizes due to the absence of plate tectonics on those planets, which on Earth leads to the formation of chains of volcanoes, such as the Hawai'ian Islands [*Carr*, 1984]. Large shield volcanoes on Mars, which have been imaged in the visible portion of the spectrum, are easily identifiable by their generally high relief, convex flanks, summit calderas with nested collapse craters, occasional presence of encircling basal scarps and concentric graben segments, and occasional dissected flanks [*Hodges and Moore*, 1994]; Fig. 1.1a shows Olympus Mons as an example, which displays most of the aforementioned features.

The Venusian terrain, by contrast, has been imaged only at microwave frequencies, which are sensitive to the surface roughness rather than reflected light – the Magellan SAR provided maps of the surface roughness on a vertical scale of 12.6 cm [*Saunders et al.*, 1990]. Global mapping of Venus has shown that morphological diversity characterises large volcanoes to a much greater extent than on Mars. Diagnostic criteria for identifying large volcanoes include the presence of distinctive radial patterns of lava flows, the frequent presence of a circular caldera or concentric fracture patterns at the summit, and the occasional presence of radial fracture patterns [*Head et al.*, 1992]; Fig. 1.1b shows Tuulikki Mons for the purpose of comparison with Olympus Mons, a similar-sized shield. In some cases, there is clearly a morphologic transition between large volcanoes and coronae on Venus; the latter are dominantly concentric or circular structures consisting of an annulus of concentric ridges or fractures, an interior that is either topographically positive or negative, a peripheral trough, and in several cases, numerous volcanic and tectonic landforms in the interior [*Barsukov et al.*, 1986; *Stofan and Head*, 1990; *Pronin and Stofan*, 1990; *Stofan et al.*, 1992; *Squyres et al.*, 1992a].

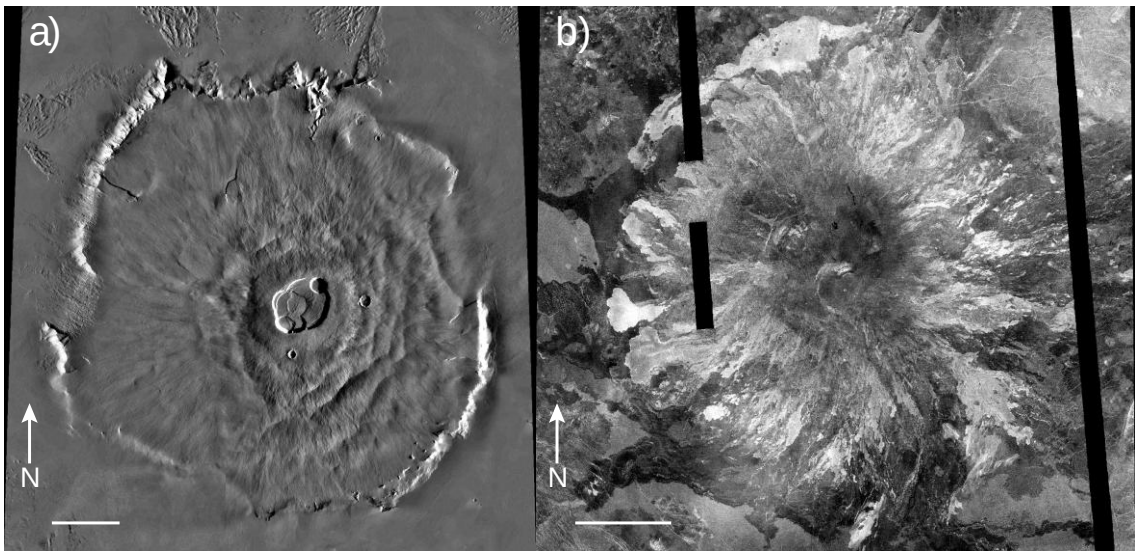

Figure 1.1. Examples of large shield volcanoes on Mars and Venus. Scale bars measure 100 km in both images. (a) Olympus Mons on Mars, which is ~600 km across at its base, reaches 26 km high above the surrounding plains, and which is surrounded by a well-defined scarp as much as 6 km high. Lava flows drape over the scarp in places and cover much of the surrounding plains. Summit caldera measures 65 by 85 km across and is almost 3 km deep. Viking Orbiter digital-image mosaic centered at 19°N, 134°W. Illumination angle differs across image; illumination is from the right for the eastern flank and summit caldera, and from the left for the western flank. (b) Tuulikki Mons on Venus, which reaches ~500 km across at its base, yet only reaches 2 km high above the surrounding plains. Medium- to high-reflectivity, overlapping digitate and fan flows radiate from the summit region down the flanks in all directions. No distinct summit caldera is present, with the summit region instead comprising medium- to low-reflectivity terrain with angular dark patches representing ponded lava. Magellan left-looking radar image centered at 10.15°N, 85.3°W.

At smaller scales, volcanism takes several forms on both planets. Venus apparently displays volcanic structures down to the limit of Magellan resolution (120 m). Global surveys have identified edifice categories that include steep-sided domes, modified domes, shields, and 'uncategorized' edifices, in addition to calderas and paterae [*Crumpler et al.*, 1991; *Head et al.*, 1992; *Krause and Grosfils*, 1999; *Crumpler and Aubele*, 2000]. In addition to large volcanoes, these features are predominantly concentrated at intermediate elevations on Venus [*Ristau et al.*, 1998], i.e. between planetary radii of 6051 and 6053 km; mean planetary radius (MPR) is 6051.8 km. A major concentration of volcanic features of all types is seen in the Beta/Atla/Themis (BAT) region, an area centered on the equator and covering about 20% of the planet; volcanic concentrations exist here at ~2-4 times the global average, suggesting that the mantle in this region may be anomalous [*Head et al.*, 1992]. On Mars, smaller volcanic edifices generally take the form of shields, domes and cones [*Hodges and Moore*, 1994], as well as fields of small conical structures that have been interpreted to be rootless cones [*Frey et al.*, 1979; *Greeley and Fagents*, 2001; *Fagents et al.*, 2002;

Fagents and Thordarson, 2007]. Relative to Venus, the distribution of volcanic features of all categories and sizes on Mars is much more localized – features of particular morphologies tend to cluster together in groups away from other types [*Hodges and Moore*, 1994]. The Tharsis rise is the most prominent volcanic centre on Mars, displaying several of Mars' largest shield volcanoes and numerous smaller shields [*Carr*, 1974; *Hodges and Moore*, 1994].

Since the discovery of volcanoes on both planets, attention has centered on explaining the diversity and distribution of volcanic landforms seen, deducing the styles of eruption associated with the construction of the landforms, inferring the internal structure of the volcanoes, and determining what influence the eruptions have had on the local and global environments. Research on volcanism on Mars and Venus has predominantly focused on large (>100 km basal diameter [*Head et al.*, 1992]) volcanoes in order to answer these questions, yet a significant discrepancy exists between the frequencies of such edifices on the two planets. On Mars, volcanoes falling into this size range are essentially confined to a group totalling around 20 edifices that occur within relatively localized clusters [*Hodges and Moore*, 1994], whereas on Venus, no less than 156 large edifices exist, which are relatively more evenly distributed across the globe [*Head et al.*, 1992]. This strong inequality in volcano frequency is reflected at smaller scales, and is not merely a consequence of the different surface areas of Mars and Venus, but also of the very different modification histories experienced by the surfaces of the two planets. There is the likelihood that the intense erosion on Mars resulting from catastrophic flooding and impact cratering during the Noachian and Hesperian eras (4.5 to ~3.1 Gyr ago [*Tanaka et al.*, 1992; *Hartmann and Neukum*, 2001; *Ivanov*, 2001]) has eliminated an unknown number of volcanic edifices from the record, with elimination tending more towards smaller edifices. Venus, with its extremely thick carbon dioxide atmosphere that is interpreted to have existed for much of the planet's history [*Kasting*, 1988], presents a surface that shows negligible evidence of erosion by water or impact cratering, and is instead dominated by volcanic processes in the form of edifice construction and lava plain emplacement – it appears that the most common mechanisms of edifice elimination on Venus are mass wasting and inundation by surrounding lava flows. The apparent paucity of efficient removal processes that are not related to volcanism throughout Venusian history has led to the present-day high concentration of volcanic features across the surface of the planet. Venus therefore

presents a more complete database of volcanic features relative to Mars, which ultimately aids when attempting to establish the role of volcanism in the planet's geological and stratigraphic history, as well as what location-dependent environmental and geological constraints are most influential with respect to determining edifice morphology and eruption style.

1.2.2 Theories regarding environmental controls on volcanic formation and modification processes on Mars and Venus

A planetary 'environment' consists of a complex array of factors, each of which contributes differently to the physical condition encountered by erupted volcanic products [*Zimbelman and Gregg*, 2000]. Such factors include the surface temperature and pressure of an atmosphere and the topography of the surface onto which the volcanic products are emplaced, as well as basic physical properties including magma density, composition and volatile content, and planetary gravity and thermal gradient. All of these will have an important influence on the generation, ascent, eruption, and morphology of volcanic deposits [*Wilson and Head*, 1981, 1983; *Head and Solomon*, 1981].

Mars and Venus are known to possess very different values for several of the aforementioned environmental and physical parameters. The present temperatures and pressures at the surface of Venus are very high (750 K and 10 MPa respectively at MPR [*Head and Wilson*, 1986]), whereas those at the surface of Mars are much lower (~140 K to 300 K and 0.00056 MPa respectively [*Kieffer et al.*, 1977; 1992]). Venus has an equatorial surface gravity that is ~2.5 times stronger than that on Mars, and while the thermal gradients of Mars and Venus are not currently well constrained, recent estimates suggest that Venus' mean surface heat flux is 78 mW m^{-2} [*Brown and Grimm*, 1999], whereas that of Mars may be ~20-30 mW m^{-2} [*Phillips et al.*, 2008; *Grott*, 2008]. Some of these parameters also differ strongly between different locations on the planets themselves, most notably atmospheric pressure on Venus, which decreases by ~0.55 MPa with every km increase in altitude [*Head and Wilson*, 1992].

Such a wide variety of environmental conditions and physical properties will inevitably translate into a diverse range of styles of volcanic activity at the surface and intrusive activity within the crust; extensive research has been dedicated to constraining exactly how influential certain environmental conditions are with respect to affecting

volcanic processes. The following sections detail what is currently known about the effects of certain environmental conditions on volcanic processes, based on theory and observations.

1.2.2.1 Factors affecting effusive eruption

The morphological features of lava flows depend on several factors: the composition- and temperature-dependent rheological properties, thermal diffusivity, and density of the erupted materials; environmental variables such as the flow cooling rate under the ambient atmospheric conditions and surface temperature, and planetary gravity; and the physical parameters of the eruption, such as vent size and shape, total lava effusion rate and volume, and slope of the ground over which the flow advances. These are not necessarily constant for a given eruption: effusion rate commonly varies during an eruption, flows advance down slopes which often vary systematically with distance from the vent, and lava rheology changes with progressive cooling. There are therefore many interdependencies among the above parameters [*Wilson and Head*, 1994].

A parameter of particular importance to volcano morphology is the length attained by lava flows, as this will influence the aspect ratio (here defined as the ratio of edifice diameter to height) of the resulting edifice. Factors which control lava flow length are the subject of some controversy. The assumption that flow length is mainly influenced by viscosity was contested by *Walker* [1973], who proposed that the length of a lava flow was dependent on the mean effusion rate, and by *Malin* [1980], who concluded that flow length was dependent on erupted volume. *Pinkerton and Wilson* [1994] reanalyzed the Hawai'ian flow data of *Malin* [1980] and showed it to be consistent with the assertion of *Walker* [1973], given that short duration and tube-fed flows are discounted. However, *Pinkerton and Wilson* [1994] found that the length of a flow can vary by a factor of 7 for a given effusion rate, and by a factor of 10 for a given volume, meaning that factors other than effusion rate and volume are clearly important in controlling the lengths of lava flows.

One such factor will be the cooling rate of a flow, which, in addition to the flow composition, greatly influences the rheological properties of the flow. Cooling rate is essentially dependent on the temperature and density of the surrounding atmosphere, which influences the cooling of the upper surface of the flow. Heat loss processes from

the base of a lava flow into the underlying surface are instead controlled by the thermal diffusivity of the substrate and are essentially the same on all silicate planets [*Hulme*, 1982]. *Head and Wilson* [1986] presented calculations of the convective and radiative heat loss rates from the upper surfaces of lava flows on Venus; *Wilson and Head* [1994] used the same methods but modified for Martian atmospheric properties. The high surface temperature of Venus acts to inhibit radiative cooling of lava flows, and the high atmospheric density means that convective cooling is likely to be more effective initially. The thin Martian atmosphere, by contrast, is ~200 to 550 times less efficient at removing heat from exposed hot surfaces by convection than the atmosphere of Venus, so that radiation dominates on Mars even at quite low excess temperatures. Up until roughly the first hour after eruption, flows would actually cool faster on Venus than their Martian counterparts by up to 65 K, with cooling thereafter being inhibited by the high atmospheric temperature [*Frenkel and Zabalueva*, 1983; *Head and Wilson*, 1986; *Wilson and Head*, 1994]. *Head et al.* [1992] and *Wilson and Head* [1994] describe how these effects would act to lengthen cooling-limited flows on Venus relative to those on Mars by about 20%, assuming flows on both planets are compositionally and volumetrically similar and typically travel for more than an hour. The faster initial cooling for Venusian flows would indicate that they would undergo a more rapid transition from pahoehoe to 'a'ā texture than terrestrial or Martian ones. In addition to influencing the cooling rate, the high atmospheric pressure on Venus will act to inhibit volatile exsolution within lavas to a much greater extent than on Mars. The viscosity of a lava decreases as the fraction of unvesiculated volatiles within a melt increases, meaning that basalts with the same initial volatile abundance will be less viscous on Venus relative to Mars, which further acts to lengthen Venusian lava flows relative to those on Mars [*Bridges*, 1997].

Effusion rate and vent size and shape have been found to be strongly influenced by planetary gravity [*Wilson and Head*, 1994]. Lower gravity will result in correspondingly slow convective fluid motions and crystal settling processes driven by positive and negative buoyancy forces, as well as slow overall diapiric ascent rates, which will allow larger diapirs to ascend to shallower depths. A consequence of this is that dike widths will be greater, and effusion rates higher, on a planet with lower gravity. Lower gravity would also result in thicker flows for a given effusion rate, lava yield strength and surface slope. The effect of lower gravity on effusion rate, vent size

and flow thickness would therefore act to lengthen flows on Mars relative to those on Venus, contradicting the negative effect of atmospheric conditions on cooling rate (for timespans greater than an hour). Based on the effect of low gravity on vent size and effusion rate, *Wilson and Head* [1994] estimated that similar cooling-limited lava flows would be about 6 times longer on Mars compared with Earth; such large flow lengths would permit the construction of very large volcanoes of the order of 500 to 700 km across, which is observed on Mars. The flow length ratio would be slightly less between Mars and Venus given that Venus has 90% of the gravity of Earth.

When all these factors are considered together, the results of the modeling of *Head and Wilson* [1986] and *Wilson and Head* [1994] imply that compositionally similar, cooling-limited lava flows would reach lengths on Mars that are approximately a factor of 4.5 longer than those on Venus for a given magma volume flux. In reality, the rheological properties of lava flows are not absolutely homogeneous throughout; for relatively high effusion rates, the lava flows instead comprise low-viscosity central channels, which accommodate most of the lava motion, bounded by high-viscosity stationary levees [*Wilson and Head*, 1994]. In some cases, the central channel may become entirely roofed over by the thickening crust to form a lava tube, thus insulating the flow and allowing it to remain fluid and mobile for longer than it would if the flow were entirely cooling-limited. The development of lava tubes would therefore allow for longer lava flows than in purely cooling-limited cases.

The great distances theoretically attained by Martian flows agree well with the observed diameters of the vast shield volcanoes and the lengths of some individual flows. *Carr et al.* [1977] mapped flows emerging from underneath younger flows at Arsia Mons that may have travelled as far as 800 km from the summit region, although it is likely that such flows are largely tube-fed. There are several flows on Venus that attain similar lengths: *Head et al.* [1992] mapped 13 lava flood-type flow fields that reached lengths over 500 km, with one exceeding 1000 km, as well as 51 volcanoes that attained diameters greater than 500 km. These lengths indicate that factors other than cooling rate, vent size and effusion rate must be affecting the lengths of flows on Venus. Such factors would likely include the volume of melt generated in the crust (see section 1.2.2.3), lithospheric stress state [*Magee and Head*, 2001], evolving edifice-reservoir dynamics, and ground slope.

1.2.2.2 Factors affecting explosive eruption

A common denominator that applies to all explosive eruptions on planets with appreciable atmospheres is that some of the clastic eruption products will become entrained in a mixture of released magmatic gases and atmospheric gases (and possibly gases derived from the thermal vaporization of near-vent volatile deposits) in such a way as to produce a convecting eruption cloud which rises into the atmosphere over the vent [*Wilson and Head*, 1994]. The atmospheric pressure strongly influences the extent to which volatile exsolution occurs in shallow, rising magmas, and as such influences whether or not explosive disruption of a gas-magma mixture will occur [*Head and Wilson*, 1986]. Rising basaltic magma containing a certain weight percent of volatiles on a planet with a low surface atmospheric pressure may undergo explosive disruption as the volume fraction of exsolved gas passes a certain threshold; for an identical magma on a planet with a greater atmospheric pressure, less gas would be exsolved, the volume fraction threshold may never be reached, and explosive disruption may never occur [*Head and Wilson*, 1992].

Given that the surface atmospheric pressure on Venus ranges from ~12,500 to 17,500 times that of Mars, this would suggest that explosive activity would be severely inhibited on Venus, and limited to cases in which bubble coalescence produced abnormally high gas content, or to situations where magma volatile content exceeded several weight percent [*Head and Wilson*, 1986]. Consequentially, extruded lavas on Venus would generally retain whatever amount of gas they exsolve and the bulk density of flows would be low. Evidence of pyroclastic activity on Venus from Magellan imagery is very rare but not entirely absent [*Campbell et al.*, 1998].

On Mars, the very low atmospheric pressure would instead promote explosive activity under almost all conditions, incorporating Hawai'ian-type fire fountaining [*Head and Wilson*, 1987] as well as strombolian and plinian eruptions [*Wilson and Head*, 1994]. The low Martian gravity and atmospheric pressure relative to Venus would result in Martian plinian eruption deposits being systematically finer grained than any found on Venus, being almost entirely sub-centimetre in size [*Wilson and Head*, 1994]; potential fields of pyroclastic debris identified on Venus have radar backscatter coefficients that imply individual clasts ranging up to 8 cm in size or larger [*Campbell et al.*, 1998]. The very different atmospheric properties on Mars and Venus will also

influence the settling rate of clasts and their resulting dispersion. The dispersal of clasts with sizes in the tens of microns to mm range will depend on the wind regimes they encounter while falling [*Wilson and Head*, 2007]; lower-atmosphere horizontal wind speeds on Venus will generally be less than those on Mars. The dispersal will also be influenced by the terminal velocities of the clasts, which depend on the atmospheric density and viscosity, clast size and density, and gravitational acceleration; these parameters will also determine whether the clasts fall in a laminar or turbulent regime as described by formulae in *Wilson and Head* [2007]. For a constant clast size and density, the terminal velocity of clasts falling in the laminar regime will be almost twice as fast on Mars compared to Venus, while the terminal velocity in the turbulent regime will be almost 40 times as fast on Mars compared to Venus. For the clast sizes expected on Mars (sub-cm) and Venus (up to 8 cm) as inferred by *Wilson and Head* [1994] and *Campbell et al.* [1998], laminar regimes should prevail on both planets. The Martian clast terminal velocity would therefore be expected to be about twice that on Venus, reducing the opportunity for dispersion, although the stronger Martian horizontal winds may counteract this effect.

The enhanced magma fragmentation that would be expected on Mars has evidently precluded the occurrence of features interpreted to result from viscous, effused lava, such as steep-sided domes (with the possible exception of some small-sized examples, e.g. *Rampey et al.* [2007]), which are common on Venus. Venusian steep-sided domes are very similar in morphology to rhyolite and dacite domes on Earth, which owe their steep sides and heights to the high viscosity of the magma [*Head et al.*, 1992]. Volatile enhancement in abnormally large Venusian reservoirs may produce basaltic 'foams' with gas bubble concentrations that on Mars or Earth would be sufficient to cause explosive disruption of the magma. However, on Venus the bubbles would remain in the magma, creating the potential for highly vesicular, high viscosity erupted lavas [*Head and Wilson*, 1992]. Such lavas would display anomalous, more viscous rheological properties, would attain great thicknesses, and would have volumes considerably larger than their dense rock equivalent. It should be noted that the basaltic bubble enhancement model is not the only mechanism proposed for the eruption of steep-sided domes on Venus. Crustal remelting and magmatic differentiation in large reservoirs may produce high-viscosity silicic magmas, in which case the production mechanism for the domes may resemble that of their rhyolitic and dacitic terrestrial

counterparts [*Pavri et al.*, 1992]. However, *Stofan et al.* [2000] argued that silicic lavas would quickly form thick crusts that would break into large blocks on the dome surface, inconsistent with the apparently smooth surfaces of the domes as inferred from Magellan SAR data; *Stofan et al.* [2000] instead advocated basaltic compositions for the domes.

1.2.2.3 Factors affecting formation of neutral buoyancy zones and the resulting landforms

The depths of terrestrial magma chambers have been interpreted to represent a state of neutral buoyancy at which the density of ascending magma equals the density of the surroundings [*Rubin and Pollard*, 1987; *Ryan*, 1987; *Walker*, 1988]. Since the crustal density profile depends on the lithostatic pressure, the depth to a given density will scale inversely with gravity [*Wilson and Head*, 1990] and atmospheric pressure [*Wilson and Head*, 1994]. A high surface atmospheric pressure will result in inefficient exsolution of volatiles from magmas as they approach the surface, which in turn will result in a low surface void fraction (and elevated bulk density) of surface rocks; this will result in a high lithospheric density profile [*Wilson and Head*, 1994]. Thus, if it is assumed that the respective densities of melt and country rock on Mars and Venus are similar, then neutral buoyancy theory predicts that on Venus, the higher gravitational acceleration (8.88 ms^{-1} on Venus relative to 3.73 ms^{-1} on Mars [*Zimbelman and Gregg*, 2000]) and atmospheric pressure (9.8 MPa at MPR on Venus [*Head and Wilson*, 1992] and 5.6×10^{-4} MPa at MPR on Mars [*Kieffer et al.*, 1992]) should result in the formation of shallower reservoirs than on Mars [*Head and Wilson*, 1992]. The modelling of *Wilson and Head* [1994] used best estimates of the surface void fractions of volcanic products on Mars and Venus to determine density profiles for each planet, and predicted that magma of identical density on each planet should stall at depths 7.9 times greater on Mars relative to Venus, for identical country rock densities in their completely compacted state and exponential decay of fractional void space with depth.

Head and Wilson [1992] hypothesized that the effect of neutral buoyancy zones on the evolution of the magma reservoirs that feed volcanic edifices is highly influential on their morphologies. Neutral buoyancy theory predicts that the very low atmospheric pressure gradient on Mars (4.95×10^{-5} MPa per km [*Kieffer et al.*, 1992]) will cause the surface void fraction to remain fairly constant as erupting lava increases the height of

the edifice, causing the density profile to shift upwards such that the neutral buoyancy zone and associated magma chamber ascend into the edifice as it grows [*Wilson and Head*, 1994]. The ascent of the chamber would cause rising magma to lengthen feeder dikes rather than increase the size of the chamber itself, which would retain a fairly constant diameter, as would the overlying caldera. As a result of the persistently shallow magma reservoir, vents on the edifice would be focused on the central summit region, dike intrusions would exist within the edifice, and a high, steep-sided edifice will be constructed.

On Venus, the high atmospheric pressure gradient (0.6 MPa per km [*Head and Wilson*, 1992]) will cause the surface void fraction to decrease as the edifice increases in height, causing the density profile to remain fairly constant and the neutral buoyancy zone and associated magma chamber to ascend at a much slower rate than it would on Mars, possibly remaining in the substrate for the entirety of the volcano's history. The vertical stabilization of the chamber would mean that magma rising into it would cause the chamber to grow laterally, enlarging the caldera and promoting lateral dike propagation over surface extrusion [*Head and Wilson*, 1992]. Vents will be widely dispersed, meaning that edifice growth would be spread over a wide area rather than concentrated at a specific point. Larger reservoirs on Venus should also encourage larger volumes for individual eruptions [*Blake*, 1981], and such eruptions would form long flows that would contribute less to the height of an edifice and more to its lateral component – this effect may counteract the shortening effect of Venus' higher gravity on the length of lava flows (see section 1.2.2.1). The combination of these various effects will result in broader and lower edifices forming on Venus compared with Mars. The contrasting scenarios of edifice growth on Mars and Venus are illustrated with Fig. 1.2. Additional factors that may contribute to lower edifices on Venus include the different density contrasts between magma and solid rock on the two planets [*Head and Wilson*, 1986]; high surface temperatures inhibiting cooling of flows [*Wood*, 1979]; high eruption volumes and rates, low-viscosity magmas, and the presence of tube-fed flows [*Schaber*, 1991]; and the relatively thin Venusian lithosphere progressively sagging under a volcano's weight as it grows [*McGovern and Solomon*, 1997].

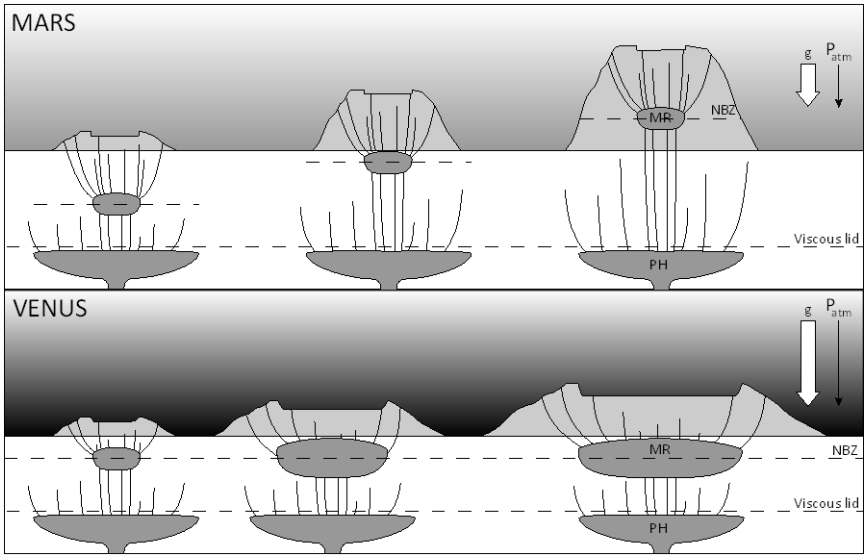

Figure 1.2. Schematics showing the expected evolution of edifice-magma reservoir systems with edifice growth on Mars and Venus. The schematics are based on the predictions of neutral buoyancy zone theory as described in *Head and Wilson* [1992]. g is gravitational acceleration, P_{atm} is atmospheric pressure gradient, NBZ is neutral buoyancy zone, MR is magma reservoir, PH is plume head. The viscous lid refers to the base of the lithosphere, which comprises the crust and the portion of the upper mantle that behaves elastically on time scales of thousands of years or greater.

Neutral buoyancy zone formation has also been hypothesized to influence the distribution of volcano morphologies [*Head and Wilson*, 1992]. On Venus the pressure gradient is such that at the lowest elevations (<6051 km planetary radius) and highest pressures, and for a range of common terrestrial magma volatile contents, the inhibition of volatile exsolution will be sufficient to prevent any neutral buoyancy zones from forming, and magmas are likely to emerge directly from deep reservoirs to the surface via massive outpourings, forming expansive lava plains. At higher elevations and lower pressures, neutral buoyancy zones are predicted to form and favour the development of shallow reservoirs, from which lava can ascend to the surface in localized eruptions, forming discrete edifices. Neutral buoyancy zones will become deeper with increasing elevation as a result of the decreasing atmospheric pressure such that at the highest elevations magma reservoirs are predicted to be large and relatively deep with low associated edifices, as well as intrusive features such as radial fracture patterns and calderas [*Head and Wilson*, 1992; *Keddie and Head*, 1994b; *Grosfils and Head*, 1995]. The very low atmospheric pressure gradient on Mars would imply that, for a given magma density, neutral buoyancy zones should exist at large and relatively consistent depths across the planet, regardless of elevation. Intrusions and dike emplacement, with low associated edifices (at least in the intermediate size range), might therefore be

expected to predominate on Mars based on neutral buoyancy theory. The contrasting distributions expected on the two planets are illustrated in Fig. 1.3.

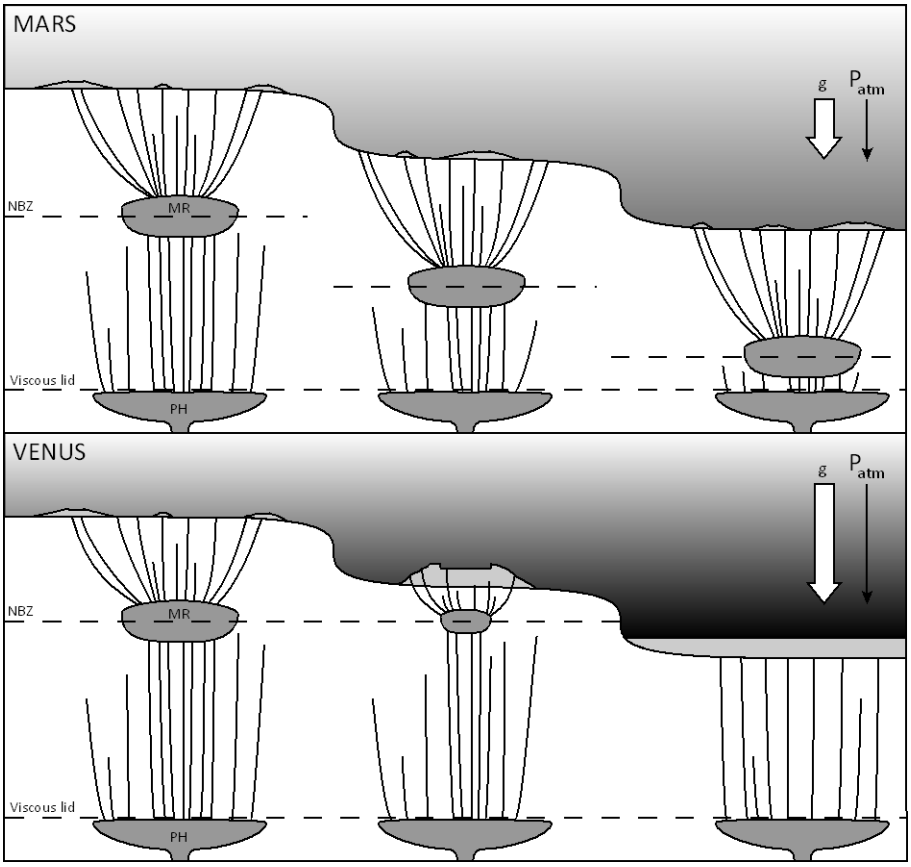

Figure 1.3. Schematics showing the expected configurations of edifice-magma reservoir systems with elevation on Mars and Venus, and the resulting distribution of edifice morphologies. The schematics are based on the predictions of neutral buoyancy zone theory as described in *Head and Wilson* [1992]. Abbreviations are the same as for Fig. 1.2.

Controversy exists as to exactly how influential neutral buoyancy zones are in affecting volcanic feature evolution and morphology. The application of neutral buoyancy zone theory to Venus was initially laid out by *Head and Wilson* [1992]. The results of subsequent studies have in some cases supported neutral buoyancy zone theory predictions. These include *Keddie and Head* [1992, 1994b], focusing on large shield volcanoes; *Grosfils and Head* [1995], focusing on dike swarms; and *Ristau et al.* [1998], focusing on intermediate volcanoes. Other studies have disagreed or are inconclusive, including *Krause and Grosfils* [1999], which focused on 'uncategorized' intermediate volcanoes, and *Stofan et al.* [2001], which focused on the large shield volcanoes Sif, Gula and Kunapipi Montes. Considering that they are specific to intermediate volcanoes, the results of *Ristau et al.* [1998] and *Krause and Grosfils* [1999] are summarized below.

Ristau et al. [1998] assessed the implications of neutral buoyancy zones for intermediate volcano formation by examining the altitudinal distribution of three separate morphological categories of intermediate volcanoes identified by *Head et al.* [1992]: 145 steep-sided domes (analogous to category D in section 2.2.1), 50 "ticks" or modified domes (analogous to categories MD1 to MD5 in section 2.2.1), and 25 "anemones" or shields with radar-bright radial flows (analogous to categories S6 and S7 in section 2.2.1). *Ristau et al.* [1998] established that the intermediate volcano population exists mainly at intermediate elevations (mean altitude of 6051.6 km), with steep-sided domes existing at a mean elevation of 6051.5 km, modified domes at a mean elevation of 6051.7 km, and radial flow shields at a mean elevation of 6052.6 km. Neutral buoyancy theory predicts a paucity of volcanic edifices below the altitude of 6051 km, yet *Ristau et al.* [1998] noted that 30% of intermediate volcanoes form at or below this altitude, hypothesizing that this may be due to the predicted depth of magma reservoir formation being deeper than the actual depth. While the distributions of steep-sided and modified domes were seen to comply with neutral buoyancy theory, that of radial flow shields did not, as these features were seen to occur at much higher altitudes than shallow magma chamber volcanoes should. *Ristau et al.* [1998] suggested that radial flow shields may represent an unusual style of volcanism on Venus that is not as dependent on the effect of neutral buoyancy zones as other volcano categories.

Ristau et al. [1998] determined that the populations of the three morphological categories are not randomly distributed as a function of altitude, suggesting that neutral buoyancy has influenced their distribution. *Krause and Grosfils* [1999] extended this research by examining the altitudinal distribution of the remaining 54 "uncategorized" intermediate volcanoes identified by *Head et al.* [1992], and determined that the altitude distribution of the uncategorized features was indistinguishable from random, which does not support neutral buoyancy theory. Yet the observed trends in mean elevation between intermediate volcanoes, large volcanoes [*Keddie and Head*, 1994b] and radiating dike swarms [*Grosfils and Head*, 1995] were found to follow the predictions of neutral buoyancy theory, progressing from intermediate volcanoes to large volcanoes to dike swarms with increasing elevation [*Krause and Grosfils*, 1999]. While size-grouped analyses indicate that neutral buoyancy zone formation has played an important role in volcanic emplacement on a global scale on Venus, various studies have advised that additional factors such as edifice morphology [*Krause and Grosfils*, 1999],

lithospheric stresses [*Stofan et al.*, 2001] and regional geologic setting [*Head and Wilson*, 1992] must be considered to a greater degree in order to better understand the process of edifice formation and growth on Venus.

1.2.2.4 Magma-water interaction

Terrestrial volcanism has been fundamentally influenced by the water cycle. The prevalence of water on the planet, whether in liquid or solid phase, has meant that interaction between water/ice and melts is a common occurrence, and the thermodynamics of such interactions and their implications for the morphologies of resulting landforms have been studied [e.g. *Wohletz*, 1986; *Wilson and Head*, 2002a]. Inevitably, the potential for water and/or ice to have influenced volcanic processes on Mars and Venus has also been considered.

Such potential appears far more likely for Mars compared with Venus. Mars displays extensive morphological, geological and chemical evidence for the past existence of large bodies of surface water [*Carr*, 1996; *Squyres et al.*, 2004; *Klingelhöfer et al.*, 2004; *Rieder et al.*, 2004; *Mustard et al.*, 2008], as well as direct evidence for the current presence of large volumes of water ice in the form of the polar caps, a shallow ice layer extending underneath much of the northern plains, and glacial landforms in the eastern Hellas region [*Thomas et al.*, 1992; *Smith*, 2009; *Feldman et al.*, 2004; *Holt et al*, 2008]. Furthermore, based on infrared spectroscopy, the composition of the dusty component of the surface regolith at the Viking Lander sites has been found to be most similar to palagonite [*Singer*, 1982; *Guinness et al.*, 1987], an alteration product from the interaction between water and basaltic melt.

Volcanism on Mars, most significantly in the Tharsis region, is regarded as having begun during the Noachian era (4.5 to ~3.6 Ga) and continued throughout the Hesperian era (~3.6 to ~3.1 Ga), waning at the advent of the Amazonian era (~3.1 Ga to present day) [*Head and Wilson*, 2002]. The timescale for large-scale, regional volcanic activity like that seen in Tharsis, Syria and Elysium therefore coincides not only with the period when the Martian surface and atmospheric environments have been interpreted to be 'warm and wet' (early- to mid-Noachian), but also with the later period when atmospheric conditions evolved to become more similar to how they are today (post-late-Noachian). A global cryosphere (i.e. the portion of the crust at a temperature below the freezing point of water) underlain by groundwater would therefore have developed

by the late Noachian, thickening with time as a result of the lessening thermal gradient, but locally thinning due to variations and perturbations related to magmatic intrusions – this configuration would essentially dictate the nature of magma-water interaction for the rest of the history of Mars [*Clifford*, 1993].

Interaction between ascending magma and hydrospheric/cryospheric bodies can take many forms on Mars, and the interaction may produce several distinct morphological features and geological facies [*Head and Wilson*, 2002]. The magnitude and relative importance of the various interaction processes that give rise to such features will have changed over the geological history of Mars as the surface and atmospheric conditions change. Magma rising from the mantle into the crust will form a variety of intrusive bodies, including plutons, sills and dikes, that will intersect the cryosphere and perturb the regional thermal gradient. Sills and plutons may heat and melt ice in the cryosphere, causing mobilization and collapse of material [*Squyres et al.*, 1987], leading to the formation of chaotic collapse terrain like the example seen in Fig. 1.4a. Dikes may be emplaced laterally for thousands of kilometres and can set up near-surface stress fields that form graben over them; if they encounter perched aquifers and ground ice, they may ultimately lead to the formation of lahars and outflow channels (see Fig. 1.4b). *Head and Wilson* [2002] hypothesized that the magma reservoirs that feed the large shield volcanoes on Mars may be shallow enough to cause near-surface melting of any ice present in the cryosphere, and that such effects may be responsible for the slumping and mass movements associated with the western flanks of the Tharsis Montes, as described by *Zimbelman and Edgett* [1992] (see Fig. 1.4c). The ground ice melting efficiency of such intrusive bodies will be increased several fold if convective hydrothermal systems are set up within the resulting meltwater, compared with scenarios where melting occurs solely by conduction of heat [*Head and Wilson*, 2002].

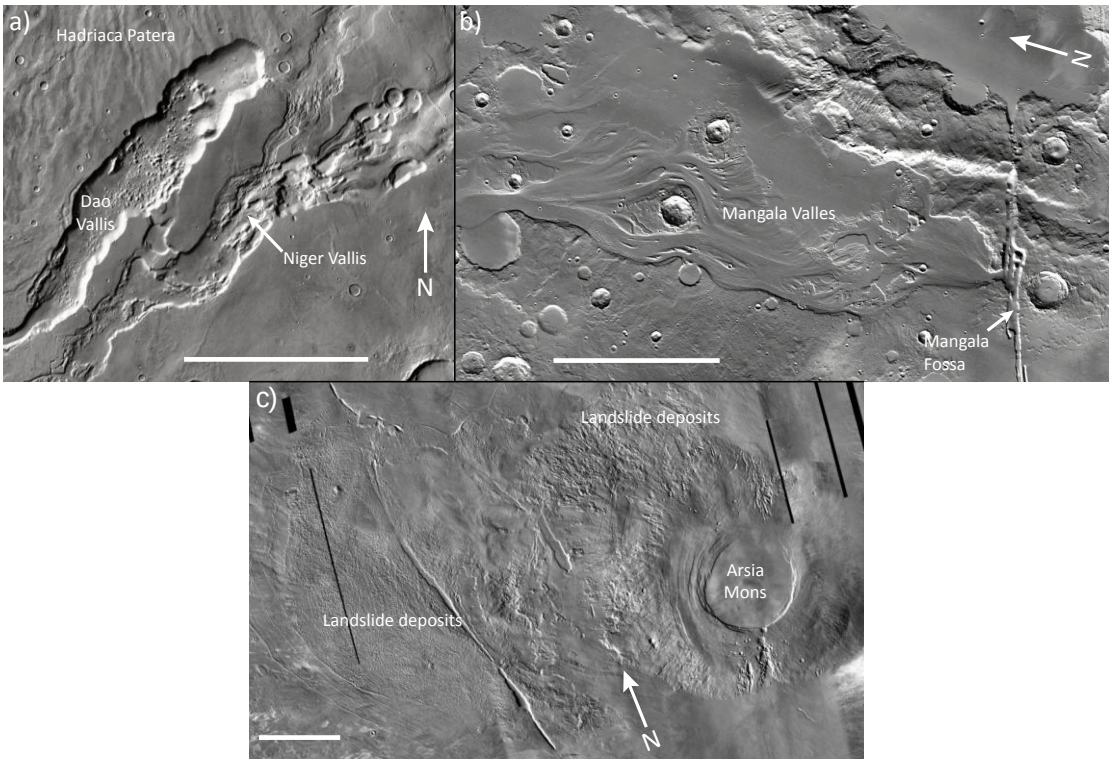

Figure 1.4. THEMIS daytime infrared mosaics showing Martian geomorphological features resulting from the melting of cryospheric ice by magmatic intrusions. Scale bar measures 100 km in all images. (a) Dao and Niger Valles, two deep troughs with chaotic terrain on their floors, that are located on the south rim of Hadriaca Patera, and which initially formed through collapse of the substrate through magmatic intrusion into volatile-rich rock [*Tanaka et al.*, 2002]. The water erupted onto the surface and flowed downslope to the southwest, forming an outflow channel. Illumination is from the left. (b) The outflow channel of Mangala Valles, which emanates from the Mangala Fossa fault, which itself may be the surface manifestation of a dike radial to Tharsis [*Tanaka and Chapman*, 1990]. Illumination is from the bottom. (c) The Tharsis shield of Arsia Mons, with the extensive landslide deposits mapped by *Zimbelman and Edgett* [1992] seen on the west flank, extending up to 500 km from the base of the shield. *Head and Wilson* [2002] interpreted the deposits as having potentially formed due to slope instability instigated by the near-surface melting of cryospheric ice by the magma reservoir. Illumination is from the left.

Volcanic edifices on Mars that are interpreted to result from the interaction of magma/lava with shallow or surface ground ice/water include features interpreted to be rootless cones and tuyas. Rootless cones form when surface lava flows heat shallow ground ice/water to form pressurized vapour that subsequently explodes through the lava flow, forming cones that in Iceland (where the terrestrial type examples exist) can reach diameters >300 m [*Thorarinsson*, 1953], but on Mars reach up to 1500 m across [*Frey et al.*, 1979; *Fagents et al.*, 2002]. Potential Martian rootless cone fields have been identified in Acidalia, Utopia, Elysium and Isidis Planitiae, Hephaestus Fossae, the north Olympus Mons aureole, and Arrhenius province [*Frey et al.*, 1979; *Frey and Jarosewich*, 1982; *Mouginis-Mark*, 1985; *Hodges and Moore*, 1994]. An example of

such a field is shown in Fig. 1.5a. The formation process of rootless cones is discussed in detail in section 1.4.

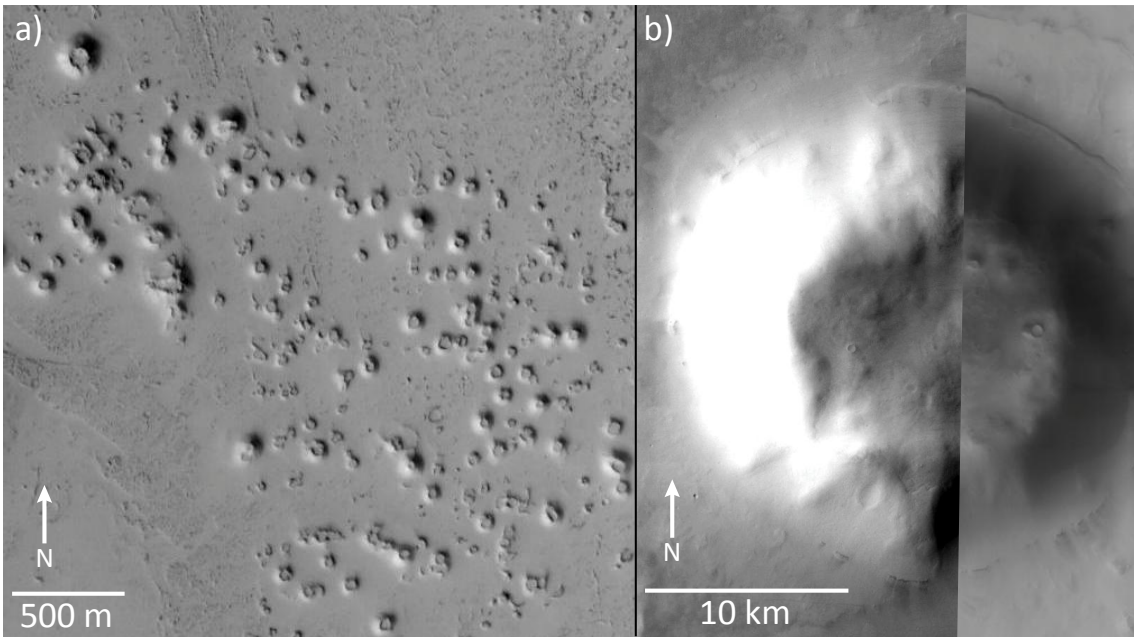

Figure 1.5. Martian geomorphological features that potentially result from the interaction of erupted lava with surface or shallow subsurface ice. (a) Portion of MOC image M0801962 showing a rootless cone field located in Amazonis Planitia at approximately 26.0°N, 170.3°E. Illumination is from the bottom-left. (b) Mosaic of two THEMIS visible images (V18173005 and V23377012) showing a steep-sided, flat-topped feature interpreted as a tuya. Edifice is located in Sisyphi Planum at 64.2°S, 7.2°E. Illumination is from the left in the left-hand image, from the bottom in the right-hand image.

Numerous studies have mapped candidate volcanic features in the north and south circumpolar regions [*Hodges and Moore*, 1994; *Garvin et al.*, 2000; *Tanaka and Scott*, 1987; *Ghatan and Head*, 2002]. Perhaps the most significant of these features are the 21 features in Sisyphi Planum identified by *Ghatan and Head* [2002] as potential tuyas, which are flat-topped, steep-sided volcanic constructs that erupt underneath ice sheets or glaciers [*Mathews*, 1947; *Einarsson*, 1966; *Smellie and Skilling*, 1994; *Smellie*, 2000]. Figure 1.5b shows an example of such an edifice; the constructs tend to be circular, with diameters ranging from 20 to 40 km, and heights ranging from 1 to 1.5 km. Many appear to be surrounded by circular depressions and channels, interpreted by *Ghatan and Head* [2002] as evidence for meltwater ponding and draining during their formation. *Ghatan and Head* [2002] suggested that they would have formed under the ice-rich Dorsa Argentea Formation, which has since retreated to its current position to the southwest. Potential tuyas, as well as hyaloclastite ridges, have been identified by *Chapman* [1994] in the Utopia basin west of Elysium, and may have been erupted beneath a thick ice sheet representing a frozen paleolake [*Scott et al.*, 1992].

The morphological features displayed in Fig. 1.4 represent examples of how intrusive igneous bodies can alter a planetary surface through melting of ground ice reserves, whereas those in Fig. 1.5 are formed through the interaction of erupted lava with surface or near-surface ice. It has been suggested that groundwater may also influence the eruption styles and resulting morphologies of the larger Martian volcanoes through its incorporation into magma reservoirs. Varying extents to which groundwater has been incorporated into magmatic systems has been regarded as an explanation for the contrasting morphologies of the steep, moderate relief Tharsis and Elysium shields and the lower relief highland paterae such as Tyrrhena and Hadriaca Paterae (see Fig. 1.6). Specifically, Tyrrhena and Hadriaca Paterae have been interpreted to be the site of pyroclastic flow deposits generated by hydromagmatic explosive eruptions involving water volumes of $\sim 7.5 \times 10^{16}$ kg and water flow rates of up to $\sim 10^5$ to 10^6 m^3 s^{-1} for Tyrrhena Patera [*Greeley and Crown*, 1990] and $\sim 10^3$ to 10^4 m^3 s^{-1} for Hadriaca Patera [*Crown and Greeley*, 1993]. Indeed, the radial channeling displayed by the lower flanks of the highland paterae has been interpreted as evidence of erosion by wind, water and mass wasting, suggesting that the lower flanks are constructed of poorly consolidated ash flows rather than lava flows [*Greeley and Spudis*, 1981]. The Tharsis volcanoes, which evidently date from a later time period than the highland paterae (early Hesperian) based on crater counting and stratigraphic relationships [*Plescia and Saunders*, 1979; *Neukum and Wise*, 1976; *Soderblom*, 1977], display morphologies and surface textures that imply formation through eruption of lava flows rather than friable pyroclastics. The change in morphology from paterae to shields, and the change in inferred eruption styles from explosive to effusive, may therefore represent a waning availability of groundwater in the megaregolith (the fractured, porous portion of the crust) with time [*Greeley and Spudis*, 1981; *Crown and Greeley*, 1993]. However, other factors will likely be responsible as well, including evolution in magma composition and changes in atmospheric pressure and density. The study of *Gregg and Williams* [1996] considered an alternative scenario whereby the highland paterae are instead constructed primarily of mafic pyroclastic rocks, rather than being the products of magma-ice interactions.

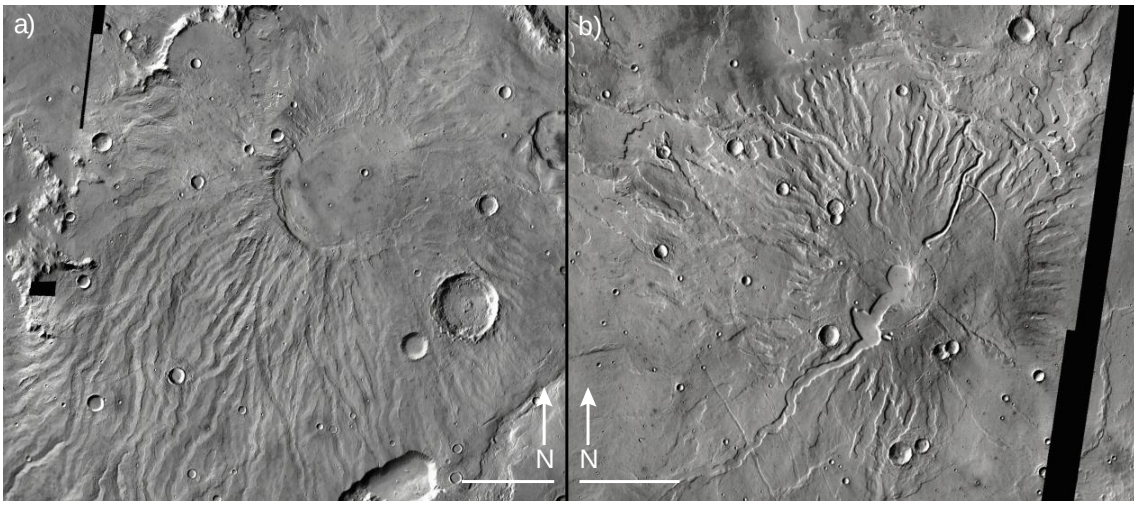

Figure 1.6. THEMIS daytime infrared mosaics showing the low-relief, radially textured highland paterae of Hadriaca Patera (a) and Tyrrhena Patera (b). Both paterae display summit calderas, circular at Hadriaca Patera and dumbbell-shaped at Tyrrhena Patera. Radial arrays of densely spaced valleys characterise the flanks – those at Hadriaca Patera are more subdued and V-shaped relative to the more sharply defined, flat-floored channels at Tyrrhena Patera. Distinct sinuous lava channels extend from the caldera and summit region at Tyrrhena Patera, but are absent from Hadriaca Patera. Scale bars measure 50 km in both images. Illumination is from the left in both images. The morphologies of these edifices may be compared with those of the Tharsis edifices, Olympus Mons and Arsia Mons, in Figs. 1.1a and 1.4c respectively.

Venus currently has a surface environment that prevents the existence of any surface water or ice, and it does not display any morphological features that are consistent with having been formed or modified by water or ice (with the possible exception of the canali [*Jones and Pickering*, 2003]). Various studies have attempted to determine whether or not the surface conditions of Venus may have been more conducive to the existence of large bodies of surface water in its distant past. Either Venus was formed of material that was very poor in water [*Lewis*, 1970], or whatever water was originally present has since disappeared as a result of a runaway greenhouse effect [*Ingersoll*, 1969], the hydrogen into space and the oxygen into the interior [*Walker et al.*, 1970]. *Müller et al.* [2008] used nightside thermal observations by the VIRTIS instrument on the Venus Express satellite to identify correlations between the emissivity variation and geomorphological features identified by Magellan SAR images. Tessera terrain generally showed lower emissivity, whereas most volcanic edifices and large lava flows showed higher emissivity; *Müller et al.* [2008] interpreted this correlation as being potentially indicative of the tessera highlands having a more felsic (possibly granitic) composition compared with the mafic volcanic edifices and lava flows. The tessera

highlands may therefore represent granitic cratons which *Taylor and Campbell* [1983] hypothesized to exist on Venus.

Measurements of the ratio of deuterium to hydrogen in the atmosphere of Venus have been used in order to attempt to constrain how much water Venus has lost since its early history. It has been determined that the early Venus would have had at least 100 times more water in the atmosphere than is presently there, with at least 0.3% of a terrestrial ocean having been outgassed, consistent with a primordial ocean several tens of metres deep [*Donahue et al.*, 1982; *Donahue and Hodges*, 1992; *Donahue and Russell*, 1997]. The results of these studies conclude that Venus would have been a wetter planet in its early history, although exactly how much water existed there, and in what phase, is currently unknown. If volcano-water interactions did take place in Venus' early history, it does not appear that any evidence of such interactions has survived to the present day. For the purposes of this study, it is assumed that volcano-water interaction has not been a factor in the formation of the volcanic features that currently exist on Venus.

1.2.2.5 Mass wasting and other post-formation erosional modification processes

Mass wasting is a universal process that will affect any geomorphological feature, and is defined as the geomorphic process by which soil, regolith, and rock move downslope under the force of gravity. The previous sections have discussed controls on volcano morphology during actual formation of the features, whereas mass wasting and other processes, such as wind and water erosion, influence the morphologies of the features after formation.

The effects of mass wasting are most commonly manifested, on both Mars and Venus, as large flow lobes extending from the bases of steep scarps existing on edifice flanks. Because mass wasting is essentially dependent on gravity, these features are commonly seen on high-relief features with steep flanks. On Mars, the most prominent examples are the several corrugated aureoles that surround the flanks of Olympus Mons, which itself displays a steep basal scarp around nearly its entire perimeter (see Fig. 1.7a), although the landslide hypothesis is just one of a number put forward to explain the deposits [*Francis and Waadge*, 1983; *Tanaka*, 1985]. *Lopes et al.* [1980] proposed that the aureoles were formed by a series of megaslides from the outer flanks of the edifice, perhaps assisted by a period of widespread melting of permafrost. Less

prominent examples of landslide debris are seen on the western flanks of Arsia, Pavonis and Ascraeus Montes, and permafrost melting is also suspected to have been involved in their formation [*Zimbelman and Edgett*, 1992]; *Head and Marchant* [2003] actually interpreted the fan-shaped deposit of Arsia Mons to be moraine deposited from a cold-based mountain glacier emerging from the upper slopes of the volcano. Similar effects of mass wasting are not seen on large Venusian shields despite the planet's higher gravity, likely due to the very low gradients of their flanks [*Bulmer and Guest*, 1996], the absence of any permafrost (the melting of which causes slope instability [*Head and Wilson*, 2002]), and the possibility that Venusian volcanoes may be basally welded to the lithosphere [*McGovern and Solomon*, 1998]. Landslide debris aprons are, however, frequently apparent surrounding modified domes (also referred to as 'ticks'), which show steep basal scarps and radial ridges, and which are interpreted to be partially collapsed versions of steep-sided domes (see Fig. 1.7b).

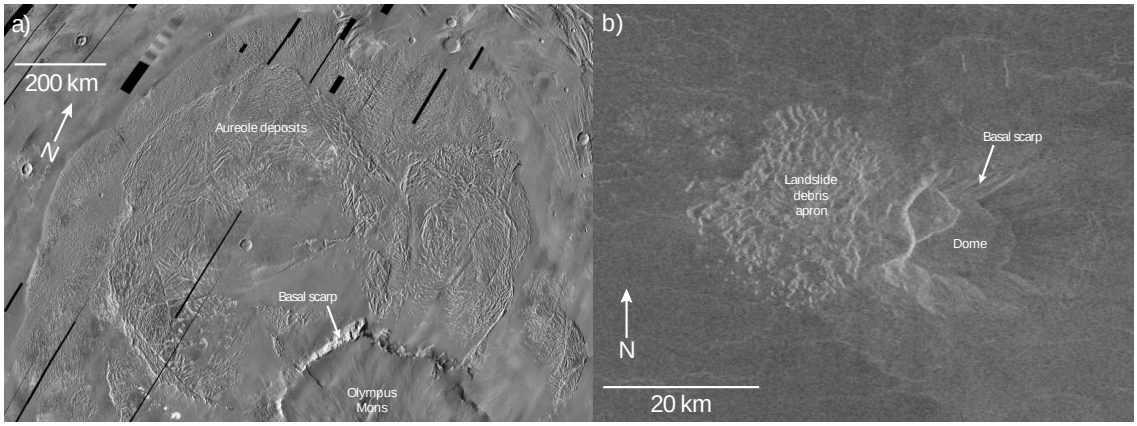

Figure 1.7. Examples of mass wasting influencing volcano morphology on Mars and Venus. (a) THEMIS daytime image mosaic showing the large aureole extending from the NW basal scarp of Olympus Mons. Image centered at 26.3°N, 219.3°E. Illumination is from the left. (b) Left-looking Magellan SAR image of Bunzi Mons on Venus, showing the landslide debris apron extending from the W basal scarp. Image centered at 46°N, 355°E.

Other forms of post-formation modification for Martian and Venusian volcanoes will include erosion by aeolian processes and impact cratering. Aeolian processes will be relatively inefficient for both Mars and Venus when compared with Earth, yet may well be the most significant surface-modification processes that are currently active. Dune fields, yardangs and wind streaks have been observed on both Mars and Venus [*Greeley et al.*, 1992a, 1992b; *Bradley et al.*, 2002], yet there is no apparent evidence on either planet that aeolian processes have significantly influenced volcanic morphology other than at a superficial level. Impact cratering has affected Martian landforms to a

much greater extent compared with Venus as a result of the much thinner atmosphere, allowing very much smaller bolides to reach the surface.

Modification of Martian volcanoes by running water manifests itself in the form of radial channelling on the larger shields and paterae, which is commonly attributed to initial formation by surface runoff and subsequent enlargement by groundwater sapping [*Baker*, 1982; *Gulick and Baker*, 1990], although some channels potentially have a mixed lava and fluvial origin. A prominent example is that of Hadriaca Patera in the southern highlands (see Fig. 1.6b). *Gulick and Baker* [1990] noted that such channels tend to form at locations on volcanoes where lava flow morphology is subdued, indicating the presence of ash mantling, rather than where solid basalt exists at the surface. This would explain why fluvial valleys are present on some Martian volcanoes but not others of the same age.

1.2.3 Aims of the study

Section 1.2.2 has examined current knowledge as well as uncertainties regarding the influence of different environmental factors on volcanic processes and morphologies on both Venus and Mars. A notable aspect of previous research is that large volcanic features (>100 km diameter) have been most commonly considered more than smaller features. Exceptions to this include the study of *Head and Wilson* [1992], who considered the effects of neutral buoyancy zones on the formation of fields of small shields (<20 km diameter), intermediate-sized (20-100 km diameter) steep-sided domes, calderas and paterae on Venus. Further Venusian studies include those of *Ristau et al.* [1998] and *Krause and Grosfils* [1999], who investigated whether the altitudinal distribution of intermediate volcanoes is consistent with neutral buoyancy theory. Martian intermediate volcanic edifices of particular morphologies have been described in separate studies (e.g. *Dohm and Tanaka* [1999]; *Ghatan and Head* [2002]; *Sakimoto* [2002]; *Bleacher and Greeley* [2008]; *Baratoux et al.* [2009]; *Wilson et al.* [2009]), and these have included some interpretation of the likely conditions of formation, but as yet there has been no attempt to identify controls on the morphologies of all intermediate volcano classes on a global scale as there has been on Venus. Similarly, studies of environmental controls on volcanism on Mars and Venus in the intermediate size range have essentially focused on each planet separately, without direct comparison of morphologies seen on the two planets. Related to the subject of the distribution of

morphological classes is that of how environmental conditions affect changes in morphology during volcano growth. Some studies have focused on the evolution of large volcanoes on Venus and Mars, e.g. *McGovern and Solomon* [1990], *Keddie and Head* [1994a], *McGovern and Solomon* [1998] and *Stofan et al.* [2001], but to date there has been no real consideration of the role of intermediate edifices in models of volcano growth.

For this portion of the thesis, global surveys of the surfaces of Mars and Venus will be performed with the intention of identifying all intermediate volcanoes of all morphologies on the two planets, including edifices and calderas. The survey will be conducted using remote sensing imagery across a range of wavelengths as well as altimetry data. The catalogue will serve as the basis for the research into how intraplanetary and interplanetary differences in environmental conditions affect volcanic processes and morphology. The specific aspects of this research that will be pursued will only be finalised once the catalogue has been compiled and significant morphological trends are identified. However, the following themes are regarded to be central to the eventual analysis:

1) Investigate the extent to which the distribution of intermediate volcanic morphologies is consistent with the predictions of neutral buoyancy theory, and identify what other environmental factors may be influential in controlling the distribution.

2) Use the morphological statistics obtained from the current survey, in addition to those of previous surveys, to identify intermediate-sized precursors of large volcanoes, and characterize the evolution of feature morphology with increasing size. Investigate what factors are influential in causing these changes.

1.3 The search for water on Mars and implications for water-magma interaction

1.3.1 Introduction

In the nearly 40 years since Mariner 9 entered Martian orbit and obtained the first pictures of outflow channel and valley systems on the surface [*McCauley et al.*, 1972; *Masursky*, 1973; *Milton*, 1973] there has been vigorous debate over the quantity of water that existed on Mars in its early history, and how much of that water has remained on Mars to the present day. It is unsurprising that water (in both its solid and liquid phases) has earned such great attention, as its presence would have profound

implications for the geological evolution of the planet (not least the volcanic evolution), as well as for speculations over whether life has ever existed (and may still exist) on it. The MARSIS instrument aboard the European Space Agency's Mars Express satellite represents the first attempt to experimentally gauge the size of the crustal water budget of Mars. This section examines current knowledge of the state of water on Mars, prior estimates of the water budget, how MARSIS should allow these estimates to be refined, and the potential implications of the water budget for the occurrence of magma-water interactions in the past.

1.3.2 The past and current state of water on Mars

Since the arrival of Mariner 9 in Mars orbit in 1971, generations of orbiting spacecraft have returned images in increasing detail of channels and valleys apparently carved by the flow of liquid water, as well as landforms and deposits indicative of the former presence of bodies of standing water (e.g. *McCauley et al.* [1972]; *Masursky* [1973]; *Milton* [1973]; *Sharp and Malin* [1975]; *Masursky et al.* [1977]; *Carr and Clow* [1981]; *Baker* [1982]; *Baker et al.* [1992]; *Cabrol and Grin* [1999]; *Poulet et al* [2005]; *Perron et al.* [2007]; *Mustard et al.* [2008]). These features stand at odds with the current Martian surface environment. The atmospheric pressure at the surface is less than 1% of that on Earth and the surface temperature ranges from 140 K during the polar winters to 300 K during equatorial summers [*Kieffer et al.*, 1977; 1992]. The phase diagram of water shown in Fig. 1.8 indicates that it should generally be unstable in its pure liquid phase under present Martian surface conditions [*Kuznetz and Gan*, 2002], although a small range of pressure and temperature conditions does exist over which liquid water would be stable. Water on Mars would not exist in its pure form, however, but would instead exist as brine containing dissolved solids; the effect of these impurities would be to depress the freezing point of the water, thereby creating a greater range of temperature conditions over which it could exist as a liquid at surface conditions [*Clark and Van Hart*, 1981]. Nevertheless, conditions on the present day Mars are far from equable, and this pressure and temperature range would exist only transiently, and not for long enough to allow the presence of quantities of surface water massive enough to carve channels on the scale observed.

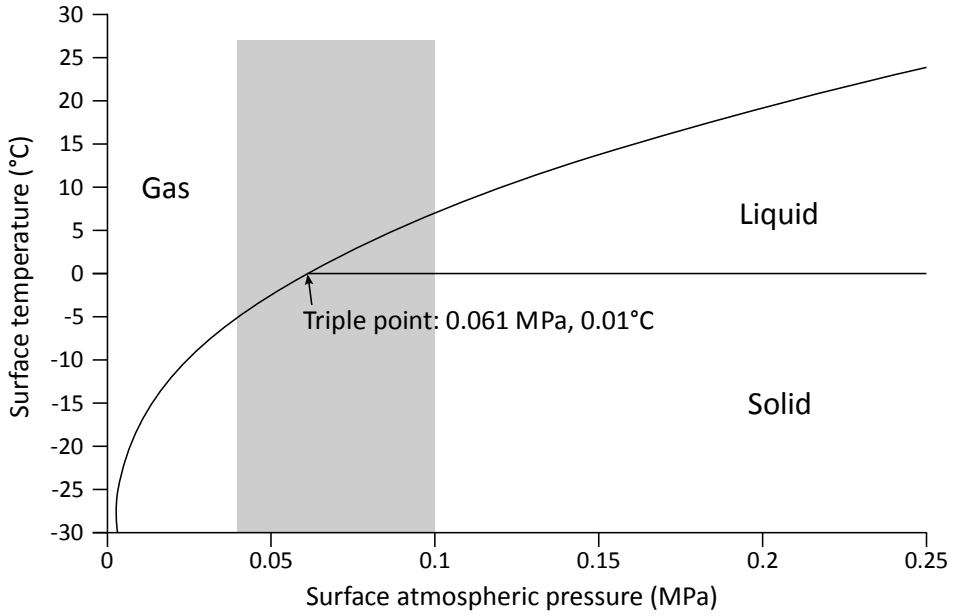

Figure 1.8. Phase diagram of pure H_2O, illustrating when it exists as a solid, liquid or vapour as a function of pressure and temperature. The temperature and pressure range observed at the Martian surface is highlighted by the grey area. Figure adapted from Fig. 3 in *Kuznetz and Gan* [2002].

A paradox therefore exists, whereby landforms exist that are indicative of the past presence of large quantities of surface water, and yet the present day surface conditions are sufficiently hostile to prevent the existence of large bodies of water for long time periods. This suggests that the channels formed during an early period in the history of Mars when higher atmospheric temperatures and pressures created a substantial greenhouse effect, allowing the sustained presence of surface water [*Sagan et al.*, 1973; *Sharp and Malin*, 1975; *Mutch et al.*, 1976]. Subsequent greenhouse gas loss would have caused deterioration of the climate and led ultimately to the conditions of the present day [*Fanale et al.*, 1992]. Proposed loss processes include photochemical reaction, driven by solar ultraviolet radiation, that can convert greenhouse gas into other gas or particulate species [*Yung and Pinto*, 1978; *Atreya and Blamont*, 1990]; various mechanisms, including hydrodynamical escape [*Watson et al.*, 1981; *Hunten et al.*, 1989] and atmospheric impact erosion [*Walker*, 1986; *Melosh and Vickery*, 1989], that may cause their loss to space; and chemical weathering processes that can convert them into components of surface rocks [*McElroy*, 1972; *McElroy et al.*, 1977; *Booth and Kieffer*, 1978; *Fanale et al.*, 1982; *Fox and Dalgarno*, 1983; *Kahn*, 1985; *Pollack et al.*, 1987; *Owen et al.*, 1988].

Determination of the timescale of such climactic deterioration has been based largely on dating the ages of fluvial features. *Fanale et al.* [1992] described how the

valley networks (Fig. 1.9a) are almost entirely confined to the heavily cratered southern highlands, which is believed to have survived from prior to 3.8 Gyr ago (i.e. towards the end of the Noachian era) when the planet was subjected to heavy meteoritic bombardment. Formation of the large outflow channels (Fig. 1.9b) is thought to have occurred mainly within the Hesperian era, ~3.6 to 3.1 Ga ago (e.g. *Milton* [1973]; *Masursky et al.* [1977]; *Carr* [1996]); the water clearly flowed into the northern lowlands, where it may have formed significant standing bodies of water (e.g *Parker et al.* [1989; 1993]). In addition, identification of narrow channels connecting thermokarst-like depressions in Ares Vallis led *Warner et al.* [2010] to conclude that these depressions were filled with standing bodies of water until the late Hesperian based on crater counting. The Martian greenhouse effect is thought to have largely deteriorated by the late Hesperian, yet transient, warm climate fluctuations may have been created through obliquity changes [*Head et al.*, 2003; *Forget et al.*, 2006], intense volcanism [*Harrison and Grimm*, 2005], large impact events [*Segura et al.*, 2002], and the formation of temporary atmospheres following major outflows [*Baker et al.*, 1991; *Santiago et al.*, 2005]. In addition to the channels, valleys and lakes, a long-standing theory has existed that the northern lowland plains were once occupied by an ocean (see e.g. *Parker et al.* [1989]; *Baker et al.* [1991]; *Parker et al.* [1993]; *Head et al.* [1998]; *Head et al.* [1999]; *Ivanov and Head* [2001]; *Clifford and Parker* [2001]; *Perron et al.* [2007]). The primary evidence for this hypothesis takes the form of a set of surface features that ring the plains for thousands of kilometres and which have been interpreted as a set of palaeoshorelines of different ages [*Parker et al.*, 1989; *Clifford and Parker*, 2001]. The ocean is regarded to have existed within the Noachian era and covered as much as a third of the planet, and would therefore have represented a very substantial proportion of the total Martian water budget [*Clifford and Parker*, 2001].

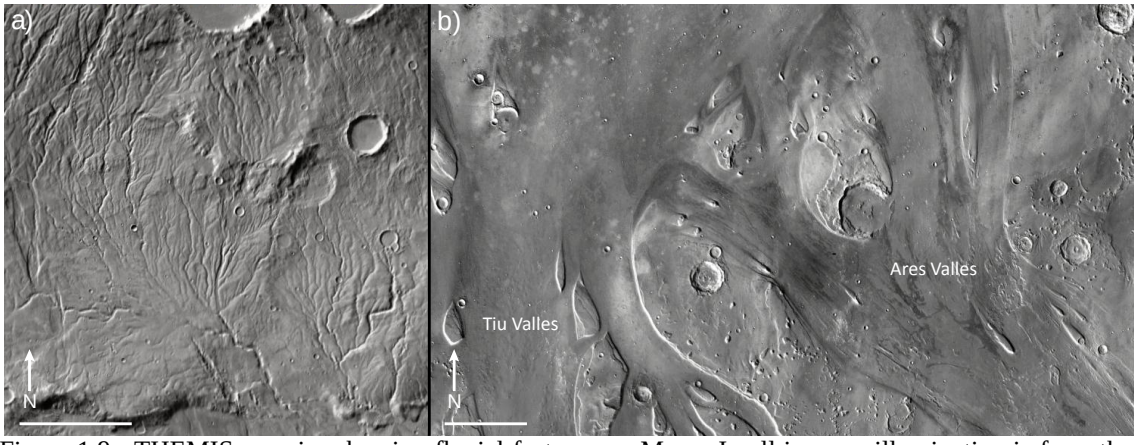

Figure 1.9. THEMIS mosaics showing fluvial features on Mars. In all images, illumination is from the left and scale bar is 50 km. (a) The Warrego Valles valley network, located within the southern highlands at 42°S, 267°E. (b) The mouths of the Tiu Valles and Ares Valles outflow channels, located at 17°N, 327°E. Flow originated from the south; note the streamlined 'islands' located within the channels.

As a result of climatic change, any liquid water present on the surface either froze or evaporated. There is no obvious way that so much water could have been lost from the planet via the inefficient mechanisms of permanent water loss that contributed to the loss of the atmosphere. *Clifford and Parker* [2001] considered the assimilation of the frozen ocean into the crust and the rise of the global water table to be a natural consequence of the deterioration of the post-Noachian climate and geothermal heat flow, and noted that a substantial relic of the ocean should continue to survive as massive ice deposits beneath the northern plains. These deposits would add to, and possibly exceed in volume, the currently known water reservoirs on Mars, namely the atmosphere, the seasonal and perennial polar caps, and the polar layered deposits.

1.3.3 Estimating the current Martian water budget

Several attempts, using quite different methods, have been made by researchers to estimate the past and present water inventories on Mars, often with widely differing results. The inventories of certain water reservoirs on Mars are generally expressed in terms of the depths of their 'global equivalent layers' (GEL), i.e. an equivalent, uniform layer of liquid spread across the entire planet [*Smith et al.*, 2001]. Past global water inventories have been estimated using volatile, noble gas and isotopic measurements of the Martian atmosphere (by the Viking landers) and the SNC (Martian) meteorites. Such studies have yielded results ranging from a global layer of depth less than 10 metres based on deuterium/hydrogen isotopes [*Yung et al.*, 1988] to several hundred

metres up to a kilometre, based on terrestrial ratios of H_2O, CO_2 and N_2 [*Pollack and Black*, 1979; *Carr*, 1986]. Likewise, models of planetary accretion and hydrodynamic atmospheric loss also give a broad range of the past and current total water inventory [*Fanale et al.*, 1992].

Attempts to estimate the water inventory on Mars have also been made by interpreting the geologic record, and the resultant estimates have tended to be less variable than those based on chemical evidence. *Carr* [1986] estimated the volume of rock material removed during the incision of the large outflow channels by assuming (conservatively) that an equal volume of water was needed to move the material; a global water inventory with a GEL of 40 metres depth was ascribed to the outflow channel waters alone. Based on palaeoshorelines skirting the northern plains, *Baker et al.* [1991] and *Parker et al.* [1989; 1993] postulated that the ocean hypothesized to cover the northern plains attained a GEL of depth 450 m. Volcanic gassing has also been thought to be an important mechanism for transferral of water from the interior. *Greeley and Schneid* [1991] estimated that a volume of water with a GEL of 150 m depth was outgassed in the last 3.8 Gyr, based on the observed record of volcanism. *Baker et al.* [1992] suggested that perhaps ten times that amount was degassed prior to preservation of the currently observable surface geology.

The values estimated for the past Martian water inventory may be compared with estimates of the current Martian water inventory. *Kieffer and Zent* [1992] estimated the volumes for known Martian water reservoirs. These reservoirs are:

- The atmosphere, which displays an average water vapour content of 0.01 kg m^{-2}, based on measurements of the Viking Mars Atmospheric Water Detector [*Farmer et al.*, 1976; 1977; *Farmer and Doms*, 1979; *Jakosky and Farmer*, 1982]. This is equivalent to a GEL of depth 10^{-5} m.
- The seasonal polar caps, which *Kieffer and Zent* [1992] presumed to contain water in approximately its atmospheric proportions, and which have a total mass of about a quarter that of the atmosphere [*Paige and Ingersoll*, 1985]. The water content is therefore equivalent to a GEL of depth 2.5×10^{-6} m.
- The perennial polar caps that remain after the summer retreat of the seasonal caps, and which differ markedly in extent and composition. *Kieffer and Zent* [1992] considered the south polar cap, which is less extensive than the north cap and is

comprised of a mixture of water and carbon dioxide [*James et al.*, 1992], to have a water content with a GEL of depth 0.6 m, and the north polar cap a GEL of depth 5.8 m.

- The polar layered deposits, which surround the perennial polar caps, and which comprise many layers of alternating light and dark albedo, caused by differing ice/dust ratios [*Thomas et al.*, 1992]. *Kieffer and Zent* [1992] estimated a GEL of depth 6.2 m. *Kieffer and Zent* [1992] arbitrarily set the thickness of both perennial caps and all layered deposits to be 1 km, and calculated their volumes based on the extents of the units as described by *Tanaka and Scott* [1987]. The ice content of the layered deposits was assumed to be 50% by volume.

There is therefore a considerable discrepancy between the currently observable water inventory (equivalent depth on a scale of metres) and the amount apparently required in order to be consistent with the aforementioned theoretical considerations (equivalent depth on a scale of hundreds of metres). *Clifford* [1993] hypothesized that the remaining water would mostly be sequestered within the early Noachian basement that had been fractured and brecciated by intense bombardment in Mars' early history. This would leave abundant pore space above the self compaction depth (that at which crustal porosity falls below 1%) that could potentially be occupied by volatiles. *Clifford* [1993] devised a model that predicts the distribution of water in both solid and liquid phase within the Martian megaregolith, based on assumed parameters including the porosity profile and various thermal properties of the crust, as well as the actual volume of water present. The thermal parameters will define the extent of the cryosphere, within which any water present will be frozen. If the cryosphere is saturated with water, any remaining water will exist beneath its base in liquid phase and will percolate down to the base of the porous region of the crust, creating a water table. The level that the water table reaches will depend on the crustal porosity profile and the volume of water beneath the cryosphere. *Clifford* [1993] created three models for the cryospheric thickness, each with different assumed parameters for the various crustal properties; these include a 'nominal' model, based on the best estimates for the values of the various physical properties at the time and which predicts an intermediate cryospheric thickness, a 'minimum' model, which predicts a very thin cryosphere, and a 'maximum' model, which predicts a very thick cryosphere. The latitudinal variation in cryospheric thickness is shown for each model in Table 4 and Fig. 5 of *Clifford* [1993], whereas the crustal profile for the nominal model is shown in Fig. 7 of *Clifford* [1993], with

illustrations of the different levels the water table would rise to for different sub-cryospheric water inventories.

Table 5 of *Clifford* [1993] displays the water storage potential of the cryosphere for each model, and for different surface porosities; the water inventories range from a GEL of depth 39 m (minimum model and a surface porosity of 20%) to 1382 m (maximum model and a surface porosity of 50%). It is therefore likely that the volume of ice present within the Martian megaregolith significantly exceeds the volume of water that has been estimated to exist within the atmosphere and various polar deposits, regardless of whether the cryosphere is saturated or not. If the cryosphere is saturated, and sub-cryospheric liquid water exists, then the aforementioned cryospheric water inventories will be underestimates for the entire water inventory of the Martian regolith; the three water table levels illustrated in Fig. 7 of *Clifford* [1993] correspond to sub-cryospheric water inventories equivalent to GELs of depths 10 m, 100 m and 250 m.

1.3.4 Evidence for shallow ground ice on Mars

The assertion by various studies that the Martian regolith should contain appreciable quantities of ground ice has been supported by observations of numerous geomorphological features on Mars that appear to result from the presence of shallow ground ice. These features include:

- *Debris flows:* Lobate debris aprons on Mars (Fig. 1.10a) appear noticeably similar to terrestrial rock glaciers, which are rock-ice masses that deform and flow viscously due to solid-state creep in the ice that cements the rocky debris (e.g. *Ives* [1940]; *Wahrhaftig and Cox* [1959]; *Thompson* [1962]; *White* [1976]). Other Martian features of apparently similar origin include lineated valley fill and concentric crater fill (Figs. 1.10b and 1.10c) [*Squyres*, 1978; 1979]. *Kargel* [2004] proposed that the massifs from which the debris flows emanate may be complex mixtures of ordinary lithic material and frozen volatiles, such as gas-bearing clathrate hydrates.
- *Rampart craters:* These craters display a thick ejecta sheet with a distinct low ridge or escarpment at its outer edge (Fig. 1.10d) [*Strom et al.*, 1992]. The ejecta sheet generally has a pronounced lobate outer margin, implying that the ejecta have been emplaced primarily as a radially directed surface flow, rather than ballistically. The most likely explanation for this is that the ejecta were emplaced as a mud flow, with the

water entrained within the ejecta having been derived from the melting of shallow subsurface ice by the impact [*Squyres et al.*, 1992b; *Gault and Greeley*, 1978].

- *Rootless cones:* These are closely spaced cinder cones, generally <100 metres across, that are interpreted to have been derived from phreatic eruptions, produced when lavas are emplaced over waterlogged or ice-rich substrate [*Thorarinsson*, 1953]. The ensuing violent vaporization of the water/ice results in expulsion of the lava from the explosion site [*Thorarinsson*, 1951; *Thorarinsson*, 1953; *Fagents and Thordarson*, 2007]. Repeated explosive pulses build a cone of disintegrated liquid and solid lava debris [*Thordarson et al.*, 1992]. Landforms imaged on Mars (Fig. 1.10e) bear a resemblance to rootless cones in Iceland that are known to form via this process. Rootless cones are the subject of study in section 1.4 and chapter 7 of the thesis.

- *Patterned ground:* Patterned ground on Earth is associated with ice wedging in periglacial regions [*Washburn*, 1973]. Polygons are the dominant form of patterned ground on Mars, and are found in close proximity to polar surface ice deposits [*Pechmann*, 1980] (Fig. 1.10f). The troughs defining them have upturned edges similar to cracks associated with active terrestrial ice-wedge polygons [*Lucchitta*, 1981], and in some cases the edges are seen to be covered with coarse boulders, which on Earth is usually attributed to freeze-thaw driven heaving and slow convection of permafrost in material composed of multiple grain sizes [*Kargel*, 2004].

- *Thermokarst and chaotic terrain:* Thermokarst is the process whereby melting of ground ice causes local collapse and formation of flat-floored, rimless depressions [*Carr and Schaber*, 1977]. Thermokarst terrain can incorporate chaotic terrain, which is characterized by jumbles of large, angular and arc-shaped slump blocks [*Sharp*, 1973]. Evidence in support of an origin related to ground ice includes several examples of large outflow channels that extend downslope from areas of chaotic terrain (Fig. 1.10g). Some areas of chaotic terrain appear to be likely centres of magma/water interaction (e.g. Dao and Niger Valles, shown in Fig. 1.3a).

- *Terrain softening:* The contrast between unsoftened and softened terrain is apparent in Fig. 1.10h. The unsoftened terrain displays sharp, angular relief, with crater rim slope profiles that are dominantly straight or concave upward. The softened terrain displays broader and gently rounded relief, with crater rim slope profiles that are dominantly convex upward. These observations suggest that in certain areas of Mars,

the crust contains a high enough proportion of ice to allow the topography to flow viscously over geological timescales [*Squyres*, 1989; *Squyres et al.*, 1992b].

The temperature and atmospheric pressure conditions at the surface of Mars are such that water ice is stable at middle to high latitudes throughout the Martian year, and perennially unstable at low latitudes [*Farmer and Doms*, 1979]. Any ice present in the megaregolith at low latitudes would gradually be lost to the atmosphere over geologic timescales. The result is an ice-free, desiccated zone at latitudes less than 30° that probably ranges from 0 to 200 metres in thickness [*Coradini and Flamini*, 1979; *Clifford and Hillel*, 1983; *Fanale et al.*, 1986; *Mellon et al.*, 1997]. Below this depth, ice may still exist, and the warm surface temperature at low latitudes would imply a shallower level of the melting isotherm. The distribution of various geomorphological features regarded to have resulted from the presence of near-surface ice has been found to correspond to predictions of where near-surface ice should exist on Mars [*Squyres and Carr*, 1986; *Costard*, 1988; 1989; *Kuzmin et al.*, 1988; 1989].

Figure 1.10 (following page). Images of geomorphological features on Mars whose appearances are considered to have been influenced by the presence of shallow ground ice. Illumination is from the left in all images, except for the HRSC mosaic in (d), where the illumination is from the right. (a) Detail of MOC narrow-angle image M18-00897 showing a Martian rock glacier or debris-covered glacier located at 38.5°S, 113°E in Hesperia Dorsa. The flow has originated from near the crest of a crater rim and flowed towards the floor of the crater. Scale bar measures 1 km. (b) Detail of THEMIS visible image V18083026 showing lineated valley fill in Nilosyrtis Mensae emanating from the hills bordering the valley. Scale bar measures 5 km. (c) Detail of HRSC image SEM80HRMD6E of a 'block' glacier in the Hellas Montes, located at 38°S, 104°E. The glacier has flowed from a flank of a massif into an impact crater, and then progressed westwards into a larger crater, 500 metres beneath. North is to the left. Scale bar measures 10 km. (d) HRSC mosaic showing Yuty, a rampart crater located at 22.5°N, 326°E. The crater displays ejecta deposits consisting of multiple overlapping lobes, indicative of ejecta emplacement by viscous flow across the terrain. Scale bar measures 10 km. (e) Detail of MOC narrow-angle image M0800090, showing a rootless cone field in the southwestern Cerberus Plains, located near 2.6°N, 144°E. Scale bar measures 1 km. (f) MOC narrow-angle image MOC2-564, showing polygonal ground located on the impact ejecta of Lyot crater at 54.5°N, 33.5°E. The polygonal margins comprise ridges with large boulders on them, apparent as dark lines. Scale bar measures 1 km. (g) THEMIS daytime infrared mosaic showing the chaotic terrain of Hydaspis Chaos, located at 3°N, 333°E. Two outflow channels emanate from the chaotic terrain, one leading to Tiu Valles to the northwest of the image, the other leading to Ares Vallis to the northeast of the image. Scale bar measures 50 km. (h) THEMIS daytime infrared mosaics comparing 'unsoftened' and 'softened' terrain. Left image displays unsoftened terrain located at 24°S, 133°E. Right image displays softened terrain located at 33°N, 45°E. Scale bar measures 20 km in both images.

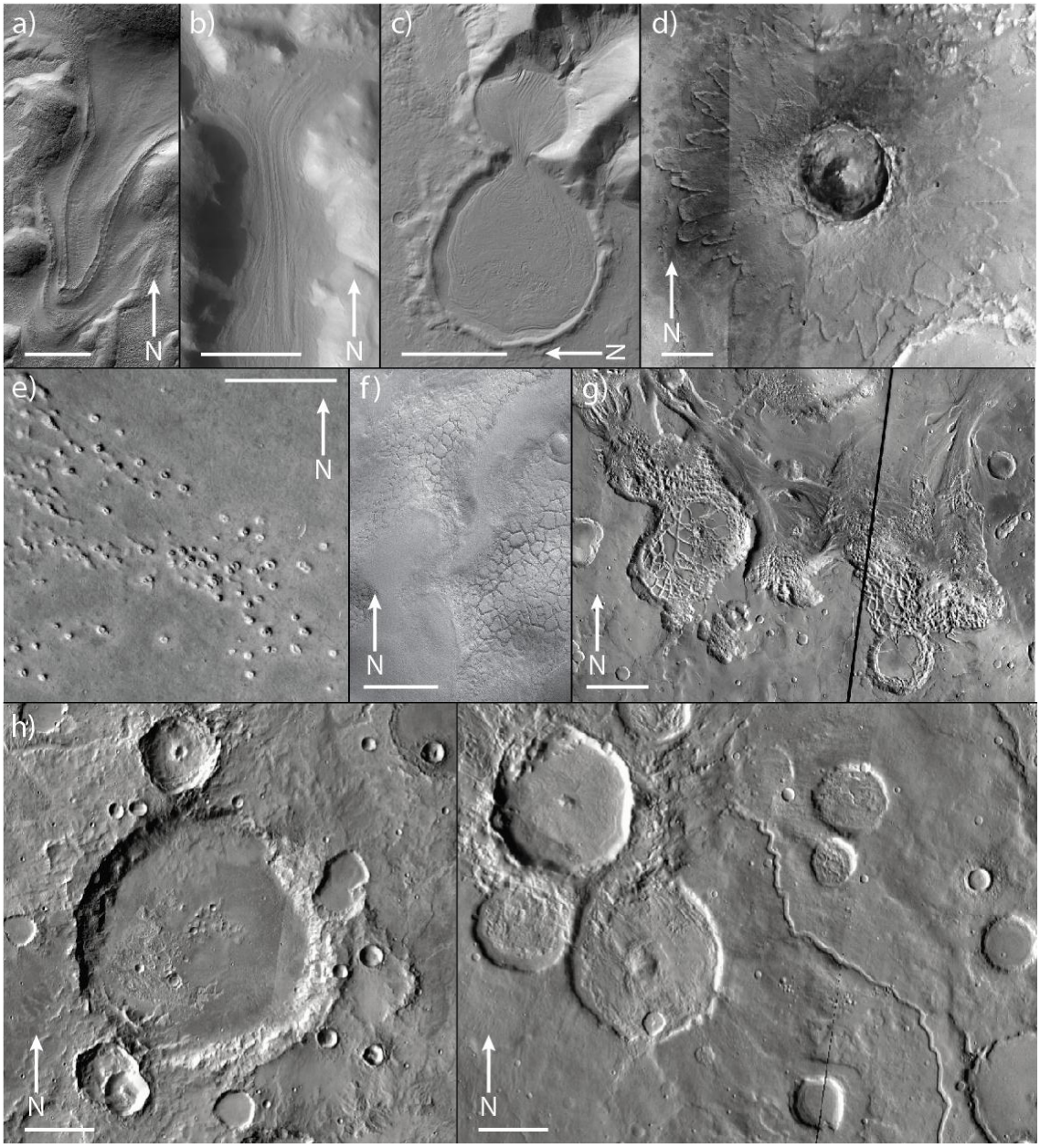

The location of ice within the cryosphere has been experimentally constrained to an extent by recent data from the Mars Odyssey orbiter and the Phoenix lander. Data acquired by the Neutron Spectrometer aboard Mars Odyssey [*Feldman et al.*, 2004] indicated that hydrogen-rich deposits ranging between about 20% and 100% water-equivalent by mass are found to a depth of ~1 metre poleward of ±60° latitude (see Fig. 1.11). Water ice was directly proven to be the source of the hydrogen signatures in 2008 when NASA's Phoenix lander touched down on polygonal terrain in the northern plains (latitude 68°N, longitude 234°E), which is located within the region where the

Mars Odyssey data predicted that near-surface ground ice should exist at concentrations of between 32% and 64%. Phoenix dug several trenches into the Martian soil, uncovering a continuous layer of ice at a depth of ~5 cm below the surface [*Smith*, 2009]. Evidence for a consistent near-surface layer of water ice at high latitudes also exists in the form of HiRISE observations of high-albedo deposits surrounding small (<10 m diameter) impact craters that have impacted into the mid-latitude (43.3°-55.6°N) northern hemisphere in the several months preceding observation [*Byrne et al.*, 2009]. Spectra obtained by CRISM (a visible/infrared spectrometer) of the largest of the bright deposits show clear water absorption features, and the deposits have been seen to sublime over a period of months.

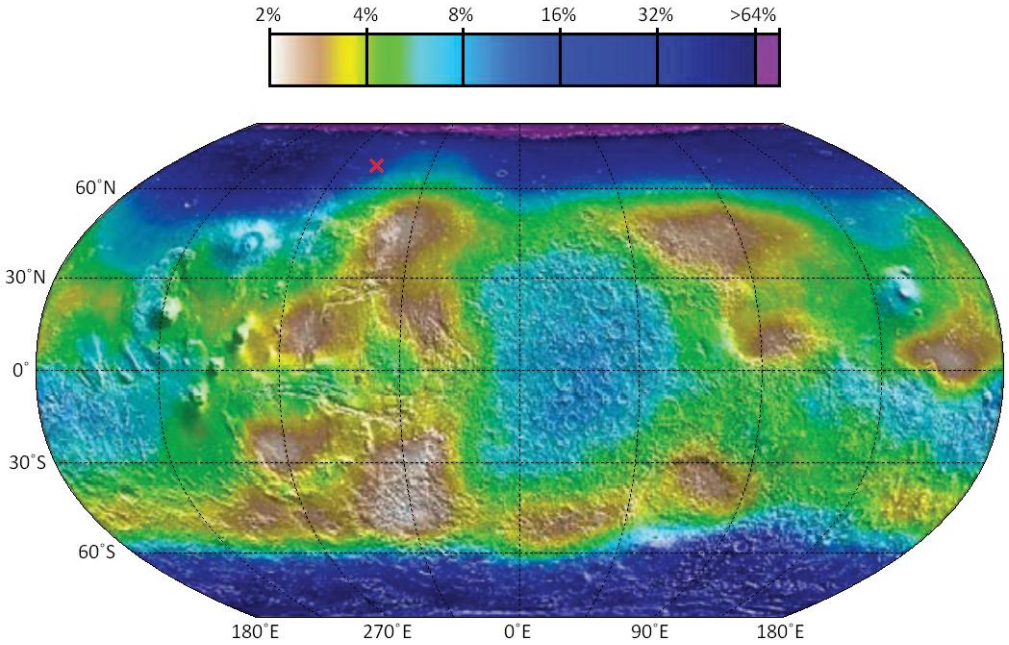

Figure 1.11. Adaptation of Fig. 4 of *Feldman et al.* [2004], showing the water-equivalent hydrogen content of the semi-infinite layer of water-bearing soils derived from epithermal-neutron counting rates, as determined by the Mars Odyssey Neutron Spectrometer. The location of the Phoenix lander is highlighted by the red cross.

1.3.5 The significance of sounding radar for constraining the Martian water budget

To date, observations at Mars have confirmed that shallow ground ice exists in apparently high concentrations within the shallow subsurface poleward of the mid-latitudes. *Squyres* [1989] attempted to estimate the depth to which such an ice layer might extend by devising a finite-element model of crater relaxation in a viscous medium, whose thickness could be varied, overlying a rigid substrate. The model indicated that the resulting crater morphology for the thinnest viscous surface layer (of 2

km) most closely matched the crater morphologies seen in areas of terrain softening. Yet despite such modelling, there is as yet no direct evidence of how deep these deposits extend, and therefore of their total contribution to the Martian water inventory. Determination of the vertical and lateral extents of the ice deposits requires a geophysical method that allows visualisation of the Martian subsurface.

The most practical method by which to accomplish such a task is through the technique of sounding radar. The theory and practice behind sounding radar will be discussed in detail in chapter 4, but the method essentially involves the transmission of an electromagnetic signal at radio frequency towards a planetary surface from an orbiting satellite. As the signal encounters boundaries between materials having different electrical properties (including the surface/atmosphere boundary as well as any subsurface discontinuities), a proportion of the energy of the signal will be reflected back upwards and recorded by the radar sounder. The magnitude of the proportion of energy returned depends on the contrast in electrical properties across the discontinuity; a stronger contrast will produce a stronger echo. The primary objective of the Mars Advanced Radar for Subsurface and Ionospheric Sounding (MARSIS) [*Picardi et al.*, 2005; *Jordan et al.*, 2009], an instrument aboard the European Space Agency's Mars Express satellite, is to resolve the boundaries of ice layers and aquifers within the Martian crust using this method. The sounder operates at low frequencies (1.4-5.3 MHz) in order for the transmitted signals to penetrate to large depths: this increases the probability of detection of an ice layer or aquifer. Based on the depth at which such an aquifer or ice layer is found to exist, the volume of water comprising the body may be estimated based on models of the crustal porosity profile, such as that presented by *Clifford* [1993].

Prior to the deployment of MARSIS, sounding radar had only been used in one instance to study the subsurface of a planetary body, namely the Apollo lunar sounder experiment (ALSE) which studied the lunar subsurface [*Phillips et al.*, 1973a; 1973b; *Porcello et al.*, 1974]. ALSE was succeeded by the Lunar Radar Sounder (LRS) aboard the Japanese SELENE lunar orbiter, which was launched in September 2007, two years after the deployment of MARSIS [*Ono and Oya*, 2000]. These sounders succeeded in identifying radar reflectors down to a depth of 1.6 km beneath the surfaces of Mare Serenitatis and Mare Crisium; these were interpreted to be basin-wide subsurface interfaces representing buried regolith layers accumulated during the depositional hiatus

of mare basalts [*Peeples et al.*, 1978; *Ono et al.* [2009]. ALSE data also aided in the interpretation of the formation of ridge systems within Mare Serenitatis [*Maxwell et al.*, 1975]. The fourth planetary radar sounder to be deployed is the Mars Shallow Radar Sounder (SHARAD) aboard NASA's Mars Reconnaissance Orbiter, which launched a few months after MARSIS was deployed [*Seu et al.*, 2007]. This sounder operates at a higher frequency than MARSIS, thereby resolving subsurface structure to a shallower depth but at a higher resolution.

MARSIS and SHARAD have already aided in constraining the locations and sizes of water reserves on Mars by resolving the bases of the polar perennial ice caps and layered deposits [*Plaut et al.*, 2007a], and by confirming the high ice content of debris flows [*Holt et al.*, 2008]. *Plaut et al.* [2007a] reported that the south polar layered deposits and perennial ice cap contain a volume of water with a GEL of depth 11 ± 1.4 m; while a corresponding volume for the northern polar cap and layered deposits has not yet been published, *Plaut et al.* [2007a] noted that MARSIS observations of the base of the northern deposits suggests that their volume will be similar to those of the southern deposits. This would imply a total contribution to the global water inventory that has a GEL of ~22 m depth, a significant increase on the 12.6 m estimate by *Kieffer et al.* [1992]; *Smith et al.* [2001] estimated a GEL of 16 to 22 m based on measurements of the Mars Orbital Laser Altimeter on board the Mars Global Surveyor. Based on SHARAD observations in the eastern Hellas region, *Holt et al.* [2008] estimated that the volume of water ice sequestered within the eastern Hellas lobate debris aprons may represent a GEL of 0.2 m depth, or 1% of the total volume contained within the polar caps.

1.3.6 Aims of the study

Current ideas regarding the effect of magma interaction with water on Martian volcanic geomorphology have been presented in section 1.2.2.4. Given the evidence for large volumes of water, whether in liquid or solid phase, to have existed on the Martian surface or within its crust throughout its history, it is inevitable that such water will have interacted variously with intrusive magma or extrusive lava at some stage. The importance of magma-water interactions would essentially have been determined by the geometry of the intruded magma or extruded lava in relation to the cryosphere and hydrosphere, and the amount of water in the hydrosphere at the time of intrusion [*Head*

and Wilson, 2002]. *Head and Wilson* [2002] noted that new insights into the geometry of interactions and their consequences from high-resolution images, radar sounding and surface exploration, and basic physical models (e.g. *Clifford* [1993]; *Wilson and Head* [1994; 2002b]), can help to decipher the record of magma-water interaction on Mars.

The results returned by MARSIS will therefore be relevant to the history of volcanism on Mars as well as the history of water. By examining and analysing the radar profiles returned from MARSIS, this study aims to identify subsurface reflections that may plausibly be caused by the presence of an ice layer or an aquifer. Based on the spatial extents, both lateral and vertical, across which such water/ice bodies are found to extend, the potential for interaction with magmatism/volcanism may be assessed. This would involve correlation of the reflections seen in the MARSIS radar profiles with volcanic geomorphology seen at the surface. Depending on the quality of the results, potential applications of this research include the following:

- The MARSIS data may be used as an additional test for determining the extent to which magma-water interaction has characterised the formation of certain volcanic landforms based on comparison of the locations of subsurface water/ice bodies and those of the volcanic features in question. If extensive crustal water/ice bodies are found to underlie such volcanic features, and exist at depths that are appropriate for intrusive magma systems to occur at, then the evidence for the occurrence of magma-water interactions will be bolstered, although the sequence of emplacement of geological units will have to be considered (i.e. whether the water body predated the volcanic edifice and associated magmatic systems). The Martian paterae (e.g. Hadriaca and Tyrrhena Paterae), where the influence of magma-water interaction has been debated (e.g. *Greeley and Spudis* [1981]; *Gregg and Williams* [1996]), are among the key sites on Mars for MARSIS radar profiles to be recorded for this purpose.
- The volume of water contained within a particular volume of the crust may be estimated based on modelling of the crustal porosity profile (e.g. *Clifford* [1993]). By estimating the size of the intrusive system beneath an edifice, the volume of water involved in the interaction may also be estimated.
- The extent to which the upper part of the cryosphere is dehydrated in equatorial regions, but hydrated at higher latitudes, may be determined. The present distribution of rootless cones and other geomorphological features indicative of surface magma-water

interactions may then be used to reconstruct ancient palaeolatitudes [*Head and Wilson*, 2002].

1.4 Rootless cones on Earth and Mars

1.4.1 Current knowledge regarding rootless cone formation processes

Rootless cones (or pseudocraters) represent one of the volcanological features that are indicative of the interaction of lava with ice/water. On Earth, the best examples are found in Iceland. While rootless cones have formed in recent history (those on the Laki flow of 1783-4 are the youngest), no written record of their formation process exists, and their currently accepted mode of formation was originally developed by *Thorarinsson* [1951]. They are formed as a result of explosive lava-water interaction, whereby flowing lava encounters a waterlogged substrate, causing violent vaporization of the water and expulsion of the lava from the explosion site [*Thorarinsson*, 1951; *Thorarinsson*, 1953; *Fagents and Thordarson*, 2007]. Repeated explosive pulses build a cone of disintegrated liquid and solid lava debris [*Thordarson et al.*, 1992] (see Fig. 1.12). As the activity at a given site wanes, explosions may be initiated elsewhere, leading to construction of a field of tens to hundreds of cones [*Fagents and Thordarson*, 2007].

Rootless cones typically have the following components in their structure, as described by *Fagents and Thordarson* [2007]: 1) a lower, broad, well-bedded apron with decimetre to metre thick beds of lapilli scoria (between 2 and 64 mm in diameter [*Fisher*, 1961]) alternating with thinner (<0.2 m), crudely laminated beds of excavated substrate sediment mixed with black ash (<2 mm in diameter [*Fisher*, 1961]); 2) an overlying, crudely bedded sequence of larger (centimetre- to decimetre-sized) spatter bombs and agglutinates; 3) a 1-2 m thick unit of rheomorphic spatter capping the cone [*Thordarson et al.*, 1992; *Thordarson and Höskuldsson*, 2002].

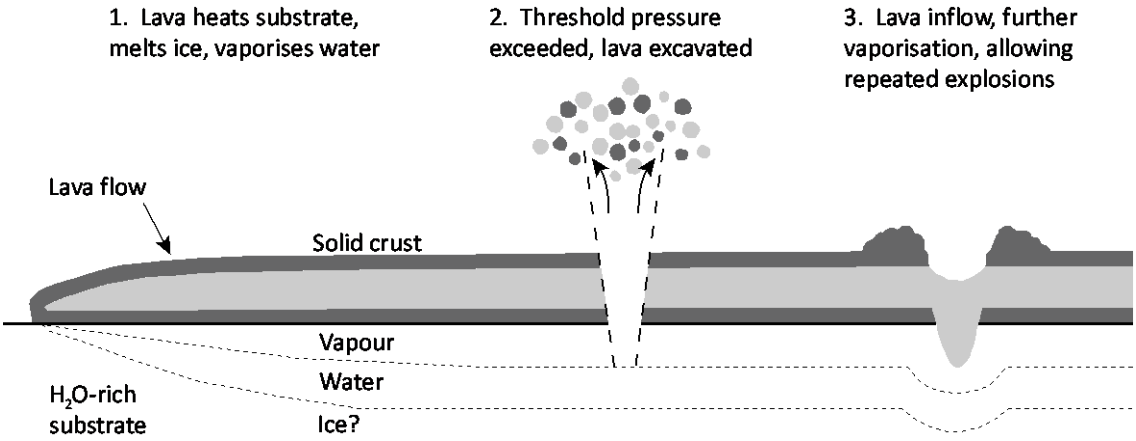

Figure 1.12. Diagram depicting stages of rootless cone formation. Figure originally shown as Fig. 9 in *Fagents et al.* [2002].

The morphologies and clast sizes of rootless cones vary between localities in Iceland. The diversity has previously been attributed to variations in the efficiency of lava-water interaction, which affects the intensity of the eruptions [*Fagents et al.*, 2002]. At Mývatn, the cones range from several metres to a few hundred metres across, have large central craters and convex flanks, sometimes exist as double (or even triple) cones, and display relatively small clast sizes (Fig. 1.13a). The Mývatn cones formed on a lava flow within a lacustrine environment [*Thorarinsson*, 1953], where the interaction between water and lava would have been particularly efficient. In contrast, the cones of the Álftaver district in south Iceland formed on a lava flow that was emplaced on a jökulhlaup floodplain, where lower water concentrations would have existed in the subsurface [*Greeley and Fagents*, 2001]; these cones generally have smaller diameters than those at Mývatn and display small or no summit craters, steep 'witches' hat' profiles with concave flanks, and coarser clast sizes, all interpreted to be indicative of less vigorous interaction (Fig. 1.13b) [*Fagents et al.*, 2002]. Factors regarded as being influential on the explosive intensity are the mass ratio of interacting water and melt, the contact geometry of the interacting materials, rate of injection of the melt, and the degree of interpenetration of melt and water [*Wohletz*, 1983, 1986; *Wohletz and McQueen*, 1984; *Zimanowski et al.*, 1991; *Fröhlich et al.*, 1993].

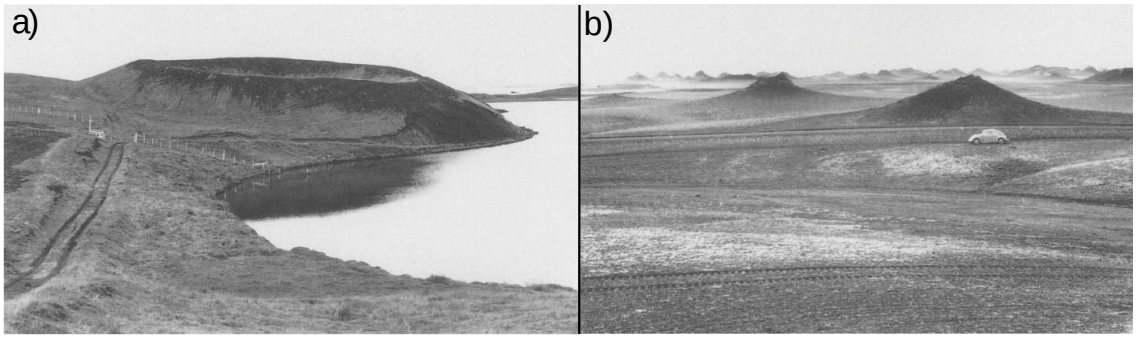

Figure 1.13. Icelandic rootless cones. (a) Rootless cones at lake Mývatn typically have large craters and steep, convex-up slopes. (b) Rootless cones of the Álftaver district typically have small craters and steep, 'witches' hat' profiles. Figure originally shown as Fig. 1 in *Fagents et al.* [2002].

In recent decades, Icelandic rootless cones have attracted attention from planetary scientists due to the observation on Mars of structures that share similar characteristics, including size, morphology and spatial distribution (see Fig. 1.14) [*Frey et al.*, 1979; *Frey and Jarosewich*, 1982; *Lanagan et al.*, 2001; *Greeley and Fagents*, 2001; *Fagents et al.*, 2002; *Fagents and Thordarson*, 2007; *Bruno et al.*, 2004]. The Martian cones were originally identified in Viking images [*Frey et al.*, 1979; *Frey and Jarosewich*, 1982], and more recently have been seen in greater detail by the Mars Orbiter Camera aboard Mars Global Surveyor (1.5 to 10 metres per pixel [*Malin et al.*, 1992]). These structures tend to occur in large groups in the plains regions of the northern hemisphere. The Martian cones are typically larger (100-500 m) than terrestrial ones (10-100 m), probably because the lower gravitational acceleration and atmospheric density allow clasts to be flung to greater distances [*Fagents et al.*, 2002].

If the Martian cones are indeed formed in a similar manner to terrestrial rootless cones, it would imply that a volatile of some sort, most likely water ice, was present in the near surface in the areas where the cones exist (often at low latitude, some only a few degrees from the equator) during the time of their formation. Impact crater-frequency relationships based on small (less than several 100 m diameter) craters indicate that the surfaces upon which the cones sit may be no older than 10 Ma [*Lanagan et al.*, 2001]. The implication that water ice has been present at shallow depths beneath the surface in such geologically recent times and so close to the equator suggests that near-surface ground ice reserves have likely existed into the present day and may be widespread across the planet. Data from the Mars Odyssey orbiter [*Feldman et al.*, 2004] and Phoenix lander [*Smith*, 2009] missions suggest that a continuous layer of ground ice exists within the top several tens of centimetres of the

Martian surface at latitudes greater than ±60°, although to what depth the ice extends is unknown. The seemingly paradoxical scenario of the continued existence of ground ice at lower latitudes, where the present mean annual surface temperature exceeds the frost point of 200 K by more than 20 K [*Squyres et* al, 1992], has been addressed in the studies of *Smoluchowski* [1968], *Kuzmin* [1978], *Clifford and Hillel* [1983], and *Fanale et al.* [1986]. The results of modelling performed by *Clifford and Hillel* [1983] indicated that the conditions necessary for the long-term survival of ground ice may exist in isolated regions within the equatorial regolith, and that if massive ground ice does currently exist there, its presence may imply the existence of a replenishment mechanism.

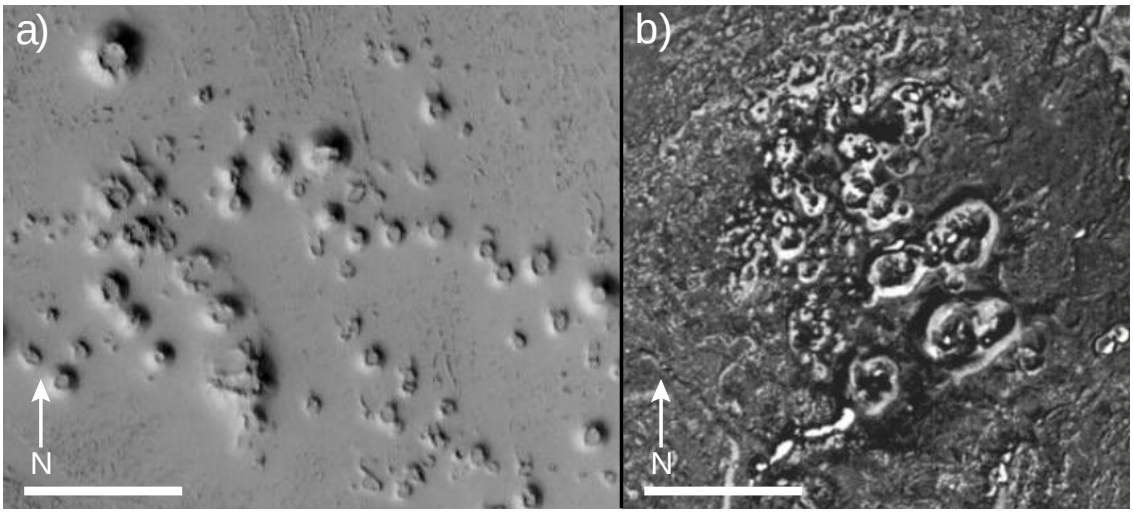

Figure 1.14. Comparison of rootless cone fields on Mars and Earth. Scale bar measures 500 m for both images. Figure adapted from Fig. 2 in *Lanagan et al.* [2001]. (a) MOC image M08/01962 (26.0°N, 189.7°W) showing a cluster of potential rootless cones north of the Cerberus plains. Image is illuminated from the left. (b) Aerial photo of rootless cone field in Laki lava flow north of Innryi Eyrar, Iceland. Image is illuminated from the right.

The progression of clast size from finer-grained ash in the outer apron to coarser lapilli scoria and ultimately agglutinate spatter at the summit is indicative of a decrease in the explosiveness of the water-lava interaction with time, which is itself indicative of a change in the water/lava mass ratio conditions [*Fagents and Thordarson*, 2007]. Knowledge of the proportions of different rock facies comprising rootless cones can therefore aid with respect to estimating the mass of water involved in forming a cone of a certain size. The diameters of some outer aprons have been measured: *Greeley and Fagents* [2001] measured those of rootless cones in Álftaver finding that the outer aprons are typically 1.2 to 10 times the inner cone width. However, actual volumes of

individual units have not been constrained, leaving their true contributions to the total volume of material erupted as yet undetermined. *Greeley and Fagents* [2001] suggested that it is likely that the majority of the cone's volume is contained within the outer apron.

Yet the proportions of different facies comprising a present-day cone are not only dependent on the evolution of the water/lava mass ratio during the formation of the cone, but also on the effects of erosion since formation. The resultant morphology will also be subject to factors including the consolidation of different facies comprising the cone, the intensity of the erosional environment in which the cones are located, and the time elapsed since the cones formed. The extent to which erosion has removed material from the cones will translate into error in calculations of the water masses required to expel the cone material. *Fagents et al.* [2002] stated that there is some uncertainty associated with Álftaver cone morphology because of erosion/deposition due to historic jökulhlaups, and the Martian rootless cones will have also likely experienced erosion/modification by aeolian and impact cratering processes to some extent since their formation. While the erosional environment is not as intense on Mars as on Earth, the Martian cones have evidently existed for much longer than the terrestrial cones – possibly several million years according to *Lanagan et al.* [2001], whereas the parent lava flows of the Icelandic cones are no more than a few thousand years old [*Thorarinsson*, 1951; *Larsen*, 2000; *Thordarson et al.*, 2001].

1.4.2 Aims of the study

Rootless cones exist within an entirely different size range to the volcanic edifices on Mars and Venus that are the main focus of the thesis. The study of rootless cones therefore remains distinct from that of intermediate-sized volcanic edifices on Mars and Venus, yet the topic of comparative volcanology of rootless cones on Earth and Mars is nevertheless regarded as being consistent with the overarching premise of the thesis. In addition, this study allows original fieldwork to be performed on terrestrial planetary analogue features.

This study primarily reports results from an expedition mounted to the Álftaver district of Iceland in August 2008. The fieldwork employed a combination of ground-penetrating radar (GPR) surveying, topographic surveying, geomorphological observation, and petrological analysis to constrain the configurations and relative

proportions of different facies in the interiors of rootless cones. The ultimate goals of the study are to assess the extent to which formation conditions and subsequent erosion/modification have influenced the current morphologies of the cones. The results will have implications for the erosional histories of the cones observed on Mars, based on comparisons between cone morphologies on both planets.

A previous expedition was made to the rootless cone field at Mývatn in July 2007, although conditions there were not favourable for radar surveying and pit-digging: much of the terrain was thickly vegetated, impeding the GPR surveys and preventing pit digging from taking place. The rootless cone field of the Álftaver district was chosen for the new survey primarily because of its suitability for GPR surveying and pit-digging. The cones generally have a widely-spaced distribution, virtually all of them are accessible, and the vegetation cover is light. The radar profile of one of the Mývatn cones is included in this study for the purposes of comparison with the Álftaver cones.

1.5 Thesis structure

This thesis comprises eight chapters. Chapter 1 has provided background on current knowledge and outstanding questions in each of the three research areas on which the thesis will focus. Chapter 2 describes the data collection methodology for the catalogue of volcanoes on Mars and Venus, the classification system of volcanic edifices, the format of the catalogue, and the results of the volcano survey. Chapter 3 interprets the results of the volcano survey. Chapter 4 describes the theory and practice of radar sounding and ground-penetrating radar. Chapter 5 surveys the reflections that have been observed by MARSIS, focusing in particular on an anomalous group of large-scale reflections in the southern highlands that are of ambiguous origin. Chapter 6 discusses the implications of MARSIS observations for constraining the location, phase and volume of crustal water on Mars, and the corresponding implications for the history of magma-water interaction. Chapter 7 presents and interprets the results of the GPR surveys performed at the rootless cone fields in Iceland, and discusses the implications of the findings there for the histories of Martian cones. Chapter 8 summarizes the findings of all three research aspects of the thesis and suggests directions of future work.

Chapter 2
Compilation and Results of the Venusian and Martian Intermediate-Sized Volcano Catalogue

2.1 Data collection methods

Data collection for this catalogue entails the compilation of global databases of the location, dimensions and morphological characteristics of all identified, intermediate-sized volcanic features on Mars and Venus. This was accomplished through detailed surveys of the available remote sensing and altimetry datasets for Mars and Venus, which for Venus include stereo images (see section 2.1.1). The datasets used are as follows:

Mars:

- Visible images from the Visual Imaging Subsystem (VIS) cameras aboard the two Viking Orbiters, which feature six bands covering wavelengths ranging from 350 to 700 nm. The entire surface of the planet is mapped at a resolution of 150 to 300 m/pixel, achieving a maximum resolution of 8 m/pixel [*Thorpe*, 1975; *Carr et al.*, 1976]. Dataset available at the USGS Map-a-Planet website: pdsmaps.wr.usgs.gov/maps.html
- Multi-spectral thermal-infrared images from the Thermal Emission Imaging System (THEMIS) aboard Mars Odyssey, which features nine ~1 μm bands covering wavelengths ranging from 6.3 to 15.4 μm. Nearly the entire planet is mapped at a resolution of 100 m/pixel [*Christensen et al.*, 2004]. Dataset available at the JPL OnMars website (onmars.jpl.nasa.gov/) and the THEMIS website (global-data.mars.asu.edu/bin/themis.pl).
- Visible images from the Mars Orbiter Camera (MOC) aboard Mars Global Surveyor, which features a narrow angle camera that covers wavelengths from 500 to 900 nm. Resolution of the narrow angle camera ranges from 1.4 to 12 m/pixel. Narrow angle camera has obtained more than 50,000 images of Mars with image sizes ranging from 2.8 km × 2.8 km to 2.8 km × 25.2 km [*Malin et al.*, 1992]. Dataset available at the JPL OnMars website (onmars.jpl.nasa.gov/) and the MOC website (www.msss.com/moc_gallery/).
- Visible images from the High Resolution Imaging Science Experiment (HiRISE) aboard Mars Reconnaissance Orbiter, which covers wavelengths from 550 to 850 nm

[*Delamere et al.*, 2009]. Resolution of HiRISE reaches 0.25 to 1.3 m/px over >1% of the planet's surface [*McEwen et al.*, 2007]. Dataset available at the HiRISE website: hirise.lpl.arizona.edu/

- Altimetry maps from the Mars Observer Laser Altimeter (MOLA), which achieves a vertical resolution of 1.5 m with a footprint of 160 m by 300 m over the entire planet [*Zuber et al.*, 1992]. Maps are available at the USGS Map-a-Planet website (pdsmaps.wr.usgs.gov/maps.html) and the raw data at the PDS Geosciences Node (pds-geosciences.wustl.edu/missions/mgs/megdr.html).

Venus:

- Magellan Synthetic Aperture Radar (SAR) full-resolution radar maps (F-Maps), obtained at a wavelength of 12 cm. Maximum resolution of the maps is 101 m/pixel cross-track and 110 m/pixel along-track [*Ford and Plaut*, 1993] over 90% of the planet's surface. Dataset available at the USGS Map-a-Planet website: pdsmaps.wr.usgs.gov/maps.html
- Magellan SAR mosaics of compressed-resolution image swaths (C1-MIDRs), obtained at a wavelength of 12 cm. Maximum resolution of 225 m/pixel [*Saunders et al.*, 1990] over 90% of the planet's surface. Dataset available at the USGS Map-a-Planet website: pdsmaps.wr.usgs.gov/maps.html
- Magellan Global Topography Data Record (GTDR) altimetry maps, which achieve a vertical resolution greater than 50 m, and a lateral resolution of ~10 km where the surface roughness is not too extreme [*Saunders et al.*, 1990]. Dataset available at the USGS Map-a-Planet website (pdsmaps.wr.usgs.gov/maps.html).

2.1.1 Magellan SAR data interpretation and stereo imaging

Radar observations represent the only method by which the surface of Venus (normally obscured by clouds across the entire globe) may be imaged. The extent to which the transmitted microwave frequency signals (λ = 12 cm, f = 2.5 GHz) are reflected back to Magellan (termed the backscatter), and therefore the resulting brightness apparent in the radar image, will depend on topographic effects, surface roughness, and electrical properties [*Ford and Plaut*, 1993], the former two of which are influenced to an extent by variations in the radar incidence angle. Terrain that slopes towards the imaging sensor appears bright relative to terrain that slopes away. Where

the incidence angle, θ, is less than 20°, small changes in slope will produce large changes in backscatter. In the absence of topographic effects, surface roughness at the scale of the radar wavelength may dominate backscatter where θ is greater than 20° and less than 60°. *Campbell and Rogers* [1994] noted that an increase in surface roughness at a scale of centimetres to metres acts to increase the strength of the SAR echo. The factors of topography and surface roughness will be most influential with respect to determining backscatter magnitude but the dielectric constant value of the surface material (controlled by composition and/or bulk density) will also affect the radar backscatter; higher dielectric constants enhance backscatter [*Ford and Plaut*, 1993].

The primary Magellan mission was divided into three 'imaging cycles', each lasting a single Venusian day (243 Earth days). In each cycle, the probe was inclined at a different 'look angle'. The first cycle was left-looking with incidence angles varying from 16° to 46° (covering 83.7% of the surface); the second cycle was right-looking with incidence angles varying from 13° to 25° (covering 54.5% of the surface); the third cycle was left-looking with incidence angles varying from 13° to 36° (covering 21.3% of the surface) [*Moore et al.*, 1992]. The cumulative coverage of the surface was 98%. This meant that a large proportion of the terrain on Venus was imaged at different incidence angles – separate points in an image seen at different incidence angles will appear to be displaced relative to each other, with the greatest displacement arising for the highest relief terrain. Smaller incidence angles produce greater distortion for a given amount of topographic relief. High areas will return an echo sooner than the surroundings, and thus are displaced toward the spacecraft in the image plane; the opposite is true for low areas [*Plaut*, 1993]. These effects are known as 'foreshortening' and 'elongation', respectively. While such effects can often complicate analyses of radar images, such a dataset has two important applications [*Moore et al.*, 1992]:

- Stereopsis achieved by simultaneous viewing of paired left-looking images of the same scene permits three-dimensional perception and interpretation of the morphologies of landforms at resolutions much finer than the altimetry footprints.
- Measurements of differences of image displacements (parallax) on paired images with known imaging geometries provide quantitative estimates of the relief and shapes of landforms.

A three-dimensional stereoscopic image of the Venusian terrain is obtained by pairing side-by-side under a stereoscope two images of the same scene that have been obtained at different incidence angles; the stereoscope directs one image of the stereo pair to one eye and the other image to the other eye [*Plaut*, 1993]. The stereo images used in Magellan stereo data are same-side (both left-looking but with different incidence angles); opposite-side (left- and right-looking) stereo image pairs are often difficult to fuse with a stereoscope. For most Magellan stereo data, the Cycle 1 image (large incidence angle) goes to the left eye, and the Cycle 3 image (small incidence angle) goes to the right eye. When the images are perceived to merge, variations in relief become apparent as a three-dimensional image. The perceived relief has a vertical exaggeration about five to ten times the actual relief, depending on the incidence angles used [*Leberl et al.*, 1992].

By comparing the distortions on two images obtained at different incidence angles, the heights of features can be determined. This method of height calculation offers a more accurate, but more time-consuming, alternative to determining heights using Magellan altimetry data, which achieves relatively poor vertical and lateral resolution. The heights of features can be determined using same-side as well as opposite-side stereo images. Both methods are illustrated in Fig. 2.1.

Equations 2.1 and 2.2 allow calculation of feature heights in Figs. 2.1a and 2.1b, respectively:

$$h = \frac{d_2 - d_1}{\cot\theta_1 + \cot\theta_2} \tag{2.1}$$

$$h = \frac{d_1 - d_2}{\cot\theta_2 - \cot\theta_1} \tag{2.2}$$

An example of identical terrain seen in opposite-side stereo images, and the resulting ‘relief displacement’, is shown in Figs. 2.2a and 2.2b. An example of identical terrain seen in same-side stereo images is shown in Figs. 2.2c and 2.2d.

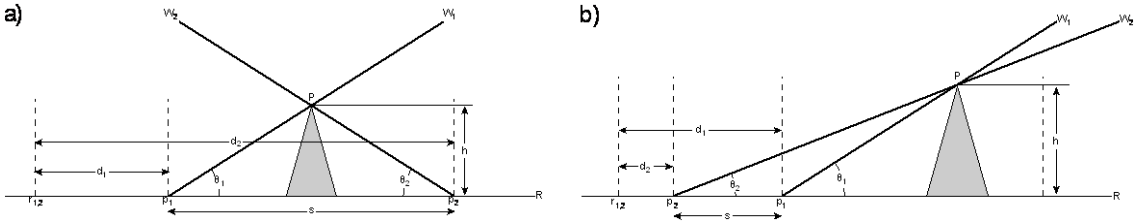

Figure 2.1. Solving for heights using opposite-side (a) and same-side (b) stereo images. Measurements are taken from the separate images of a stereo image pair to determine the height of point *P* above the reference plane, *R*. W_1 and W_2 are separate wavefronts travelling at different incidence angles during different imaging cycles of Magellan – both intercept point *P*. The projection in range space (i.e. time delay) places the echoes from *P* at points p_1 and p_2 on plane *R* for wavefronts W_1 and W_2 respectively. The distances between a point $r_{1,2}$, located in a low-relief area on the plane *R*, and points p_1 and p_2 are measured on the respective images. The difference between these distances ((d_2-d_1) in the case of (a) and (d_1-d_2) in the case of (b)) is s, the parallax of point *P*. Using the incidence angles of the two observations (θ_1 and θ_2) allows the height *h* of the feature to be obtained by dividing *s* by the parallax-to-height ratio ((cot θ_1 + cot θ_2) in the case of (a) and (cot θ_2 – cot θ_1) in the case of (b)).

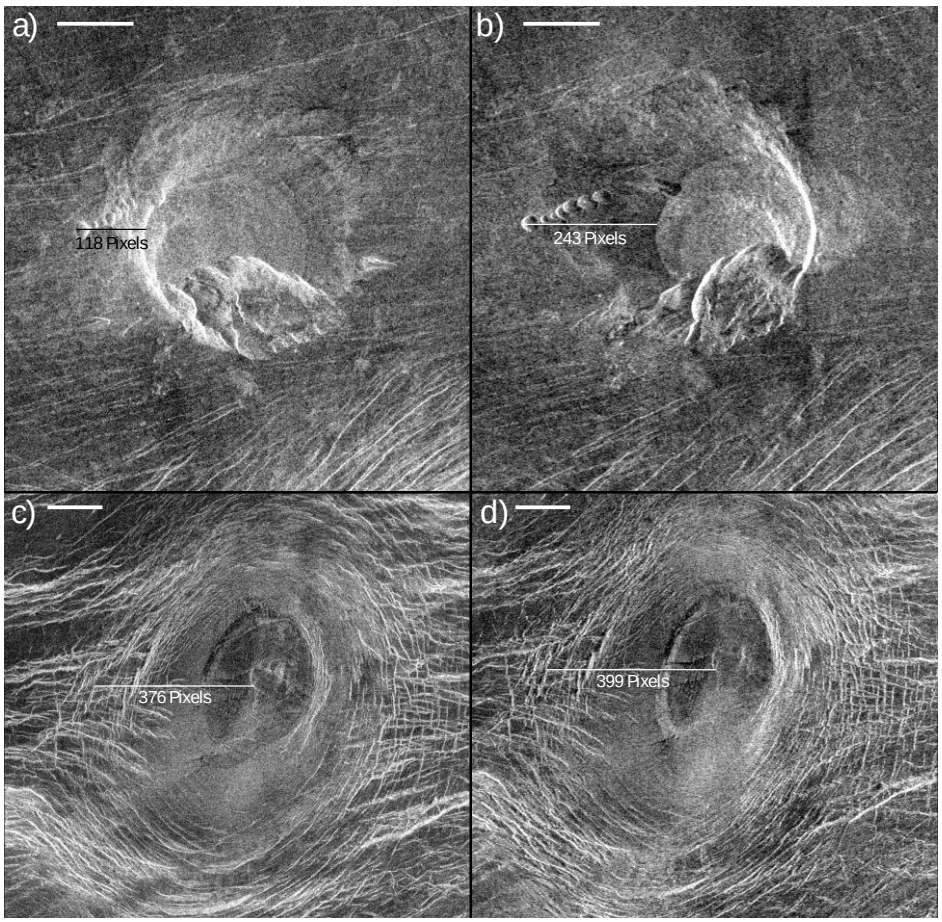

Figure 2.2. (a) and (b): Opposite-side stereo images of a volcanic dome with collapsed margins. Centre coordinates are 16.2°S, 148.25°W. Parallax difference between the two pixel distances in the two images yields a dome height of 2810 m, derived through the method shown in Fig. 2.1a. (a) Cycle 1 image with illumination from the left at an incidence angle of 40°. (b) Cycle 2 image with illumination from the right at an incidence angle of 25°. Scale bar is equal to 10 km in all images. Figures adapted from Figs. 4-7 and 4-8 in *Plaut* [1993]. (c) and (d): Same-side stereo images of a caldera. Centre coordinates are 9.5°S, 69°W. Parallax difference between the two pixel distances in the two images yields a caldera depth of 495 m, derived through the method shown in Fig. 2.1b. (c) Cycle 1 image with illumination from the left at an incidence angle of 42.5°. (d) Cycle 2 image with illumination from the left at an incidence angle of 22.7°.

2.1.2 Test for the random distribution of features

A statistical test may be performed in order to quantitatively determine how features belonging to each morphological class are distributed across their respective planets. The surface areas of Mars and Venus may each be divided into a number of equal-sized subareas, such that each subarea (or 'quadrat') contains a number of features belonging to a particular volcano class [*Davis*, 1986]. If the features are distributed randomly across the planet, each quadrat should contain the same number of features. The definition of random distribution therefore depends on the number and size of quadrats chosen; the greater the number and the smaller the size of quadrats chosen, the more efficient will be the test of random distribution. The chi square method may be used to test how far away from random the distribution of a set of features is, and is theoretically independent of the shape or orientation of the quadrats. For a random distribution, the expected number of features in each quadrat is E, i.e. the total number of features divided by the total number of quadrats. A chi square test of goodness-of-fit of the expected (random) distribution to the observed distribution is given by:

$$\chi^2 = \sum \frac{(O-E)^2}{E} \tag{2.3}$$

where O is the observed number of data points in one quadrat. The test has $v = (T - 2)$ degrees of freedom, where T is the number of quadrats. The number of degrees of freedom corresponds to a critical value of χ^2; if the calculated value of χ^2 exceeds the critical value of χ^2, the distribution of the features is not regarded as being uniform. The critical value of χ^2 depends on the chosen value of the significance level, α, which is an indication of how likely a result is due to chance. A significance level of 0.05 indicates that there is a 5% chance that the result of the distribution test is false. Smaller values chosen for α (i.e. smaller chances that the result will be false) result in larger critical values of χ^2.

This study will consider the standard significance level of 0.05 when performing chi square tests. The surface areas of the planets are divided into 24 quadrats (12 each in the northern and southern hemispheres, each measuring 30° of longitude and 90° of latitude), giving a value of v of 22, and a corresponding critical χ^2 value of 33.92 (obtained from a χ^2 table at home.comcast.net/~sharov/PopEcol/tables/chisq.html).

2.2 Definition of a volcanic feature and classification of features on Mars and Venus

The criteria for identification and classification of volcanic features on both planets have been based to an extent on previous cataloguing studies, including those of *Head et al.* [1992], *Crumpler and Aubele* [1978], and *Bulmer and Guest* [1996], but in general have been drawn from first principles. Despite the different wavelengths at which the surfaces of Mars and Venus have been imaged, the criteria for identification of volcanic features essentially remain the same, and include texture, surface reflectivity, and topographic information [*Senske and Stofan*, 1993]. The individual categories are defined not on the basis of their geology, which includes the identification of stratigraphic units, but on the basis of their geomorphology, i.e. their exterior shape regardless of their interior structure.

As a general rule, a volcanic edifice must comprise a spatially-localized feature (i.e. not flood-type lava flow fields) that displays an identifiable boundary between itself and the surrounding terrain. This boundary may be defined by a difference in surface brightness (at visible and microwave wavelengths on Mars and Venus respectively) and/or surface texture. Textural features such as digitate flow terminations and lava tubes and channels are diagnostic of a volcanic origin. Ideally, a volcanic edifice should display at least one vent, but this is not always necessary – in some cases the vent may be obscured or filled by flows. If a potential edifice appears similar to confirmed volcanic edifices, but lacks a vent, it may be regarded as a volcanic edifice, particularly if the edifice is located within a field of similar features. Vents take the form of depressions that are generally, but not always, located towards the centre of the edifice. They may display low roughness flows on their floors, which on Venus display low backscatter in SAR images. Volcanic edifices should ideally display a positive topographic signature, whether it is manifested in altimetry data or variations in the brightness (or radar backscatter) on opposite sides of the edifice; this may not always be the case if the edifice is of low relief or the altimetry data is of a low enough resolution such that the topography of the feature is not recorded.

Calderas (or paterae) represent the only volcano category that displays negative rather than positive relief, and are commonly thought to originate through collapse following removal of subsurface magma. In Magellan imagery, calderas generally appear as circular to elliptical features bounded by an annulus of concentric fracturing

with dark, homogeneous flows covering the interior and potentially extending beyond the confines of the annulus. The fracture annulus may in some cases be raised above the caldera interior and surrounding topography. Some calderas display no concentric fracture annulus, and have a boundary instead represented by a single scarp leading down to the floor of the caldera. This latter category is generally the form taken by the few calderas that exist on Mars.

These criteria for the identification of volcanic features essentially represent a guide, and it is recognized that individual cases should often be regarded in their own context, particularly on a planet such as Venus where there is a very high volcano population and considerable variety in volcano morphology. The following sections define each individual category for Venus and Mars – separate classification systems were created for Mars and Venus, although some categories on one planet corresponded well to certain categories on the other. Venusian volcanoes have been separated into five broad geomorphologic categories, with a total of 24 subcategories distributed between them. Martian volcanoes have been separated into four broad geomorphologic categories, with a total of ten subcategories distributed between them. Examples of each Venusian and Martian sub-category are displayed in Figs. 2.3 and 2.4, respectively, in the form of plan view geomorphological maps as well as cross-sections interpreted from the maps. Specifications relating to each of the Venusian and Martian example landforms are shown in Table 2.1. The key to the geomorphological units in Figs. 2.3 and 2.4 is shown in Table 2.2.

2.2.1. Classification of Venusian volcanic features

1) **Cones.**

- Edifices may often display steep upper flanks, surrounded by gently sloping outer apron flows.
- Planforms ranging from circular to elliptical.
- Flanks generally display homogeneous, intermediate backscatter; digitate flows aligned radially to the edifice may sometimes be discerned. Margins of edifice are not always easily visible, but tend to appear smooth.
- Flanks may display concentric fracturing.

- Edifices generally, but not always, display summit vents, often with low backscatter flows covering their floors; in some cases, numerous vents are visible in the summit region.
- Edifices may display steep-sided domes at their summits.
- Edifices display relatively high relief, having a mean relief of 827 m above the surrounding terrain, with a standard deviation (σ) of 439 m. Diameter to height ratio has a mean of 100.2, with a σ of 57.4.
- Diameter distribution of edifices is spread fairly equally across the range 20 to 100 km.

Four subcategories of conical edifices exist. They are defined as follows:

C1: Relatively small conical edifices with or without summit vents, and which are surrounded by apron flows. The margin between the base of the edifice and the surrounding apron flows is generally well-defined. Edifices generally display high to intermediate radar backscatter.

C2: Broad conical edifices with summit vents, which can be large or small relative to the diameter of the edifice and are very often filled with flows. Features generally display intermediate to low radar backscatter, and may display flanks covered by separate flows of contrasting backscatter. Features often display complex summit regions, sometimes showing multiple vents instead of a single one, as well as small edifices and multiple flow fields.

C3: Broad conical edifices with no apparent primary summit vent. Either no vents exist, or multiple similar-sized vents/pits exist in summit region. A poorly-defined dark region may exist at the summit that may represent flows erupted by a vent. Otherwise, the edifices have similar attributes to class C2. Small (km-sized) edifices may exist in the summit region and on the flanks.

C4: Broad conical edifices with a dome (which itself may be an intermediate-sized volcano) located at their summit. These edifices generally do not show calderas. Otherwise, they show similar attributes to class C2.

2) **Steep-sided domes.**

- Edifices display narrow, steep outer flanks (indicated by a radar-bright foreslope), leading to a flat upper surface. Margins of edifices are smooth.
- Planforms are generally circular.

- Edifices generally display homogeneous, intermediate to low backscatter.
- Radial fracturing is sometimes visible on the surface.
- Edifices generally, but not always, display central vents, which can vary considerably in size and depth. The larger ones often display low backscatter flows covering their floors. Some domes lacking vents instead display downwarping of the upper surface, leaving a raised rim.
- Edifices display medium relief, having a mean relief of 684 m above the surrounding terrain, with a σ of 429 m. Diameter to height ratio has a mean of 76, with a σ of 53.6.
- Diameter distribution of edifices is confined strongly to the range 20 to 40 km.

Four subcategories of domical edifices exist. They are defined as follows:

D1: Edifices display no central vent. Edifices always display nearly homogeneous backscatter, and show no fracturing.

D2: Edifices display a relatively large vent, sometimes with a raised rim, located at its centre. Vents may be deep and show low backscatter flows on their floor. In some instances a concentric fracture exists in place of a specific vent, sometimes enclosing a complex fracture network. Radial fracturing is sometimes seen emanating from the summit region. Upper surfaces of edifices range from being flat to convex. Edifice/caldera diameter ratio is smaller than 6⅔.

D3: Edifices display a relatively small vent (in the form of a pit) located at their centre. Radial fracturing is sometimes seen emanating from the summit region. Edifice/caldera diameter ratio is larger than 6⅔.

D4: Edifices display downwarped central upper surfaces, leaving the margins raised. Dark flows are sometimes seen pooling at the centre of the downwarped surfaces. No central pits are apparent.

3) **Modified domes.**

- Edifices display steep, scalloped, and fluted outer flanks which, due to the high relief of the edifices, are frequently foreshortened in Magellan imagery. Margins of edifices range from being smooth to angular. Edifices often (but not always) display mottled debris aprons skirting their bases.
- Planforms range from circular to slightly elongate.
- Edifices generally display homogeneous, intermediate to low backscatter.

- Radial fracturing is sometimes visible on the surface.
- Modified domes display similar summit features to unmodified domes – summit regions may display vents of varying size (sometimes with flows covering their floor), no vents, or summit downwarp.
- Edifices display high relief, having a mean relief of 1321 m above the surrounding terrain, with a σ of 868 m. Diameter to height ratio has a mean of 40.1, with a σ of 39.4.
- Diameter distribution of edifices is confined strongly to the range 20 to 50 km.

Six subcategories of modified domical edifices exist. They are defined as follows:

MD1: Edifices display no central vent.

MD2: Edifices display a relatively large vent located at their centre. Vents may be deep and show low backscatter flows on their floor. Radial fracturing is sometimes seen emanating from the summit region. Edifice/caldera diameter ratio is smaller than 6⅔.

MD3: Edifices display a small central vent, often with similar-sized vents scattered across the dome surface. Edifice/caldera diameter ratio is larger than 6⅔.

MD4: Edifices feature downwarped summit regions that sometimes display dark flows pooled on their floors. No apparent central vents.

MD5: Edifices display much more extensive degradation than the previous classes, with half or more of the main edifice having collapsed, giving the edifice an elongate planform. The original D-class edifice type cannot be determined. Edifices are frequently surrounded by debris aprons.

MD6: These edifices differ from the previously described modified domes in that they do not show clearly defined scalloped margins and summit regions. Instead, these edifices appear to have been chaotically fragmented by numerous fractures running through them in all directions. Central calderas are generally not observed. Margins of edifices are indistinct.

4) **Shields.**

- Due to their low relief, edifices display gently sloping flanks with a constant gradient, with no bright foreslope in Magellan images. Margins of edifices range from being smooth to highly angular.
- Planforms range from circular to very elongate.

- Edifices generally display homogeneous, intermediate to low backscatter. Some categories display digitate flow morphologies that brighten with distance from the vent.
- Concentric fracturing is sometimes seen on the flanks.
- Edifices generally (but not always) display summit vents, which can vary in size. The larger ones may be seen to display dark flows on their floors. Some edifices have been erupted from long fissures rather than point vents.
- Edifices display low relief, having a mean relief of 414 m above the surrounding terrain, with a σ of 273 m. Diameter to height ratio has a mean of 164.1, with a σ of 126.7.
- Diameter distribution of edifices is mostly confined (about 75% of edifices) to the range 20 to 50 km.

Seven subcategories of shield edifices exist. They are defined as follows:

S1: Edifices feature a small central summit caldera with an edifice/caldera diameter ratio larger than 6⅔.

S2: Edifices feature a small, steep-sided edifice at their summits, which display their own central caldera.

S3: Edifices feature a large central summit caldera with dark flows on its floor. Flanks often display concentric fracturing. Edifice/caldera diameter ratio is smaller than 6⅔.

S4: Edifices do not display any apparent summit caldera.

S5: Small pit vents that are surrounded by flow fields with irregular, sometimes angular margins that appear to match the contours of the surrounding topography. Pit can occur at any place in the flow field, depending on whether the topography is flat or sloped.

S6: Edifices displaying a dark caldera surrounded by a dark apron flow field with radiating digitate flows superimposed on it. Digitate flows are initially dark, but brighten with increasing distance from the caldera.

S7: Long fissure vents from which emanate bright, radiating digitate flows.

5) **Calderas.**

- The boundaries of calderas are generally defined by an annulus (more often incomplete than complete) of parallel, concentric fracturing which may be raised above

the surrounding terrain in some instances. Alternatively, no fracture annulus is present and the boundary is represented by a single scarp leading down to the caldera floor.

- Planforms range from circular to elongate.
- Calderas very often display low backscatter, homogeneous flows on their floors, which may superpose and extend beyond the fracture annulus in some instances. Flows may also be observed emanating from the annulus fractures.
- Calderas display medium, negative relief, having a mean relief of 728 m below the surrounding terrain, with a σ of 761 m.
- Diameter distribution of calderas tends towards the range 20 to 70 km, but is fairly evenly spread across the entire range of 20 to 100 km relative to other volcanic feature categories.

Three subcategories of calderas exist. They are defined as follows:

K1: Negative relief calderas comprising a circular to elliptical annulus of concentric fracturing surrounding a caldera interior that may or may not be filled with dark intrinsic flows.

K2: Calderas have similar attributes to class K1, but display raised rims coinciding with the annulus. Features display dark interior flows and exterior radiating flows more often than for class K1 features.

K3: Calderas whose rims are defined only by a steep scarp, with little or no concentric fracturing surrounding it.

Figure 2.3 (following four pages). Plan view and cross-sectional representations of the 24 sub-groups of intermediate volcanic features identified on Venus. Plan views comprise geomorphological maps of exemplary features from each sub-group, overlain on Magellan imagery, which are all left-looking with the exception of the K3 class caldera. The cross-sections, which are vertically exaggerated, are interpreted from the plan views. Scale bars accompanying all plan views measure 20 km; vertical heights of features are indicated where known. Morphological parameters of each feature are described in Table 2.1, and the key to the geomorphological units is shown in Table 2.2. Different feature classes are described in section 2.2.1.

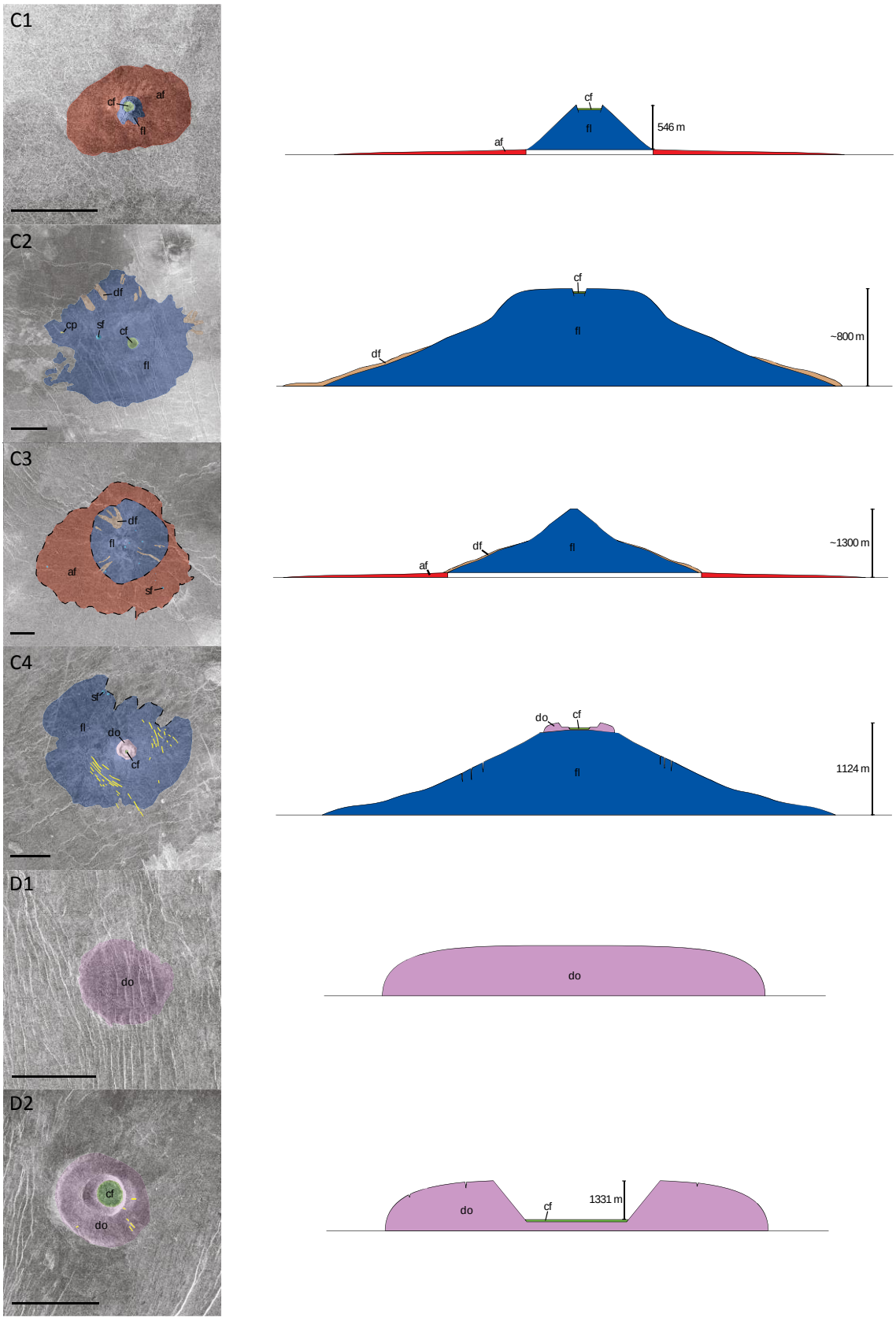
C1
cf
af
fl
546 m
C2
df
cp
sf
cf
fl
~800 m
C3
df
fl
af
sf
~1300 m
C4
sf
fl
do
cf
1124 m
D1
do
D2
cf
do
1331 m

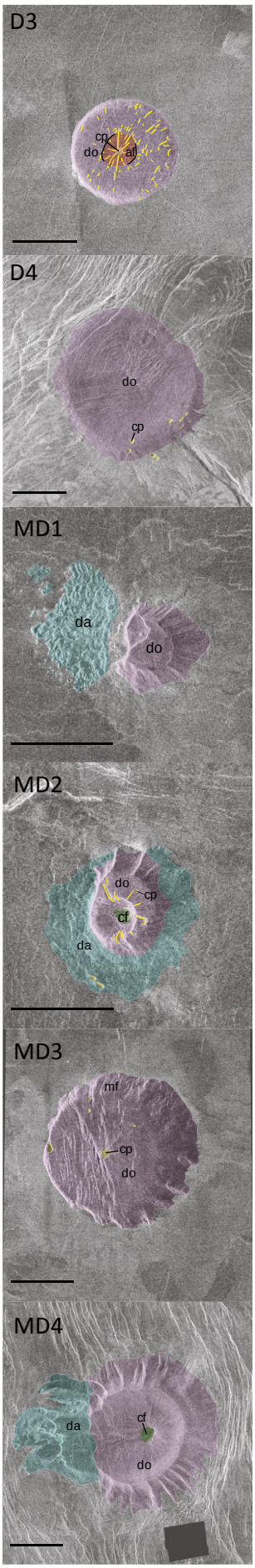
D3
cp
do
af
D4
do
cp
MD1
da
do
MD2
do
cp
cf
da
MD3
mf
cp
do
MD4
da
cf
do

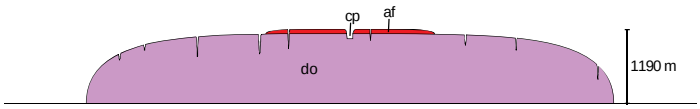
cp
af
do
1190 m

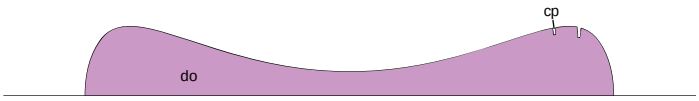
cp
do


da
do

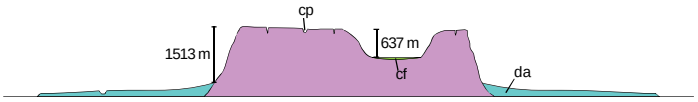
cp
1513 m
637 m
cf
da

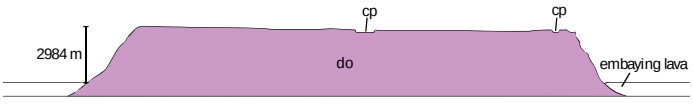
cp
cp
2984 m
do
embaying lava

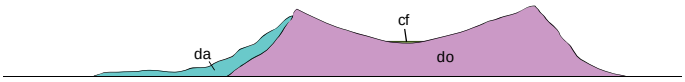
cf
da
do

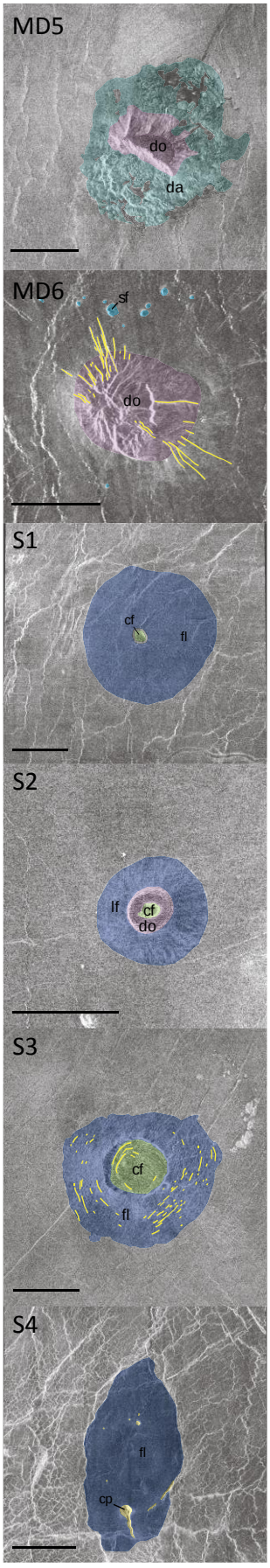
MD5
do
da
MD6
sf
do
S1
cf
fl
S2
lf
cf
do
S3
cf
fl
S4
fl
cp

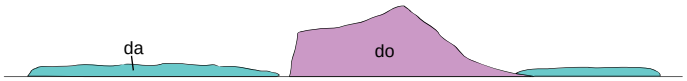
da
do

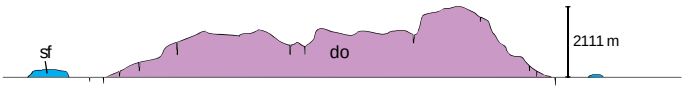
sf
do
2111 m

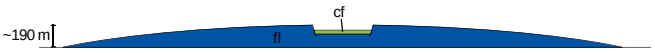
~190 m
cf
fl

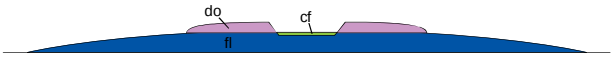
do
cf
fl

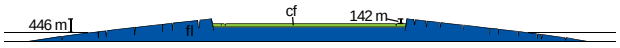
446 m
fl
cf
142 m


cp
fl

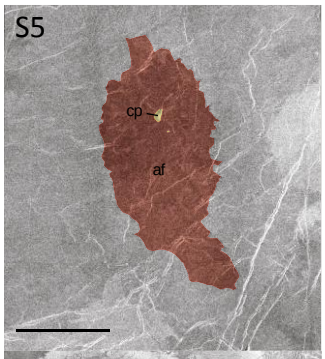
S5
cp
af


af
cp

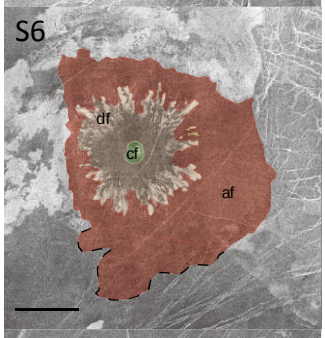
S6
df
cf
af


204 m
cf
df
af

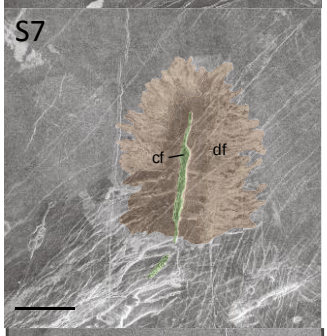
S7
cf
df

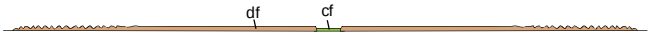
df
cf

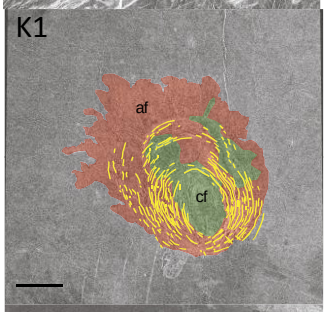
K1
af
cf

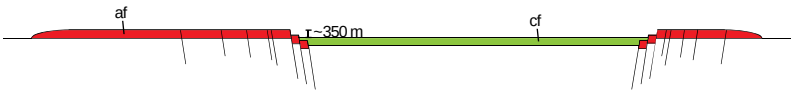
af
~350 m
cf

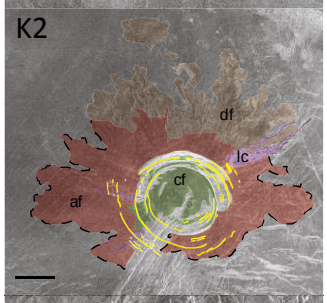
K2
df
lc
cf
af

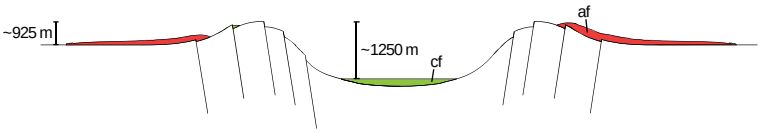
~925 m
~1250 m
cf
af

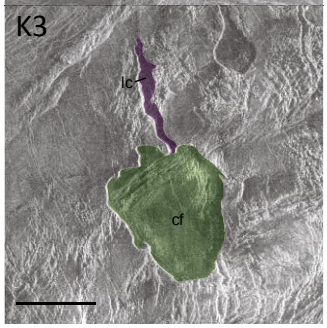
K3
lc
cf


278 m
cf

2.2.2. Classification of Martian volcanic features

1) **High-relief shields.**

- Planforms range from circular to slightly elongate.
- Edifices generally, but not always, display broad summit calderas, which may sometimes be filled to the rim with lavas. In some cases, nested calderas are visible within the main calderas.
- Radial lava channels may be visible emanating from the main caldera, or from sites on the upper flanks.
- Margins of edifices are generally smooth and well-defined.
- Preservation state of edifices ranges from smooth and relatively pristine to rugged and degraded.
- Edifices display high relief, having a mean relief of 2045 m above the surrounding terrain, with a σ of 649 m. Diameter to height ratio has a mean of 33.5, with a σ of 15.2.
- Diameter distribution of edifices clusters around the range 50 to 70 km, with a mean of 61 km and a σ of 16 km.

Two subcategories of high-relief shields exist, depicted in Fig. 2.4. They are defined as follows:

Hrs1: Three intermediate examples of this subcategory exist, all located within the Tharsis rise. Edifices are well-preserved and display smooth flanks and well-defined margins, but have been embayed by flood lavas from the large Tharsis shields. Edifices show prominent summit calderas.

Hrs2: Seven intermediate examples of this subcategory exist, all located within the Thaumasia and Coprates quadrants. Edifices appear irregular and degraded and are not particularly distinctive among their surroundings. They display rough flanks, radial dissection, and angular, sometimes poorly-defined margins. Edifices sometimes show remnants of summit calderas.

2) **Cones (C).**

- Edifices are similar in morphology to the Hrs category, but display high relief, having a mean relief of 2227 m above the surrounding terrain, with a σ of 63 m. Diameter to height ratio has a mean of 12.8, with a σ of 0.3.

- Planforms are equidimensional.
- Only two examples are known. One edifice appears to display a circular summit caldera that is filled to the rim by lava (compare with Tongariro volcano in New Zealand [*Hodges and Moore*, 1994]). The other displays no apparent caldera, instead displaying a wide valley occupying the centre of the edifice, which may have eradicated a previously existing caldera.
- Profiles of edifices are unusually symmetrical. Flanks of both edifices display strong radial dissection (more so than for Hrs category edifices), characterised by narrow, sharply incised valleys and fluting.
- Margins of edifices are generally angular but well-defined.
- Edifices display a mean diameter of 28.5 km with a σ of 1.5 km.

3) **Low-relief shields (Lrs).**

- Planforms range from equidimensional to elongate.
- Edifices generally, but not always, display vents, often taking the form of small pits a few km across. In some cases, the flows appear to be emanating from chains of collapse pits or fissures, which are aligned with regional fracturing in the vicinity.
- Edifices either display well-defined, overlapping digitate and fan flows, with associated lava tubes and channels, and angular margins, or relatively homogeneous apron flows with smoother, generally less well-defined margins. The homogeneous surface texture may in some cases be due to masking by dust cover, and such edifices often have higher crater counts than the former type.
- Edifices display low relief, having a mean relief of 154 m above the surrounding terrain, with a σ of 76 m. Diameter to height ratio has a mean of 261.6, with a σ of 176.3.
- Diameter distribution of edifices is concentrated in the range 20 to 50 km, with a mean of 33 km and a σ of 13 km.

Six subcategories of high-relief shields exist, depicted in Fig. 2.4. They are defined as follows:

Lrs1: Edifices display well-defined digitate and fan flow morphologies that emanate from an equidimensional vent (length/width ratio <4:1). Lava tubes and channels are often apparent.

Lrs2: Edifices display well-defined digitate and fan flow morphologies that emanate from an elongate vent or fissure (length/width ratio >4:1). Lava tubes and channels are often apparent.

Lrs3: Edifices display homogeneous apron flows that emanate from an equidimensional vent (length/width ratio <4:1). Lava tubes and channels are not apparent.

Lrs4: Edifices display homogeneous apron flows that emanate from an elongate vent or fissure (length/width ratio >4:1). Lava tubes and channels are not apparent.

Lrs5: Edifices display homogeneous apron flows that do not appear to emanate from any vent, which may be obscured. Lava tubes and channels are not apparent.

Lrs6: Only one example of this subcategory exists, located in the southern highlands. A central elongate, irregularly-shaped, raised rim surrounds an interior depression, interpreted as a caldera. The walls of the caldera are steep and have experienced collapse in several places along the perimeter, and are entirely absent on the north rim. The outer slopes of the raised rim grade gently into low roughness, homogeneous apron flows that fill the surrounding low topography, with very poorly defined margins.

4) **Tuyas (Tu).**

- Planforms are generally equidimensional and rectangular.
- Edifices do not display vents.
- Edifices comprise blocky massifs, with the best-preserved often displaying steep outer flanks leading to flat summit regions, and relatively smooth, well-defined margins, often surrounded by basal troughs. The less well-preserved appear rugged, with high-relief outcrops of the tuya itself emerging from beneath what appears to be a coating layer of dust, and with tenuous, angular margins.
- Edifices display medium relief, having a mean relief of 1381 m above the surrounding terrain, with a σ of 521 m. Diameter to height ratio has a mean of 29.3, with a σ of 14.9.
- Diameter distribution of edifices is strongly concentrated in the range 20 to 40 km, with a mean of 35 km and a σ of 12 km.

5) **Calderas (K).**

Only one example of an intermediate caldera structure has been identified. The caldera comprises an incomplete, elliptical raised rim (rising 1373 m above the surrounding terrain) surrounding an interior at the same elevation as the surrounding terrain. An area of high relief at the centre (reaching 1623 m in height) may represent a resurgent dome (compare Cerro Galán caldera in Argentina [*Hodges and Moore*, 1994]). As at Cerro Galán, the rim displays dense radial channeling. The caldera has been extensively degraded by the regional fracturing of Tempe Fossae that cut through it.

Figure 2.4 (below and following two pages). Plan view representations of the 11 sub-groups of intermediate volcanic features identified on Mars, accompanied by five cross-sectional views interpreted from the plan views. Plan views comprise geomorphological maps of exemplary features from each sub-group, overlain on THEMIS visible and infrared imagery; the cross-sections, which are vertically exaggerated, are interpreted from the plan views. (a) High-relief shield class features (Hrs) (b) Cone class features (C). (c) Low-relief shield class features (Lrs). (d) Caldera class features (K). (e) Tuya class features (Tu). Scale bars accompanying all plan views measure 20 km. Morphological parameters of each feature are described in Table 2.1, and the key to the geomorphological units is shown in Table 2.2. Different feature classes are described in section 2.2.2.

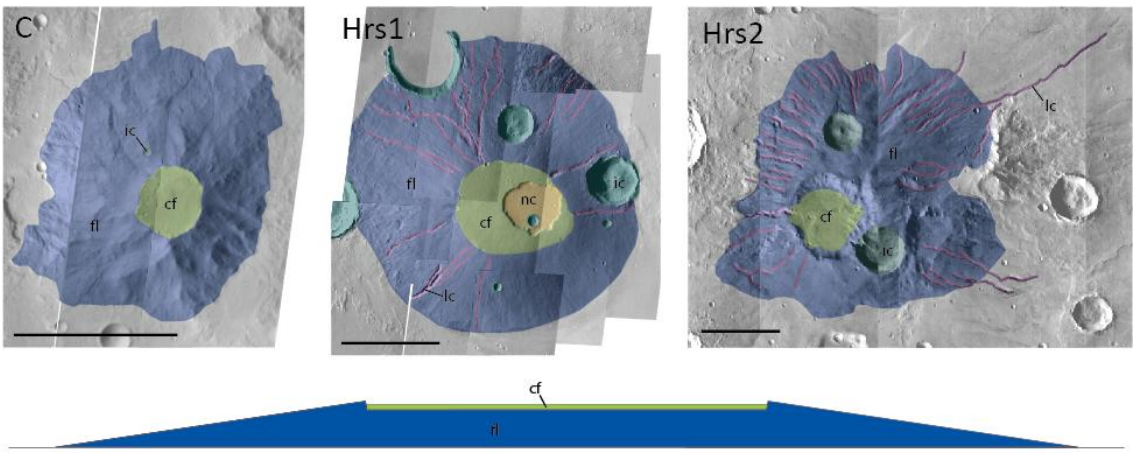

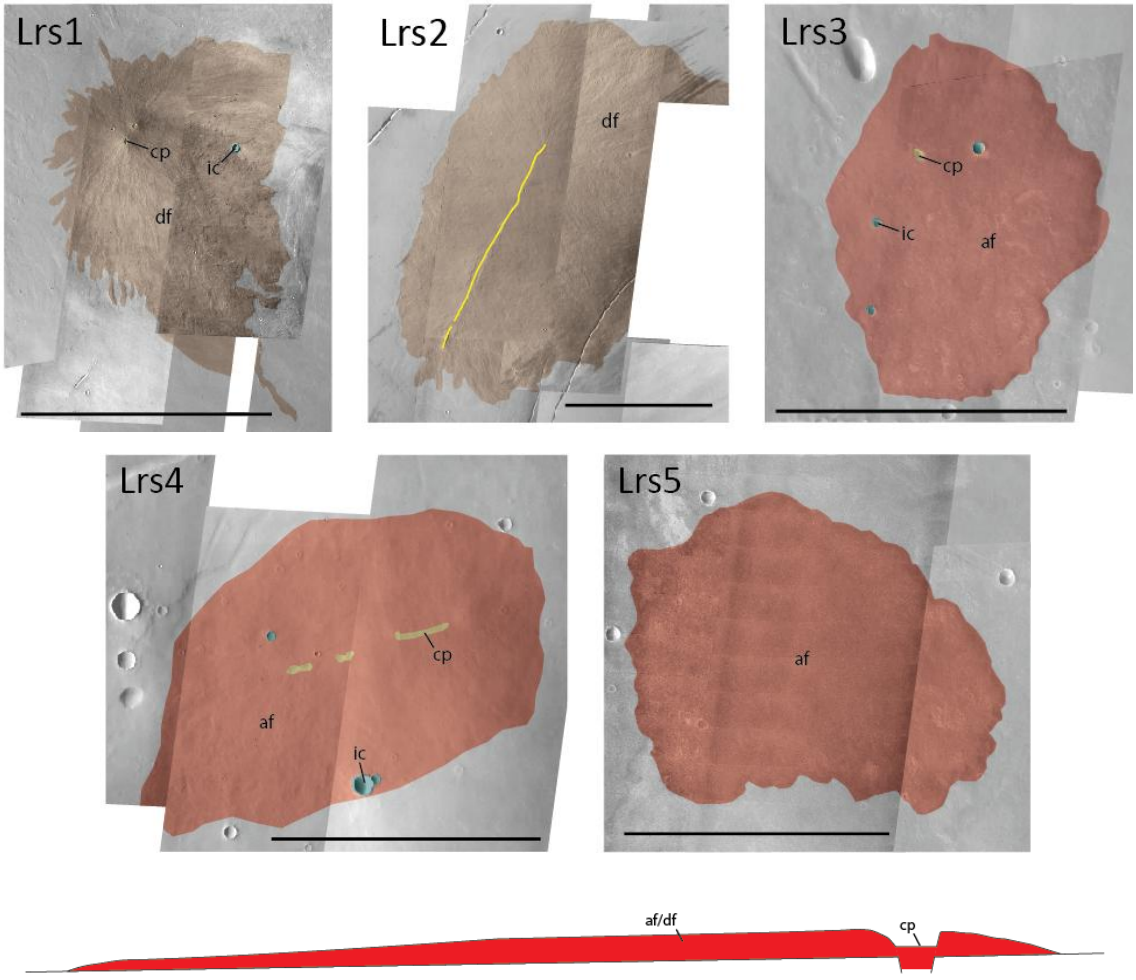
Lrs1
cp
ic
df
Lrs2
df
Lrs3
cp
ic
af
Lrs4
cp
af
ic
Lrs5
af
af/df
cp
Lrs6
af
sr
cf
af
cr
cf

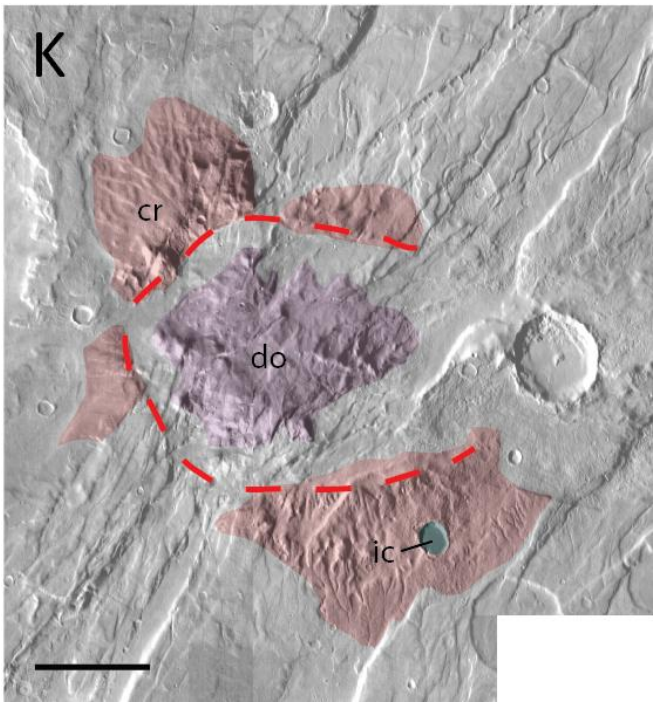
K
cr
do
ic


cr
do
cr

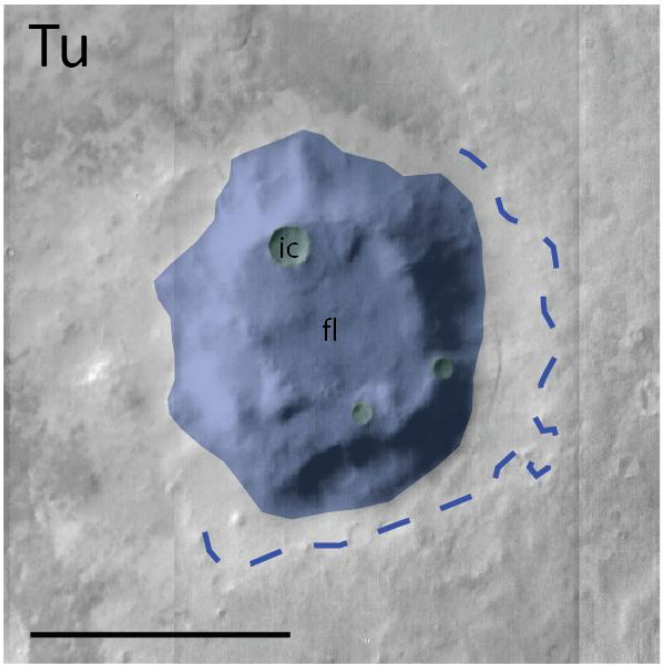
Tu
ic
fl


fl
tr

Table 2.1. Various specifications (where known) relating to the examples of each of the 24 Venusian and 11Martian intermediate volcano subclasses as shown in Fig. 2.3 and 2.4. Venusian vertical relief measurements are obtained either through Magellan altimetry or parallax measurements; the measurement method is indicated next to the value. Vertical relief measurement is not always possible due to the lack of Magellan stereo data, as well as the absence of Magellan altimeter measurements, over a relevant area. Martian vertical relief measurements are all obtained through MOLA altimetry. N/A = not applicable. a.f.c. = after flank collapse.

Planet	Class	Latitude	Longitude	Edifice/flow field diameter (km)	Caldera diameter (km)	Basal height of edifice (m)	Caldera/downsag depth below rim (m)	Altitude above MPR (m)
Venus	C1	10°N	269.5°E	30 by 19.5	2	546 (parallax)	Unknown	-738
	C2	5.5°N	277°E	105 by 75	6	~800 (altimeter)	Unknown	-233
	C3	16.5°N	325°E	116	N/A	~1300 (altimeter)	N/A	-314
	C4	13°N	78°E	70 by 62	7	1124 (parallax)	Unknown	-31
	D1	6.5°S	333.5°E	22	N/A	Unknown	N/A	120
	D2	16.5°N	41.5°E	22.5 by 20.5	10	Unknown	1331 (parallax)	1541
	D3	3°S	151°E	33	2	1190 (parallax)	Unknown	413
	D4	18°N	195.5°E	58	N/A	Unknown	Unknown	2892
	MD1	46°N	355°E	18 by 17 (a.f.c.)	N/A	Unknown	N/A	-749
	MD2	32°S	260°E	21 by 16 (a.f.c.)	7	1513 (parallax)	637 (parallax)	-534
	MD3	61.5°N	248°E	50 (a.f.c.)	3	2984 (parallax)	Unknown	-483
	MD4	18°S	5.5°E	64 (a.f.c.)	N/A	Unknown	Unknown	-349
	MD5	7.5°S	256°E	27 by 15.5 (a.f.c.)	N/A	Unknown	N/A	-568
	MD6	47.5°S	228°E	28.5 by 23	N/A	2111 (parallax)	N/A	-834
	S1	57.5°N	264°E	48 by 46.5	5	~190 (altimeter)	Unknown	-459
	S2	2°N	228.5°E	21	3	Unknown	Unknown	323
	S3	19°S	70.5°E	48 by 40.5	19.5 by 16.5	446 (parallax)	142 (parallax)	-532
	S4	35°N	41°E	61.5 by 31.5	N/A	Unknown	N/A	-879
	S5	24°N	301°E	58.5 by 31.5	3 by 1.5	Unknown	Unknown	483
	S6	9.5°S	201°E	71 by 64	6	204 (parallax)	Unknown	1284
	S7	7°S	199.5°E	64.5 by 49.5	43.5 by 3	Negligible (parallax)	Unknown	1441
	K1	49.5°N	334°E	90.5 by 68.5	63 by 48	N/A	~350 (altimeter)	-337
	K2	20.5°N	247.5°E	~108	67 by 49.5	~925 (altimeter)	~1250 (altimeter)	-738
	K3	4.5°S	119.5°E	N/A	34.5 by 30	N/A	278 (parallax)	2014
Mars	Hrs1	26°N	262.5°E	60	23 by 18	2830	485	2097
	Hrs2	18°S	300.5°E	73 by 61	23 by 19	2223	1499	4131
	Lrs1	4°S	246.5°E	27.5 by 17	0.5 by <0.5	225	Unknown	7574
	Lrs2	1°N	255°E	50 by 30	28.5 by 0.5	177	Unknown	5400
	Lrs3	15°S	260°E	23.5 by 19	1 by 0.5	154	Unknown	7243
	Lrs4	8.5°S	254.5°E	28 by 20	7 by 0.5	82	Unknown	6904
	Lrs5	16.5°S	261°E	27.5 by 21	N/A	105	Unknown	6630
	Lrs6	75.5°S	341.5°E	~61 by ~48	18 by 5	418	275	1684
	Tu	63.5°S	3.5°E	28.5 by 24	N/A	1171	N/A	1225
	C	20°S	173°E	30	8	2290	-397	762
	K	44.5°N	290°E	91 by 82	53 by 47.5	1373	N/A	584

Table 2.2. Key to the geomorphological units and features highlighted in the plan views of intermediate Venusian and Martian volcanic features in Figs. 2.3 and 2.4.

Unit	Colour/Indication	Description
fl		Comparatively steep (relative to surrounding flows) flanks of conical and shield volcanoes. Contribute most to the vertical relief of the edifice. Displays intermediate to low relief.
af		Gently sloping apron/fan flows, often extending beyond the margins of the steep edifice (or caldera), with smooth margins and low relief.
df		Digitate flows, displaying dendritic, angular terminations. Flows sometimes show increased relief (higher backscatter on Venus) towards their terminations.
do		Dome-forming material. Generally displays intermediate to low, homogeneous backscatter. Features display steep flanks (indicated by foreslope brightening) and broad, flat summit regions.
da		Debris apron from flank collapse. Displays blocky, mottled texture.
cf		Caldera flow, ponded on the floor of a caldera and generally displaying low relief.
cr		Raised caldera rim, sometimes showing concentric graben.
nc		Later collapse zone existing within an earlier caldera.
lc		Radial lava channel emanating either from a main caldera or from secondary flank vents.
sf		Small volcanic feature (cone or dome) existing on the surface or in the close vicinity of the feature.
cp		Collapse pit existing on the surface or in the close vicinity of the feature.
ic		Circular, bowl-shaped or flat-floored craters featuring a narrow, raised rim, and occasionally showing a central peak.
-		Fractures intrinsic to the volcanic feature.
tr		Margin of a basal trough (specific to category Tu).
-		Poorly defined caldera rim (specific to category K).
-		Poorly defined or uncertain unit boundary.

2.3 Format of the catalogues

2.3.1 Venus and Mars catalogues

The catalogues of the Venusian and Martian intermediate volcanoes are contained within separate sheets (labeled 'Venus' and 'Mars' respectively) on the accompanying Microsoft Excel file, Volcanoes.xls. For each feature catalogued, there are several fields recording different information about it. The Venusian and Martian catalogues share the same fields. The individual fields are described below:

Feature: As defined in sections 2.2.1 and 2.2.2.

Name: A small number of intermediate volcanoes on Mars and Venus will have names, which are stated here.

Latitude/Longitude (°): The latitude and easterly longitude of the centre of the feature are stated to the nearest half-degree.

Flow diameter (km): The diameter of features displaying outer low-roughness flows is defined by the extent of the flows as opposed to the extent of the topographic signature of the feature. For features with an identifiable topographic signature, the flow diameter refers to the extent of these surrounding, low roughness flows. For features that have no identifiable topographic signature and are comprised entirely of low roughness flows, only the flow diameter (rather than the edifice diameter) is defined. For elliptical features, the maximum and minimum diameters are stated.

Edifice diameter (km): The diameter of the portion of the edifice that displays topographic relief, which may be evident in remote sensing imagery and/or topographic data. For an elliptical topographic signature, the maximum and minimum diameters are stated.

Mean diameter of whole edifice (km): The mean diameter of whichever portion of the edifice displays the greatest diameter, i.e. either the topographic signature or the flows.

Edifice length/width ratio: The ratio of the longest dimension of the edifice to the shortest dimension.

Main vent diameter (km): For cones, domes, and shields, this is the diameter of the main summit vent of the edifice; if multiple vents of apparently equal importance are present, the diameter of each is stated. For calderas, this is the diameter of the caldera rim itself; in the case of most Venusian calderas it is the distance from the outermost

visible concentric fracturing on one side to the outermost fracturing on the opposite side. For elliptical vents, the maximum and minimum diameters are stated.

Mean main vent diameter (km): The mean diameter of the main summit vent for edifices; if multiple vents of apparently equal importance are present, the mean diameter stated is that for a vent whose area is the total of the separate vents. For calderas, this is the mean diameter of the caldera rim itself.

Main vent length/width ratio: The ratio of the longest dimension of the vent to the shortest dimension.

Vertical relief of edifice (m): The difference in elevation between the terrain at the edge of the edifice (determined by taking the mean of numerous measurements) and the highest point of the edifice.

Vertical relief of main vent (m): The difference in elevation between the terrain at the rim of the caldera or main vent of an edifice (determined by taking the mean of numerous measurements) and the lowest point of the vent.

Edifice diameter/height ratio: The ratio of the mean diameter of the edifice to the elevation from its base to its summit.

Basal elevation above MPR (m): The difference in vertical elevation between the elevation of the terrain at the edge of the feature (determined by taking the mean of numerous measurements) and the MPR of the host planet.

Geological setting: This describes certain geomorphological/tectonic characteristics of the area in which the feature is located. A number of these characteristics are defined for Venus and Mars – combinations of characteristics can apply for a certain feature (e.g. it could be located within smooth plains as well as adjacent to a corona). Examples of each environmental characteristic are illustrated in Fig. 2.5, and the terrain coordinates are listed in the text below.

Venusian geological settings:

- Featureless plains (Fig. 2.5a, 6.5°S, 320.5°E): Low-relief plains, unaffected by fracturing or volcanism, displaying relatively consistent backscatter. Any changes in backscatter across the terrain are marked by gradational, rather than sharply-defined, boundaries.

- Fractured plains (Fig. 2.5b, 1°S, 4°E): Terrain is often undulating (relative to smooth plains) and displays a high density of fractures. Fractures can be aligned into distinct groups, each displaying a particular orientation, and range from being sharply-

defined to tenuous, and straight to curved. Fractures tend to be aligned in one direction in linear fracture belts, and chaotically oriented in several directions in zones where fracture belts meet. In some instances the opposite sides of particularly wide and/or sharply defined fractures can be resolved.

- Wrinkle ridge terrain (Fig. 2.5c, 40°S, 194.5°E): Lava plains with linear wrinkle ridges aligned roughly parallel across them. Some fields show distinct sets of wrinkle ridges with different orientations, giving a polygonal pattern. Wrinkle ridge fields can range from comprising thick ridges that are aligned parallel and widely-spaced to thin ridges that are aligned in different orientations, forming finely-spaced polygonal networks. Wrinkle ridges generally show higher relief than fractures do, and often show small-scale lobate morphologies.
- Flow field (Fig. 2.5d, 9°N, 311°E): Terrain displaying numerous distinct and relatively inextensive flows of differing backscatter. Flows are often equidimensional, although digitate morphologies are also seen. Low-relief shields are frequently seen within this terrain.
- Tessera terrain (Fig. 2.5e, 4.5°N, 135°E): High relief, high elevation, intensely fractured, intermediate to high backscatter terrain.
- Dome/shield field (Fig. 2.5f, 29.5°S, 12°E): Feature exists as a member of, or merely within, a field of closely-spaced (km to tens of km) domes/shields.
- Corona/caldera (Fig. 2.5g, 26°S, 80°E): Feature may exist within, exactly on, or near to (i.e. the centre of the edifice/caldera must be within 100 km) the rim of the corona or caldera.
- Volcano summit/flank (Fig. 2.5h, 44.5°S, 273°E): Feature exists either at the summit or on the lower flanks of a large or intermediate volcano.

Martian geological settings:

- Smooth plains (Fig. 2.5i, 16.5°N, 228.5°E): Generally featureless, low-relief plains, unaffected by fracturing, and with a low impact crater count. Smooth plains may display fan and digitate flow textures, particularly in the Tharsis area, indicating that they comprise extensive flood lavas emanating from large volcanoes and/or fissure eruptions.
- Fracture belt (Fig. 2.5j, 25°N, 253°E): Regional fracturing on Mars is most commonly organized into belts of closely-spaced, parallel graben fractures, with the most prominent examples extending radially from the Tharsis region.

- Shield field (Fig. 2.5k, 14.5°S, 259°E): Feature exists as a member of, or merely within, a field of closely-spaced shields. Shields often share boundaries in such fields.
- Cratered highlands (Fig. 2.5l, 34°S, 204°E): Occupying much of the southern hemisphere of Mars, this terrain is characterised by high relief, a high impact crater density, and extensive modification by fluvial channels.
- Rough, knobbly plains (Fig. 2.5m, 68°S, 353.5°E): This environment is specific to that in which the tuya (Tu) class edifices reside in the southern hemisphere. The terrain is characterised by numerous knobs and small massifs, and has a dissected appearance, with the surface layer having been stripped away across wide swaths of the landscape, leaving rimless depressions (possible thermokarst terrain). The terrain displays a low density of large impact craters relative to the cratered highlands.

Edifice description: A textual description of the general appearance of the feature.

Fracture description: A textual description of the appearance and configuration of any intrinsic fractures associated with the feature.

Flow description: A textual description of the appearance and configuration of any low-roughness flows associated with the feature.

Superposition: States whether the feature has been superposed and by what (e.g. by surrounding flows, large impact craters, regional fractures).

Figure 2.5 (below and following two pages). Examples of each of the different environment categories on Venus and Mars identified in the volcano surveys on each planet. Venusian environments are depicted in (a) to (h), Martian environments in (i) to (m). Scale bar below each illustration measures 20 km. Each environmental category is described in the text.

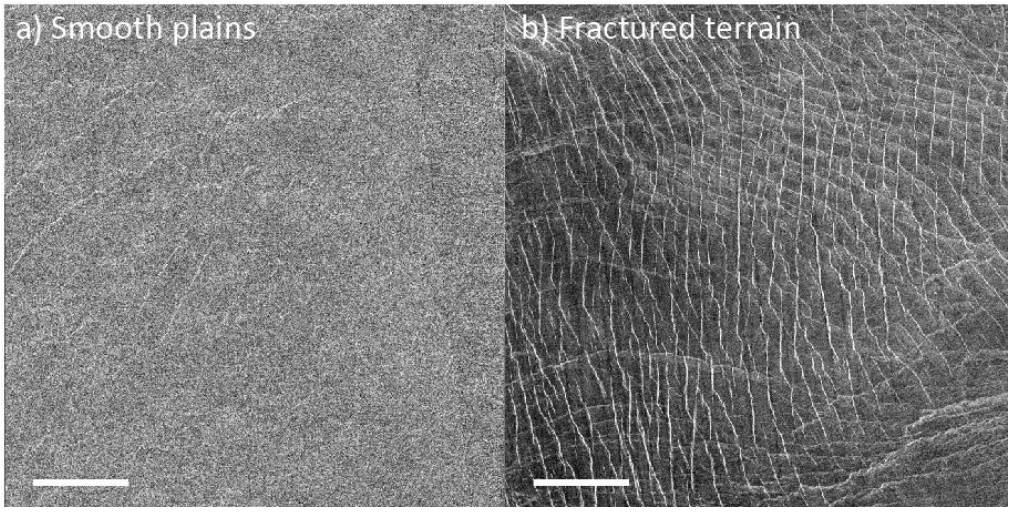

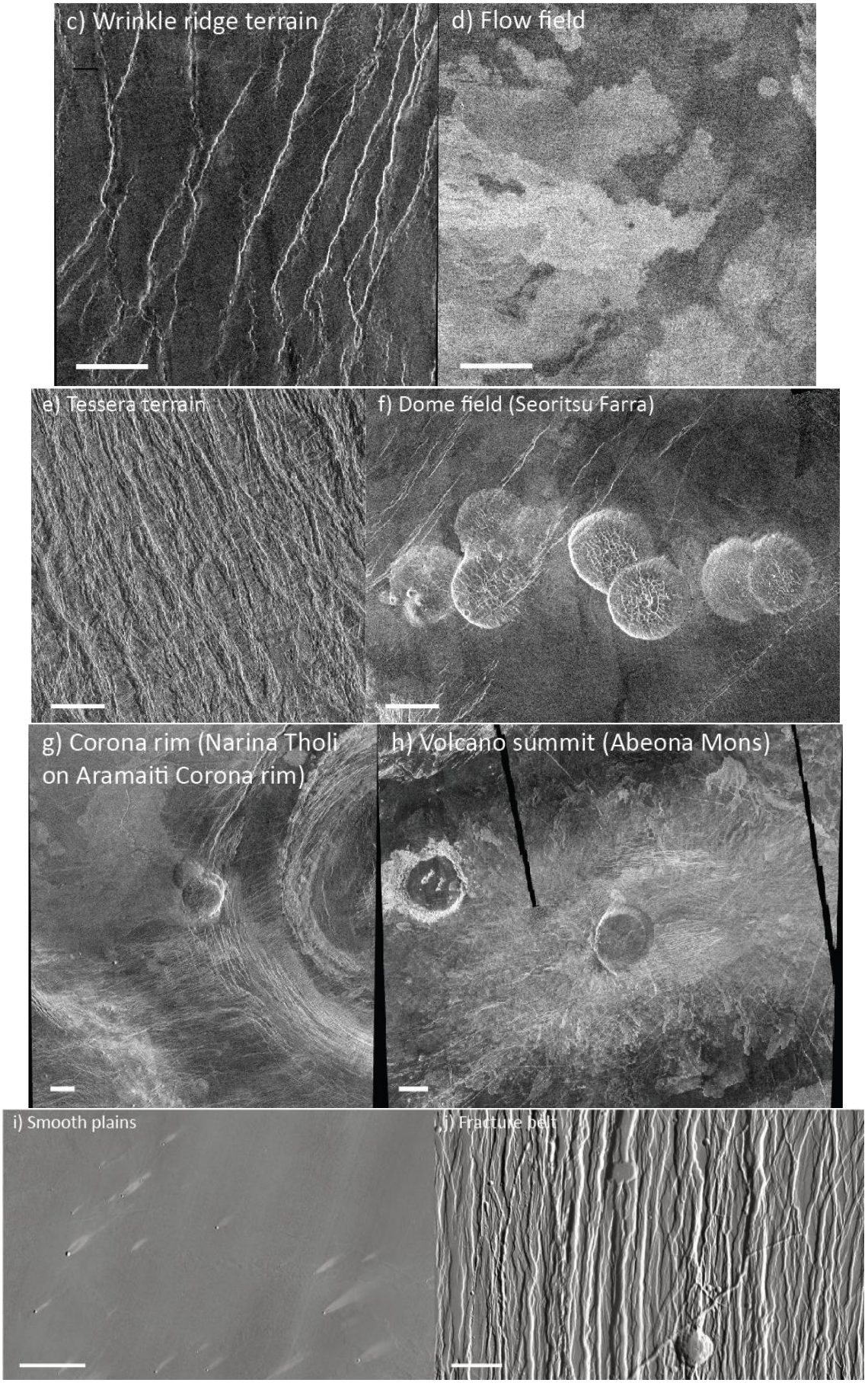
c) Wrinkle ridge terrain
d) Flow field
e) Tessera terrain
f) Dome field (Seoritsu Farra)
g) Corona rim (Narina Tholi on Aramaiti Corona rim)
h) Volcano summit (Abeona Mons)
i) Smooth plains
j) Fracture belt

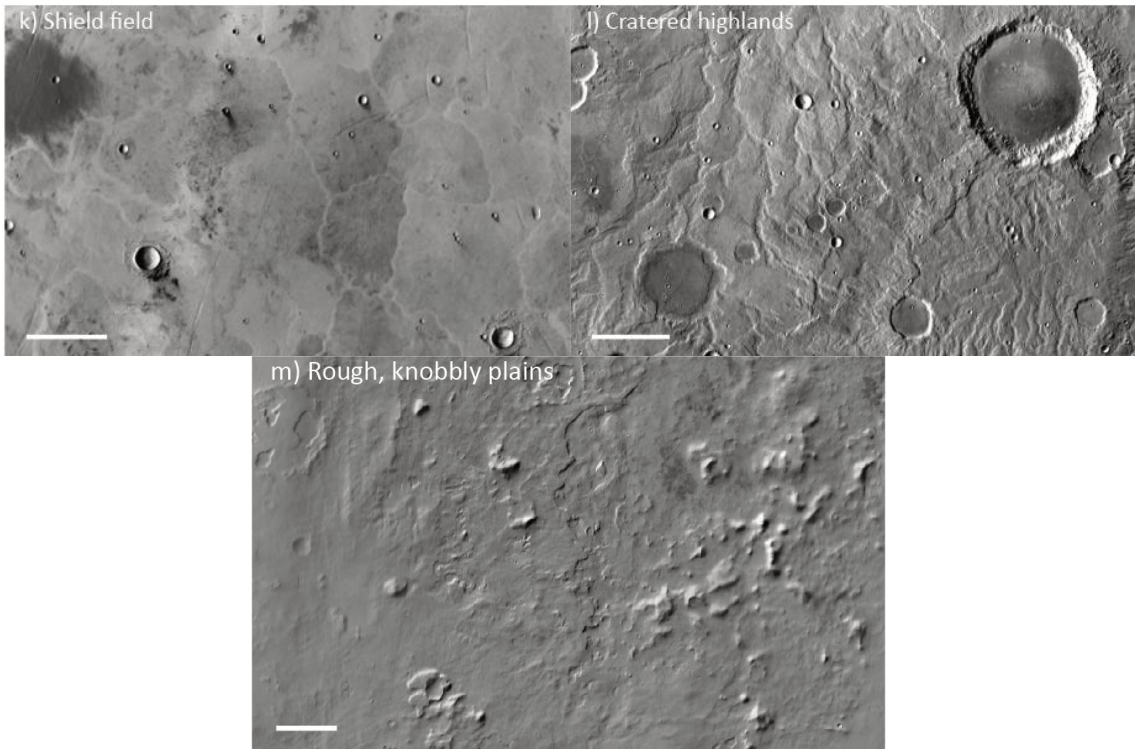

2.3.2 Catalogue of Venusian intermediate cones and large volcanoes

The third sheet in the Volcanoes.xls file (Volcano size comparison) is relevant to the topic of the evolution of intermediate cone-type volcanoes into large volcanoes that will be examined in section 3.2. The sheet reiterates various statistics for cone-type intermediate volcanoes from the 'Venus' sheet, while including a new column, 'summit elevation above MPR', obtained by adding the basal elevation of the edifice above MPR to the elevation of the edifice summit elevation above its base. Beneath the rows listing information for the intermediate cones, the same information for 132 of the 134 large volcanoes catalogued by *Brian* [2001] is listed (two edifices catalogued as intermediate cones in the present survey were also catalogued as large volcanoes by *Brian* [2001]). To the right of these columns, further information is listed that classifies the occurrence of different flow morphologies, the configurations of the summit region, main vent, and fracturing, and the locations of small edifices and vents, for each edifice. For the large volcanoes, the classifications of *Brian* [2001] for each edifice have been transferred directly to the present sheet; for the intermediate cones, the classifications for each edifice have been obtained through the present survey, using the same system as *Brian* [2001]. The classifications are described as follows:

Flow type: Flow morphology is divided into three categories, digitate, fan and sheet, using the same criteria for categorization as shown in Table 2 of *Stofan et al.* [2001]. For each edifice, the presence of a particular flow type is confirmed by specifying where the flows emanate from (either summit or flanks); if a particular flow type is not present, the field is left blank. It should be noted that the catalogue of *Brian* [2001] did not catalogue flow morphologies for each large volcano, other than those erupted from flank vents.

Summit class: The classification of summit characteristics is similar to that used by *Crumpler et al.* [1997]. Classification 4 may coexist with classifications 1, 2, and 3:

1: Simple summit structure with no main summit vent or collection of vents.

2: Presence of a main summit vent.

3: Presence of two or more summits, each of which may include its own summit vent.

4: Elongate summit region.

Summit vent class: The morphologies of summit vents are classified by their shape and complexity. Classifications A and E may coexist with classifications S and C:

A: Circular or near circular vent.

E: Elliptical vent.

S: Vent comprises a simple collapse depression.

C: Vent displays several collapse stages or nested pits.

Tectonic class: Four different classifications of tectonic characteristics are recognized. Each classification may coexist with any other:

A: Fractures radiate away from the centre or topographic summit of the edifice.

B: Fractures exist on the flanks, arrayed generally in a radial direction to the edifice.

C: The edifice exists on the axis of a rift or fracture zone, with the fractures either cutting directly across or curving around the flanks of the edifice.

D: Fractures are concentric to the centre or topographic summit of the edifice.

Small edifice and vent location: The location of small shields, cones, domes and vents situated on the edifice is described. More than one location classification may exist if small edifices are situated at different points on the edifice.

u: Edifices/vents located in the summit region/upper flanks of the edifice.

l: Edifices/vents located on the lower, outer flows of the edifice.

b: Edifices/vents located around the break of slope between the steep main edifice and outer lower flanks.

r: Edifices/vents associated with regional rifts/fracturing cutting across the edifice.

2.3.3 Chi square test results

The fourth sheet in the Volcanoes.xls file presents the results of the chi square tests performed for each of the major volcano categories on Venus and Mars. The total number of features within each quadrat is listed for each volcano category, with the various calculations of the chi square test (as described in section 2.1.2) presented below. The figures in red at the right of the sheet are the calculated χ^2 values for each volcano category. The cone (C) and caldera (K) categories on Mars do not number more than two features, so χ^2 values are not calculated for each of these categories.

2.4 Statistics of the Venus and Mars catalogues and observed patterns

The Volcanoes.xls file presents the Venus and Mars catalogues in their raw formats. Statistical information relating to each principal morphological category has also been tabulated and plotted graphically, allowing correlations and differences between the morphological and distributional characteristics of the various categories to be identified. The results are presented in the form of one table and nine figures. Table 2.3 collates altitude, χ^2 distribution, latitude, and various morphological statistics for each of the ten primary feature categories identified on Venus and Mars, including associated standard deviations. Distributional and morphological statistics of the various morphological groups are described below. The figures have been placed within Appendix I at the back of the thesis.

Table 2.3. Information relating to the frequency, altitude, distribution and morphology of each of the volcanic feature subcategories (in regular font) and major categories (in bold) identified on Venus and Mars by the survey. Associated standard deviations are included for feature elevation and dimension categories. Mean latitude values and χ^2 test results are shown only for the major morphological categories.

Planet	Class	Frequency	Mean basal elevation above MPR (m)	χ^2 (critical value = 33.92 at α = 0.05)	Mean latitude (°)	Mean edifice diameter (km)	Mean height (m)	Mean aspect ratio	Mean caldera diameter (km)	Mean caldera length/width ratio	Mean edifice/caldera diameter ratio
Venus	C1	10	-481 ± 461	-	-	36.7 ± 22	749 ± 467	62 ± 28	1.9 ± 1	1.014 ± 0.039	23.0 ± 11
	C2	21	-49 ± 633	-	-	63.7 ± 23	798 ± 336	93 ± 47	7.7 ± 5.4	1.246 ± 0.355	13.9 ± 11.1
	C3	21	-343 ± 365	-	-	65.3 ± 21.8	743 ± 347	110 ± 71	-	-	-
	C4	33	-277 ± 473	-	-	73.9 ± 21.3	928 ± 517	98 ± 55	5.3 ± 3.1	1.061 ± 0.131	23.5 ± 16.2
	D1	31	-126 ± 546	-	-	29.3 ± 8.3	898 ± 545	50 ± 39	-	-	-
	D2	32	117 ± 713	-	-	26.4 ± 8.1	639 ± 331	56 ± 28	7.8 ± 3.4	1.149 ± 0.254	3.8 ± 1.6
	D3	85	-278 ± 482	-	-	31.1 ± 11.3	653 ± 410	85 ± 58	1.3 ± 0.7	1.062 ± 0.222	26.1 ± 11
	D4	19	93 ± 946	-	-	33.4 ± 16.7	463 ± 0	113 ± 0	1 ± 0	1 ± 0	25.6 ± 5.7
	MD1	17	277 ± 1227	-	-	28.7 ± 11.7	1805 ± 753	21 ± 12	-	-	-
	MD2	58	104 ± 694	-	-	25.6 ± 7.4	1445 ± 927	29 ± 20	9.6 ± 4.6	1.270 ± 0.364	3.2 ± 1.7
	MD3	11	-615 ± 435	-	-	32.1 ± 10.7	1306 ± 835	46 ± 36	1.6 ± 0.7	1.091 ± 0.193	23.3 ±10.3
	MD4	33	22 ± 550	-	-	34.5 ± 12.8	484 ± 146	90 ± 62	4.3 ± 0.8	2.2 ± 1.166	8.2 ± 2.3
	MD5	8	-242 ± 240	-	-	24.5 ± 7.9	1032 ± 568	31 ± 16	-	-	-
	MD6	5	-395 ± 309	-	-	33.6 ± 8.4	1214 ± 624	38 ± 28	-	-	-
	S1	49	42 ± 860	-	-	41.1 ± 18.2	389 ± 265	166 ± 114	2.4 ± 1.7	1.145 ± 0.295	23.1 ± 16.6
	S2	22	245 ± 763	-	-	29.6 ± 13	450 ± 97	96 ± 42	3.1 ± 2	1.281 ± 0.886	13.9 ± 0
	S3	53	277 ± 858	-	-	36.6 ± 18.6	408 ± 207	137 ± 100	11.3 ± 5.9	1.425 ± 0.761	3.6 ± 1.5
	S4	13	-406 ± 421	-	-	38.4 ± 11.4	695 ± 424	84 ± 63	-	-	-
	S5	59	-96 ± 556	-	-	31.5 ± 10.9	117 ± 24	507 ± 30	1.6 ± 1.6	1.089 ± 0.329	26.0 ± 10.9
	S6	17	793 ± 819	-	-	39.0 ± 20	383 ± 156	232 ± 89	6 ± 5.6	1.467 ± 0.741	10.8 ± 7.9
	S7	5	688 ± 794	-	-	42.9 ± 12.4	347 ± 84	124 ± 4	10.9 ± 3.2	16.089 ± 16.986	4.1 ± 1.4
	K1	139	59 ± 839	-	-	-	-837 ± 791	-	53.2 ± 20.7	1.272 ± 0.269	-
	K2	25	-351 ± 371	-	-	-	-293 ± 154	-	61.9 ± 22.1	1.352 ± 0.528	-
	K3	12	13 ± 911	-	-	-	-278 ± 0	-	38.0 ± 16.8	1.315 ± 0.241	-
	C	**85**	**-261 ± 512**	**61.0**	**21.6 ± 16**	**64.9 ± 24.6**	**827 ± 439**	**97 ± 58**	**5.8 ± 4.9**	**1.152 ± 0.291**	**18.1 ± 13.1**
	D	**167**	**-136 ± 628**	**61.6**	**32.2 ± 18.2**	**30.1 ± 11.2**	**684 ± 429**	**76 ± 54**	**3.1 ± 3.4**	**1.084 ± 0.233**	**20.1 ± 13.6**
	MD	**132**	**4 ± 751**	**67.3**	**30.6 ± 20.1**	**29.0 ± 10.7**	**1313 ± 846**	**39 ± 37**	**8 ± 5.1**	**1.323 ± 0.515**	**6.5 ± 8.2**
	S	**218**	**125 ± 802**	**85.9**	**25.7 ± 19.7**	**36.0 ± 16.4**	**414 ± 273**	**162 ± 125**	**5.1 ± 5.5**	**1.620 ± 3.614**	**16.4 ± 14.2**
	K	**176**	**-3 ± 807**	**131.1**	**26.7 ± 18**	**-**	**-722 ± 740**	**-**	**53.4 ± 21.3**	**1.286 ± 0.319**	**-**
	All categories	**778**	**-22.5 ± 743**	**169.4**	**27.7 ± 19**	**-**	**-**	**-**	**-**	**-**	**-**
Mars	Hrs1	3	2838 ±1054	-	-	70.8 ± 20.9	1755 ± 816	49 ± 19	33 ± 15.6	1.358 ± 0.27	2.3 ± 0.5
	Hrs2	10	4236 ± 596	-	-	55.3 ± 10.7	2101 ± 493	27 ± 6	-	-	-
	Lrs1	31	4389 ± 3161	-	-	36.2 ± 13.1	149 ± 85	324 ± 237	1.3 ± 0.7	1.862 ± 0.901	35.0 ± 19.7
	Lrs2	23	4133 ± 3209	-	-	35.3 ± 13.9	148 ±73	279 ± 151	2.5 ± 1.4	14.675 ± 16.33	18.4 ± 10.1
	Lrs3	17	6591 ± 1561	-	-	27.7 ± 5.6	169 ± 54	173 ± 41	0.9 ± 0.4	1.848 ± 0.689	33.3 ± 12
	Lrs4	9	6555 ± 456	-	-	26.0 ± 5.6	142 ± 58	206 ± 69	2 ± 0.8	13.985 ± 12.075	16.4 ± 7.9
	Lrs5	9	6813 ± 478	-	-	24.3 ± 3.8	137 ± 51	202 ± 78	-	-	-
	Lrs6	1	1684 ± 0	-	-	54.1 ± 0	418 ± 0	129 ± 0	9.5 ± 0	3.6 ± 0	5.7 ± 0
	Hrs	**13**	**3914 ± 936**	**118.1**	**26.9 ± 10.3**	**58.8 ± 15.2**	**2021 ± 602**	**32 ± 14**	**33 ± 15.6**	**1.358 ± 0.27**	**2.3 ± 0.5**
	Lrs	**90**	**5168 ± 2835**	**974.5**	**13.3 ± 11.6**	**32.3 ± 12.1**	**154 ± 76**	**258 ± 174**	**1.7 ± 1.4**	**6.866 ± 11.414**	**27.5 ± 16.9**
	Tu	**18**	**1204 ± 76**	**288.7**	**64.5 ± 4.5**	**34.9 ± 11.9**	**1381 ± 521**	**29 ± 15**	**-**	**-**	**-**
	C	**2**	**741± 22**	**-**	**18.8 ± 1.2**	**28.5 ± 1.5**	**2227 ± 63**	**13 ± 0**	**8 ± 0**	**1 ± 0**	**3.8 ± 0**
	K	**1**	**584 ± 0**	**-**	**44.5 ± 0**	**86.4 ± 0**	**1373 ± 0**	**63 ± 0**	**50.2 ± 0**	**1.116 ± 0**	**1.7 ± 0**
	All categories	**124**	**4353 ± 2863**	**959.9**	**22.5 ± 20.9**	**-**	**-**	**-**	**-**	**-**	**-**

2.4.1 Frequencies

Figure App.1 displays a column chart of the frequencies of all the morphological subcategories on both planets. The number of catalogued intermediate volcanic features on both planets totals 902. 778 of these occur on Venus. For comparison, 360 intermediate volcanoes and calderas were identified by *Head et al.* [1992], and 386 by *Crumpler and Aubele* [2000]. 176 calderas have been identified (compared with 86 by *Head et al.* [1992] and 97 by *Crumpler and Aubele* [2000]); 167 steep-sided or unmodified domes (compared with 152 by *Head et al.* [1992] and 153 by *Crumpler and Aubele* [2000]); 127 fluted or modified domes (compared with 50 by *Head et al.* [1992] and 57 by *Crumpler and Aubele* [2000]); and 22 radial flow shields (compared with 25 by *Head et al.* [1992] and 24 by *Crumpler and Aubele* [2000]). *Head et al.* [1992] and *Crumpler and Aubele* [2000] identified 47 and 55 'undivided' volcanoes, respectively. The significant contrast between the values obtained by the various surveys may be caused in part by differences in how a volcanic edifice is defined. For instance, the survey of *Crumpler and Aubele* [2000] divides intermediate volcanic edifices into fluted or modified domes, radial flows, steep-sided domes, calderas, and an undefined category. With the exception of radial flows (analogous to S6 and S7 shields), edifices matching the descriptions of the cone and shield groups in this survey do not seem to have been described by previous surveys. Cones and non-radial flow shields mapped in the present survey may fall into the undefined category, yet that category features only 55 edifices, in contrast to 281 identified in the present survey.

Assuming that unmodified domes and modified domes represent different preservation states of the same landform, together these categories represent the most numerous volcanic feature (38.5% of the total), followed by shields (28%), calderas (22.5%) and cones (11%). 139 K1 calderas have been identified, making them the most prevalent subcategory. 132 modified domes have been identified in contrast to 167 domes, indicating that almost half the domes on Venus have experienced significant collapse. However, the populations of corresponding unmodified dome and modified dome categories do not always correlate well with one another. For instance, the ratio of the number of D2 features to MD2 features (which display wide, deep calderas) is 1:1.81, whereas the ratio of the number of D3 features to MD3 features (which display small, shallow 'pit' calderas) is 7.73:1.

124 intermediate volcanic features have been catalogued on Mars. Almost 75% of the intermediate volcanic features on Mars take the form of low-relief shields, which comprise just over 25% of the population on Venus. In order of frequency, low-relief shields are followed by tuyas (14.5%), high-relief shields (10.5%), cones (1.5%) and a single caldera (1%).

2.4.2 Global distribution

Figures App.2a and App.2b show the distribution of features of each major morphological category overlain on global topographic maps of Venus and Mars respectively. The locations of the Beta-Atla-Themis (BAT) and Tharsis regions, which display high concentrations of volcanic features, are indicated on the Venusian and Martian maps, respectively. Figures App.3a and App.3b display the latitudinal distributions of each of the major morphological categories for Venus and Mars respectively; the latitude ranges on the *x*-axis define regions of equal area.

Figure App.2a confirms previous observations that the BAT region on Venus displays significantly higher concentrations of volcanic features relative to the rest of the planet. 357 intermediate volcanic features, or almost 46% of the total, exist within the BAT region, an area that covers just over 25% of the surface area of the planet; this gives a concentration of intermediate volcanic features in the BAT region that is 2.5 times that for the rest of the planet. Cones and calderas are particularly concentrated within the BAT region, which holds 59% of cones and 56% of calderas, but the distribution of shields and domes is less influenced by it: 46% of shields and 35% of domes (31% of unmodified domes and 39% of modified domes) exist within the region.

Table 2.3 shows the results of the χ^2 tests for the Venusian volcanic features; lower χ^2 values correspond to distributions that are closer to being random than distributions with higher χ^2 values. The distribution of cones is that which is the least random, with a χ^2 value of 61.0. Thereafter, the distributions of shields, all dome types and calderas become progressively less random, with respective χ^2 values of 85.9, 87.2, and 131.1. The χ^2 value for all features is 169.4. The concentration of features within the BAT region is the main influence on the skewing of the distributions of all features away from uniform.

Figure App.3a and Table 2.3 show that cones cluster most towards the equator (mean latitude of 21.6°), whereas all dome types more commonly occur at higher

latitudes (mean latitude of 31.5°), with shields and calderas falling in between (mean latitudes of 25.7° and 26.7° respectively). The latitudinal distributions of the different feature categories reflect the extents to which they are concentrated within the BAT region, which is itself centred on the equator.

Despite the concentration of Venusian intermediate volcanic features within the BAT region, such features do exist across most of the planet; in contrast, Fig. App.2b shows that Martian intermediate volcanic features are heavily concentrated in localized areas, to the exclusion of all other areas of the planet. 79% of all intermediate volcanoes are located within the Tharsis region. High- and low-relief shields are all located within the Tharsis region and the immediate surrounding area, with the exception of one low-relief shield existing in the southern highlands (the only example of subcategory Lrs6) and five existing in Cerberus Planitia. All 18 tuya features are concentrated within Sisyphi Planum in the southern highlands. The highly localized nature of the distributions is apparent in the χ^2 test values (118.1 for high-relief shields, 974.5 for low-relief shields, and 288.7 for tuyas), and in the latitudinal distribution as shown in Fig. App.3b and by the mean latitudes in Table 2.3. Because of this strong localization of particular morphological categories, the latitudinal distributions generally peak strongly around certain latitude ranges; in the case of the cone and caldera categories, this is an artefact associated with their low frequencies.

2.4.3 Altitudinal distribution

Figures App.4a and App.4b are scatter charts showing the mean basal elevations and associated standard deviations for all subcategories and major categories on Venus and Mars respectively, whereas Figs. App.5a and App.5b are line charts showing the altitudinal distributions of the major categories on Venus and Mars respectively.

Figures App.4a and App.5a show that 58.8% of Venusian intermediate volcanic features are located below the MPR of 6051.8 km, with a mean basal elevation across all categories of 22.5 m below MPR, with an associated standard deviation of 743 m. *Ristau et al.* [1998] obtained a mean basal elevation of ~200 m below MPR for steep-sided domes, modified domes, radial flow shields and 'undivided' volcanoes. Cones exist at the lowest mean elevation (261 m below MPR), whereas shields exist at the highest mean elevation (125 m above MPR), with 386 m difference between the two. Intermediate are all dome types, at 75 m below MPR, and calderas, at 3 m below MPR.

Radial flow shields (categories S6 and S7) are found to exist at abnormally high elevations (mean of 768 m above MPR), agreeing well with the value of ~800 m above MPR determined by *Ristau et al.* [1998]. Cones exist across the narrowest range of elevations, displaying a standard deviation of 512 m, whereas calderas exist across the widest range of elevations, with a standard deviation of 807 m.

Figures App.4b and App.5b show that the vast majority (96%) of Martian volcanic features exist above MPR, with the exception of five low-relief shields existing in Cerberus Planitia. This distribution is largely a consequence of the clustering of many of the low relief shields, the most populous morphology, in the high-lying Tharsis rise. The mean basal elevation across all categories is 4353 m above MPR, with an associated standard deviation of 2863 m, almost four times that on Venus. The high standard deviation stems from the broad altitudinal distribution of low and high-relief shields, which form the majority of Martian intermediate volcanic features. The altitudinal distributions of the other categories cluster around very localized altitude ranges; in the case of the cone and caldera categories, this is an artefact associated with their low frequencies.

2.4.4 Geological setting

The stacked column charts in Figs. App.6a and App.6b show the percentages of each morphological subcategory and major category existing within each geological setting on Venus and Mars respectively. Tables 2.4 and 2.5 show the same information in tabular form. Notable correlations between volcano morphologies and parent environments are described below.

On Venus, fractured plains are the most common variety of plains environment in which volcanic features are found. 38.9% of all features exist in this terrain, including 53.4% of calderas and 50.6% of cones. 21.3% of all features exist in wrinkle-ridge plains, 19.9% in lava flow fields, and 16.7% in smooth plains. 24.2% of modified domes exist on volcano flanks or summits, but only 7.2% of steep-sided domes. 32.9% of steep-sided domes and 23.5% of modified domes are found either proximal to (within 100 km) or within coronae; for comparison, *Stofan et al.* [2000] noted that 45% of intermediate-sized steep-sided domes are proximal to (within ~150 km) or within coronae. 29% of steep-sided domes are located within dome fields, whereas only 14% of modified domes are; for comparison, *Stofan et al.* [2000] found that 38% of steep-

sided domes are located within chains of steep-sided domes. 28.9% of shields are found within shield fields. Few features of any type are found in or proximal to tessera terrain (6.3% of all features).

Table 2.4. Percentages of each morphological subcategory (in regular font) and major category (in bold) existing within each geomorphological environment on Venus. The mean basal elevation all features within the smooth plain, fractured plain, wrinkle-ridge plain and tessera environments are shown at the bottom.

Morphological class	**% of morphological class features existing within the geomorphological environment**							
	Smooth plains	**Fractured plains**	**Wrinkle-ridge plains**	**Tessera**	**Flow field**	**Shield/dome field**	**Corona/ caldera**	**Volcano summit/flank**
C1	30	30	30	0	0	0	10	0
C2	9.5	57.1	28.6	14.3	23.8	9.5	9.5	0
C3	0	61.9	23.8	4.8	38.1	19	0	0
C4	12.1	45.5	30.3	3	24.2	12.1	9.1	0
D1	25.8	32.3	9.7	0	12.9	45.2	29	12.9
D2	6.3	40.6	28.1	3.1	15.6	15.6	37.5	15.6
D3	31.8	32.9	22.4	8.2	10.6	43.5	38.8	0
D4	5.3	26.3	10.5	0	10.5	15.8	52.6	15.8
MD1	5.9	41.2	11.8	5.9	11.8	5.9	35.3	23.5
MD2	12.1	25.9	10.3	0	10.3	19	27.6	32.8
MD3	36.4	18.2	18.2	0	9.1	54.5	36.4	9.1
MD4	3	39.4	12.1	0	9.1	9.1	24.2	24.2
MD5	0	12.5	62.5	12.5	50	0	0	0
MD6	20	0	60	0	0	20	20	0
S1	24.5	26.5	20.4	6.1	36.7	14.3	16.3	4.1
S2	9.1	45.5	27.3	4.5	27.3	50	4.5	0
S3	17	39.6	20.8	1.9	20.8	24.5	15.1	13.2
S4	15.4	30.8	38.5	7.7	30.8	0	15.4	0
S5	32.2	22	6.8	10.2	44.1	32.2	5.1	1.7
S6	23.5	52.9	0	0	29.4	58.8	11.8	0
S7	40	40	0	20	20	100	0	0
K1	11.5	54	27.3	10.1	59.7	6.5	13.7	0.7
K2	16	44	24	16	80	8	20	4
K3	0	66.7	16.7	25	50	0	8.3	0
C	**10.6**	**50.6**	**28.2**	**5.9**	**24.7**	**11.8**	**7.1**	**0**
D	**22.8**	**33.5**	**19.0**	**4.8**	**12**	**35.3**	**38.3**	**7.2**
MD	**10.6**	**28.8**	**16.7**	**1.5**	**12.1**	**16.7**	**26.5**	**24.2**
D+MD	**17.4**	**31.4**	**18.4**	**3.3**	**12**	**27.1**	**33.1**	**14.7**
S	**22.9**	**33**	**16.5**	**6**	**32.6**	**29.8**	**11**	**4.6**
K	**11.4**	**53.4**	**26.1**	**11.9**	**15.9**	**6.3**	**14.2**	**1.1**
All categories	**16.8**	**38.9**	**20.7**	**6.3**	**19.9**	**21.5**	**19.8**	**7.2**
Mean elevation above MPR (m)	-92 ± 674	-30 ± 685	-313 ± 452	612 ± 1040	-	-	-	-

Table 2.5. Percentages of each morphological subcategory (in regular font) and major category (in bold) existing within each geomorphological environment on Mars.

Morphological class	**% of morphological class features existing within the geomorphological environment**				
	Smooth plains	**Fracture belt**	**Shield field**	**Cratered highlands**	**Rough, knobbly plains**
Hrs1	100	0	66.7	0	0
Hrs2	30	70	0	90	0
Lrs1	80.6	16.1	74.2	0	0
Lrs2	65.2	34.8	82.6	0	0
Lrs3	0	5.6	100	0	0
Lrs4	0	0	100	0	0
Lrs5	11.1	0	88.9	0	0
Lrs6	0	0	0	100	0
Hrs	**46.2**	**53.8**	**15.4**	**69.2**	**0**
Lrs	**45.6**	**15.6**	**84.4**	**1.1**	**0**
Tu	**0**	**0**	**0**	**16.7**	**83.3**
Cc	**0**	**0**	**0**	**100**	**0**
Ca	**0**	**100**	**0**	**0**	**0**
All categories	**37.9**	**19.4**	**62.9**	**12.1**	**12.1**

On Mars, almost 75% of intermediate volcanic features are low-relief shields, with the consequence that almost 63% of all intermediate Martian volcanic features exist in shield fields (84.4% of low-relief shields). High- and low-relief shields are the only features to be found in smooth plains (comprising lava flows in the Tharsis and Cerberus regions), with 46.2% of high-relief shields and 45.6% of low-relief shields found in such an environment. High-relief shields are the most common in fracture belts and cratered highlands, with 53.8% and 69.2% of them occurring in the two environments respectively.

2.4.5 Diameter and height characteristics

Figures App.7a and App.7b are line charts showing the diameter distributions of the major categories on Venus and Mars, respectively, whereas Figs. App.8a and App.8b are scatter charts showing the mean edifice diameters and associated standard deviations for all subcategories and major categories on Venus and Mars respectively. Figures App.9a and App.9b are scatter charts showing the mean heights and associated standard deviations for all subcategories and major categories on Venus and Mars respectively. It should be noted that for Venus, height measurements have been obtained for only 46% of catalogued features (the proportion that display topographic signatures in GTDR data); in some cases, only one measurement has been obtained for an entire subcategory. For this reason, height distribution line charts are not shown. Figures App.10a and App.10b are scatter charts showing the mean aspect ratios and associated standard deviations for all subcategories and major categories (discounting calderas) on Venus and Mars respectively.

On Venus, cones have the largest mean diameter (64.9 km), followed by calderas (53.4 km), shields (36.0 km) and all domes (29.6 km). The mean diameters of unmodified domes (30.1 km) and modified domes (29.0 km) are virtually identical. The diameter distribution lines in Fig. App.8a show that all dome types and shields tend strongly towards diameters below 40 km, whereas the diameters of cones and calderas are more evenly distributed across the range 20 to 100 km; the frequency of cones actually increases steadily from diameters of 60 to 100 km. These distributions are reflected in the larger standard deviations associated with the mean diameters for cones and calderas relative to domes and shields. Domes are the tallest volcanic edifices (mean height of 980 m for all dome types), followed by cones (827 m) and shields (414

m), with calderas having an average depth of 722 m. Modified domes display mean heights that are almost twice as high as unmodified domes, with the exception of the MD4 category, which likely displays a lower mean height due to the altitude being measured from the downsagged summit region rather than the high rim. Domes display the greatest range of heights (standard deviation of 745 m for all types), followed by cones (439 m) and shields (273 m). Shields have the greatest aspect ratios (mean of 162), followed by cones (97) and all dome types (58). The S5 shield category has the anomalously high aspect ratio of 507, based on three height measurements. There is a notable correlation in the relative mean diameters, mean aspect ratios and (to a lesser extent) mean heights between the corresponding D1 to D4 and MD1 to MD4 subcategories, which is apparent in Figs. App.8a, App.9a and App.10a, and Table 2.3. The similarities in dimensional parameters between corresponding subcategories, which are defined by characteristics of their calderas, reinforces the hypothesis that each MD subcategory is a modified version of its corresponding D subcategory, as originally postulated by *Bulmer and Guest* [1996].

On Mars, after the single caldera with a diameter of 86.4 km, high-relief shields display the greatest mean diameter (58.8 km), followed by tuyas (34.9 km), low-relief shields (32.3 km), and the two cones (28.5 km). The diameter distribution lines in Fig. App.8b show that low-relief shields and tuyas tend strongly towards diameters below 50 km, whereas high-relief shields mostly have diameters between 30 and 70 km. Standard deviations associated with the mean diameters of high- and low-relief shields and tuyas are fairly similar. After the two cones, which have a mean height of 2227 m, high-relief shields display the greatest heights (mean height of 2021 m), followed by tuyas (1381 m) and low-relief shields (154 m). The standard deviations associated with high-relief shields (602 m) and tuyas (521 m) are much higher than that associated with low-relief shields (76 m). Low-relief shields display the largest aspect ratios (mean of 258, not dissimilar to the corresponding value of 232 for class S6 shields on Venus). High-relief shields display a mean aspect ratio of 32, which is in fact a lower mean ratio than that for edifices described as domes on Venus. Tuyas and cones display still lower aspect ratios of 29 and 13, respectively.

2.4.6 Vent and fracture characteristics

Table 2.3 shows three columns which detail the mean caldera diameter, mean caldera length/width ratio and edifice/caldera diameter ratio for all subcategories and major categories. Figure App.8 includes the mean diameters of the calderas and associated standard deviations for all subcategories and major categories on Venus and Mars respectively. On Venus, shields most commonly display summit vents (90.8%), followed by unmodified domes (71.3%), modified domes (58.3%) and cones (44.7%). Aside from the caldera category itself, modified domes are found to have the largest calderas, with a mean caldera diameter of 8 km, followed by cones (5.8 km), shields (5.1 km) and unmodified domes (3.1 km). 6.5% of all the surveyed domes display calderas with diameters greater than 50% of the diameter of the parent edifice; the study of *Stofan et al.* [2000] obtained a corresponding figure of 14% of domes. Shields have a notably high mean caldera length/width ratio (1.62); class S7 shields, which appear to erupt from fissure vents have the highest ratio at 16.09. Modified domes have an anomalously small edifice/caldera diameter ratio relative to the other edifice categories.

On Mars, 90% of shields display summit vents. Only Hrs1 category high-relief shields are seen to display definite summit calderas; Hrs2 category edifices display potential calderas in some cases, but these cannot be easily distinguished from impact craters. The mean caldera length/width ratio for low-relief shields is 6.87, considerably higher than the value for shields on Venus. The edifice/caldera diameter ratio for low-relief shields is very high at 27.5.

In addition to the central pits/calderas of Venusian domes, 31% of all dome types were found to display collapse pits elsewhere on their surfaces; such collapse pits may be equidimensional, as well as elongate and fissure-like, in which case they are sometimes aligned parallel to regional fracturing. 14% display radial fracturing (including radial chains of collapse pits). These proportions barely vary for steep-sided and modified domes: 31% of steep-sided domes and 32% of modified domes display collapse pits, whereas 15% of steep-sided domes and 13% of modified domes display radial fracturing. The similarities in the proportions of the steep-sided and modified domes which show such features represent further evidence that modified domes are evolved forms of steep-sided domes.

Chapter 3
Investigation of Environmental Controls on Volcanic Feature Morphology on Mars and Venus

3.1 Introduction

Several hundred intermediate-sized volcanic features on both Venus and Mars have been catalogued, with comprehensive qualitative morphological descriptions and quantitative locational and morphological information provided for each feature. Given the very large quantity of data that has been obtained through compilation of this catalogue, this chapter will not attempt to examine and interpret all of the data, but will instead focus on three topics that are integral to the subject area of this thesis, and for which analysis of the available data is regarded to yield the most comprehensive results. These topics are:

- Identification of evolutionary precursors of large volcanoes on Venus, and interpretation of similarities and differences between the morphologies of volcanoes of different sizes with respect to the evolution of their intrusive systems.
- Investigation of the causes of the similarities and differences in morphology between low-relief shield volcanoes on Venus and Mars, the only morphological class to exist in appreciable quantities on both planets.
- Identification of the environmental controls that are most influential in determining the morphologies of domes on Venus, the morphological category that displays the most internal variety.

3.2 Evolutionary precursors of large volcanoes on Venus

3.2.1 Introduction

The evolution of the morphologies of large Venusian volcanoes has been the subject of several studies, including *Rogers and Zuber* [1998], *McGovern and Solomon* [1998], *Kiefer and Potter* [2000], *Stofan et al.* [2001], *Barnett et al.* [2002], and *Brian et al.* [2004]. These studies have approached the topic from different aspects, but have generally focused on the extent to which the formation and growth of large volcanoes are related to lithospheric thickness; for instance, *McGovern and Solomon* [1998] modelled the evolution of stress and deformation in growing volcanic edifices in order

to determine the conditions and processes that account for differences in the structure, tectonics and evolution of large volcanoes on Venus, Earth and Mars. The study of *Stofan et al.* [2001] focused on three large volcanoes with differing morphologies on Venus (Sif, Gula and Kunapipi Mons), with the intention of inferring the nature of their magma storage systems and the extent to which they evolve over time based on their flow, caldera and bulk morphology characteristics.

While these studies have contributed to the understanding of how the evolution of large volcano morphologies on Venus is governed, their focus has been exclusively concentrated on large volcanoes themselves, and has not considered evolutionary precursors of such edifices that are less than 100 km in diameter. Identification of such precursors will introduce an extended population of features that will allow changes in edifice morphology and intrusive configuration with growth to be characterised to a better degree than has been achieved based on observations confined to large volcanoes. Based on morphological comparisons between large volcanoes and edifices belonging to the cone (C) class of intermediate volcanoes as catalogued in this study, it is considered that the cone class represents these precursors. This section will describe the observed morphological similarities and differences between the cone class and large volcanoes, and discuss the implications of the observations for the evolution of the morphologies of these volcano types and their relation to the evolution of the intrusive systems feeding the volcanoes.

3.2.2 Morphological comparisons between intermediate C-class and large volcanoes

Various morphological relationships appear to indicate that C-class intermediate volcanoes are evolutionary precursors to large volcanoes on Venus. The evidence is described below:

Size distribution: Figure App.7a displays the diameter distribution of intermediate cones, shields, steep-sided domes and modified domes on Venus. The frequencies of the shield and dome categories decrease with increasing size, eventually tailing off to near zero at the 90 to 100 km diameter increment. However, the frequency of cone category edifices increases with increasing size; this distribution would suggest that the occurrence of such edifices would continue beyond the 100 km upper limit on intermediate volcano diameter. Figure 3.1 displays the diameter distribution of the intermediate cones catalogued in this study as well as the 134 large volcanoes

catalogued for the study of *Brian* [2001]. It can be seen that the edifice frequency decreases with increasing size according to an approximately exponential relationship, which the curve overlain on the chart represents. This indicates that the total number of catalogued intermediate cones is consistent with the size distribution displayed by the large volcanoes, implying that intermediate cones and large volcanoes are representatives of the same volcano population.

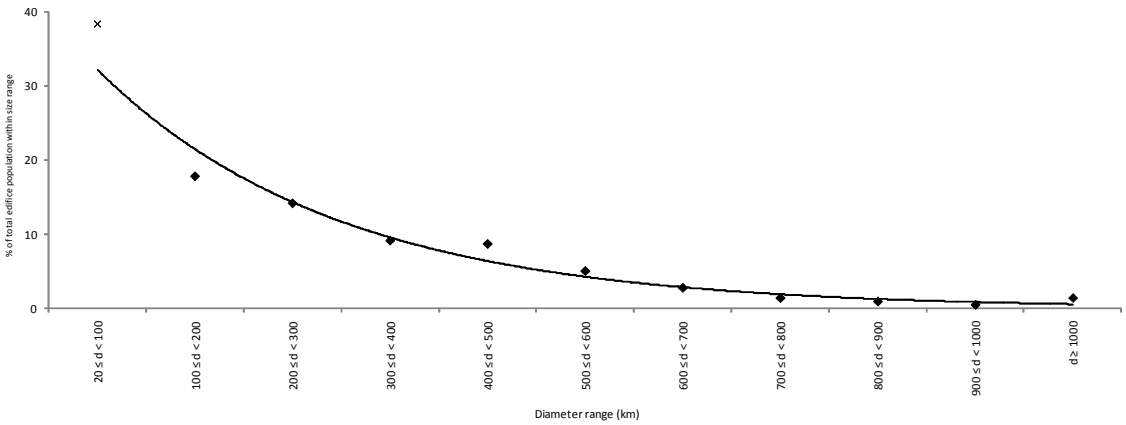

Figure 3.1. Diameter distribution of intermediate cones catalogued by this study (cross data point) and large volcanoes catalogued by *Brian* [2001] (diamond data points). Black curve represents the closest-fit exponential relationship to the size distribution, the formula of which is $y = 48.145e^{-0.404x}$.

Quantitative morphology: There is a notable consistency in certain morphological statistics between intermediate cones and large volcanoes. Figure 3.2 displays four graphs plotting various morphological statistics against edifice diameter for intermediate cones, shields and domes, as well as large volcanoes. Linear trendlines have been added to each dataset.

- For the graph of edifice aspect ratio plotted against edifice diameter (Fig. 3.2a), the large volcano trendline is slightly negative (-0.076). While those of the intermediate volcanoes are all positive, that for the cones is least positive (0.783, compared with 2.144 for domes and 3.073 for shields).
- For the graph of edifice height plotted against edifice diameter (Fig. 3.2b), the positive gradient displayed by the large volcano trendline (3.533) is most closely matched by that of the cone trendline (6.894, almost twice that of the large volcano trendline), rather than that of the shield trendline (1.364, about a third that of the large volcano trendline), whereas the dome trendline displays a negative gradient (-10.727).

Figure 3.2 (below and following page). Four graphs plotting various morphological statistics against edifice diameter for intermediate cones, domes, shields and large volcanoes, with linear trendlines plotted for each individual dataset on each graph. (a) Edifice aspect ratio. (b) Edifice height. (c) Caldera diameter. (d) Ratio of edifice diameter to caldera diameter.

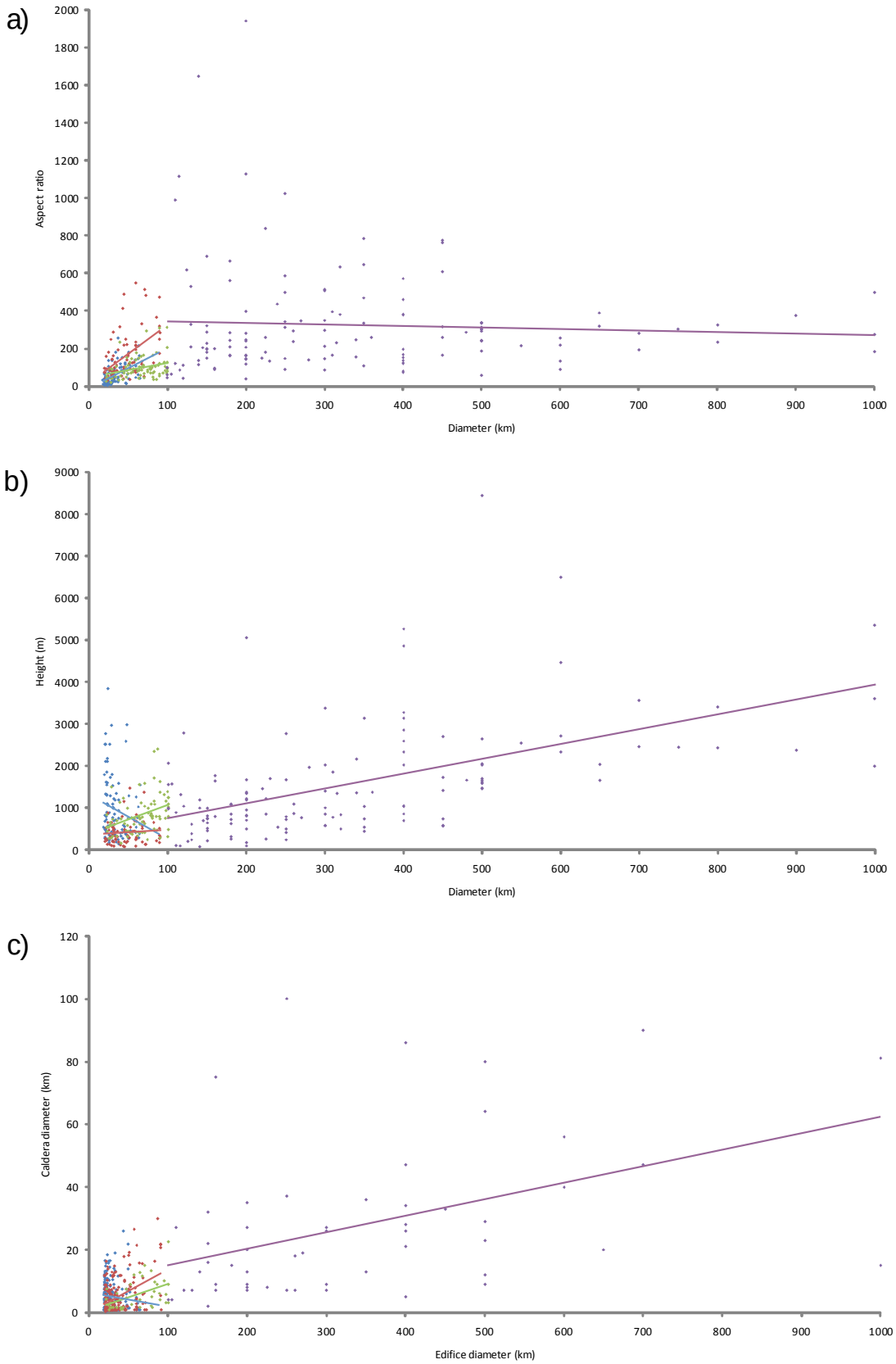

d)

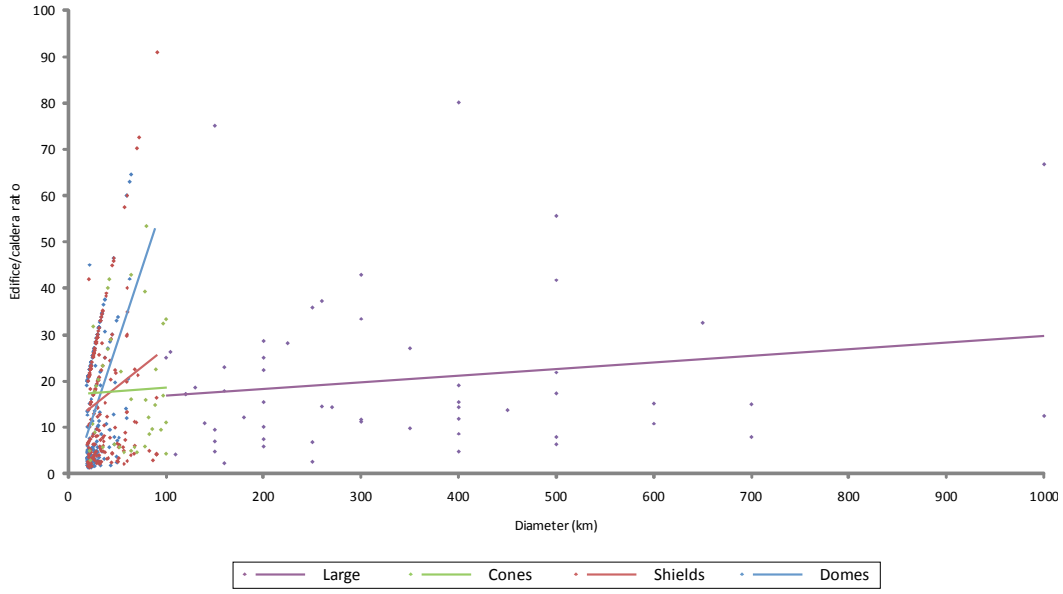

- For the graph of caldera diameter plotted against edifice diameter (Fig. 3.2c), the positive gradient displayed by the large volcano trendline (0.052) is most closely matched by that of the cone trendline (0.083), rather than that of the shield trendline (0.136) or dome trendline (-0.043).
- For the graph of edifice/caldera diameter ratio plotted against edifice diameter (Fig. 3.2d), the positive gradient displayed by the large volcano trendline (0.014) is exactly matched by that of the cone trendline (0.014), whereas the shield trendline has a gradient of 0.165 and the dome trendline a gradient of 0.635.

Despite the considerable scatter within the data, it can be seen that across all the graphs, the gradient of the trendline for the cones most closely matches that of the trendline for the large volcanoes.

Qualitative morphology: Large volcanoes on Venus typically display two main structural components: the main edifice, which tends to have flank slopes of 1-3°, and the outer lava apron, with slopes of <1° [*Stofan et al.*, 2001]. The surface resolution cell of the Magellan GTDR altimetry maps measures ~10 km in diameter [*Saunders et al.*, 1990], meaning that topographic profiles of intermediate volcanoes cannot reveal bulk morphology as they can for large volcanoes that are several hundred kilometres across. However, the qualitative bulk morphology of these volcanoes can be determined from observations of backscatter intensity and the locations of flows of certain types on their flanks, as well as stereo image analysis. Scrutiny of the intermediate cones catalogued in the survey revealed that 31% display the morphological configuration of a steep

central edifice surrounded by a broad outer flow apron, whereas 98% of large volcanoes catalogued by *Brian* [2001] display such a configuration. The remaining intermediate volcanoes appear to lack a distinct steep central edifice. Despite the disparity between these proportions, domes never display such a configuration, uniformly comprising steep flanks leading to a flat summit region, whereas shields generally display consistently gently sloping flanks leading to the summit vent. In addition, cones are the only intermediate volcanoes that are seen to display steep-sided domes at their summits, a trait that also characterises some large volcanoes. Figure 3.3 compares the bulk morphology of an intermediate cone with that of the large volcano Tuulikki Mons.

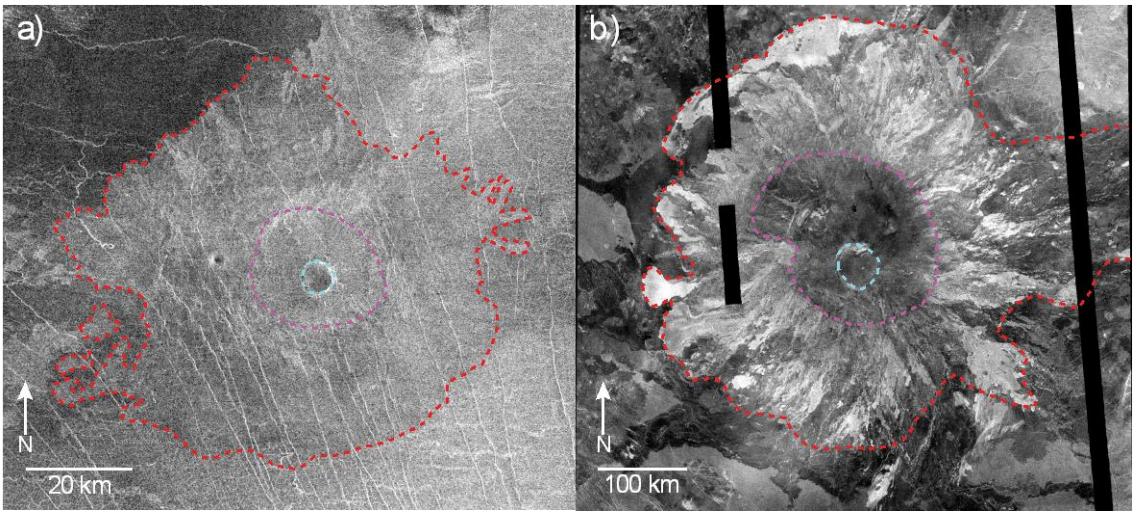

Figure 3.3. Comparison of the bulk morphologies of an intermediate cone located at 5.5°N, 277°E (a) and Tuulikki Mons (b), a large volcano located at 10.5°N, 274.5°E. In both images, the red dashed line marks the margin of the outer flow apron, which in both cases displays radial, high reflectivity digitate flows; the purple dashed line marks the margin of the steep central edifice; the cyan dashed line marks the margin of the summit caldera. Both images are left-looking Magellan images.

3.2.3 Relation of summit structure to intrusive processes

The summit structures of volcanoes, and in particular the configuration of their vents, can aid in the interpretation of their magma storage and plumbing systems. *Head and Wilson* [1992] concluded that the rate of ascent of neutral buoyancy zones and associated magma reservoirs on Venus would be very slow, and that for edifices less than ~2.5 km in elevation above MPR, the magma reservoir would not enter the edifice. *Mouginis-Mark* [1994] and *Stofan et al.* [2001] countered this assertion by citing examples of large volcanoes of similar elevations above MPR that displayed quite different summit structures (e.g. Sif and Kunapipi Mons [*Stofan et al.*, 2001]), as well as large volcanoes of very different elevations above MPR that display very similar

summit structures (e.g. Sif and Maat Mons [*Mouginis-Mark*, 1994]). The summit structure will be strongly influenced by the depth of the magma reservoir, and *Stofan et al.* [2001] interpreted these observations to imply that factors other than neutral buoyancy, such as the stress field, have also played a role in controlling magma chamber location with time. The survey of intermediate cones, when combined with the large volcano survey of *Brian* [2001], provides a further test for the extent to which neutral buoyancy is governing the summit configurations of these edifices. Various observations are described below.

Presence of a summit caldera: Previous studies have established that a collapse caldera can provide evidence for a shallow magma reservoir that is comparable in diameter to the caldera [*Fiske and Kinoshita*, 1969; *Koyanagi et al.*, 1972; *Ryan et al.*, 1983; *Marsh*, 1984; *Mouginis-Mark and Rowland*, 2001; *Stofan et al.*, 2001; *Folch and Marti*, 2004]. Neutral buoyancy theory [*Head and Wilson*, 1992] predicts that large magma reservoirs should form with widely distributed pathways to the surface as volcanoes grow, accompanied by a consequential transferral from extrusion to diking at the summit [*Head and Wilson*, 1992]. *Mouginis-Mark and Rowland* [2001] considered such a scenario to promote the formation of broad shields with multiple source vents. If magma reservoirs do become deeper with increasing edifice height [*Head and Wilson*, 1992], then it would be expected that large volcanoes would display summit calderas less frequently than intermediate volcanoes, as large volcanoes display a mean height of 1527 m [*Brian*, 2001] relative to 827 m for intermediate volcanoes. The summit calderas of larger edifices would be infilled by flows, distorted by tectonism and obscured by late edifice (e.g. dome) construction. *Stofan et al.* [2001] noted that the two centres of activity at the summit of Kunapipi Mons (which displays no summit caldera) reside on an elliptical plateau, which they hypothesized may have formed from short flows emanating from the summit, or may instead indicate an earlier summit caldera that has been filled and subsequently had centres built upon it; the latter scenario has been observed at Mount Etna, where multiple cones have been built upon the summit.

However, similar proportions of intermediate and large volcanoes are found to display summit calderas: 45% of intermediate volcanoes and 42% of large volcanoes. In addition, the mean diameter of edifices displaying calderas is 223 km compared with 226 km for edifices that do not display calderas; the corresponding mean heights are

1227 and 1339 m respectively. Figures 3.4a and 3.4b display the diameter- and height-frequency distributions respectively for intermediate and large volcanoes that display summit calderas. The *y*-axis represents the percentage of the total number of edifices within each *x*-axis parameter division that display a summit caldera. The grey bars indicate the volcano population within each parameter division. If magma reservoirs become deeper with increasing edifice size, it would be expected that the frequency of caldera occurrence would decrease with increasing edifice size, yet in both graphs the distribution is erratic across all diameter ranges, even those with appreciable volcano populations (i.e. 20 to 600 km diameter and 0 to 4 km height). The graphs indicate that there is no identifiable trend linking summit caldera occurrence to either volcano height or diameter.

There also does not appear to be any correlation between the presence of a summit caldera and summit elevation above MPR. Figure 3.4d displays a graph showing the altitudinal distribution of the summits of intermediate and large edifices that feature summit collapse calderas and those that do not. *Head and Wilson* [1992] asserted that a magma reservoir should not enter an edifice for summits less than ~2.5 km in elevation above MPR; if collapse calderas are interpreted to be manifestations of high-level magma reservoirs within edifices, then it would be expected for a smaller proportion of volcanoes with summits below 2.5 km above MPR to show summit calderas. Indeed, 42% of summits below 2.5 km above MPR display calderas, whereas 54% of summits above 2.5 km above MPR display calderas. However, the absolute number of volcanoes with summit calderas below 2.5 km above MPR is actually very high: 85% of summits with calderas exist at elevations below this elevation, compared with 90% of summits without calderas. A smaller number of summit calderas would be expected to exist below 2.5 km above MPR if the assertion of *Head and Wilson* [1992] was valid. The fact that the profiles of the two distribution lines in Fig. 3.4d closely resemble each other indicates that the summit elevation above MPR does not appear to significantly influence the magma chamber level within the edifice or the formation of an associated collapse caldera. This fact is also demonstrated by the frequency distribution curve in Fig. 3.4c, which indicates the percentage of the total volcano population within each elevation division that displays a summit caldera. For elevation divisions with appreciable volcano populations (i.e. -1 to 3 km above MPR), the proportion of volcanoes within each elevation range that displays a summit does not differ

significantly from 39%, with the exception of the spike to 52% at the 0.5 to 1 km above MPR range; above 3 km above MPR, the volcano populations in each division are very low, with the curve becoming more erratic as a result.

Figure 3.4 (below and following page). Frequency distribution graphs of volcanoes displaying summit calderas. (a-c) Distribution curves of the proportions of the total number of volcanoes within each edifice diameter range (a), each edifice height range (b), and each summit elevation range (c) that display a summit caldera. (d) The altitudinal distribution of the summits of volcanoes displaying summit calderas (in black) and those displaying no summit calderas (in grey). The vertical dashed line marks the elevation of 2.5 km above MPR.

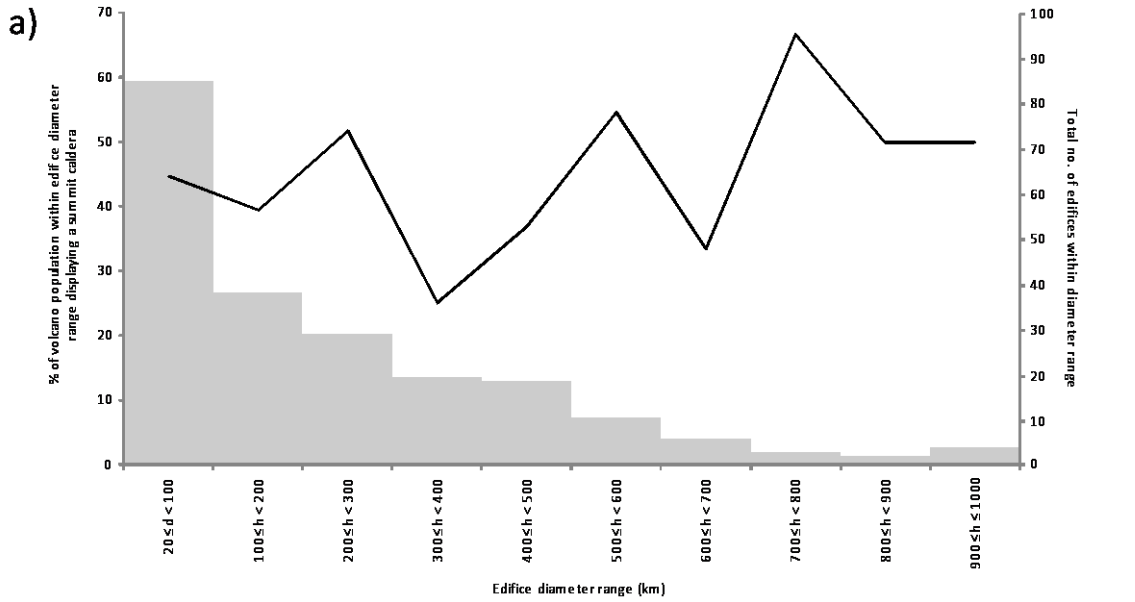

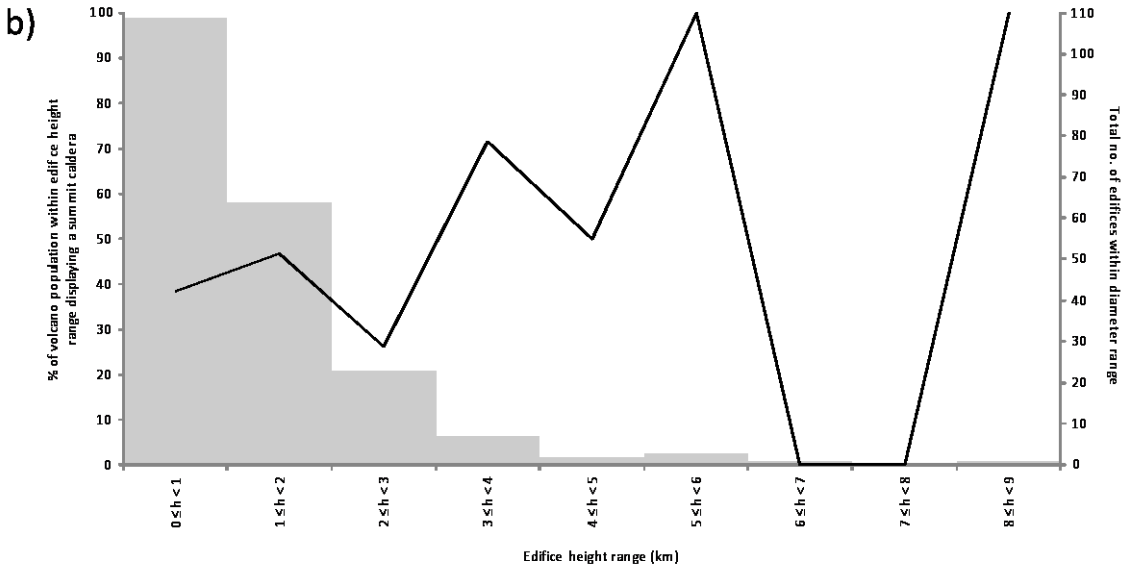

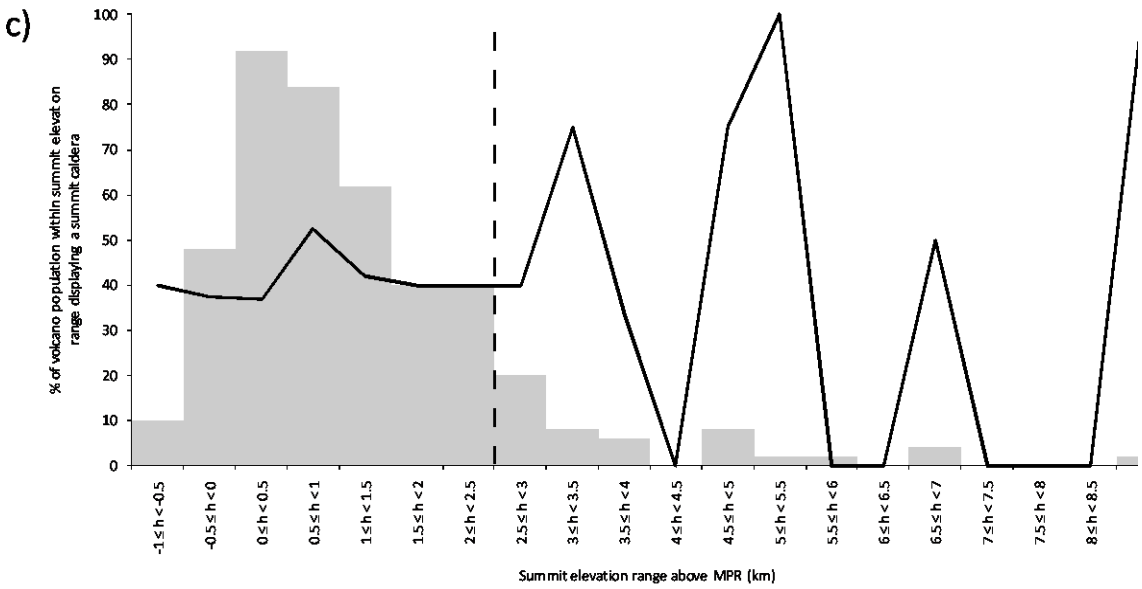

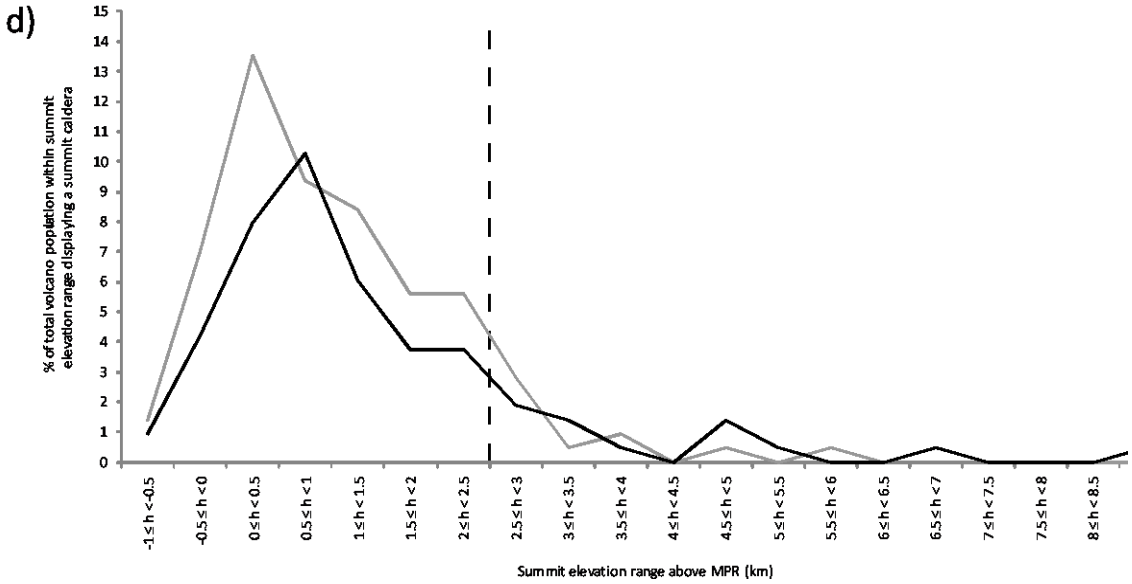

Caldera diameter: Neutral buoyancy theory predicts that the size and depth of magma reservoirs should increase with increasing edifice height and summit elevation above MPR [*Head and Wilson*, 1992], and these effects will influence caldera diameter. Shield caldera diameters on Venus and Mars have been seen to routinely reach much larger sizes than those on Earth, leading *Wood* [1984] to propose that magma chambers on Mars and Venus are significantly larger and/or deeper than their terrestrial counterparts. Inferring the reservoir diameter and depth from the caldera diameter is complicated by the fact that it is unlikely that a reservoir will be completely emptied during eruption; if a small proportion of the reservoir is emptied, a minimal area of

collapse will result at the surface [*Mouginis-Mark and Rowland*, 2001]. *Keddie and Head* [1994a] suggested that caldera size may only reflect the diameter of the shallowest portion of the reservoir. These factors suggest that the actual diameter of a reservoir will generally be greater than the diameter of the caldera implies.

The mean caldera diameter for intermediate cones is 5.8 km (σ of 4.9), whereas that for large volcanoes is 27.6 km (σ of 24.5). The mean edifice/caldera diameter ratio for intermediate cones is 18.1 (σ of 13.1), whereas that for large volcanoes is 20.2 (σ of 17.1). These statistics indicate that caldera diameter, and presumably reservoir diameter, remains roughly in equal proportion to edifice diameter as volcano growth occurs. However, the change in reservoir depth with increasing edifice size cannot easily be interpreted based on the increasing caldera size; all that can be deduced is that a high-level magma reservoir has existed below the summit at some point in the volcano's history, not necessarily recently. *Stofan et al.* [2001] noted that the bulk of recent activity at Gula Mons is rift-associated, with magma probably ascending directly from a deep-seated source, while the two calderas at either end of the summit rift indicate high-level chambers in the past.

Figure 3.5 shows three graphs plotting edifice diameter, edifice height and summit elevation above MPR against caldera diameter for intermediate and large volcanoes. Each of the graphs shows considerable scatter, although the positive trendlines in each graph do suggest a general positive relationship between caldera diameter and edifice diameter, height and summit elevation above MPR. These trends are interpreted to indicate that magma reservoir diameter generally increases with edifice size and summit elevation, with the scatter interpreted to result primarily from variations in reservoir depth not predicted by neutral buoyancy theory, as well as the extent to which caldera collapse has occurred. It is notable that the amount of scatter does not appear to vary significantly with edifice size, indicating that the variations in reservoir depth and caldera collapse extent occur during all stages of volcano growth.

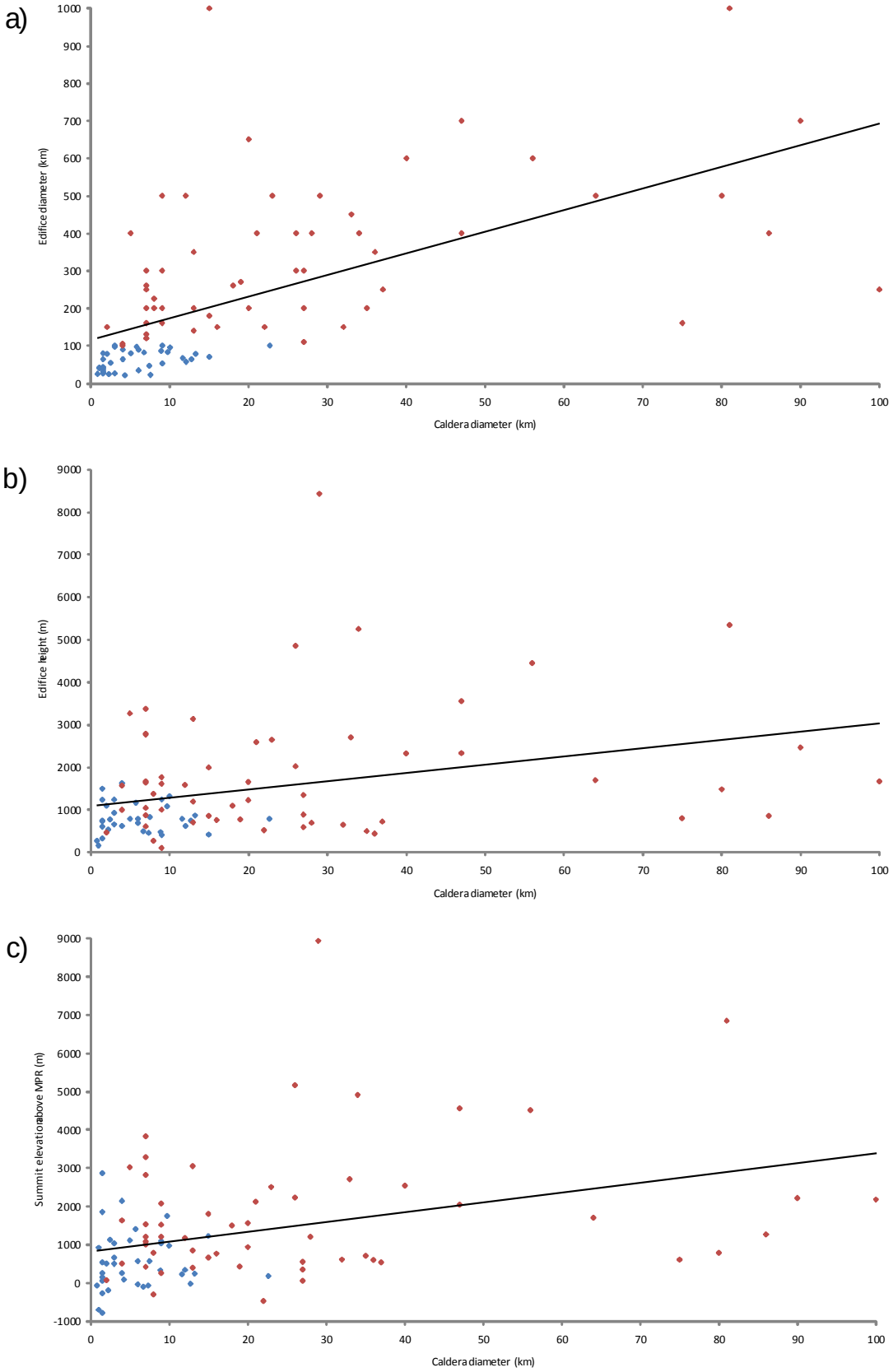

Figure 3.5. Three graphs plotting various morphological statistics against caldera diameter for intermediate cones and large volcanoes. (a) Edifice diameter. (b) Edifice height. (c) Summit elevation above MPR. Intermediate cones are represented by blue points and large volcanoes by red points. Linear trendlines are plotted for the entire dataset in each graph.

Multiple collapse zones: Most calderas display complex morphologies that indicate that they are composed of multiple rather than single collapse features [*Strong and Jaquot*, 1971; *Macdonald*, 1972]. The separate collapse features are usually at different depths within a caldera complex, and may be obvious near-circular structures that are barely joined to each other (e.g. Mauna Loa), or may merely be large scallops in the outline of the caldera (e.g. Kilauea). The separate collapse structures may be combined through infilling by later intra-caldera lavas, the presence of which indicate replenishment of the magma reservoir after caldera formation [*Stofan et al.*, 2001]. It is also possible for physically separate calderas to form on the same volcano (e.g. Kaua'i in Hawai'i, and Alba Patera and the complex within Syrtis Major on Mars) [*Macdonald*, 1972; *Schaber*, 1982; *Mouginis-Mark et al.*, 1988].

Mouginis-Mark and Rowland [2001] interpreted the presence of multiple collapse features within basaltic calderas in any context to be evidence for a subsurface plexus of storage zones rather than a single void. The conclusion of *Fiske and Kinoshita* [1969] that such interconnected voids could fill and empty one after another in response to either falling or rising magma pressure would imply that numerous collapse and infilling episodes would characterize the active life of a volcano. It has been proposed that the separate chambers may form at shallow depths within the edifice, and are fed by a deeper, primary reservoir; this scenario was suggested for Tepev Mons on Venus by *Rogers and Zuber* [1998]. *Stofan et al.* [2001] considered the overlapping, nested summit calderas of Sif Mons to imply periods of high-level storage within the edifice, and cited the Hawai'ian volcanoes (particularly Kaua'i [*Macdonald*, 1972]) and Mount Etna [*Guest and Duncan*, 1981; *Duncan and Guest*, 1982] as terrestrial examples of where varying levels of magma storage have resulted in the development of nested and discrete collapse features. The existence of discrete collapse zones at many Venusian volcanoes has been regarded as evidence against the neutral buoyancy theory hypothesis that the magma source will increase in depth with volcano growth, particularly given the general absence of a relationship between summit structure and elevation above MPR (e.g. *Stofan et al.* [2001] and *Mouginis-Mark* [1994]). Changes in plumbing at Etna have been interpreted to result from changes in local and/or regional stress patterns [*Guest and Duncan*, 1981; *Duncan and Guest*, 1982], and *Stofan et al.* [2001] regarded the stress field as being influential in controlling magma chamber location with time at Venusian volcanoes. Figure 3.6 displays three examples of the occurrence of multiple

collapse zones on Earth and Venus, highlighting the fact that similar summit configurations can result from shifts in plumbing at a wide variety of different scales, and for very different atmospheric conditions.

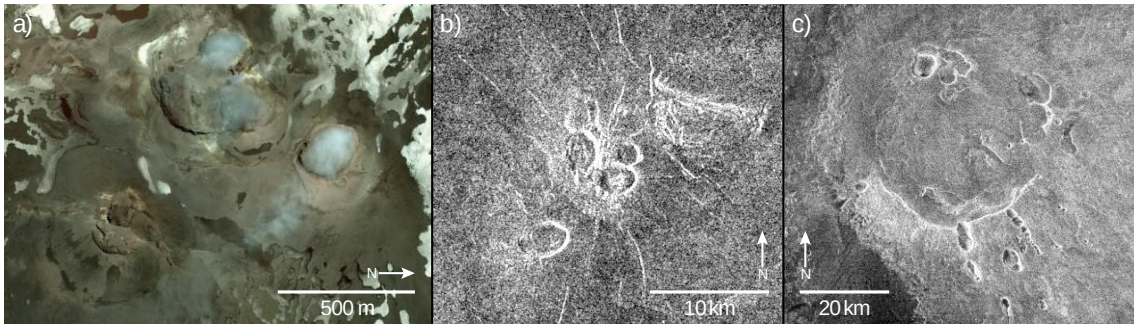

Figure 3.6. Comparison of the summit regions of (a) Etna volcano, located in Sicily, Italy, (b) an intermediate C-type volcano on Venus located at 11.7°N, 272.35°E, and (c) Sif Mons, a large volcano on Venus located at 21.7°N, 351.75°E. Venusian images are left-looking Magellan images. Visible terrestrial image obtained from GoogleEarth, illumination is from the bottom of the image.

The occurrence of multiple collapse zones has been found to be at least as frequent, if not more so, among intermediate volcanoes relative to large volcanoes. 27% of intermediate cones have been found to display either single summit vents featuring multiple stages of collapse or multiple, discrete vents clustered within the summit region. By comparison, the study of *Brian* [2001] determined that 11% of catalogued large volcanoes displayed main summit calderas that showed 'several collapses, nested pits or calderas'. The mean diameter of edifices displaying multiple collapse zones is 199 km compared with 230 km for edifices that do not; the corresponding mean heights are 1484 and 1253 m respectively. The diameter-frequency distribution curve for intermediate and large volcanoes in Fig. 3.7a is erratic across all diameter ranges, although it can be established that a lower proportion of large volcanoes display multiple collapse zones within each diameter range compared with intermediate volcanoes, at least among diameter ranges with appreciable populations (i.e. 100 to 600 km). The corresponding height-frequency distribution curve in Fig. 3.7b shows that the proportions of volcanoes that display multiple collapse zones within each height range remains fairly constant at around 17% among height ranges with appreciable populations (i.e. 0 to 4 km).

If the occurrence of multiple collapse zones at the summit of an edifice is interpreted to represent the emptying of a plexus of discrete, shallow magma reservoirs through eruption [*Rogers and Zuber*, 1998; *Stofan et al.*, 2001], then the fact that multiple collapse zones characterize intermediate volcanoes more than they do large volcanoes

would imply that periods of high-level storage occur more commonly for intermediate volcanoes. The multiple collapse zones accumulated during earlier evolutionary stages may have been eliminated by flow superposition, tectonic distortion, and late edifice construction. However, the relatively unvarying occurrence of multiple collapse zones with increasing edifice height as illustrated in Fig. 3.7b contrasts with the decreasing occurrence of multiple collapse zones with increasing edifice diameter. These distributions indicate that the less frequent occurrence of shallow reservoirs and associated summit eruptions among large volcanoes relative to intermediate volcanoes is not necessarily a result of the generally taller heights attained by large volcanoes.

The graph in Figure 3.7d shows the altitudinal distribution of the summits of intermediate and large edifices that feature summit multiple collapse zones and those that do not. Similar to the altitudinal distribution of primary summit collapse calderas, 16% of summits below 2.5 km above MPR show multiple collapse zones compared with 19% of summits above 2.5 km above MPR, whereas 86% of summits with multiple collapse zones and 88% of summits without were found to exist at elevations below 2.5 km above MPR. The mean summit elevation of edifices displaying multiple collapse zones is 436 m above MPR, very similar to the 419 m above MPR mean summit elevation for edifices that do not. The frequency distribution curve in Fig. 3.7c indicates the percentage of the total volcano population within each elevation division that displays multiple collapse zones. For elevation divisions with appreciable volcano populations (i.e. -1 to 3 km above MPR), the distribution curve is fairly erratic when compared with the relatively flat distribution seen for the occurrence of primary summit collapse calderas seen in Fig. 3.4c. These statistics echo the earlier finding that the proportions of edifices with and without primary summit collapse calderas do not differ significantly with summit elevation, and that shallow magma reservoirs are not confined to edifices with summits greater than 2.5 km above MPR.

Figure 3.7 (below and following page). Frequency distribution graphs of volcanoes displaying multiple collapse zones. (a-c) Distribution curve of the proportions of the total number of volcanoes within each edifice diameter range (a), each edifice height range (b), and each summit elevation range (c), that display multiple collapse zones. (d) The altitudinal distribution of the summits of volcanoes displaying multiple collapse zones (in black) and those displaying no multiple collapse zones (in grey). The vertical dashed line marks the elevation of 2.5 km above MPR.

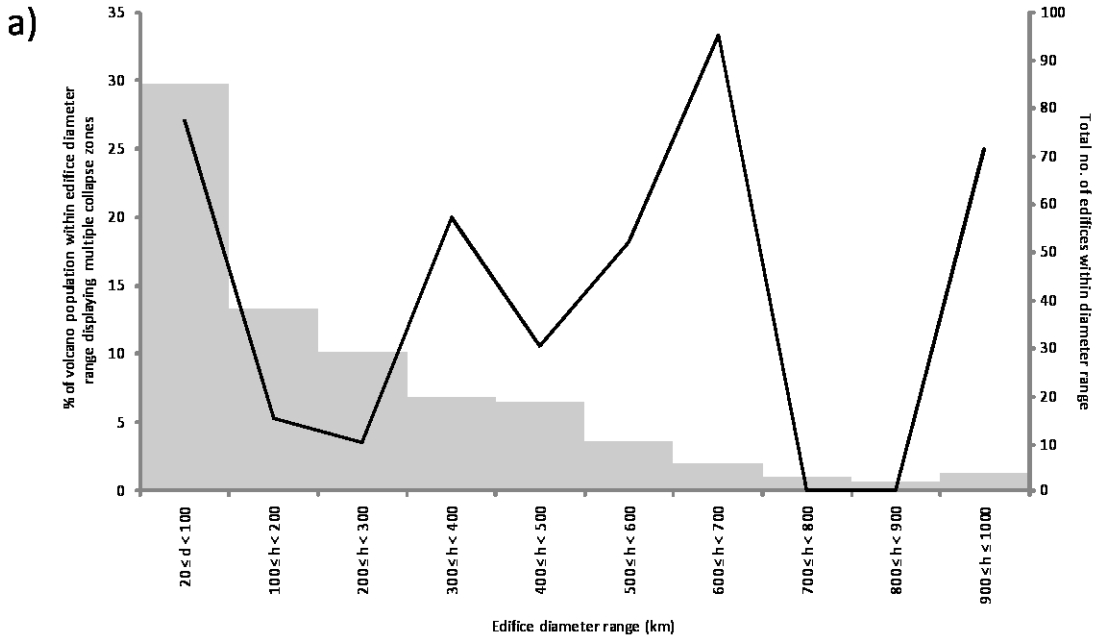

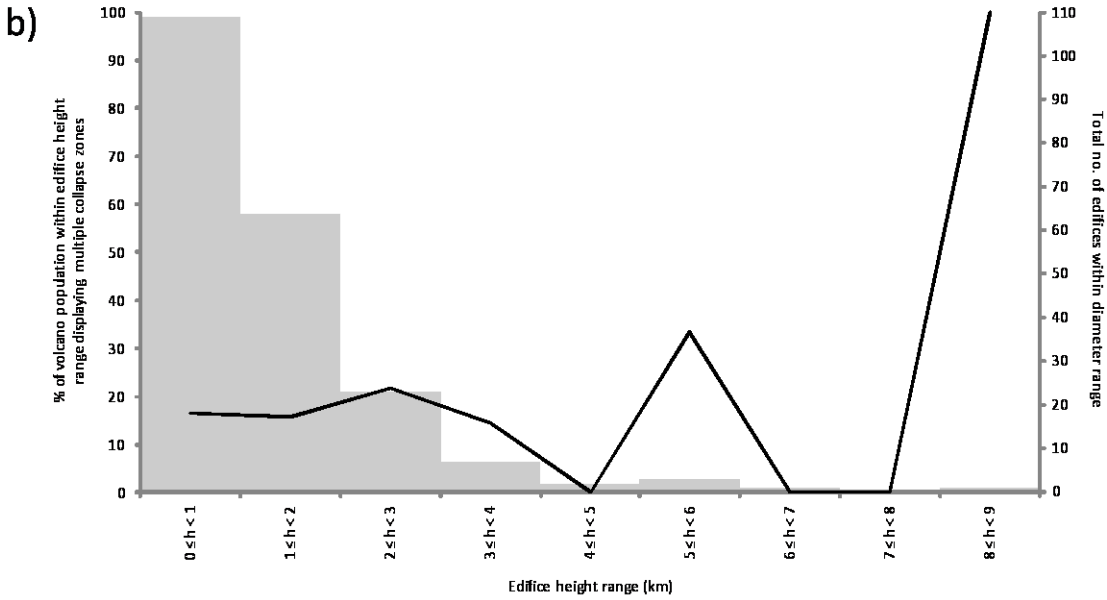

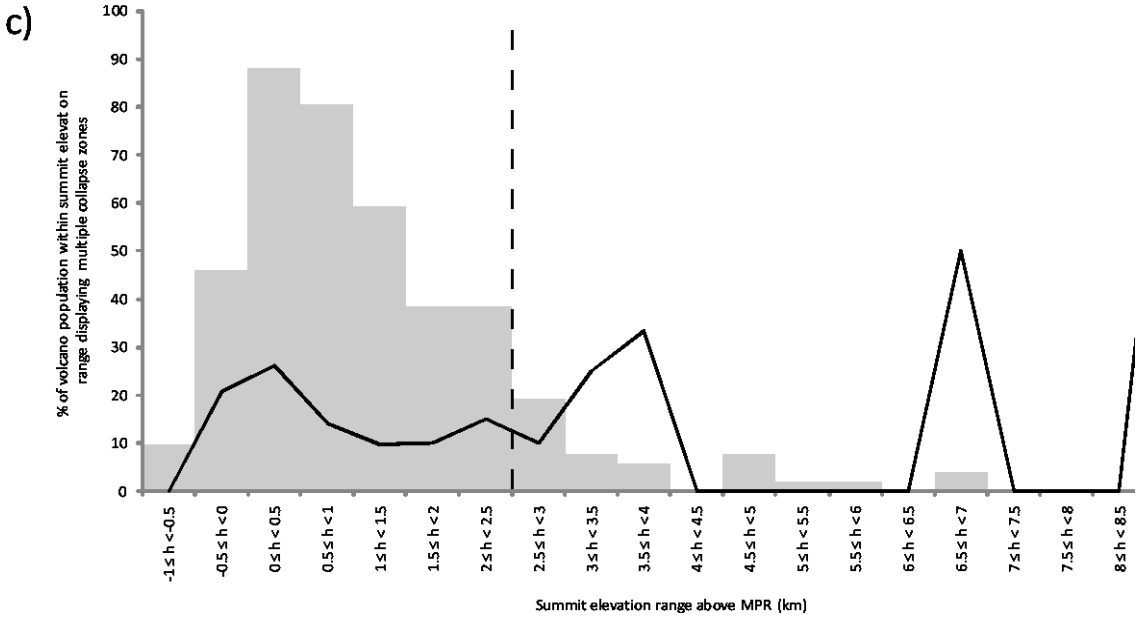

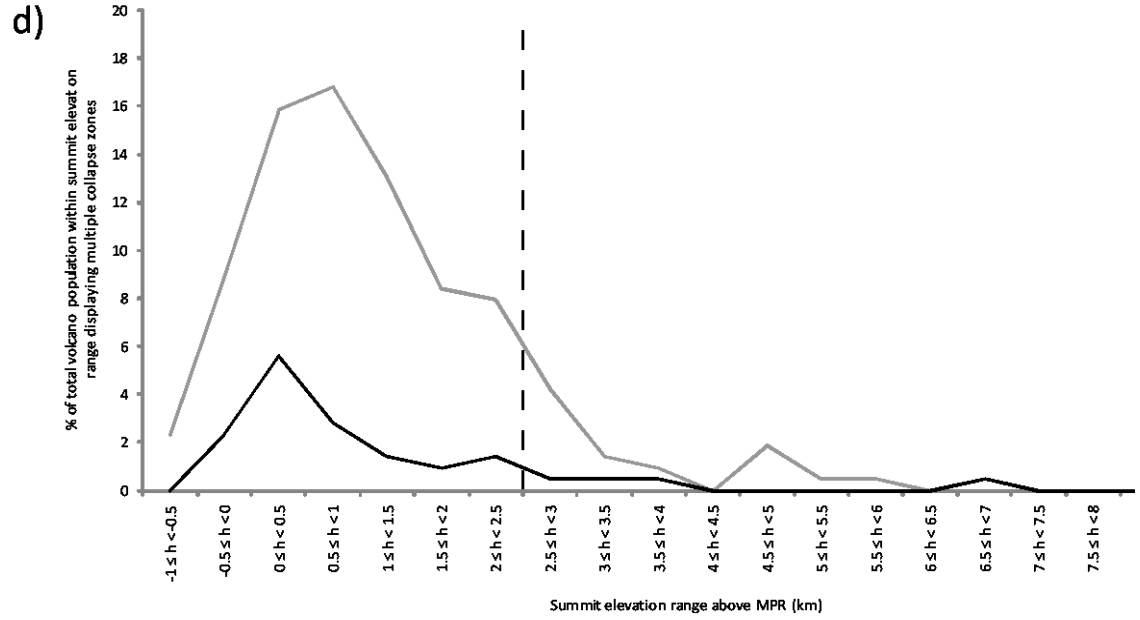

Summit domes: Intermediate cones and large volcanoes are the only Venusian volcano types that are seen to display steep-sided domes at their summits. The topic of steep-sided dome morphology will be addressed in detail in section 3.4; this section focuses on the implications of steep-sided dome occurrence for the evolution of the parent volcanoes. *Stofan et al.* [2001] noted that the domes located at the summit of Gula Mons display rough surfaces and extensive fracturing, unlike most other steep-sided domes on Venus, and hypothesized that these summit domes may display more evolved compositions, or may reflect differing late-stage eruption conditions at the

summit; as will be described in section 3.4.4, the summit domes of Venusian volcanoes may be regarded as analogues to silicic domes within the calderas of terrestrial stratovolcanoes. *Stofan et al.* [2001] considered the small percentage of possible products of evolved composition on the summits of many large Venusian volcanoes, such as the Gula domes, to indicate that magmas do not have long residence times in a reservoir, or that reservoirs are thoroughly emptied in Venusian eruptions. The small proportion of magma that does develop an evolved chemistry can only do so after having resided and differentiated within the reservoir for a given amount of time. The relative frequencies of summit domes on intermediate and large volcanoes can help in providing an indication of the timescale that the dome-forming magmas reside within the reservoir for.

Summit dome occurrence evidently differs little with changing parent edifice size. 39% of intermediate cones display such domes, whereas 36% of the large volcanoes catalogued by *Brian* [2001] do. Figure 3.8 shows the frequency of summit/flank dome occurrence with edifice diameter; it can be seen that the proportions of volcanoes that display summit domes do not differ considerably from 38% within diameter ranges showing appreciable volcano populations (20 to 600 km). In addition, 73% of domes located at the summit or on the flanks of volcanoes have been found to display collapsed flanks; this may be a result of the uneven surfaces onto which the domes are erupted, or it may result from modification by continued eruptive activity at these volcanoes. Some domes, generally located on the upper flanks rather than the summit, appear to have been embayed by later flows erupted from their parent volcanoes (Fig. 3.9).

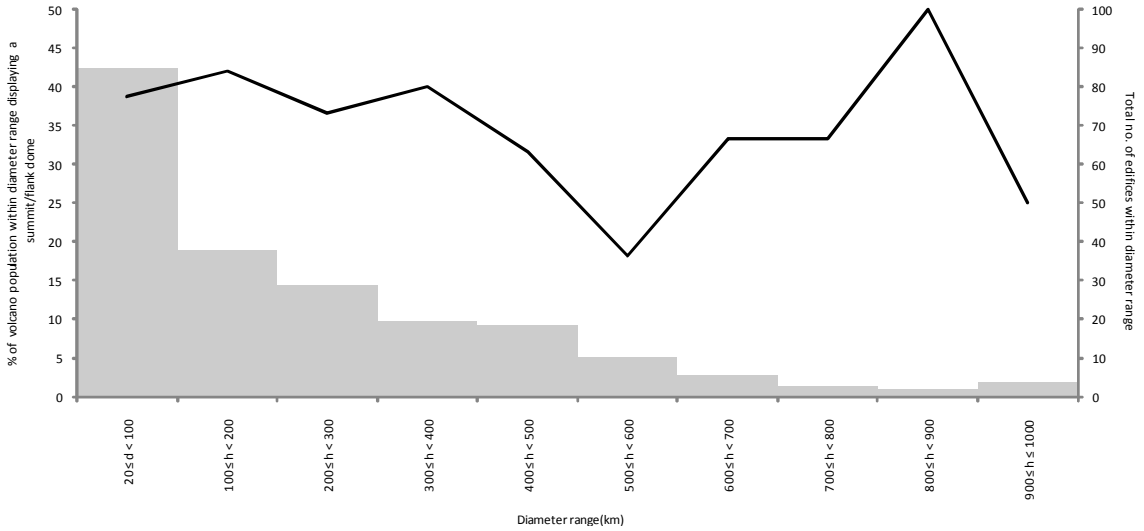

Figure 3.8. Diameter-frequency distribution curve showing the proportions of the total number of volcanoes within each edifice diameter range that display summit domes. Grey bars indicate the total volcano population within each diameter division.

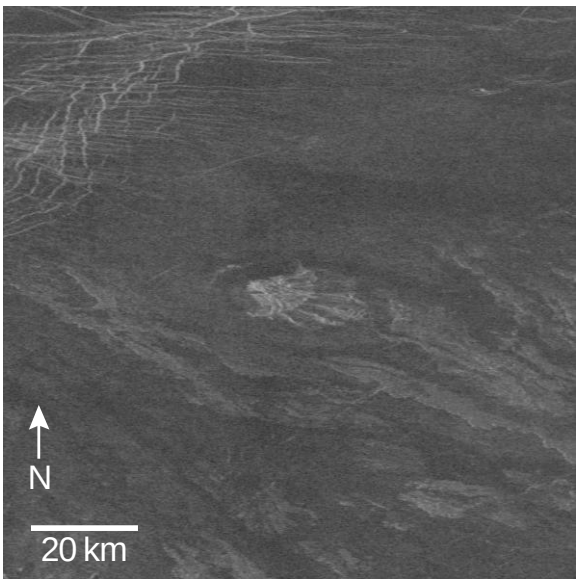

Figure 3.9. Left-looking Magellan image centred at 62.2°N, 120.8°E, showing a modified steep-sided dome on the south-east flank of the large volcano Melia Mons. Low/intermediate reflectivity, digitate flows emanating from the summit of the volcano to the north-west have embayed the dome and superposed its north-west half.

The superposition of domes by later volcanic deposits, in addition to the presence of summit domes on volcanoes of widely varying diameters, indicates that a summit dome does not necessarily represent the final lavas erupted at the end of a volcano's active life, but may instead represent the final lavas erupted at the culmination of one of numerous eruptive phases that occur throughout the active life of the volcano. This interpretation indicates that magma need not reside within a reservoir for the duration of a volcano's lifetime in order to develop an evolved chemistry that is sufficient to

produce dome morphologies; if this was the case, it would be expected that the occurrence of summit domes would be confined to large volcanoes. Instead, the timescale of a single magma storage and eruption phase is sufficient for magma to develop such an evolved chemistry. The majority of the magma is erupted before it can develop such a chemistry, however, leaving only a minimal amount that remains within the reservoir for the entire duration of the cycle, and which is erupted to form the summit dome at the cycle's culmination. This conclusion would appear to support the assertion of *Stofan et al.* [2001] that the minimal volume of evolved lavas visible at the summits of volcanoes implies short residence times for the majority of the magma within the reservoirs; however, a quantitative value for the residence time cannot be established as it is not known how many eruption cycles characterize the growth of a volcano, the number of which would presumably determine the length of each cycle.

3.2.4 Relation of edifice aspect ratio and flow morphology to intrusive processes

Aspect ratio: A hypothesis of neutral buoyancy theory is that lateral growth should be enhanced over vertical growth for Venusian volcanic edifices, which has been interpreted to occur due to the lateral growth of vertically-stabilized magma reservoirs and the lateral propagation of dikes, with the consequential dispersed distribution of flank vents [*Head and Wilson*, 1992; *Mouginis-Mark and Rowland*, 2001]. Comparing the results of the present survey and that of *Brian* [2001], the mean height of intermediate cones is 833 m (σ of 438 m), compared with 1581 m (σ of 1327 m) for large volcanoes, whereas the mean aspect ratio of intermediate cones is 97 (σ of 58), compared with 315 (σ of 250) for large volcanoes. The mean height of intermediate cones is therefore about half that of large volcanoes, yet the mean aspect ratio is just under a third that of large volcanoes, meaning that these volcanoes increase in diameter relative to height as they grow.

Based on the findings of previous studies that have focused on the large volcanoes Sif, Gula, Kunapipi [*Stofan et al.*, 2001] and Sapas Mons [*Keddie and Head*, 1994a], a correlation has been identified whereby edifices with large aspect ratios tend to display a larger contribution to their volume from flows erupted from flank vents. Flank vents may take the form of both small edifices and pit vents, which have both been observed at the Hawai'ian shield volcanoes, and which have been interpreted to represent the presence of magma conduits [*Jaggar*, 1947; *Macdonald*, 1972; *Klein et al.*, 1987;

Walker, 1988]. Flank vent occurrence has been found to be identical (64%) for large volcanoes and intermediate volcanoes, although flank vents at large volcanoes are distributed to greater distances from the summit region relative to those of intermediate volcanoes. The occurrence of flows emanating from flank vents has also been found to be similar for intermediate and large volcanoes: 34% of large volcanoes that feature flank vents display identifiable flows emanating from the vents, compared with 39% of intermediate volcanoes that display flank vents.

The similar occurrence of flank vents and flows erupted from them among intermediate and large volcanoes indicates that flank eruptive activity does occur during all stages of volcano growth. The larger aspect ratios of large volcanoes relative to intermediate volcanoes will in part result from the flows erupted from large volcanoes being longer and more voluminous relative to those of intermediate volcanoes. The three volcanoes studied by *Stofan et al.* [2001] each displayed flows that reached up to ~600 km from the summit; the flank flows of intermediate volcanoes rarely reach more than a few tens of kilometres. *Stofan et al.* [2001] note that the volume of an eruption will be governed by the amount of melt available within the reservoir, the effusion rate, and the eruption duration. The more voluminous flows emanating from the flanks of larger volcanoes are regarded to result from the larger magma reservoirs that have been interpreted to form beneath large volcanoes as interpreted from the larger calderas displayed by large volcanoes relative to intermediate volcanoes (see section 3.2.3). Through comparison of the occurrence of summit calderas and multiple collapse zones between intermediate and large volcanoes, it has been determined that summit eruptive activity does persist with edifice growth, yet the increasing contribution to the volume of the edifice from flank vents with increasing edifice growth is consistent with the hypothesis that widely distributed magma pathways to the surface should develop due to the vertical stabilization and lateral growth of magma reservoirs, which is consistent with neutral buoyancy theory [*Head and Wilson*, 1992; *Mouginis-Mark and Rowland*, 2001].

The increase in aspect ratio with edifice growth may also reflect the progressive sagging of the relatively thin Venusian lithosphere under the volcano's increasing weight [*McGovern and Solomon*, 1997; 1998]. Flexural moats formed by the vertical load of the edifice on the lithosphere are observed around only 5% of intermediate cones; their rareness may result from a combination of their loads being insufficient to

cause flexure that is detectable by the Magellan altimeter, and of the moats becoming infilled by apron flows from the volcanoes, a process that has been interpreted to contribute to the paucity of flexural moats and flexurally induced extensional faulting around large volcanoes on Venus [*McGovern and Solomon*, 1997].

Flow morphologies: The morphological configuration of gently-sloping outer flanks leading to a steeper summit region is much more commonly seen among large volcanoes compared with intermediate volcanoes. This contrast in bulk morphology should be reflected by differences in the occurrence of particular flow morphologies between intermediate and large volcanoes; different flow morphologies are regarded to reflect variations in effusion rate, eruption duration and vent geometry rather than magma composition [*Hughes et al.*, 1990; *Stofan et al.*, 2001]. In their examination of Sif, Gula and Kunapipi Montes, *Stofan et al.* [2001] noted that Gula Mons displays the most digitate flows and the steepest flanks, Kunapipi Mons displays the most sheet flows and the lowest flank slopes, and Sif Mons displays a mixture of flow types, with intermediate slopes. A similar diversity of flow morphologies is seen at terrestrial volcanoes such as Mount Etna in Sicily, where long, narrow flows present on the western and northern flanks have been interpreted to be associated with high effusion rates and shorter duration eruptions [*Guest et al.*, 1987; *Hughes et al.*, 1990], whereas broader flows on the eastern flanks are associated with long duration, low effusion rate eruptions [*Wadge*, 1977; *Hughes et al.*, 1990]. Based on this terrestrial comparison, *Stofan et al.* [2001] interpreted the digitate flows that dominate the flanks of Gula Mons to indicate high effusion rate, short duration, and low volume eruptions mainly originating from the summit rather than flank vents. Sif Mons displays more flank eruptions with varying flow morphologies, interpreted by *Stofan et al.* [2001] to represent a range of eruption durations, effusion rates, and vent geometries, whereas the low flank slopes and dominant sheet flow morphologies of Kunapipi Mons were interpreted to represent higher volume, longer duration eruptions. However, *Stofan et al.* [2001] cautioned that these were generalized interpretations and that the Venusian flows were likely to have been emplaced under a wider range of effusion rates and eruption durations than their typical terrestrial counterparts, based on the widely differing flow lengths (some reaching over 350 km at Gula Mons) and the fact that some are channel-fed whereas others are tube-fed.

Previous studies of large Venusian volcanoes have suggested that most volcanoes exhibit a progressive change in flow morphology from sheet-like to digitate, with sheet-like morphologies characterizing older outer apron flows and digitate morphologies characterizing younger main edifice flows [*Senske et al.*, 1992; *Keddie and Head*, 1994a; 1995]. Mount Etna [*Guest*, 1982] and volcanoes of the western Galapagos Islands [*Simkin*, 1972; *Chadwick and Howard*, 1991; *Naumann and Geist*, 2000] display similar profiles, with numerous short flows from the summit forming a steep upper edifice and occasional long flows forming the shallowly sloping outer flanks. *Stofan et al.* [2001] argued that the morphologies of volcanoes on both planets have evolved similarly, with the long outer apron flows erupting at infrequent intervals throughout the whole history of the volcano, and the more frequent, shorter summit flows constructing the main edifice. *Stofan et al.* [2001] interpreted the short edifice-building flows at the summit to result from lower magmastatic pressure causing lower effusion rates for summit eruptions.

The present survey of intermediate cones allows further investigation of how the configuration of eruption centres and the occurrence of different flow types reflect changes in the intrusive systems and eruption styles of these volcanoes as they grow. Sheet flows have been found to be the most common flow morphology displayed by intermediate volcanoes, with 98% of such volcanoes displaying this morphology relative to 19% displaying fan flows and 14% displaying digitate flows. No specific statistics of the occurrence of different flow types across all large volcanoes across Venus are available, yet the proportions of different flow morphologies among the three large volcanoes examined by *Stofan et al.* [2001] indicate that digitate flows characterize large volcanoes to a much greater degree, and sheet flows to a much lesser degree, compared with intermediate volcanoes. The mean proportions by area of the different morphologies across Sif, Gula and Kunapipi Mons are 42.67% for digitate flows, 7.67% for fan flows, and 49.67% for sheet flows. Specific values for the mean proportions by area of the different morphologies for intermediate volcanoes are not available, yet sheet morphologies are regarded to dominate by area on a qualitative basis, as the homogeneous low backscatter that characterizes many intermediate volcanoes from their summits to their bases implies extensive cover by sheet flows. The strong predominance of sheet flow morphologies among intermediate volcanoes is consistent with the assertion that such flows are characteristic of the early evolutionary

stages of these volcanoes, and the general absence of digitate flows is consistent with the frequent lack of steep upper edifices among volcanoes in this size range relative to large volcanoes.

The digitate and fan flows of intermediate volcanoes are generally poorly defined relative to those of large volcanoes, and tend to exhibit ambiguous, diffuse margins. Based on their observations of Sif, Gula and Kunapipi Montes, *Stofan et al.* [2001] noted that the sources of digitate flows were generally concentrated at the summits of the large volcanoes, whereas the sources of sheet flows tended to be concentrated on the lower flanks. In contrast, the sheet flows of intermediate volcanoes nearly always originate from the summit region and extend to beyond the topographic base of the edifice. The ambiguous margins of the digitate flows can sometimes obscure identification of their source locations, yet they have been observed to emanate both from the flanks and summit (5 edifices display summit digitate flows, 9 display flank digitate flows).

Based on the correlations between flow morphology and eruption style described by *Hughes et al.* [1990] and *Stofan et al.* [2001], the transition in flow morphology observed between intermediate and large volcanoes is interpreted to reflect changes in the volume and rate of magma supply. These changes are themselves interpreted to stem from changes in magma reservoir depth and associated driving pressure with increasing edifice height. The magma reservoir of an intermediate volcano will exist at a relatively shallow depth given the low height of the edifice above it. Considering that the magma rises only a relatively short vertical distance from the reservoir in order to erupt at the surface, the driving pressure at eruption would be expected to be relatively high. Consequently, large quantities of magma would be expected to erupt over long durations, and when considered with the fact that the slopes onto which the flows are emplaced will be relatively gently sloping, the voluminous flows would spread out and form the almost ubiquitous sheet flows that characterize intermediate volcanoes. The occasional occurrence of digitate and fan flows indicates less frequent, low volume, shorter duration eruptions. Given that the magma is ascending from a narrow magma reservoir, and that eruptive activity will therefore occur across a relatively small area at the surface, the eruption sites of the digitate and fan flows will coexist with those of the sheet flows; intermediate volcanoes have not yet developed a dichotomy in the eruption

sites of digitate and sheet flows, and as such display the configuration of steep upper flanks surrounded by gently-sloping outer flanks less often than large volcanoes.

As eruptions continue and intermediate edifices grow, neutral buoyancy zone theory predicts that the magma reservoir should stabilize vertically and spread laterally as new melt ascends from the mantle [*Head and Wilson*, 1992], resulting in eruption sites becoming more widely distributed across the surface as new conduits branch off from the expanding reservoir. The frequent occurrence of digitate flows at the summit regions of large volcanoes is interpreted to be consistent with the hypothesis of a stable magma reservoir. As the height of the summit increases, the increasing depth of the magma reservoir will mean that once magma has risen as far as the summit, its driving pressure will have fallen considerably. Consequentially, the magma supply to the summit should decrease, and flows erupted at the summit would be expected to have low volumes and short durations, as hypothesized by *Stofan et al.* [2001]. The relatively steep slopes expected at the summit should prevent the flows erupted there from spreading out as much as they would if they were erupted lower down the flanks, which may contribute to their often digitate morphologies. Given that the lateral extent of the magma reservoir is expected to be wide under large volcanoes, the distal portions of the reservoir will exist at a shallower depth beneath the surface compared with the central portion. Magma erupting at the surface at the outer flanks will therefore display a higher driving pressure than magma erupting at the summit, meaning that flank eruptions at large volcanoes should be characterized by larger volumes and longer durations than at the summit. The type of voluminous, long duration eruptive activity that had occurred almost ubiquitously among intermediate volcanoes is therefore confined to the lower, outer flanks of large volcanoes, whereas the lower eruption volumes and durations that characterize the summit region give rise to the steep main edifices that are so common among large volcanoes. The aforementioned correlation of bulk edifice morphology to intrusive processes for intermediate and large volcanoes is displayed schematically in Fig. 3.10. Deducing actual eruption rates from the different morphologies of the flows is not straightforward; digitate flows at Mount Etna have been interpreted to result from high effusion rates whereas broader flows have been associated with low effusion rates [*Wadge*, 1977; *Guest et al.*, 1987; *Hughes et al.*, 1990], yet *Stofan et al.* [2001] interpreted the short digitate flows that form the main edifice to result from low eruption rates. Given that high driving pressures would be

expected for magma erupting at intermediate volcanoes and the lower flanks of large volcanoes, it would be expected that eruptions at such locations would generally display higher effusion rates relative to eruptions at the summits of large volcanoes.

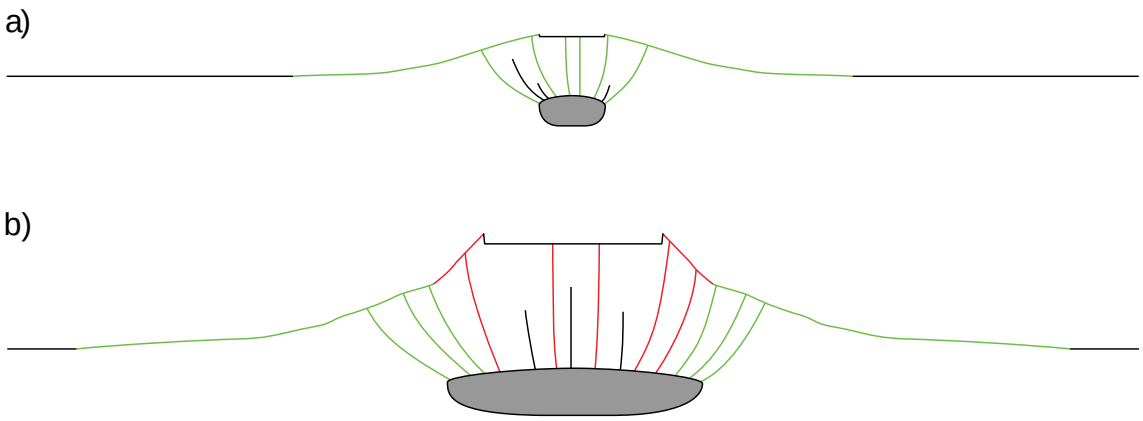

Figure 3.10. Schematic displaying the interpreted relationship of bulk morphology and distribution of flow morphologies to intrusive system configuration for intermediate (a) and large (b) volcanoes. Green portions of the flanks are the gently-sloping flanks formed from sheet flows erupted from conduits (in green) linking the shallow portions of the magma reservoir (in grey) to the surface; red portions of the flanks are the steeper upper flanks formed from digitate flows erupted from conduits (in red) linking the deeper portions of the magma reservoir to the surface.

Stofan et al. [2001] suggested that periods of intrusion at the summit, which lead to radial diking, may also reflect a decrease in the supply rate of magma from the reservoir. Only 18% of intermediate volcanoes catalogued in the present survey display summit/flank radial fracturing compared with 39% of large volcanoes catalogued in the survey of *Brian* [2001]. The increasing occurrence of radial fracturing (interpreted to represent subsurface diking [*Head and Wilson*, 1992; *Stofan et al.*, 2001]) with increasing edifice size would therefore lend support to the assertion that magma supply to the edifice, notably its summit region, should decrease with edifice growth, and also that intrusion should predominate over extrusion in the later stages of volcano growth. It should also contain implications for the changing stress state of volcanoes as they grow. Production of radial dikes is allowed when the least compressive principal stress is horizontal [*Grosfils and Head*, 1994; *Stofan et al.*, 2001; *Grindrod et al.*, 2005]. If Venusian volcanoes are welded to the lithosphere, then they will be characterized by high horizontal compressive stress, yet the presence of a pressurized magma reservoir within an edifice may be sufficient to create a stress regime allowing magma ascent and radial dike propagation [*McGovern and Solomon*, 1998]. The increasing pressure

exerted on the magma reservoir by the weight of the growing edifice may pressurize the reservoir to the extent that such dike propagation is permitted.

3.2.5 Implications for environmental effects on evolution of edifice morphology

This study has succeeded in identifying a category of intermediate volcano on Venus that has been interpreted to represent precursors to large volcanoes, based on size distribution and similarities in quantitative and qualitative morphological characteristics. Statistics relating to different morphological aspects of the intermediate and large volcanoes have been compared in order to determine how the morphologies of these edifices change with edifice size and summit elevation, as well as to interpret the changing morphologies in terms of the evolution of the magma reservoir and plumbing system. The main observations and their implications for neutral buoyancy theory are summarized below:

- The similar occurrence of summit collapse calderas for intermediate (45%) and large volcanoes (42%) is interpreted to mean that shallow magma reservoirs exist with similar frequency across all size ranges, which is not predicted by the neutral buoyancy theory hypothesis of *Head and Wilson* [1992]. Multiple collapse zones, interpreted to represent localized zones of collapse within large shallow magma reservoirs or small-scale, shallow reservoirs that have stemmed from a larger, deeper reservoir, are more common among intermediate volcanoes (27%) than large volcanoes (11%). 48.5% of the volcano population displays no identifiable summit caldera or multiple collapse zones, indicating that shallow magma storage is not manifested at the summits of these volcanoes at present, either because such shallow storage never existed, or because a past caldera may have been eliminated.

- A higher proportion of volcano summits above 2.5 km above MPR display primary collapse calderas and multiple collapse zones compared with summits below 2.5 km above MPR, but the majority of summit calderas and multiple collapse zones exist at elevations below 2.5 km above MPR, with no apparent positive or negative trend in summit caldera/multiple collapse zone frequency with increasing summit elevation above MPR. These observations contradict the neutral buoyancy theory hypothesis of *Head and Wilson* [1992] that magma reservoirs should not enter an edifice (i.e. become ‘shallow’) for summit elevations below 2.5 km above MPR.

- The diameters of summit collapse calderas tend to increase with increasing edifice size and summit elevation above MPR. These trends are consistent with the neutral buoyancy hypothesis of *Head and Wilson* [1992], yet there is considerable scatter within the data that is interpreted to represent the influence of other environmental factors on the relationship between caldera size and edifice size/summit elevation.
- Large volcanoes display a mean aspect ratio that is more than three times greater than that of intermediate volcanoes. Similar proportions of intermediate and large volcanoes display flank eruption sites, and of these, a similar proportion display flows emanating from those sites. The change in aspect ratio with increasing edifice size is therefore interpreted to result from the increasingly wide spatial distribution of flank vents and the increasing flow volumes erupted from them; the large volumes are consistent with the large summit calderas (and by implication, large magma reservoirs) observed among large volcanoes. The similar occurrence of summit collapse calderas among intermediate and large calderas is interpreted to mean that the difference in aspect ratio is not necessarily a result of increasing reservoir depth with edifice size.
- The morphological configuration of gently-sloping outer flanks leading to steeper upper flanks is seen more commonly among large volcanoes compared with intermediate volcanoes. This is interpreted to be related to the different proportions of flow morphologies observed at intermediate and large volcanoes, with the different flow morphologies reflecting variations in effusion rate, eruption duration, flow volume, and slope of emplacement surface. The prevalence of sheet flows at intermediate volcanoes and the lower flanks of large volcanoes is interpreted to imply long-duration, high-volume eruptions onto gently-sloping surfaces, whereas the prevalence of digitate flows at the upper flanks of large volcanoes is interpreted to imply short-duration, low-volume eruptions onto steeper surfaces. Higher effusion rates are generally thought to characterize eruptions at intermediate volcanoes and the lower flanks of large volcanoes than at the summits of large volcanoes. These different eruption styles are themselves interpreted to derive from the vertical stabilization and increasing depths of magma reservoirs as volcanoes grow in height, an interpretation that is consistent with the neutral buoyancy hypothesis of *Head and Wilson* [1992].

The conclusions regarding the behaviour of the intrusive systems that are drawn from these separate interpretations are therefore not always consistent; specifically, a

static magma reservoir beneath a growing edifice is inferred in some cases, but not in others. Larger magma reservoirs are consistently inferred beneath large volcanoes relative to intermediate volcanoes, based on the increase in caldera size and increasing contribution of flank flows to the edifice volume. Yet the disparity in flow morphologies between intermediate and large volcanoes is interpreted to indicate a deepening magma reservoir with volcano growth, whereas the similar occurrence of calderas and collapse zones at the summit regions of intermediate and large volcanoes is interpreted to indicate that shallow magma storage is a fairly consistent phenomenon with increasing volcano size. This paradox suggests that different morphological parameters may be sensitive to different aspects of the plumbing system. The primary magma reservoirs of the volcanoes may grow laterally and deepen as the volcanoes increase in height, resulting in the expanding caldera size, but with smaller pockets of melt rising to shallower levels within the edifice and stalling to create discrete collapse zones.

This inconsistency may therefore imply that movement of magma that is not predicted by neutral buoyancy theory is a common occurrence, and that other environmental factors are influencing the movement and storage of magma within these edifices. *Hughes et al.* [1990] and *Stofan et al.* [2001] hypothesized that the stress field, in addition to neutral buoyancy, will influence magma chamber location with time as well as the effusion rate, vent geometry and duration of eruptions. It has been observed that cone-type intermediate volcanoes occur relatively commonly within fractured plains (comprising 50.6% of the total), and it is likely that some fraction of those located within smooth plains and wrinkle-ridge plains (comprising 38.8% of the total) may originally have formed within fractured plains that are now covered by flood lavas. In addition to this, 13% of intermediate cones are seen to directly influence the regional fracturing around them, whereby the fracturing either curves concentrically around or radially towards the edifices; this phenomenon has previously been described for large Venusian volcanoes by *López et al.* [2008], who hypothesized that concentric and radial deflection represent compressional and tensional stress fields, respectively. The relatively frequent occurrence of cone-type volcanoes within fractured terrains may therefore represent a potential measure of the extent to which crustal stress conditions have influenced the intrusive processes of these volcanoes.

The survey of intermediate volcanoes has also provided new insight into the individual eruption cycles that characterize the active lives of these volcanoes. Specifically, this has been accomplished through quantification of summit dome occurrence at intermediate and large volcanoes. The occurrence of summit domes is very consistent across all volcano sizes and some domes are embayed by later flows emitted by their parent volcano; these observations are interpreted to mean that summit domes do not necessarily represent the final lavas erupted at the end of the active lives of these volcanoes, but are instead the final lavas erupted during one of numerous eruptive phases. The lava forming the domes represents the small volume of magma that has resided within the reservoir for the entire duration of a single storage and eruption cycle, and which has therefore developed a chemistry that is more evolved than the magmas erupted earlier in the cycle. Magma residence times within the reservoir may therefore be short, as proposed by *Stofan et al.* [2001], although the specific residence time is presumably determined by the number of storage and eruption cycles that occur throughout a volcano's active lifetime.

3.3 Low-relief shield morphologies on Venus and Mars

3.3.1 Introduction

Low-relief shields (category S on Venus, category Lrs on Mars) are the only intermediate volcanic features that exist in appreciable numbers on both planets: 218 on Venus, 90 on Mars. The diameters of low-relief shields are comparable on the two planets, yet significant differences have also been identified: Venusian shields display larger calderas, a wider range of caldera sizes and greater heights (and therefore greater volumes) relative to Martian shields, whereas Martian shields display fissure vents, digitate flows and lava channels more frequently than Venusian shields. However, it should be noted that significant differences exist between the resolutions of Magellan radar imagery (max. resolution of ~100 m) and the highest-resolution visible imagery of the Martian surface (max. resolution of <1 m for HiRISE), meaning that small-scale and intricate features that are easily apparent on Martian shields, such as lava channels, may be undetectable on Venusian shields. In addition, radar backscatter displayed by Venusian flows is essentially a function of their roughness on the scale of the Magellan wavelength of 12 cm; except for the highest resolution HiRISE images, visible images

of the Martian surface will not resolve the surface texture at such a scale, meaning that care must be taken when comparing the textures of shield flows on the two planets.

Low-relief shields are therefore the most appropriate intermediate volcanic features to study in order to understand how the eruption of volcanic structures with generally similar bulk morphological parameters occurs on planets with very different environmental conditions, and what factors contribute to the morphological differences observed. This section will consider the distribution of low-relief shields on both planets in order to identify what environmental conditions may be contributing to similarities and differences between the edifices on the two planets.

3.3.2 Morphological comparisons between Martian and Venusian low-relief shields

Low-relief shields on Mars (category Lrs) and Venus (category S) have similar mean diameters: 36 km on Venus, 32.3 km on Mars. In contrast, shields on Venus tend to reach greater heights than those on Mars, with a mean height of 414 m as opposed to 154 m on Mars (although it should be noted that only 40% of shields on Venus show measurable topographic signatures in Magellan altimetry data; only three of the 59 evidently very low-relief S5 shields show a measurable topographic signature). A consequence of this is that shields on Venus have a greater mean volume than those on Mars: assuming a conical shape for the shields, Venusian shields display a volume that is, on average, 3.3 times greater than Martian shields. Shields also show a smaller mean aspect ratio on Venus, where the mean ratio is 162, compared with Mars where the corresponding value is 258.

Caldera diameters and shapes differ greatly for low-relief shields on Venus and Mars. Martian shields display a mean caldera diameter of 1.7 km, whereas Venusian shields display a mean of 5.1 km. The range of caldera length/width ratios also varies greatly between Venus and Mars. The mean caldera length/width ratio for Martian shields is 6.9, whereas the corresponding value for Venusian shields is 1.6. These values reflect the fact that fissure vents and chains of small collapse pits (or single collapse pits) represent all summit vents seen on Martian shields, whereas single, generally equidimensional calderas of very variable size are seen at the summits of Venusian shields, and which often display radar-dark flows on their floors. S7 shields, with a mean caldera length/width ratio of 16, represent the few Venusian shields that display fissure vents.

Notable similarities in bulk morphology and flow texture have been identified between certain subcategories on the two planets. Specifically, Venusian S6/7 shields and Martian Lrs1/2 shields frequently display low roughness proximal to their vents, with the roughness increasing towards the edges of the shield, accompanied by the appearance of well-defined radial digitate flows and (for Martian shields) lava channels. For Venusian shields, this increase in roughness is represented by an increase in radar backscatter towards the edge of the shield. When not embayed by surrounding flows, the margins of these shield types often display digitate flow terminations. The shields on both planets display elongate vents, whether in the form of fissures, chains of collapse pits, or elongate collapse calderas: S6/7 shields display a mean caldera length/width ratio of 4.9, whereas Lrs1/2 shields display a mean caldera length/width ratio of 7.3. The shields also tend to display higher aspect ratios relative to other shield types on their respective planets. S6/7 shields display a mean aspect ratio of 189 whereas S1-5 shields display a corresponding value of 160; Lrs1/2 shields display a mean aspect ratio of 305 whereas Lrs3-6 shields display a corresponding value of 187. Other shield types on the two planets display more homogeneous reflectivity/backscatter and, in the case of Venusian shields, display larger and more equidimensional calderas. Lrs1/2 shields comprise 60% of all low-relief shields on Mars, whereas S6/7 shields comprise only 10% of all low-relief shields on Venus.

3.3.3 Distributional comparisons between Martian and Venusian low-relief shields

Low-relief shields on Mars are strongly concentrated within the equatorial Tharsis rise, and as such they have a high mean elevation: 5168 m above MPR (σ ± 2835 m). The shields in the Tharsis region exist within four discrete fields, defined by shield type and geomorphological environment as well as location. The largest field is located within Syria Planum, located at the summit of the Tharsis rise in the vicinity of Noctis Labyrinthus; this area was described by *Hodges and Moore* [1994] as an eruptive centre consisting of small shield volcanoes, fissure-related lava flows, tube-fed flows, collapse pits, and a variety of "knobs and blisters" (Fig. 3.11a). The shields here are closely-spaced, often sharing margins and forming a 'mosaic-like' pattern [*Hodges and Moore*, 1994]. 94% of the shields in Syria Planum are Lrs3-5 shields, and display below-average diameters (mean of 27 km), intermediate heights (mean of 159 m), and low

aspect ratios (mean of 188). *Webb et al.* [2001] considered the Syria Planum area to represent a several thousand kilometre-wide centre of intrusion and extrusion in the Tharsis region during the Noachian and Hesperian, and compared its volcanic style to shield fields on Venus.

A second concentration of shields is seen to the northwest, located on lava plains interstitial to the Tharsis Montes and Noctis Labyrinthus, as well as on fan-shaped deposits emanating directly from the south flank of Pavonis Mons (Fig. 3.11b). The shields are more dispersed compared with those in Syria Planum, and rarely have overlapping flows. All of the shields in this region are Lrs1/2 shields, and display below-average diameters (mean of 30 km), below-average heights (mean of 137 m), and intermediate aspect ratios (mean of 243).

The other Tharsis shield concentrations are located on the northern margins of the Tharsis rise, one at Ceraunius Fossae (Fig. 3.11c), and the other at Tanaica Montes and Tanais Fossae (Fig. 3.11d). These groups are located >1000 km apart, but resemble each other in that the shields in both groups have been emplaced on dense fracture belts. 95% of the shields in this region are Lrs1/2 shields, and display relatively large diameters (mean of 40 km), above-average heights (mean of 178 m), high aspect ratios (mean of 280), surfaces characterized by radial digitate flow and lava channel morphologies, digitate margins and low impact crater densities.

The five low-relief shields identified in Elysium Planitia (Fig. 3.11e), which have a mean elevation of 2772 m below MPR, display very similar morphologies to the Tharsis shields. All are Lrs1/2 category shields, displaying subtle digitate flow morphologies and lava channels. The margins of the shields are often difficult to distinguish in either image or altimetry data.

Figure 3.11 (following two pages). Daytime THEMIS mosaics of Martian low-relief shield fields. Red lines indicate the orientations of fissure vents belonging to low-relief shields. Dashed green lines mark the boundaries of shield fields or individual shields. Scale bar measures 100 km in each image. (a) Shield field in Syria Planum, centred at 14.9°S, 259.9°E. The shield volcanoes in the centre of the image form a mosaic-like pattern and are generally equidimensional. (b) Shield field to the southeast of the Tharsis Montes, centred at 2.3°S, 250.1°E. Shields are present in two main groups, one in the centre and top right of the image, the shields of which sometimes display fissure vents aligned with regional fracturing; the other is seen in the centre-left of the image and features shields situated on a fan-shaped deposit extending from the south flank of Pavonis Mons. (c) Shield field located at Ceraunius Fossae, centred at 23.7°N, 249.7°E. The flows of several shields superpose the fractures of Ceraunius Fossae, and in some cases the shields display fissure vents aligned with the N-trending fractures. (d) Shield field located at Tanaica Montes and Tanais Fossae, centred at 38.2°N, 270.9°E. Shield volcanoes are present in the centre and left of the image. In some cases the shields display fissure vents aligned with the ENE-trending fractures of Tanais Fossae. (e) Shields located in Elysium Planitia, centred at 8.3°N, 160.9°E. Both of the shields display fissure vents aligned with the WNW-trending fractures of Cerberus Fossae.

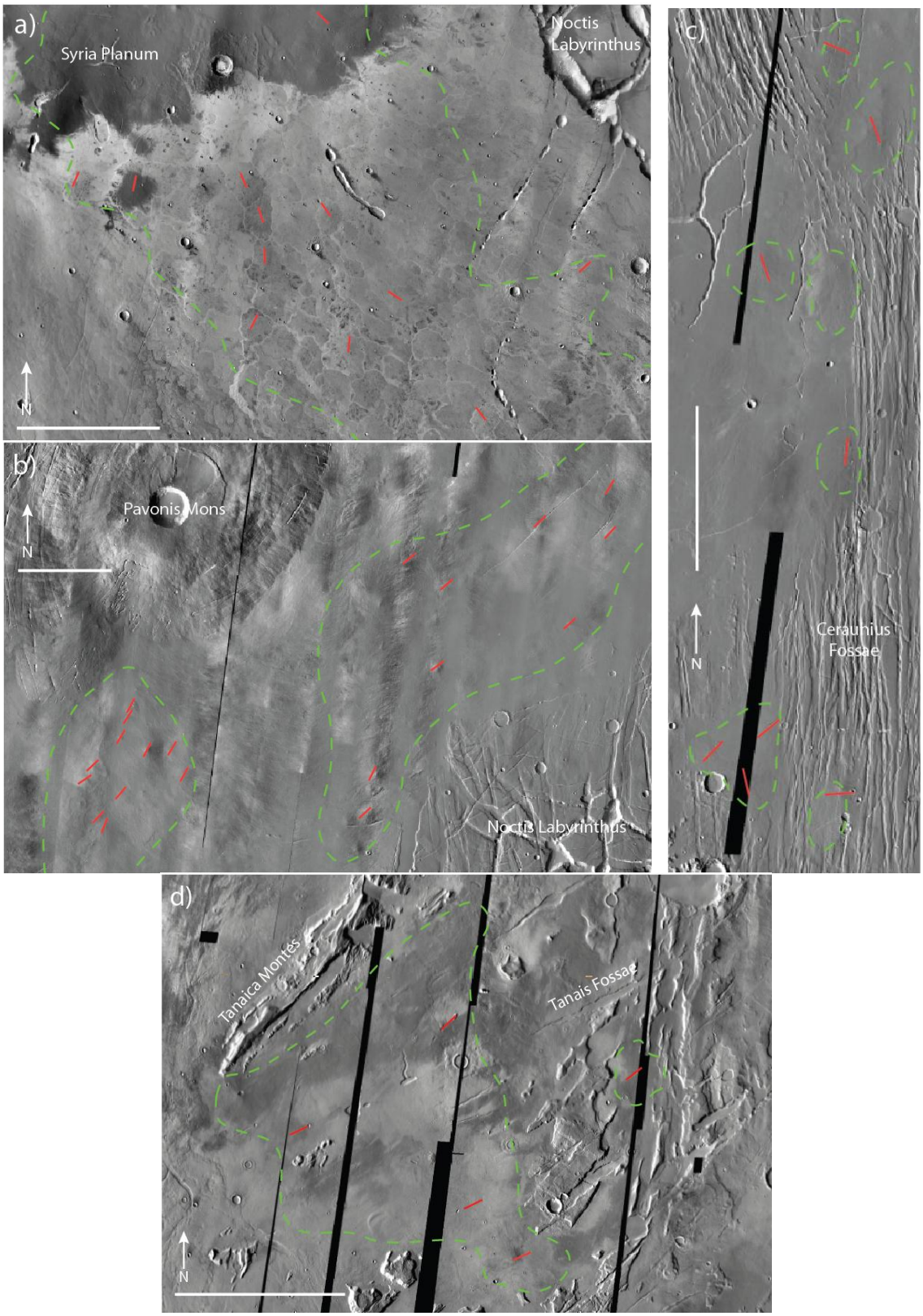
a)
Syria Planum
Noctis Labyrinthus
N
b)
Pavonis Mons
N
Noctis Labyrinthus
c)
N
Ceraunius Fossae
d)
Tanaica Montes
Tanais Fossae
N

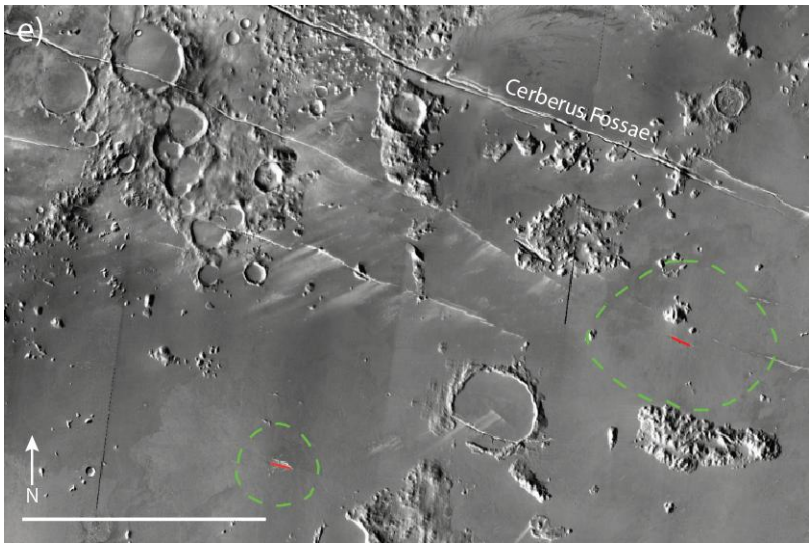

Many of the shields in these fields display fissure vents that are aligned parallel to regional fracturing in the area, and which in some cases are linked directly to regional fractures. At Syria Planum, surface fracturing is fairly scarce relative to other areas, yet the alignment of fissure vents seen on many low-relief shields allows the crustal stress pattern to be determined (see Fig. 3.11a). The observed configuration of clusters of low shields with vents aligned along rift zones has been compared with the style of volcanism seen in the Snake River Plain, Idaho [*Greeley*, 1982; *Hodges and Moore*, 1994].

In contrast to Mars, low-relief shields are distributed across most of the surface on Venus, with 47% of shields existing within the BAT region, including 64% of S6/7 shields, but only 45% of S1-S5 shields. Venusian shields have been emplaced within a broad range of environments, with most occurring within fractured plains (33%) and flow fields (32.6%), and fewer occurring in smooth plains (22.9%) and wrinkle-ridge plains (16.5%). There are no notable correlations between shield categories and geological settings for S1-5 shields, but there is a notable tendency for S6/7 shields to cluster in shield fields (68.2% of S6/7 shields compared with 24% of other shield types), and to be emplaced within fractured terrain (50% of S6/7 shields compared with 31% of other shield types). Similar to Martian Lrs2/4 shields, the fissure vents of most S7 shields are aligned parallel to regional fracturing in the area (Fig. 3.12).

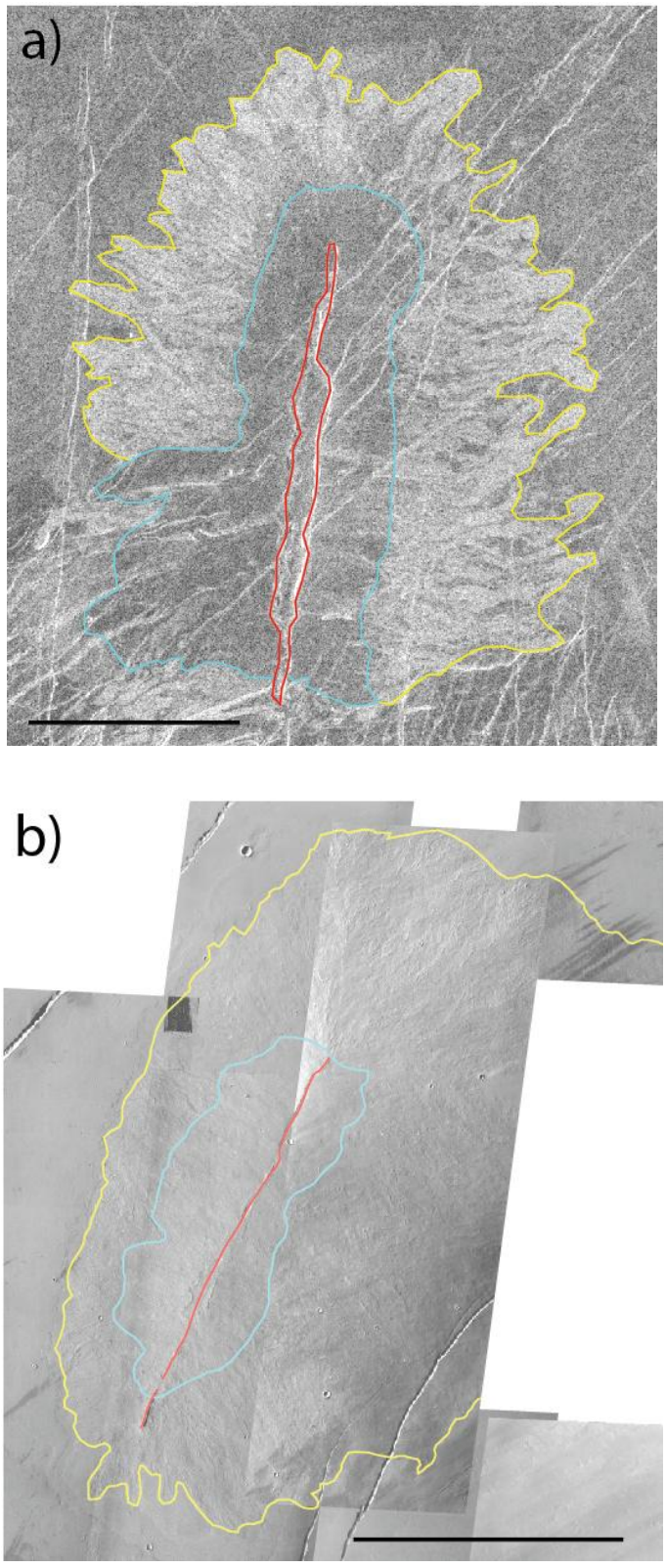

Figure 3.12. Comparison of the morphologies of an S7 shield on Venus (a) and an Lrs2 shield on Mars (b). (a) is a Magellan radar image, (b) is a mosaic of THEMIS images. In both cases, the red lines highlight the margins of the fissure vent, the cyan lines highlight the margins of the inner, low-roughness zone surrounding the vent, and the yellow lines highlight the margins of the outer high-roughness, digitate flows. Scale bars both measure 20 km. Magellan radar image is left-looking. Illumination in THEMIS mosaic is from the left.

Regarding elevation, shields fall into one of two groups: categories S1-5 generally exist at intermediate elevations (mean of 56 m above MPR ± σ of 769 m), whereas the S6/7 categories generally exist at much higher elevations (mean of 768 m above MPR ± σ of 814 m). This observation supports the observation of *Ristau et al.* [1998] that "anemone" volcanic features (analogous to S6/7 shields in the present study) exist at mean elevation of 800 m above MPR. This fact, in addition to their distinct appearances from the other shield types and their strong tendency to group together in shield fields, would seem to imply that S6/7 shields are the consequence of a style of volcanism that differs from that which produces the S1-5 shields.

3.3.4 Interpretation

3.3.4.1 Differences in shield morphology and distribution

Caldera size and shape: The generally large (diameters of several kilometres) and equidimensional collapse calderas exhibited by most Venusian shields (particularly S1, S2, and S3 shields) may be regarded as indicative of shallow magma chambers of sizes comparable to those of the calderas [*Mouginis-Mark and Rowland*, 2001; *Stofan et al.*, 2001]. The variety seen in shield caldera size on Venus, notably within the S1-3 categories, stems from combinations of magma reservoir size, depth and extent of collapse. In contrast, the universal manifestation of vents as narrow fissures, collapse pit chains and single collapse pits in Martian shields is interpreted to indicate that all the catalogued low-relief Martian shields are fed by dikes from a deeper magma source, the dimensions of which are not reflected by the dimensions of the vent. The fact that fissure and collapse pit chain vents (and associated regional fractures) appear to trace out regional stress patterns within the Tharsis rise implies that rising magma is exploiting regional fracturing, but whether the magma derives from a shallow magma reservoir or directly from a deeper source region in the crust or mantle is not immediately certain.

Edifice relief: Of those Venusian shields for which vertical relief measurements have been obtained, most display smaller aspect ratios (mean of 162) compared with Martian shields (mean of 258). This may potentially result from a number of factors. *Wilson et al.* [2009] suggested that the low viscosity of the lavas of the Tharsis low-relief shields as inferred from their flow morphologies represents the best evidence that

the lavas are more likely to be primitive mantle melts erupted directly from great depth rather than the evolved products of prolonged shallow crustal storage. The lavas forming the Venusian shields may have instead become more evolved through prolonged residence within such shallow reservoirs, resulting in them having more viscous, though still basaltic, rheologies. In addition, magma ascent speeds and associated eruption rates are expected to be lower on Venus relative to Mars, resulting in shorter flows [*Wilson and Head*, 1994] and increased superposition of lavas to produce smaller aspect ratios for Venusian shields. The minimum and maximum limits on magma ascent speeds are both predicted to be smaller on Venus compared with Mars. The lower limit on magma ascent speed is set by the requirement that the magma must not cool so much during its rise that its yield strength becomes large enough to prevent it moving through the fissure system [*Fedotov*, 1978; *Wilson and Head*, 1981; *Delaney and Pollard*, 1982]; if magma on Venus ascends from reservoirs at shallower depths than those on Mars, then a lower ascent rate is possible for it still to erupt at the surface, and a lower eruption rate will result. The upper limit on magma ascent speed is set by the mean width of the widest dike that can be formed in a stress environment; as described in section 1.2.2.1, a planet with low gravity will display slow diapiric ascent rates, allowing large diapirs to ascend to shallow depths, and increasing the probability of large dike widths and associated high effusion rates [*Wilson and Head*, 1994].

Clustering of shields: Venusian intermediate shields are not found in closely-packed fields to the same extent as Martian shields (28.9% of shields on Venus compared with 84.4% of shields on Mars). On Mars, in addition to the apparent correlation of many shields to regional-scale crustal fracturing, the dense clustering of shields in regional fields reaching several hundred kilometres across (particularly at Syria Planum) implies that all shields within a particular field originate from a broad, single source that lies at an undetermined depth. Venusian shields, which are more commonly isolated, are interpreted to instead derive from discrete, smaller crustal magma bodies that are likely to occur at shallow depths. Numerous shield fields do exist on Venus (*Head et al.* [1992] counted 556 across the planet with a mean diameter of ~150 km), but the constituent shields are almost always less than 20 km across. *Head et al.* [1992] interpreted such shield fields to be the surface manifestations of large sources of magma at depth, although uncertainty remains as to whether the magma ascends uninterrupted to the surface from a mantle source, or stalls at an intermediate level. Except for that at

Syria Planum, the shields in Martian fields are generally more dispersed and spread over a wider area than those on Venus. 150 km is essentially a lower limit for Martian shield field diameters; the Syria Planum field has a mean diameter of ~350 km.

These various lines of evidence appear to support the interpretation that most Venusian shields derive from shallow crustal magma bodies, whereas Martian shields derive from larger and possibly deeper sources.

3.3.4.2 Formation processes and conditions of radial flow shields

Formation process: It has been noted in section 3.3.2 that Venusian S6/7 shields display morphological characteristics that bear a notable resemblance to those of Martian Lrs1/2 shields. These shields display a rough, radially-oriented surface texture towards the margins of the shield, which on both planets is coincidental with the appearance of digitate flows, whereas the surface texture immediately surrounding the vent is smoother and more homogeneous (see Fig. 3.12). In section 3.3.3 it was noted that these shield types are often associated with fractured terrain and cluster within fields more commonly than other shield types. As a consequence, they display vents whose morphologies appear to have been shaped by diking associated with such fracturing; these include fissures (S7 and Lrs2 shields), single pits or chains of pits (Lrs1 shields) and elongate collapse calderas (S6 shields). Martian Lrs3/4 edifices also display either fissure or collapse pit vents, yet display lower aspect ratios compared with Lrs1/2 shields, and do not display digitate flow morphologies. Lrs3/4 shields occur predominantly in Syria Planum, and their low aspect ratios may be partly the result of their being closely-packed in fields such that they frequently share margins with each other and do not have the space to spread out. In addition, the relatively featureless surface textures and smooth margins of these shields, and their relatively high impact crater frequencies, indicate that they are older than those seen in other fields in the Tharsis region; *Webb et al.* [2001] regarded the Syria Planum shields to be late Hesperian in age. These shields are interpreted to have formed in an analogous manner to Lrs1/2 shields, yet their circumstance of formation and greater ages have resulted in them acquiring different morphological characteristics.

The study of *Wilson et al.* [2009] focused on a group of six Tharsis vent systems proximal to Jovis Tholus that, in the present study, mostly belong to category Lrs2. Based on examination of the morphologies of these shields, *Wilson et al.* [2009]

determined that the lavas displayed particularly low yield strengths and viscosities with respect to other flows on Mars, and investigated the extent to which these anomalies may be explained by composition, pre-eruptive storage and eruption conditions. By identifying spatter ramparts bordering the fissures of these shields and streamlined levees distributed amongst the flows, *Wilson et al.* [2009] inferred that the digitate flows of the shields are rootless flows fed by molten lava clasts descending from fire fountains driven by volatile release. The digitate flows appear to stem from a region of smooth and homogeneous material (at the 100 m/pixel resolution of THEMIS imagery) immediately surrounding the vents, which generally extends to ~5 km from the vent [*Wilson et al.*, 2009]. Referred to as "spatter" by *Wilson et al.* [2009], this study interprets this smooth material to represent lava ponding that formed from coagulating, molten lava clasts deposited from the fire fountain. This type of activity has been observed extensively on Earth, notably at Hawai'i (e.g. *Wilson and Head* [1981], *Head and Wilson* [1987], *Head and Wilson* [1989], and *Parfitt et al.* [1995]).

Wilson et al. [2009] expressed uncertainty regarding the depth of the source for the lavas forming these shields, yet regarded the low viscosities of the flows forming them to be indicative that these are primitive mantle melts erupted directly from a great depth. *Head and Wilson* [1989] noted that the clast temperature and eruption rate must both be high upon eruption in order to ensure the clasts remain molten for long enough in order to coagulate and form lava ponds and flows stemming from them; the modelling of *Wilson et al.* [2009] determined a magma temperature of 1450 K and an eruption rate of 5000 to 10,000 m^3s^{-1} for the Tharsis shields. As mentioned in section 3.3.4.1, high eruption speeds and high lava temperatures would be expected if the lavas had been erupted directly from a great depth, in order that the magma does not cool and solidify in the dike [*Fedotov*, 1978; *Wilson and Head*, 1981; *Delaney and Pollard*, 1982].

The fact that the Venusian deposits are radar-dark indicates that they are smooth at the scale of the radar wavelength (12 cm), whereas the Martian lava ponding is observed to be smooth at a quite different scale (the maximum image resolution of 100 m). Yet despite the fact that the roughness of these deposits cannot be determined at the same scale, their configurations around their parent fissure vents are identical on both planets, and they are therefore considered to have formed analogously. The transition of the radar-dark spatter deposits into the radar-bright digitate flows on Venus mirrors the increasingly rough and digitate texture of the flows of the Martian shields. These

morphological analogies would appear to point to the interpretation that S6/7 shields represent rare occurrences of fire fountain activity on Venus. *Head and Wilson* [1986] predicted the necessary conditions of magma volatile content and mass eruption rate that will allow fire fountain activity for a given surface atmospheric pressure on Venus, and determined that in order for such fire fountain activity to take place anywhere on the planet, the magma must contain a much higher volatile component than magma on Mars in order to ensure sufficient exsolution and expansion upon eruption to allow magma fragmentation. The reduced gas exsolution on Venus relative to Mars will also result in lower eruption speeds, and therefore a lessened ability to fragment the magma, but the higher density of the exsolving gas on Venus will compensate for this.

Magma volatile content: Magmatic volatiles on Earth are generally dominated by H_2O or CO_2. *Head and Wilson* [1986] demonstrated that for conditions appropriate for MPR on Venus (10 MPa surface pressure, 750 K ambient temperature), a minimum H_2O content in basalt of 2.5 wt % is required to ensure explosive activity in magma, whereas for highland conditions (4 MPa surface pressure, 650 K ambient temperature), a minimum H_2O content in basalt of 1.1 wt % is required. For CO_2 in any magma, the equivalent contents are 4.7 wt % and 2 wt %, respectively. Terrestrial basalts with H_2O contents as high as 1 wt % or CO_2 contents as high as 0.4 wt % are very rare [*Head and Wilson*, 1992], and may also be rare on Venus. CO_2 may currently be the major magma volatile on Venus given the predominance of CO_2 in the atmosphere [*Wilson and Head*, 1986], and the overall very dry state of Venus [*Lewis*, 1970; *Ingersoll*, 1969; *Walker et al.*, 1970]. However, *Head and Wilson* [1992] noted that there is as yet no direct evidence that Venusian magmas do not contain appreciable amounts of H_2O. If CO_2 and H_2O were both present in the ascending magmas, the CO_2 should exsolve before the H_2O will, as the solubility of H_2O is several times greater than that of CO_2 [*Mysen*, 1977]. This has been predicted in the model of *Gerlach* [1986] for the exsolution of CO_2 and H_2O from Kilauea magma as it rises from a shallow crustal reservoir; the model indicated that most H_2O remains dissolved down to pressures as low as 2 to 3 MPa, whereas most CO_2 is exsolved above 10 MPa. Given the magnitude of the Venusian surface atmospheric pressure (10 MPa at MPR, 4 MPa for the highlands), it would be expected that CO_2 would be the predominant exsolved volatile upon eruption, and that which will precipitate fire fountain activity, with most of the H_2O remaining dissolved. *Mysen* [1977] noted that the presence of dissolved H_2O acts to depolymerise

a melt and reduce its viscosity, whereas dissolved CO_2 will instead enhance polymerization and increase the viscosity of a melt. The low reliefs of S6/7 shields may therefore imply a low lava viscosity resulting from a high H_2O content that has not exsolved from the erupted lava, although other factors such as eruption rate will also hold influence.

It should be noted that the occurrence of the hawaiian-style activity that is interpreted to form the shields may not necessarily require a high bulk volatile content in the magma reservoir. A mechanism has been proposed by *Head and Wilson* [2003] to explain how terrestrial submarine pyroclastic eruptions can occur at depths greater than a few hundred metres, where the high ambient pressure of the seawater would normally suppress gas exsolution, and suggested that this mechanism may also be applicable for the similarly high-pressure environment at the surface of Venus. The mechanism involves magmatic gas buildup occurring over a protracted time period in a reservoir by the upward drift of gas bubbles (mainly CO_2), such that a layer of foam builds up at the top of the reservoir in a sufficient concentration (>90%) to exceed the volatile content necessary for disruption and hawaiian-style activity.

S6/7 shields generally exist at much higher elevations than other low-relief shields on Venus (mean of 768 m above MPR for all S6/7 shields relative to 56 m above MPR for S1-5 shields). *Wilson and Head* [1986] note that the nature of explosive activity at the surface is mainly controlled by the final pressure reached by the gas as it expands in the conduit, i.e. the atmospheric pressure. Therefore, for a given volatile concentration, the lower atmospheric pressures that exist at such elevations would ensure more efficient volatile exsolution and decompression as the magma ascends to the surface, and more extensive magma fragmentation upon eruption. The paucity of S6/7 shields on Venus (only 22 have been catalogued across the entire planet) presumably reflects the fact that only in very rare instances does the correct combination of volatile content and elevation of eruption occur to allow sufficient volatile exsolution to promote the sort of fire fountain activity that has been interpreted by *Wilson et al.* [2009] to be the eruption process for the Martian shields. Such high volatile contents are not necessary for the explosive disruption of magmas on Mars, permitting this type of activity to occur much more frequently than on Venus; *Wilson et al.* [2009] determined the equivalent magma H_2O content of the Tharsis shields they studied to be ~0.1-0.2 wt %. *Head and Wilson* [1986] estimated that most ballistic pyroclasts will land within one vent radius

of the edge of the vent. While it would be expected that raised spatter ramparts similar to those seen in Martian shields would be seen around the fissure vents of Venusian shields, such ramparts are not discernible around the fissure vents of the shield in Fig. 3.12a. This may result from their narrow dimension being less than the minimum resolution of Magellan (101 m cross-track, 110 m along-track), and their vertical dimension being too small to merit a reflection; spatter ramparts for Martian fissure vents reach a few hundred metres across and less than 5 m in height.

The ability of a batch of melt to reach the surface rather than stall at a neutral buoyancy zone depends on the difference between the rate at which the density of the melt decreases upward due to volatile exsolution and the rate at which the density of the country rock layers decreases upward due to the nature of the compaction process [*Head and Wilson*, 1992]. The density profiles will be different because the silicate phase in what has become the country rock will be solid rather than liquid, and hence denser, and because the compression under loading of the fixed mass of the gas phase in the new country rock will differ from the decompression of the gas phase in the rising magma, where the gas mass increases as exsolution occurs. Venusian S6/7 shields typically exist at high elevations where low atmospheric pressures will prevail, and where the shallow crust would be expected to display a relatively high void space fraction and a correspondingly low bulk density as a result of the strong exsolution of volatiles from erupting lavas that form the crust [*Head and Wilson*, 1992]. This would mean that the volatile content of the magma within the dikes feeding the shields must be high enough, not only to ensure that fire fountain activity is sustained, but also that the magma density remains lower than the country rock density and positively buoyant until the surface is reached, or at least low enough at depth to compensate for any negative buoyancy that develops in shallower magma. Assuming that the magma forming the country rock has basaltic volatile concentrations of 1 wt % H_2O and 0.4 wt % CO_2 (a likely upper limit for terrestrial basalts [*Lofgren et al.*, 1981]), and erupts at 2 km above MPR with a surface atmospheric pressure of 8.645 MPa (the altitude of the highest catalogued S6/7 shield), *Head and Wilson* [1992] calculated that the resulting bulk density would be 1322 kg m^{-3}. For an eruption altitude at MPR and a surface atmospheric pressure of 9.811 MPa, *Head and Wilson* [1992] calculated the corresponding value to be 1471 kg m^{-3}. Depending on the altitude of eruption, the ascending magma that will erupt to form the S6/7 shields must therefore contain a

combined concentration of volatiles that results in a lower surface rock bulk density. Given that total volatile concentrations of 2 to 4 wt % (depending on altitude) are required to sustain fire fountain activity at Venus, any magma with a volatile concentration sufficient to allow fire fountain activity upon eruption should also have a volatile concentration sufficient to prevent stalling at a neutral buoyancy zone within the crust. In addition, if overpressurization within the plume head from which the dikes originate applies a continuous driving pressure to the magma within the dikes (creating buffered conditions [*Parfitt and Head*, 1993]), and considering that the dikes are interpreted to exploit pre-existing crustal fracturing in order to propagate, the magma could progress to the surface without stalling at a density or rheological boundary.

Geological setting and distribution: The alignments of the fissure vents of Martian shields, and associated regional fracturing, trace out regional stress patterns, which has led to the interpretation that these shields are being fed by dikes exploiting regional fracturing, although the depth of the source regions of these dikes cannot unambiguously be determined. However, because the Martian shields are generally grouped closely together within broad fields, it would suggest that all shields belonging to a particular field are derived from a shared source that displays comparable lateral dimensions to the extent of the field. The Tharsis volcanic province itself is thought to have resulted from a long-lived mantle plume producing episodic batches of melt [*Wilson et al.*, 2001]. *Webb et al.* [2001] attributed the very different styles of volcanism seen at the volcanic centres of Syria Planum and the Tharsis Montes to differences in the depth, nature and evolution of the magma reservoir; Syria Planum would have been characterized by eruption from a deeper magma reservoir, with a higher intrusion/extrusion ratio, and the lack of a vertically migrating magma reservoir dominated by an evolving neutral buoyancy zone. In addition, *Wilson et al.* [2009] considered the low lava viscosities of low-relief shields as inferred from their flow morphologies to imply a primitive mantle composition erupted directly from great depth rather than an evolved composition obtained through prolonged, shallow crustal storage. Based on these considerations, and the morphological evidence for a deep magma origin, the potential exists for the 'deep reservoirs' from which the magmas forming the low-relief shield fields originated to be zones of pressure-release melting within the mantle plume underlying Tharsis.

63% of S6/7 shields exist within the BAT region, which covers just over 25% of the surface area of the planet; given the high concentration of volcanic features that exists there, the BAT region potentially represents the surface manifestation of a thermal anomaly and major upwelling in the mantle [*Head et al.*, 1992]. This suspected anomaly may represent a megarise similar to the Tharsis region on Mars, although the BAT region differs in that it is essentially made up of a series of rises and volcanic features, each representing different scales of convective instabilities, rather than a single broad megarise [*Head et al.*, 1992]. The magmas that erupt to form S6/7 shields are interpreted to display a high volatile content; such magmas must originate from a deep source region, as the solubility of volatiles increases with increasing pressure according to relationships as described by *Wilson and Head* [1981]. In addition, S6/7 shields also display analogous distributional characteristics to the low-relief Tharsis shields, i.e. an association with regional fracturing and the tendency to occur in shield fields. These characteristics have been considered to be indicative of a deep, potentially mantle plume origin for the Martian magmas [*Wilson et al.*, 2009], and are regarded to have the same implications for the origin of the magma feeding the Venusian shields.

3.3.4.3 Evolution of caldera morphologies of radial flow shields

It has been asserted by this study that S6/7 shields are comprised of lavas that have been sourced directly from great depth, potentially from the head of a mantle plume, based on their morphology, distribution and geological setting. Yet the collapse calderas seen to exist at the summits of S6 shields are not consistent with a formation process by fire fountain activity from a fissure. Indeed, a feature of radial flow shields on Venus that is not replicated on Mars, and which may represent differing evolutions of the intrusive systems feeding these edifices, is the apparent development of elliptical calderas in shields displaying fissure vents. The shield field displayed in Fig. 3.13 features three prominent radial flow shields that represent three stages in this development. The vent of shield 1 is represented by a single, continuous fissure that is aligned parallel to the north-south-oriented regional fracturing in the vicinity; this shield is an archetypal S7 shield. Shield 2 has also been catalogued as an S7 shield, and displays a north-south-oriented, discontinuous fissure vent, yet surrounding the fissure vent is a 20 by 13.5 km, elliptical annulus of continuous concentric fracturing that

reaches 1 km thick, and whose long dimension is aligned parallel to the fissure vent. The annulus truncates radar-bright digitate flows emanating from the fissure vent. Shield 3 has been catalogued as an S6 shield, and displays an elliptical caldera measuring 21.5 by 12.5 km whose long dimension is aligned parallel to north-south-oriented regional fracturing. No fissure is apparent. Smaller shields and collapse pits mark the flanks of the shield.

The apparent continuity in vent morphology from fissures through to elliptical calderas that is observed in Fig. 3.13 implies that shallow magma reservoirs may develop underneath these edifices after their initial emplacement [*Mouginis-Mark and Rowland*, 2001; *Stofan et al.*, 2001]. Shield 2 in Fig. 3.13 is an ideal example of a shield that appears to be in a transitional stage, with the outline of the forming caldera (represented by the concentric fracturing) truncating the radar-bright digitate flows emanating from the fissure vent that it encloses. The annulus of concentric fracturing is interpreted to eventually develop into an elliptical caldera such as that belonging to shield 3. The caldera has evidently reached its present configuration late in the history of the shield, as its rim truncates radar-bright, digitate flows from a smaller shield that has formed on the southwest flank of shield 3. No remnant of a fissure vent survives in shield 3, yet it may have been entirely eliminated by formation of the elliptical caldera, the long dimension of which is itself aligned parallel to regional fracturing.

The prevalence of S6 shields (17) relative to S7 shields (5) on Venus indicates that caldera formation in these shield types is common, and whereas evidence exists that such calderas can truncate earlier fissure vents, it is not certain as to whether this is always the case, or if calderas can form with no fissure precedent. S6 shields are the shield type most associated with regional fracturing, and the fact that the calderas of S6 shields are generally more elongate than those of the S1-3 shield types (displaying mean length/width ratios of 1.467 and 1.287 respectively) does imply that the calderas of S6 shields derive their shape from crustal stresses and associated fracturing and diking to a greater degree than those of other shield types.

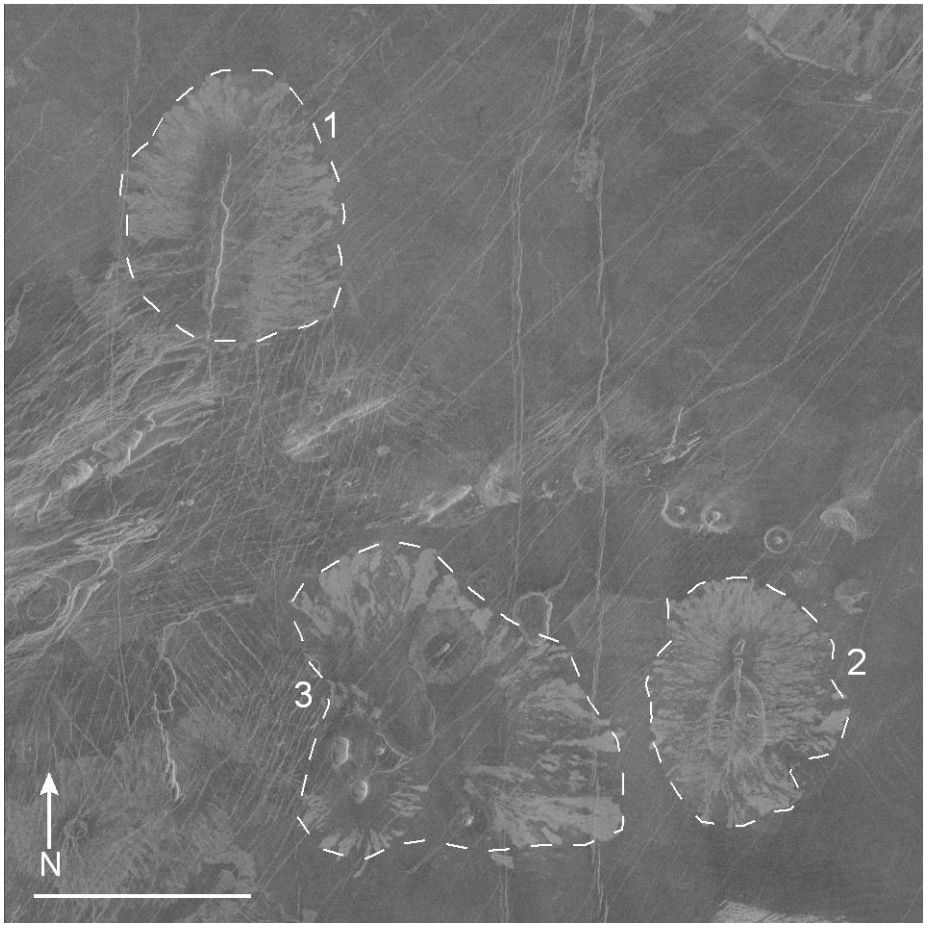

Figure 3.13. Magellan left-looking radar image showing two Venusian S7 shield volcanoes (shields 1 and 2) within a shield field located within Atla Regio. The two shields display N-aligned fissure vents that are aligned parallel to three prominent regional graben, two located just to the centre-right of the image, one located on the left. The NE-aligned regional fracturing occurred after the N-aligned fracturing, as its fractures superpose the N-aligned graben. Shield 3 is a S6 shield. Scale bar measures 50 km. Image centred at 7.4°S, 199.9°E.

The cause of the development of these shallow magma bodies is interpreted to be related to a lessening in the volatile content of the magma supplying the shields, and the appearance of shallow neutral buoyancy zones as a result. If a magma rising toward the surface of a planet contains a volatile having a pressure-dependent solubility, there are two critical pressure levels, and hence depths, through which the magma must pass [*Head and Wilson*, 1992]. The first is the nucleation level, at which point the local pressure equals the pressure at which the magma becomes saturated in the volatile. Provided that the atmospheric pressure is less than the nucleation pressure, the volatile will subsequently exsolve to form bubbles. The second is the fragmentation level, at which point the pressure is such that expanding bubbles of exsolved gas occupy ~75% of the total magma volume, thereby fragmenting the magma into a spray of released gas and entrained pyroclasts [*Sparks*, 1978]. Both of these pressure levels will occur at

greater depths for magma with a high volatile component relative to one with a small component. As a result, the density of the magma will be higher at a particular depth for magma with a low volatile component relative to one with a high component.

In order for magma to rise directly to the surface, the density of the magma must be lower than that of the surrounding country rock throughout the entire crustal column. This is interpreted to be the case during initial formation of S7 shields. Exsolution of a volatile with decreasing pressure will reduce the bulk magma density [*Wilson and Head*, 1997]. To prevent stalling, the volatile content of the magma is required to be high, thereby ensuring volatile exsolution commences at a deep level, and also ensuring that the fragmentation level is reached before the magma erupts, resulting in fire fountain activity. Yet if the volatile concentration decreases sufficiently, the concurrent raising of the nucleation level, decrease in volatile exsolution and increase in magma density will cause a neutral buoyancy zone to appear beneath the surface, and progress downwards as the volatile concentration continues to decrease. As magma continues to propagate upwards, a shallow magma reservoir will form that is centred on the level of neutral buoyancy. The volatile concentration of the magma will decrease to the extent that the fragmentation level is never reached, and the magma effuses onto the surface with no explosive activity. Thus, the eruption style of the shield will shift from frequent fire fountain activity at a fissure vent to one characterized by caldera collapse above the newly-formed shallow reservoir, a process that is currently in its early stages for shield 2 in Fig. 3.13. These calderas would fill periodically with radar-intermediate to radar-dark, homogeneous flows erupted from the shallow reservoir, such as that of shield 3 in Fig. 3.13, resulting in transition to an S6 shield. *Stofan et al.* [2001] considered a decrease in volatile content, as well as a drop in the magma supply, to be a possible mechanism for the transition from effusive to intrusive activity observed at the large volcano Kunapipi Mons.

The absence of such caldera formation in the Martian shields indicates that shallow magma reservoirs have not formed beneath these edifices, and that throughout their formation history the magma feeding them has maintained a density less than that of the surrounding country rock. *Head and Wilson* [1992] noted that if no factors intervene to modify the densities of the crust and of any melts rising through it, then the melts of basaltic parent materials would always be less dense than their solid equivalents and would thus be positively buoyant at all depths between their source regions and the

surface. *Head and Wilson* [1992] argue that volatile exsolution within Venusian magmas will produce vesicular, low density surface layers, assuming the fragmentation level is not reached, which will generally be the case given the inhibitive effect of the high atmospheric pressure. Such surface layers would be more likely to equate with the densities of rising, positively buoyant magma, thereby ensuring stalling of magma and formation of shallow magma reservoirs. If the volatile content of the magmas that form the shallow crust in this area of Venus is high (an upper limit of 1.4 wt % for terrestrial basalts has been cited [*Lofgren et al.*, 1981], then it follows that the shallow crust here will be of relatively low density, increasing the likelihood of neutral buoyancy zones forming. On Mars, the very low atmospheric pressure means that any volatiles that are exsolved from the magma will be lost to the atmosphere rather than retained as large vesicles within the magma. In addition, very large magma volatile contents are not necessary to facilitate the fire fountain activity that is interpreted to form the Martian shields, which further lessens the probability of the shallow crust of Mars displaying a high vesicularity and a correspondingly low density. As a result, the density profile of the Martian crust will be such that the ascending magma will be positively buoyant at all depths throughout the formation history of the shields.

3.3.5 Summary

- Neutral buoyancy zones have strongly influenced the distribution of caldera sizes of shields on both planets. Neutral buoyancy zones are expected to be shallower on Venus relative to Mars due to the varying crustal density profiles that result from volatiles within the magmas exsolving to different degrees on the two planets. The large calderas seen in most Venusian shields are interpreted to be surface manifestations of these shallow reservoirs. The fissure and pit vents seen in Martian shields are regarded as evidence for these shields being fed by dikes from a deep source. Neutral buoyancy theory predicts that magma reservoirs should become deeper as elevation increases on Venus; the radial flow shields with fissure vents, which tend to occur at high elevations, are also regarded to derive from deep sources like the Martian shields.
- The fissure vents of radial flow shields are often aligned parallel with regional fracturing in the vicinity on both planets, implying that magma has exploited crustal fracturing resulting from a tensile stress regime. The fact that these shields are

associated with fractured terrain more commonly than other shield types on Venus indicates that the presence of such crustal fracturing is an important factor in permitting the ascent of dikes that feed such edifices. The regional extent of the fracturing and the frequent clustering of radial flow shields within broad fields are taken to imply that the magma feeding the shields in a particular field is ultimately derived from a single, large, deep reservoir, which may take the form of a mantle plume. Radial flow shields tend to concentrate in fields within the Tharsis and BAT 'megarises' on Mars and Venus respectively, which have been interpreted to be underlain by thermal anomalies and zones of mantle upwelling.

- *Wilson et al.* [2009] interpreted the Martian shields to have formed by fire fountain activity based on identification of spatter deposits around the rims of their vents. The Venusian fissure vent shields are also interpreted to have formed in this manner based on morphological comparisons, although the necessary combination of magma volatile content and atmospheric pressure that will allow such activity will occur only rarely on Venus, and such shields are themselves rare as a result. Low atmospheric pressures, which occur at high elevations, and high magma volatile contents, which may derive from magmatic gas buildup occurring towards the top of a reservoir, are necessary for the magma to fragment upon eruption. On Mars, the very low atmospheric pressure means that high magma volatile contents are not necessary to permit fire fountain activity, thereby allowing such activity to occur much more commonly than on Venus, and across all elevations.

- There is an observed transition of eruption style in Venusian radial flow shields from fire fountain activity through fissure vents to more effusive activity accompanied by caldera collapse. This is interpreted to result from the development of neutral buoyancy zones, and accompanying shallow magma reservoirs, beneath these shields as the volatile content of the magma feeding them decreases, and the density of the magma starts to equalize with that of the surrounding country rock. The reduced volatile exsolution that accompanies the decrease in volatile content will also prevent fragmentation of the magma upon eruption. The development of a shallow magma reservoir will result in formation of a collapse caldera that subsequently fills with effused lava. Similar caldera formation is not seen on Mars, interpreted to be because the density profile of the Martian crust will never be such that a rising magma will stall before it reaches the surface, even if the magma is very depleted in volatiles.

3.4 Dome morphologies on Venus

3.4.1 Introduction

Steep-sided domes (category D) and modified domes (category MD) are intermediate volcanic features that are prevalent on Venus yet absent on Mars. Domes represent the morphological category that displays the largest number of subcategories, defined mostly by variations in caldera size and flank modification. This section will examine morphological and distributional correlations both within and between the steep-sided and modified dome categories, and use such correlations to infer what processes are influential in shaping them.

Venusian domes display a very wide range of morphologies and preservation states, with 42% of the domes having experienced extensive flank collapse. The results of this study have supported the hypothesis that modified dome subcategories MD1 to MD4 are collapsed versions of the corresponding D1 to D4 steep-sided dome subcategories, based on mean diameter, height and aspect ratio comparisons between the various subcategories, in addition to similarities in the proportions of steep-sided and modified domes that display collapse pits and radial fracturing. MD5 domes have collapsed to the extent that their original unmodified dome categories cannot be determined. The following characteristics tend to distinguish modified domes from steep-sided domes: they are taller (and therefore have smaller aspect ratios), display larger caldera diameters and smaller edifice/caldera diameter ratios, and they are more commonly located on volcano flanks/summits. The implications of these characteristics for emplacement and modification are discussed in the following sections.

3.4.2 Heights and aspect ratios of domes

Internal causes of slope failure during emplacement of domes [*Williams*, 1932; *Swanson et al.*, 1987; *Beget and Kienle*, 1992; *Nakada and Fujii*, 1993] can arise from overloading of a slope by lavas (for endogeneous growth), excess weight of lavas at the top of a slope (for exogeneous growth), and from rapid emplacement leading to oversteepening of a flow front [*van Bemmelen*, 1949; *Francis et al.*, 1974; *Ui*, 1983; *Siebert*, 1984; *Guest et al.*, 1984]. Steep-sided and modified domes display very similar diameters: the mean diameter of steep-sided domes is 30.1 km, whereas that of modified

domes is 29 km. However, the mean heights attained by the respective dome types are very different: 684 m for steep-sided domes and 1313 m for modified domes, different by a factor of almost two (it should be noted that height values were obtained for 38% of all dome types). Consequentially, the mean aspect ratio for steep-sided domes is 76, whereas that of modified domes is 39. Low aspect ratios and greater heights correspond to steeper slopes and greater slope instability, and increase the likelihood of slope failure.

Figure 3.14a shows the distribution of heights for steep-sided domes and modified domes, and Fig. 3.14b shows the distribution of aspect ratios (for the 38% of domes for which heights have been recorded). Both steep-sided and modified domes display height distributions that peak at relatively low heights (in the range 200 to 600 m), but the distribution for modified domes extends to higher values than that of steep-sided domes. The aspect ratio distributions of both types of dome peak at low aspect ratios (in the range 20 to 30), but the distribution for steep-sided domes extends to higher values compared with that for modified domes. A threshold height may therefore be defined above which a steep-sided dome is likely to undergo collapse (specifically 1800 m), and a threshold aspect ratio may be defined above which a steep-sided dome is unlikely to undergo collapse (specifically 120). However, there remains the fact that many steep-sided domes and modified domes display comparable heights and aspect ratios: 100% of steep-sided domes and 74% of modified domes display heights below 1800 m, whereas 98% of modified domes and 79% of steep-sided domes display aspect ratios below 120. Slope oversteepening may be regarded as an important cause of flank collapse in steep-sided domes, yet the overlap in height and aspect ratio for many steep-sided and modified domes indicates that other factors are influential as well. The origin of the wide variety in height and aspect ratio of steep-sided domes will be related to factors such as effusion rate and the range of viscosities of the lava forming the domes; lavas with higher yield strengths, and which are erupted at lower effusion rates, will form domes with smaller aspect ratios and possibly greater heights [*Best*, 2003]. Viscosity and yield strength are themselves related to parameters such as lava composition and cooling rate.

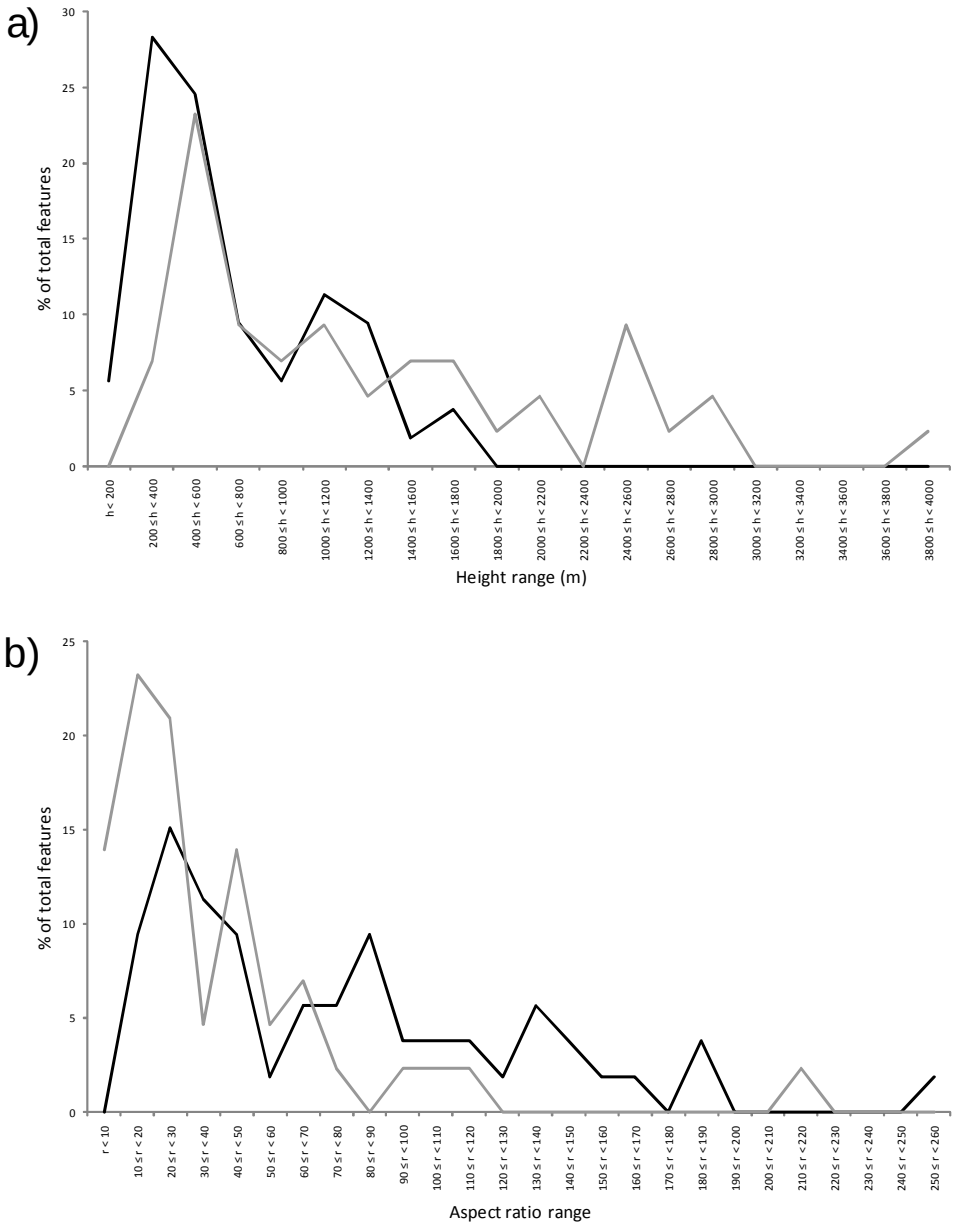

Figure 3.14. Height (a) and aspect ratio (b) distributions of steep-sided domes (black line) and modified domes (grey line).

Collapsed flanks are essentially absent in the cone and shield categories, as well as for large volcanoes. All of these categories display mean aspect ratios that are larger than those of domes, and generally display shallow slope gradients from their margins to their summit, whereas domes display steep margins and flat summit regions. There is therefore a correspondingly smaller likelihood of collapse through flank oversteepening in cones and shields. *McGovern and Solomon* [1998] hypothesized that basal welding to the lithosphere, primarily caused by the lack of water on Venus, may be preventing deeply rooted flank failure and basal slip in large Venusian volcanoes, while the absence of pore fluid pressure and the low flank slopes will prevent shallow flank

failure. It would be expected that such inhibiting factors would be even more effective in intermediate cones and shields, where the stresses experienced within the edifices and the instability of their flanks will be less relative to those of large volcanoes based on their smaller sizes.

3.4.3 Caldera sizes of domes

The unmodified D1 to D4 dome categories and their corresponding modified MD1 to MD4 dome categories are defined partly by their caldera characteristics. Type 2 domes are characterized by large summit calderas (mean of 9.0 km) and Type 4 domes are characterized by downsagged summit regions, whilst Type 1 domes display no summit caldera and Type 3 domes display small central pits (mean of 1.4 km). However, there are notable differences in the relative frequencies of corresponding unmodified and modified categories, which indicate that dome flank collapse and caldera collapse may be related. Specifically, 65% and 89% of Type 1 and Type 3 domes are unmodified, respectively, whilst only 36% and 37% of Type 2 and Type 4 domes are unmodified, respectively. It is therefore apparent that domes which display large calderas or downsagging of the summit region are more likely to have undergone flank collapse.

Small, shallow pits at the summit and along the margins of terrestrial domes (similar to those seen on Type 3 Venusian domes) are interpreted to have been formed by small explosions caused by venting of accumulated gas or by disruption of the carapace by dome growth [*Heiken and Wohletz*, 1987; *Bulmer and Guest*, 1996]. However, larger summit depressions on terrestrial domes ranging from shallow saucers to deep funnel-shaped pits (similar to those seen in Type 2 and 4 Venusian domes) have been interpreted to be formed by collapse due to withdrawal of magma or cooling [*Pavri et al.*, 1992; *Smith*, 1973]. *Bulmer and Guest* [1996] regarded the summit region downsags of Type 4 domes to have formed by magma withdrawal or release of volatiles by non-explosive degassing after dome emplacement. In many cases the voids created by caldera collapse or summit region downsag in Type 2 and Type 4 domes appear to occupy a considerable proportion of the dome volume. For example, the void created by the caldera in the MD2 dome shown in Fig. 2.3 is estimated to have a volume of 9.6 km^3 and account for ~3.5% of the entire volume of the dome in its present modified state. The void created by the downsag in the MD4 dome shown in Fig. 2.3 is estimated

to have a volume of 13.3 km^3 and account for ~13.5% of the entire volume of the dome in its present modified state. In both of these cases it is assumed that the caldera/downsag is circular and is represented by a flat floor surrounded by walls of constant slope, the value of which is determined by measurements of the diameters of the floor and rim of the caldera, and of the caldera depth via parallax. Several calderas and downsags display dark flows covering their floors, indicating that they were originally even deeper [*Mouginis-Mark and Rowland*, 2001]. Caldera collapse/downsagging on such a scale must be related to large-scale movement of magma beneath the domes, in contrast to the explosive events that form the smaller pits on the dome surfaces.

This study hypothesizes that the magma withdrawal that leads to the formation of the large calderas and downsags of Type 2 and 4 domes is related to the formation of the domes by endogenous growth [*Stofan et al.*, 2000]. In contrast to the exogenous growth of cone- and shield volcanic edifices on Venus, where magma passes through a central conduit to erupt at a summit crater and deposit itself on top of older lavas, the endogenous growth of domes involves internal inflation, whereby a continuous magma supply that pushes upwards and outwards from a vent at the base of the dome expands the dome from beneath [*Griffiths and Fink*, 1992; *Fink*, 1993]. New interior is continuously exposed as material flows out radially from the vent [*Stofan et al.*, 2000]. The emplacement regime would initially be core-dominated [*Kilburn*, 1993], where the outer crust offers little significant resistance to flow. As the dome continues to form, the weight of the dome will increase and the core-dominated regime will transfer to a crust-dominated regime, whereby the crust thickens to the extent that it will act to slow the spreading of the dome. *Bridges* [1997] concluded that rhyolites will solidify more quickly and develop thicker crusts on Venus relative to basalts (at timescales >1 hour), meaning that more silicic dome-forming lavas should transfer to a crust-dominated regime quicker than less-silicic lavas.

Dome growth can therefore be modeled as a brittle shell enclosing pressurized magma [*Best*, 2003]. The erupting magma experiences increasing resistance both from the overlying weight of the dome as it grows as well as from the increasing yield strength of the lava associated with the transition to a crust-dominated regime; the overlying pressure may eventually exceed that of the rising magma, forcing the magma to withdraw and perhaps be intruded into the crust beneath the dome instead. Factors

including the timescale of magma withdrawal and the rheology of the dome at the time of the withdrawal (which itself will depend on the lava composition and cooling rate) will determine whether a caldera or a downsag will form.

Pavri et al. [1992] note that, based on terrestrial observations, high-effusion, high-volume eruptions result in the emplacement of large volumes with insufficient time for cooling to cause solidification and inhibition of lateral growth, with the resulting edifices displaying large aspect ratios. In contrast, a low-effusion, low-volume eruption will result in the small volume of erupted lava piling up and cooling around the vent rather than spreading laterally. Type 4 domes would appear to conform to the former description, considering that they display a relatively high mean diameter (34.1 km) and mean aspect ratio (93.3). Type 2 domes instead match the latter description, displaying a relatively small mean diameter (25.9 km) and mean aspect ratio (35.7). For comparison, Type 1 and 3 domes display a mean diameter of 30.5 km and a mean aspect ratio of 69. The morphologies of Type 2 and 4 domes are also consistent with the rheologies expected in both types. The summit downsags of Type 4 domes are indicative of magma withdrawal occurring over a protracted timescale during which the rheology of the dome remains viscous enough to accommodate downsag without large-scale concentric fracturing. *Stofan et al.* [2000] noted that the formation of a surface pit requires the presence of a brittle crust, with the depths of the pits reflecting the minimum crustal thickness at the time of their formation. Type 2 domes often display deep calderas with sharply-defined margins and whose walls display sheer, unbroken slopes down to their floors, indicative of a brittle rheology extending throughout much of the body of the dome at the time of magma withdrawal.

Three potential scenarios for magma withdrawal (or lack of) are therefore interpreted to exist, which are illustrated in Fig. 3.15.

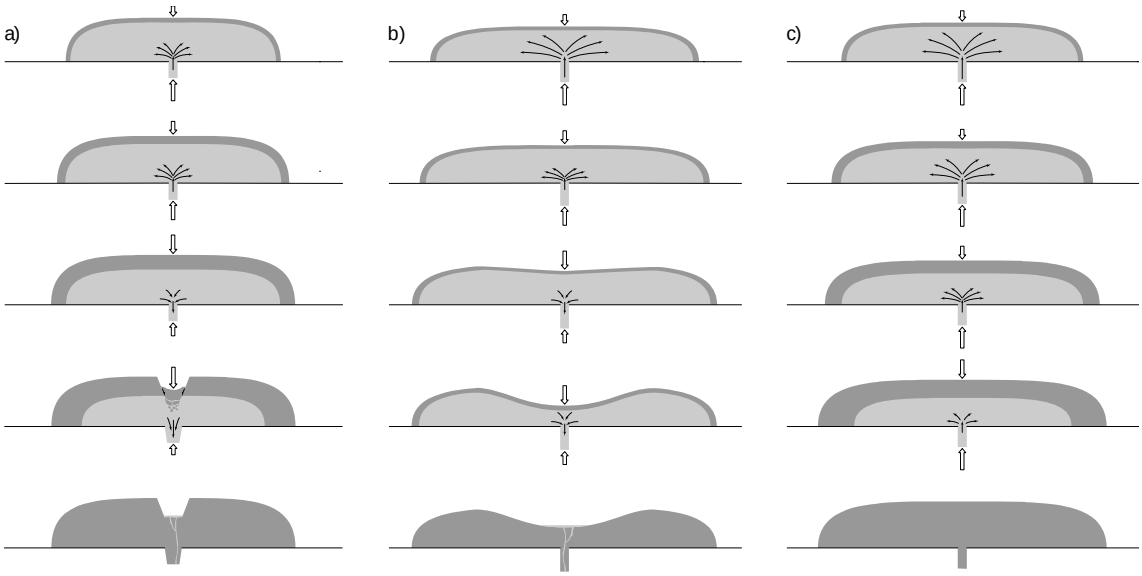

Figure 3.15. Three scenarios depicting the conditions interpreted to result in the formation of a large caldera (a), summit region downsag (b) and no caldera (c) in Venusian steep-sided domes. Lengths of the thin arrows qualitatively represent the rate of magma movement either into or out of the dome. Lengths of the thick arrows qualitatively represent the relative magnitudes of the upwards pressure of the rising magma and downwards pressure exerted by the dome weight/yield strength; the net pressure determines whether the magma rises or subsides. Dark grey areas represent solidified lava, light grey areas represent molten lava.

1) (Fig. 3.15a) A large proportion of the dome solidifies during its formation, the result of a low magma supply rate and/or a relatively silicic lava composition. This generally results in the dome having a small diameter and aspect ratio. The increasing overlying pressure caused by the increasing dome weight and yield strength act against the upwards pressure of the rising magma, and eventually exceed it altogether, causing it to withdraw. The emplacement regime of the dome is crust-dominated, and the rheology of the dome dominantly brittle, at the time of withdrawal, resulting in the localized collapse of a caldera to form a Type 2 dome. The collapse event leaves a funnel-shaped, talus-lined depression, rather than a flat floor that has dropped like a piston; later infilling by lava usually buries the talus leaving a flat floor [*Mouginis-Mark and Rowland*, 2001]. Several Type 2 domes display caldera benches that, in the calderas of terrestrial volcanic edifices, are interpreted to represent earlier levels of ponded lava left behind by continued small-scale collapse [*McBirney and Williams*, 1969; *Simkin and Howard*, 1970].

2) (Fig. 3.15b) The dome remains predominantly molten throughout its formation, the result of a high magma supply rate and/or a relatively basaltic lava composition. This generally results in the dome having a large diameter and aspect ratio. The increasing overlying pressure caused by the increasing dome weight acts against the

upwards pressure of the rising magma, and eventually exceed it altogether, causing it to withdraw. The emplacement regime of the dome is core-dominated, and the rheology of the dome dominantly viscous at the time of withdrawal, resulting in subsidence and downsag of the summit region to form a Type 4 dome. Type 4 domes do not display concentric fracturing that would indicate the existence of a thick crust at the time of subsidence. In several cases, later infilling by lava has covered the floor of the downsag.

3) (Fig. 3.15c) Regardless of the magnitude of the magma supply rate to the dome, it remains sufficient to counter the downwards pressure exerted by the overlying dome for the duration of formation. No withdrawal of magma occurs as a consequence, leaving the interior and summit region of the dome undisrupted, and forming a Type 1 or 3 dome.

Perhaps the most direct terrestrial analogy for the Venusian Type 2 and Type 4 domes is a dome belonging to the Mono Crater chain of rhyolite domes in eastern California, and which was noted as a potential analogy for Venusian domes in the study of *Stofan et al.* [2000]. The specific dome is referred to as the 'cratered dome' by *Smith* [1973], is 365 m across by 58 m high, is circular in planform, and displays talus slopes coating the steep flanks around the whole circumference (see Fig. 3.16). A summit depression that is 180 m across and 46 m deep is composed of a terrace (depressed 5 to 26 m below the rim of the dome) and a central wedge-shaped crater completely surrounded by the terrace. *Smith* [1973] regarded the terrace as being the floor of a crater that formed as a result of the collapse of the summit of the dome owing to subsidence of lava in the vent. Among the evidence that *Smith* [1973] cited to support such an interpretation was an inward-dipping slickensided surface with well-developed fault steps on the wall of the depression, which suggests normal movement. *Smith* [1973] interpreted this to be a surface along which subsidence occurred, and such a surface may be analogous to the sheer walls of the large calderas seen in the Type 2 domes in Fig. 2.3.

Smith [1973] described how the subsidence crater would subsequently have been disrupted by the formation of the central crater, 75 m by 35 m wide and 20 m deep. *Smith* [1973] noted that the crater walls were covered with ash, lapilli and blocks, and interpreted the crater to be an explosion pit that resulted directly from a vent-clearing eruption which may have been the precursor of a new eruptive episode. Similarly, the

presence of radar-dark lava flows covering the floors of several calderas and downsags of Venusian Type 2 and Type 4 domes appears to indicate that small-scale effusive eruption can continue after summit region collapse, perhaps instigated by the release of overlying pressure.

Figure 3.16. Oblique aerial photograph of the 'cratered dome' in the Mono Crater rhyolite dome chain in California. Dome is 365 m across. Figure originally shown in *Smith* [1973].

The association of large calderas and downsags with domes that display collapsed flanks is noteworthy, and suggests that the formation of these features may be related. Given the volumes occupied by the calderas and downsags, the process of magma withdrawal, whether gradual or abrupt, will induce strain in the entire structure of the dome. In both scenarios, the susceptibility of the flanks to collapse will be increased, particularly if the flanks are already particularly steep. Indeed, Type 2 and Type 4 domes display a greater mean height (1098 m based on 38 measurements) compared with Type 1 and Type 3 domes (881 m based on 56 measurements).

Large calderas and collapsed flanks may alternatively be associated in that collapse of the flanks will itself initiate explosive activity leading to the creation of a large caldera. It has been observed that flank collapse of terrestrial domes can in turn lead to decompression of the magma beneath the dome, thereby causing an explosion [*Gorshkov*, 1959; *Voight et al.*, 1981; *Fisher et al.*, 1987; *Fink and Kieffer*, 1993]. Such an explosion can result in pyroclastic flows and surges [*Walker and McBroome*, 1983; *Cas and Wright*, 1987; *Sato et al.*, 1992; *Nakada and Fujii*, 1993], but on Venus

formation of a convective plume is unlikely unless the magma volatile content, initial eruption temperature and altitude of eruption are high [*Thornhill*, 1993]. *Bulmer and Guest* [1996] interpreted 54 debris aprons surrounding modified domes to have been deposited by ground-hugging pyroclastic flows, most notably the dark deposits coating the summit regions and flanks of the two modified domes at the summit of Sapas Mons. The same collapse-generated explosive eruptions might potentially result in the collapse and widening of the summit calderas of modified domes, yet *Bulmer and Guest* [1996] argued that the formation of such deposits would more likely have required only localized volatile concentrations rather than a large explosive eruption. Furthermore, it would be expected that Type 2 domes would display volcanic flows resembling those covering the Sapas Mons domes if explosive activity had taken place during their formation, yet they are not evident. Instead, the sharply-defined rims of the calderas and absence of any raised topography around them for the Type 2 domes in Fig. 2.3 indicate that there was no outwards eruption of material associated with their formation, and that the movement of material was entirely downwards.

3.4.4 Location of modified domes on volcano flanks/summits

Domes are the only Venusian volcano category in the intermediate size category to exist on other volcanoes with any regularity: 15% of all domes exist either at the summit or on the flanks of intermediate or large volcanoes, and of those that do, 73% are modified. 24% of all modified domes exist in such an environment, but only 7% of steep-sided domes. Steep-sided domes instead tend to cluster within the plains: 29% of steep-sided exist within dome clusters as opposed to only 14% of modified domes. As large calderas are more commonly associated with modified domes, the mean caldera diameter for summit domes is 5.5 km, whereas that for domes in other environments is 3 km. The existence of domes at volcano summits has been noted in previous studies [*Bulmer and Guest*, 1996; *Stofan et al.*, 2000], but their distributional tendency towards such environments has not been explicitly highlighted. The frequent occurrence of domes on volcano summits is related to the wider issue of their emplacement mechanism and composition.

Silicic domes within the calderas of terrestrial stratovolcanoes represent potential analogues for the Venusian summit domes. The formation of many have been well-documented, recent examples being the dacitic dome at Mount St. Helens [*Swanson et*

al., 1987], the rhyolitic dome at Chaitén [*Lara*, 2009], and the andesitic dome at Soufrière Hills [*Watts et al.*, 2002]. The high viscosity of the lavas forming terrestrial domes has been attributed both to the generally high silica contents of the lavas (although dome compositions may cover the whole spectrum of silica contents) as well as to degassing of low-viscosity magma [*Fink and Anderson*, 2000]. These explanations resemble the models that *Pavri et al.* [1992] postulated to explain the morphologies of Venusian domes: a compositionally evolved magma model, where the high apparent viscosity is due to differentiation of basaltic magma to produce silicic magmas, and a basaltic bubble enhancement model, whereby the high apparent viscosity is due to the extrusion of basaltic foams following volatile enhancement in the upper part of a magma reservoir.

The validity of these models for the formation of Venusian domes has been questioned since their inception, notably by *Stofan et al.* [2000], who interpreted the apparently smooth surface textures of most steep-sided domes to be indicative of basaltic rather than silicic compositions. However, both of the models may be better disposed to explain the formation of domes at volcano summits compared with the remainder that exist in plains environments. Terrestrial silicic domes display very rough surfaces on the decimetre to metre scale; these lava textures typically result from brittle deformation, at a variety of scales, of a cooled, rigid flow exterior during emplacement. This is in contrast to basalt flows, whose smoother surface morphologies are controlled largely by ductile deformation prior to solidification [*Fink and Anderson*, 2000]. Rough surface textures at the scale of the Magellan wavelength (12 cm) and fracturing characterize Venusian summit domes to a greater extent than plains domes which led *Stofan et al.* [2000] to regard them as perhaps being more representative of evolved magma composition. This study interprets the evolved composition to derive from fractionation in the magma chamber that is the reservoir both for the dome and the volcanic edifice upon which it sits, which will be comprised of more basaltic, less viscous lava. The chemistries of the lavas comprising domes located within plains environments would instead represent the bulk chemistries of the magma reservoirs feeding the domes, and would therefore be more basaltic in composition. Regarding bubble expansion, in their examination of the two modified domes at the summit of Sapas Mons, *Bulmer and Guest* [1996] noted that the reduced atmospheric pressure at

the high elevations associated with the summits of large volcanoes would allow for greater expansion of exsolved bubbles in magmas rising in conduits.

In addition to surface roughness, Venusian summit domes appear to resemble terrestrial domes in that flank collapse is a commonly observed phenomenon for both populations. Observation of terrestrial domes has established that such collapse results from buildup of pressure beneath the cooled outer carapace of the dome, which is released as a violent explosion when the dome front collapses due to oversteepening [*Gorshkov*, 1959; *Voight et al.*, 1981; *Fisher et al.*, 1987; *Fink and Kieffer*, 1993]. This event will initiate pyroclastic flows and surges, which may travel tens of kilometres from the dome [*Walker and McBroome*, 1983; *Cas and Wright*, 1987; *Sato et al.*, 1992; *Nakada and Fujii*, 1993]. As described in section 3.4.3, *Bulmer and Guest* [1996] have identified 54 modified domes on Venus that are surrounded by debris aprons with characteristics indicative of a pyroclastic flow origin, the type examples of which are the two domes at the summit of Sapas Mons. Considering that slope oversteepening is the event that initiates such collapse and the subsequent release of pyroclastic flows, it would be expected that summit domes display greater heights than domes in plains environments, making them more vulnerable to collapse. Indeed, type 1-4 steep-sided and modified domes located on volcanoes display a mean height of 1225 m (based on 19 measurements), whereas the mean height for the same dome types located in other environments is 904 m (based on 75 measurements). The greater heights of summit domes may also imply a lower initial aspect ratio and yield strength, which would correspond to a more evolved composition [*Best*, 2003], consistent with the high surface roughness displayed by many summit domes.

In contrast to the pyroclastic events generated by dome collapse, explosive eruptions postdating or contemporaneous with dome emplacement, and which eject new material from the volcanic conduit or magma chamber beneath the volcano on which the dome is situated, may contribute to the partial or total destruction of Venusian summit domes. *Best* [2003] noted that many terrestrial domes grow in craters produced by the preceding explosive eruption of more volatile-rich magma from the top of the supply chamber (e.g. Panum Dome in the Mono Crater chain [*Smith*, 1973]), and that explosive activity may continue during effusion of the dome-forming lava. Alternation of crater dome formation with explosive eruptions that destroy them has been recorded many times at terrestrial volcanoes, e.g. those that formed at Mount St. Helens in the years 1980 to

1983 [*Swanson et al.*, 1987], Mount Pinatubo in 1991 [*Daag et al.*, 1996], and Mount Redoubt in 1991 [*Miller*, 1994]. While it would be expected for such explosive activity to be inhibited by the high atmospheric pressure experienced throughout the Venusian lowland terrain, the lower pressures existing at the summits of large volcanoes may be sufficient to allow it, particularly if the magma has an initially high volatile content [*Bulmer and Guest*, 1996].

The location of domes on volcano summits may also increase the likelihood of flank collapse based on the slope conditions that may exist in such an environment. Domes located elsewhere on Venus tend to exist in very flat plain environments, with slopes of virtually 0°. Domes existing in volcano summit regions will be emplaced on terrain that is more uneven and which displays steeper slopes; *Stofan et al.* [2001] regarded the steepest flanks of large volcanoes as having slopes of 1-3°. Because of their situation, such domes will be more susceptible to collapse in response to seismic activity after formation; the collapse of a dacite dome on the shoulder of Mount Lassen, California several hundred years after its extrusion is regarded as occurring in response to an earthquake [*Fink and Anderson*, 2000].

3.4.5 Summary

- Flank oversteepening is a significant cause of flank collapse in steep-sided domes. Steep-sided domes with aspect ratios below 120 and heights above 1800 m are regarded as being particularly susceptible to collapse, although it remains the case that many steep-sided and modified domes share similar heights and aspect ratios. The origin of the wide variety in height and aspect ratio of steep-sided domes is related to factors such as effusion rate and the range of viscosities of the lava forming the domes; lavas with higher yield strengths, and which are erupted at lower effusion rates, will form domes with smaller aspect ratios and possibly greater heights [*Best*, 2003]. Viscosity and yield strength are themselves related to parameters such as lava composition and cooling rate.
- Previous studies have reached variable conclusions regarding the composition of Venusian steep-sided domes, with compositions ranging from rhyolitic to basaltic [*Guest et al.*, 1992; *Head et al.*, 1992; *McKenzie et al.*, 1992; *Fink et al.*, 1993; *Bridges*, 1997; *Stofan et al.*, 2000]. This study hypothesizes that the summit domes of Venusian

volcanoes may represent a compositionally discrete category from domes that exist within the plains. *Stofan et al.* [2000] hypothesized that the low reflectivities of most domes on Venus implied smooth surfaces that are indicative of entrainment and annealing of surface fractures and irregularities until late in the formation of the dome. Such behavior would be consistent with a basaltic composition. Yet the generally taller heights (and lower aspect ratios) of summit domes, and their rougher and more fractured surfaces may be indicative of a more evolved lava composition that forms flows with higher yield strengths, and which form thick, rubbly crusts that cannot easily be entrained during emplacement. The flank collapse frequently displayed by summit domes may be a consequence not only of their taller heights, and therefore steeper flanks, but also of the unstable volcanic environment and slope conditions in which they are situated.

- Flank collapse is evidently also influenced by the formation of large calderas and summit downsags through withdrawal of magma during dome emplacement. Magma withdrawal is interpreted to take place as a result of the restricting pressure exerted by the weight of the dome and the yield strength of the thickening crust exceeding the upward pressure of the rising magma. The formation of a large caldera or a summit downsag is interpreted to depend on the rate of withdrawal of magma and the rheology of the dome at the time of withdrawal. Magma withdrawal is not interpreted to have occurred in domes that display no large caldera or summit downsag. The stresses inflicted on domes by magma withdrawal and the formation of large calderas and summit downsags are regarded as being influential in causing flank collapse based on the prevalence of MD2 and MD4 domes over D2 and D4 domes, and the prevalence of D1 and D3 domes over MD1 and MD3 domes.

Chapter 4
Introduction to Space- and Ground-Based Radar Sounding

4.1. Introduction

Probing the subsurface by means of radar sounding is a technique that has been used at the surface of the Earth, from aircraft, and from orbit around planetary bodies. Although the techniques and capabilities of each of these approaches differ considerably, many of the same basic principles apply. In each case, a short pulse of radio-frequency electromagnetic waves is transmitted towards the surface, a fraction of which is reflected back upwards when the waves encounter electrical boundaries. The reflected signal is recorded by the sounder and processed to create a radar profile or 'radargram' showing reflection intensity as a function of horizontal distance along-track and two-way travel time of the radio waves. The time delay of the echo can be converted to depth, provided the propagation speed of the waves in the medium is known, and the intensity of the reflection can be analysed to estimate the reflectivity at the interface and the attenuation properties of the intervening layers [*Picardi et al.*, 1998]. While this method allows the mapping of subsurface dielectric discontinuities, it does not always provide precise indications of their nature – knowledge regarding the geological environment of the location in question may be required as well. The aim of this section is to explain some of the basic theory regarding radar subsurface sounding and define terms that will be used throughout chapters 5, 6 and 7, introduce the MARSIS instrument itself, and describe the process of fieldwork and data collection using ground-penetrating radar.

4.2. Theory of radar sounding

4.2.1 Reflectivity and attenuation of radar signals from surface and subsurface interfaces

The success of radar sounding is dependent on the fact that different geological facies, which will generally have different compositions, will create dielectric contrast boundaries in the subsurface that will reflect the transmitted electromagnetic waves encountering them. The specific electrical parameter that defines the scale of the dielectric contrast is the relative static permittivity, more commonly referred to as the

dielectric constant (ε_r). This is defined as the ratio of the static permittivity of the material (ε_s, which describes a material's ability to transmit an electric field, and is measured in farads per metre, F m^{-1}) relative to the static permittivity of a vacuum (ε_0) (which by definition has a value of 1) under given conditions:

$$\varepsilon_r = \frac{\varepsilon_s}{\varepsilon_0} \tag{4.1}$$

Being a ratio, the dielectric constant is dimensionless. Materials forming planetary crusts will generally display some degree of porosity, with a volatile material or a vacuum filling the pore space. Dielectric constant values for various host materials and pore-filling materials that may be expected in planetary crusts are shown in Table 4.1.

Table 4.1. Typical range of dielectric constants of various materials expected to be encountered in planetary crusts [*Picardi et al.*, 1998].

Material type	**Material**	**Dielectric constant, ε_r**	**Loss tangent, tan δ**
Pore-filling	Vacuum/Air	1	0
	Freshwater (20°C)	88	0.0001
	Brine (20°C)	50-70	0.5-1.0
	Ice	3.15	0.00022
Host	Dry basalt	7.1	0.017
	Dry andesite	3.5	0.005

A planetary crust will exhibit a decrease in porosity with depth, eventually leading to the self-compaction depth (that at which the crustal porosity falls below 1%). The porosity, φ, at depth z is described as:

$$\varphi(z) = \varphi(0)e^{-z/K} \tag{4.2}$$

where K is the decay constant, and $\varphi(0)$ is the porosity at the surface [*Binder and Lange*, 1980]. Assuming that the crustal porosity is a function only of depth according to Eq. 4.2, and using the dielectric constants of the selected materials, a host-inclusion mixture model may be used to describe the dielectric constant of a solid/pore-filling mixture (ε_m) at depth z, such that:

$$\varepsilon_m(z) = \varepsilon_h \frac{1+2\varphi(z)y}{1-\varphi(z)y} \tag{4.3}$$

where:

$$y = \frac{\varepsilon_i - \varepsilon_h}{\varepsilon_i + 2\varepsilon_h} \tag{4.4}$$

where ε_h is the dielectric constant of the host material and ε_i is the dielectric constant of the pore-filling material [*Picardi et al.*, 2004]. The scenario of a host-inclusion mixture is particularly relevant when considering the potential for the existence of subsurface icy layers and aquifers on Mars.

As opposed to the response of a vacuum, the response of normal materials to external fields generally depends on the frequency of the field. For this reason permittivity (and by analogy the dielectric constant) is often treated as a complex function of the frequency of the applied field (f) such that ε_r is represented as $\hat{\varepsilon}(f)$. The complex permittivity is divided into real and imaginary parts, with the real part (ε') being related to the stored energy within the medium and the imaginary part (ε'') being related to the dissipation of energy within the medium:

$$\hat{\varepsilon}(f) = \varepsilon'(f) + i\varepsilon''(f) \tag{4.5}$$

where i is the imaginary unit ($i^2 = -1$). The complex permittivity relates the dielectric constant to the loss tangent ($\tan\delta$), a parameter of a dielectric material that quantifies its inherent dissipation of electromagnetic energy. The loss tangent is defined by the following equation [*Ramo et al.*, 1994]:

$$\tan\delta = \frac{\varepsilon''+\sigma}{\varepsilon'} \tag{4.6}$$

where σ is the electrical conductivity (in siemens per metre, S m^{-1}).

Figure 4.1 displays the scenario that applies to the following formulae: two dielectrically contrasting layers characterize the upper portions of a planetary crust, one overlying the other, with each layer being dielectrically homogeneous throughout. A fraction of the electromagnetic energy transmitted by a radar sounder towards the surface is reflected from the surface back to the sounder, with a fraction of the

remaining energy being reflected from the subsurface dielectric contrast interface (at depth *z*', in m) back to the sounder. A larger contrast in the dielectric constant between the surface and subsurface layers will result in a greater fraction of the electromagnetic energy being reflected from the interface compared with if the difference was small. The intensity of the reflection from this subsurface interface may therefore be used to ultimately derive the dielectric constants of the surface and subsurface layers.

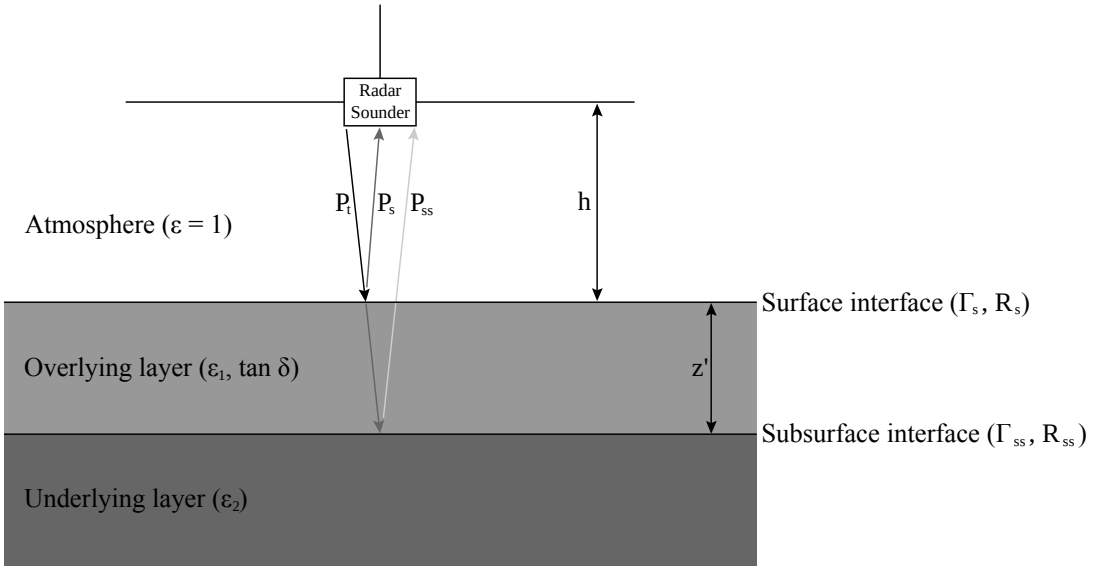

Figure 4.1. Schematic depicting a scenario whereby a radar sounder detects surface and subsurface reflections for two layers of varying bulk dielectric constants within a planetary crust. Relevant parameters relating to properties of the crust and the radar transmissions are included, and which are defined in the text.

For a particular reflection, the power returned to the radar sounder from the interface (*P*, in Watts), and the peak effective transmitter power of the radar sounder antenna (P_t) will be known, in addition to the antenna gain (*G*), the wavelength of the transmitted radio waves (λ, in m), and the altitude of the radar sounder (*h*, in m). They may be used to calculate the Fresnel reflectivity of an interface, Γ (in dB, which describes the intensity of an echo from a dielectric contrast interface relative to the intensity of the transmitted signal), and, in the case of a reflection from a subsurface interface, the loss tangent of the overlying layer, tan δ. In the case of a reflection from the surface [*Porcello et al.*, 1974]:

$$P_s = P_t \left(\frac{G\lambda}{8\pi h} \right)^2 \Gamma_s \tag{4.7}$$

In the case of a reflection from a subsurface interface [*Porcello et al.*, 1974]:

$$P_{ss} = P_t\left(\frac{G\lambda}{8\pi(h+z')}\right)^2 (1-R_s^2)^2 R_{ss}^2 \cdot 10^{-2.74\tau f \tan\delta} \tag{4.8}$$

$$R_{ss}^2 = \left|\frac{\sqrt{\varepsilon_1}-\sqrt{\varepsilon_2}}{\sqrt{\varepsilon_1}+\sqrt{\varepsilon_2}}\right|^2 \tag{4.9}$$

The Fresnel reflectivities and reflectivity coefficients of the surface and subsurface interfaces are related to the dielectric constants of the underlying and overlying layers as follows:

$$\Gamma_s = R_s^2 = \left|\frac{\sqrt{\varepsilon_1}-1}{\sqrt{\varepsilon_1}+1}\right|^2 \tag{4.10}$$

$$\Gamma_{ss} = R_{ss}^2 (1-\Gamma_s)^2 10^{-0.1\int_0^{z'}\alpha(z)dz} \tag{4.11}$$

where P_s and P_{ss} are the powers of the reflected energy from the surface and subsurface interfaces respectively, Γ_s and Γ_{ss} are the Fresnel reflectivities of the surface and subsurface interfaces respectively, R_s and R_{ss} are the dimensionless reflectivity coefficients of the surface and subsurface interfaces respectively, ε_1 and ε_2 are the dielectric constants of the overlying and underlying layers respectively, τ is the two-way time delay between the surface and subsurface reflections (in s), f is the frequency of the transmitted radio waves (in Hz), and α is the two-way wave attenuation due to dielectric dissipation in the overlying layer, (in dBm^{-1}) [*Picardi et al.*, 2004].

The loss tangent may be used to assess the value of α at a relevant depth, z:

$$\alpha(z) = 1.8\times10^{-7} f_0 \sqrt{\varepsilon(z)} \tan\delta(z) \tag{4.12}$$

where f_0 is the frequency of the transmitted radio waves in a vacuum (in Hz), $\varepsilon(z)$ is the dielectric constant of the material at depth z, and tan $\delta(z)$ is the loss tangent of the material at depth z [*Picardi et al.*, 2004].

The depth to the subsurface interface, z', may be calculated as follows:

$$z' = \frac{\pi c}{2\sqrt{\varepsilon_1}} \tag{4.13}$$

where c is the speed of light in a vacuum (299,792,458 ms^{-1}).

Equations 4.5 to 4.11 represent the basic formulae required to infer the electrical properties of crustal layers whose boundaries are detected by a radar sounder. However, these formulae are based solely on the effects of the intrinsic electrical properties of the layers on the radar pulse. Sections 4.2.2 and 4.2.3 detail the quantification of the scattering of the radio waves by surface roughness and crustal heterogeneity, which must also be considered when inferring properties of the layers based on the strengths of received signals.

4.2.2 The effect of off-nadir surface backscatter on interface detection

Sounding radars that transmit radio signals to the surface from a height above it will not only transmit nadir-oriented signals to the surface, but off-nadir signals as well. Off-nadir waves will also reflect from the surface, and some will reflect such that they are returned to the radar sounder. Due to the orbital sounding geometry, off-nadir surface returns or 'clutter' might be received at the same time as are subsurface echoes; the echoes reflected from a rough surface will therefore reduce the visibility of the subsurface echoes, and may potentially totally eclipse them. As the surface becomes smoother, the return echoes from off-nadir angles will decrease [*Picardi et al.*, 2004].

In order to detect a subsurface interface, the backscattering cross-sections of concurrent echoes coming both from the surface and subsurface interfaces must be evaluated. *Picardi et al.* [2004] evaluate surface backscattering by considering two main contributions: the large-scale scattering, resulting from gentle surface undulations on a scale of many hundreds to thousands of metres, and the small-scale scattering, resulting from slight variations of the surface height over a horizontal scale of tenths of metres. The surfaces in both models have an associated root mean square (rms) slope, $s(\lambda)$ (in radians), which is an estimate of the slope distribution of the surface extrapolated at a scale equal to the wavelength of the transmitted signals; rougher slopes will have higher rms slope values. For each model, the surface backscattering coefficient, σ_0 (in dB), may be calculated for a particular radar signal incidence angle, θ

(in radians), by taking into account the Hagfors backscattering model [*Biccari et al.*, 2001]:

$$\sigma_0 = \Gamma_s \frac{C}{2} \left(\cos^4 \theta + C \sin^2 \theta \right)^{-3/2} \tag{4.14}$$

where C is calculated as follows:

$$C = \frac{1}{(2\pi)^2 s^4 (\lambda)} \tag{4.15}$$

For a particular equivalent depth, r (in metres), of the off-nadir surface waves, the value of σ_0 will dictate the minimum subsurface signal strength, Γ_{ss}, required for the subsurface interface to be detected. r is related to the incidence angle as follows:

$$r = \frac{h}{\sqrt{\varepsilon_1} \sin \theta} \tag{4.16}$$

4.2.3 The effect of volume scattering on the passage of radar signals

In addition to attenuation of the radar signals via electromagnetic losses within the crust, attenuation may also occur via volume scattering. Volume scattering involves the dispersion of the radar signals by physical heterogeneities within the crust, in particular fracturing. Volume scattering within planetary crusts such as those of the Moon and Mars is expected to be particularly high as a result of the extensive fracturing and brecciation that exists within the crusts, which dates from the early history of these bodies.

Quantification of volume scattering has been attempted for terrestrial lava flow environments, notably in the study of *Heggy et al.* [2006a], which involved performing ground-penetrating radar surveys on volcanic features at the Craters of the Moon volcanic field in Idaho to investigate firsthand the penetration of radio waves in mafic environments, which will be discussed in further detail in Chapter 6. *Heggy et al.* [2006a] combined the results of the survey with laboratory measurements of field-collected samples in order to isolate the electromagnetic attenuation and volume

scattering losses from the total losses, thereby allowing quantification of both the effects on radar penetration depth.

For GPR penetration through the flank of a scoria cone, *Heggy et al.* [2006a] determined the theoretical electromagnetic attenuation and associated theoretical penetration depth experimentally from the collected samples. The observed penetration depth and attenuation were calculated using the radar profiles obtained from the radar survey. In all cases, the theoretical losses were less than the observed losses, and the theoretical penetration depth was greater than the observed penetration depth, the difference being the volume scattering contribution. The difference was seen to increase with increasing frequency due to the greater potential for volume scattering mechanisms to dominate as the wavelength decreases. *Heggy et al.* [2006a] concluded that for frequencies less than 114 MHz, electromagnetic attenuation dominated the signal losses, whereas for frequencies greater than 114 MHz, volume scattering dominated the signal losses. This critical frequency mainly varies as a function of the subsurface geoelectrical and geometrical properties (i.e. layering, interface roughness, etc.). The results of *Heggy et al.* [2006a] indicate that for sounding radar operating at MARSIS frequencies, volume scattering may induce losses that reach 15% to 20% of the total attenuation.

Given that a precise geometrical description of the subsurface heterogeneity for bodies such as Mars and the Moon does not exist (and such a description will be site specific), the volume scattering cannot easily be estimated for their entire crusts. *Heggy et al.* [2006a] advised that their loss value estimates for the scoria cone should not be considered as fully representative of the expected values of all types of terrestrial and planetary terrains. The extensive cratering experienced by the surfaces of Mars and the Moon would imply a significantly brecciated crust, which would have an increased heterogeneity relative to most terrestrial terrains, and which would increase the effect of volumetric scattering.

4.2.4 The penetration depth of a radar sounder

Eq. 4.8 indicates that the power of a signal reflected from an interface is inversely proportional to the signal frequency; lower frequencies will result in a higher fraction of the peak transmitter power being returned to the radar sounder from the interface. The study of *Heggy et al.* [2006a] stated that the radar penetration depth for a given

frequency is constrained by the total signal loss affecting the radar wave during its propagation through the subsurface. Total signal loss can be summarised as the sum of individual losses from ground coupling (i.e. surface scattering behaviour), geometrical spreading, electromagnetic attenuation and volume scattering [*Reynolds*, 1997].

In order for the round-trip attenuation not to entirely absorb a signal reflected from a subsurface interface, and for the radar sounder to detect the echo, the dielectric contrast characterizing an interface separating dielectrically distinct layers must be great enough to reflect a sufficient proportion of the energy. A radar sounder will be able to detect a subsurface interface with a strong dielectric contrast at a greater depth than an interface with a lesser contrast, as a higher proportion of the incident energy will be reflected for the former case.

In addition to the physical properties of the crust itself, the detection of a subsurface interface will also rely on the dynamic range of the radar sounder (i.e. the range of reflected powers detectable by the sounder, measured relative to the peak transmitter power) not being reduced by factors such as system thermal noise and galactic background. The penetration depth can therefore be defined for an interface of a particular dielectric contrast as the threshold depth at which the combined factors of crustal electromagnetic attenuation and volume scattering, off-nadir surface clutter, and intrinsic system constraints are sufficient to attenuate the signal and reduce the dynamic range of the radar sounder such that no reflected signal is detected by the sounder.

4.3 The MARSIS instrument

MARSIS (the Mars Advanced Radar for Subsurface and Ionospheric Sounding) is an instrument on board the European Space Agency's Mars Express satellite. It is a multi-frequency, synthetic-aperture, nadir-looking, orbital sounding radar and altimeter (*Picardi et al.*, 1998). Its primary objective, as described in the original instrument proposal by *Picardi et al.* [1998], is to map the distribution of water, both liquid and solid, in the upper portions of the Martian crust. Secondary objectives include determination of the thicknesses and properties of sedimentary units and the polar layered deposits.

MARSIS consists of two antenna assemblies and an electronics assembly (Fig. 4.2). The first antenna assembly consists of a 40-metre long primary dipole antenna, parallel to the surface and perpendicular to the direction of motion, used to transmit the radio

signals and receive echoes reflected by the Martian surface and subsurface. The second assembly comprises a 5-metre long secondary monopole antenna, oriented along the nadir, used to receive only off-nadir surface returns. In its subsurface modes, MARSIS operates in four frequency bands centred at 1.9, 2.8, 3.8 and 4.8 MHz, each with a 1 MHz instantaneous bandwidth, giving a total frequency range of 1.4 to 5.3 MHz in its subsurface modes. Viewing the same profile at a range of frequencies will allow features at great depth to be resolved (at low frequencies) as well as shallow features to be seen in high resolution (at high frequencies). On the dayside of Mars, ionospheric interference does not allow the use of frequencies less than around 3.5 MHz. Subsurface operations of MARSIS are therefore constricted to the nightside of Mars. MARSIS obtains data via generating and transmitting a 'chirp' signal by the primary antenna at each operating frequency for a period of about 500 microseconds. The instrument then switches to receive mode and records the echoes from the surface and subsurface for the expected duration. The whole process lasts on the order of a few milliseconds, depending on the altitude. Data are collected when the elliptical orbit of Mars Express brings the spacecraft to an altitude of 250 to 800 km above the surface.

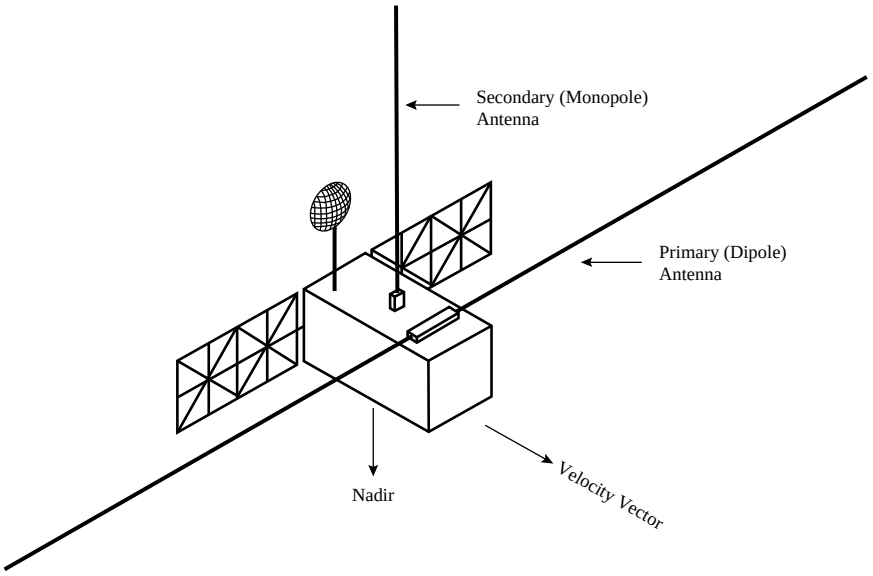

Figure 4.2. MARSIS deployment configuration. Schematic originally shown in *Picardi et al.* [1998].

Lateral spatial resolution depends on surface roughness characteristics, but for most Mars surfaces, the cross-track footprint is 15 to 30 km and the along-track footprint, narrowed by onboard synthetic-aperture processing, is 5 to 10 km. The nominal vertical (depth) resolution of MARSIS in the subsurface is about 50 to 100 m for the expected

materials, depending on the wave propagation speed. MARSIS has a peak transmitter power of 1.5 to 5 W with an estimated dynamic range of 40 to 50 dB [*Jordan et al.*, 2009].

MARSIS transmits signals with a wide beam, meaning that echoes are often received from off-nadir surface reflectors. The nadir-pointing monopole was designed to record off-nadir reflections in order that they could be cancelled from the radargrams, but it malfunctioned at the beginning of data collection and has not been operational for the entire mission. MARSIS data are therefore susceptible to clutter from off-nadir topography and possibly off-nadir subsurface structure. The potential for whether or not apparently 'subsurface' reflections are originating from off-nadir topography can be determined by creating ground-range projections, which model the time-delays at which off-nadir reflections should appear in a MARSIS radargram based on knowledge of the path of the spacecraft groundtrack and the topography from Digital Terrain Models. Reflections that appear at identical locations and time-delays in both modelled and observed radargrams will be originating from off-nadir surface topography.

The Martian ionosphere may attenuate, delay and disperse MARSIS echoes by magnitudes depending on the free electron density in the column directly beneath the spacecraft [*Safaeinili et al.*, 2007]. The dispersion is due to the frequency dependence of the radio wave propagation speed in the ionosphere [*Budden*, 1985]; the 1 MHz bandwidth of each MARSIS frequency band means that wave speeds may vary significantly for frequencies at opposite extremes of the bandwidth, creating serious dispersion and severely compromising interpretability of the data. Unlike attenuation, which causes a reduction in signal to noise ratio and is irreversible, the dispersion and the delay are generally reversible and are corrected during MARSIS ground data processing [*Safaeinili et al.*, 2007].

4.4 Ground-Penetrating Radar

In contrast to orbiting, low-frequency radar sounders such as MARSIS that produce deeply penetrating radar profiles reaching several hundred kilometres in length, ground-penetrating radar (GPR) is a ground-based geophysical technique that transmits higher frequency signals to produce near continuous, higher resolution profiles of the shallow subsurface across much smaller distances (typically metres to several hundred metres) [*Jol and Bristow*, 2003]. In the case of the GPR used in the Icelandic fieldwork as

described in Chapter 7, the antennas are handheld and are in contact with the ground when the electromagnetic pulse is transmitted into the ground. One of the antennas transmits a pulse, which is reflected back to the surface from interfaces between materials having different dielectric properties, which in terrestrial rocks are often due to changes in water content associated with various sediment types, grain size, porosity and compaction [*Jol and Bristow*, 2003]. The amplitude of the returning energy is proportional to the relative permittivity contrasts in the shallow subsurface. The return pulse is collected by a second, matched receiving antenna and is recorded as a function of two-way travel time.

In order to construct a radar profile, the transmitting and receiving antennas are separated by a constant distance, and are moved in constant increments along a survey line across the relevant field location, with a measurement being taken at each increment. The data are transferred through a processing station via optic cables and stored on a laptop, which are carried along the survey line behind the antennas (see Fig. 4.3).

Figure 4.3. Configuration of the GPR setup during surveying. The box containing the car battery, processing station, and laptop is in the foreground. This is connected via optic fibre cables to the transmitter and receiver antennas being moved in constant increments along the survey line in the background.

As with radar sounding from orbit, the aim of the GPR survey is to detect the dielectric contrast boundaries between different rock facies. However, in radar

sounding profiles such as those recorded by MARSIS, the dielectric contrast manifests itself as a single reflection. In GPR profiles, a boundary might manifest itself in the form of a strong, continuous reflection separating two facies, or more subtly in that it is not defined by a specific reflection, but instead by a change in the patterns of reflections characterizing different 'radar facies' that represent different rock facies. These are defined as mappable, three-dimensional sedimentary units comprised of reflections whose parameters differ from adjacent units [*Jol and Bristow*, 2003].

Each radar profile features an 'air wave' and 'ground wave', with the air wave appearing immediately above the ground wave at the top of each profile. The air wave represents the direct transmission of the pulse from the transmitter to the receiver through the air at the speed of light, whereas the ground wave represents the transmission of the pulse from the transmitter to the receiver through the ground (at a lower velocity, hence it arrives slightly later). The surface is located at the point of inception of the air wave. Each reflection is comprised of a waveform with a crest (white) that arrives first, and trough (black) that arrives afterwards. The exact location of the boundary between the layers of different dielectric constants that are causing the reflection is at the point where the waveform is initiated, i.e. at the point where the crest begins.

By measuring the velocity of the radio waves in the ground, the two-way travel time to the boundaries can be converted to depth. This is accomplished using a common mid-point survey: the two antennas are positioned at the same distance on either side of the midpoint of the survey line and are moved further apart in constant increments until they reach a few tens of metres apart, at which point the survey is terminated. This produces a graph of antenna separation plotted against pulse travel time, with the ground wave represented by a steeply dipping line on the graph. The gradient of this line represents the velocity of the pulse in the ground at the surface in the field locality.

Chapter 5
Interpretation of Reflections Observed by MARSIS

5.1 Introduction

MARSIS has been operational for more than four years since June 2005, during which time it has obtained global coverage of the Martian subsurface in at least one of four frequency bands. As a consequence of its polar orbit, coverage over the polar regions is dense whereas that over the equatorial regions is sparser. Several thousand individual radargrams have been obtained, yet the data quality varies considerably within the dataset due to interference from the ionosphere. Despite the extensive coverage, subsurface reflections are seen in a relatively restricted range of geological environments across the planet. These environments are as follows, and are displayed in the map in Fig. 5.1:

- The north and south polar layered deposits.
- The Medusae Fossae Formation, located on the equator at the hemispheric dichotomy which borders the southern margin of Amazonis Planitia.
- The Dorsa Argentea Formation, located at 78°S, 327°E which borders the south polar layered deposits.

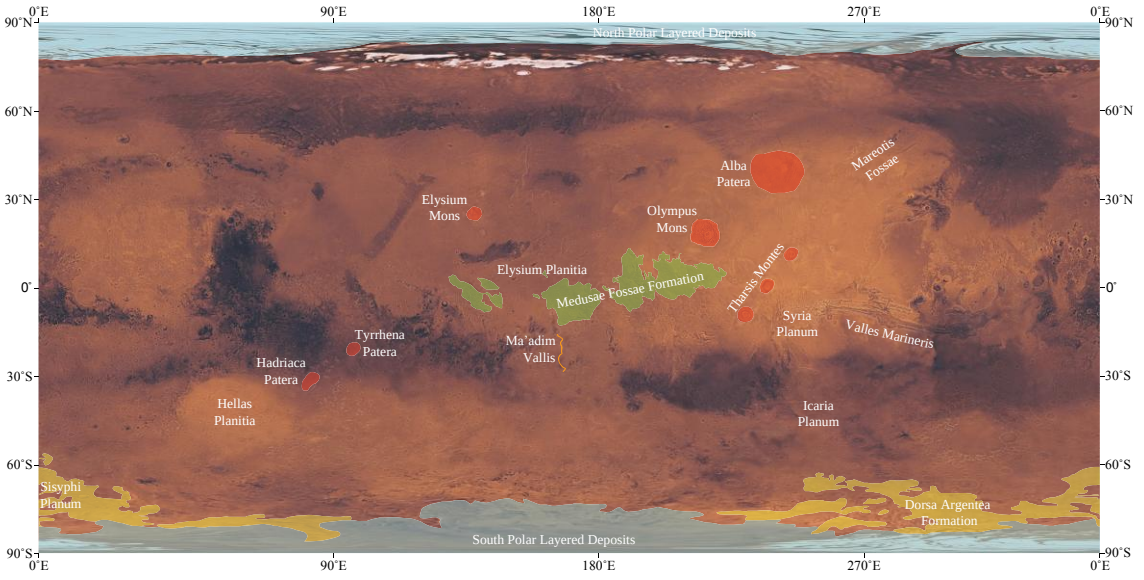

Figure 5.1. Viking Mars Digital Colour Image Map showing the locations of the various geological units that display subsurface reflections in MARSIS data: the North and South Polar Layered Deposits (in blue), the Dorsa Argentea Formation (in yellow), and the Medusae Fossae Formation (in green). Major topographic features as well as those that are of relevance to both this chapter and later chapters are also highlighted, including volcanic edifices (in red) and Ma'adim Vallis (in orange).

The first two of these environments are characterised by thick, laterally extensive deposits emplaced on flat plains; this allows the approximate thickness of the deposits to be estimated from their vertical relief above the surrounding plains, which allows the dielectric constant of the material comprising the deposits to be calculated using the time delay and strength of the basal reflection. The third environment displays deposits that are not emplaced on planar terrain, and whose thickness cannot therefore be gauged from remote sensing-based altimetry measurements.

Outside of these locations, radargrams either display no reflections or reflections whose authenticity is suspect, i.e. they display eccentric morphologies that cannot readily be linked to the geomorphological environment in which they occur and so may be originating due to factors other than subsurface heterogeneity, e.g. ionospheric interference. These reflections often take the form of very laterally extensive parabolas, sometimes reaching several hundred kilometres, that also extend to very deep time delays. Notable examples include the several that occur within the northern plains and a dense cluster located to the west of Ma'adim Vallis. Yet most importantly, MARSIS has not detected any deep, consistent reflections suggestive of a deep aquifer or an ice-rich layer; this aspect of MARSIS data will be discussed in Chapter 6.

This chapter aims to determine why MARSIS reflections are seen where they are. The characteristics of the various groups of reflections recorded by MARSIS are described and their implications for the geological and physical properties of the surface deposits that they represent are interpreted. Most of the reflection groups that are known to be caused by subsurface interfaces have been the subject of previous studies. However, this chapter will also describe and interpret MARSIS reflections whose morphological characteristics and distribution lend a strong ambiguity to their origin; particular attention is focused on the cluster of reflections seen in the Ma'adim Vallis region.

5.2 Review of echoes observed by MARSIS to date

The reflections discussed in this section have been the subject of previous studies. The observations and conclusions of these studies are summarized for each locality where reflections have been observed.

5.2.1 The Polar Layered Deposits

The Amazonian polar layered deposits (PLD) are found at both poles and are similar in gross morphology and thickness [*Smith et al.*, 2001]. They are roughly domical in shape, are about 1000 km across, and have a maximum relief above the surrounding terrain of about 3.5 km. They consist of dozens of layers of contrasting albedo, thought to be caused by varying mixtures of ice and dust [*Plaut et al.*, 2007a]; it has been estimated that a small fraction of dust (<10%) is needed to lower the albedo of pure ice to the observed levels [*Kieffer*, 1990]. Figure 5.2 shows a HiRISE image of the PLD.

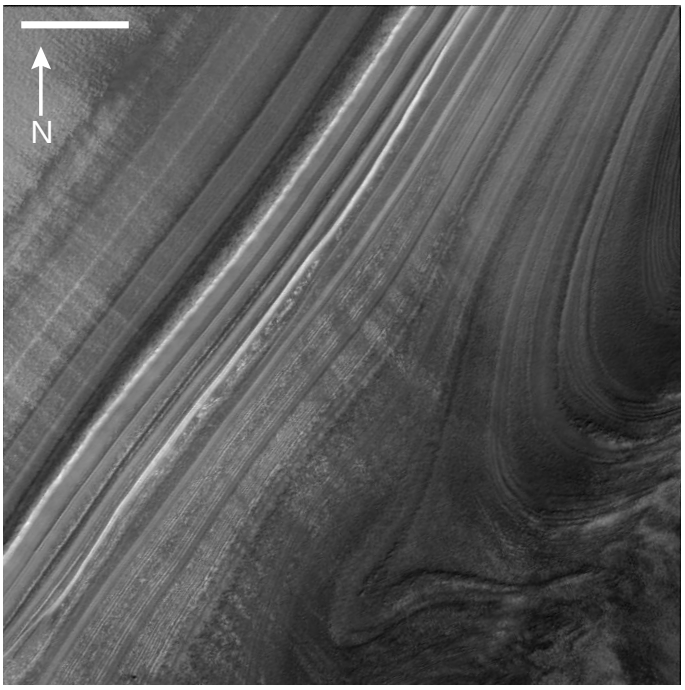

Figure 5.2. HiRISE image PSP_001332_2620 showing an exposure of polar layered deposits with an angular unconformity. The alternating light and dark banding represents separate layers with varying concentrations of ice and dust trapped within them. Image is centred at 81.8°N, 48.8°E. Scale bar measures 1 km. Scene is illuminated from the bottom of the image.

These deposits have been mapped at a high areal resolution by MARSIS due to the polar orbit of Mars Express. A typical example of a MARSIS radargram over the south polar layered deposits (SPLD) is shown in Fig. 5.3, accompanied by the groundtrack superimposed on Mars Orbiter Laser Altimeter (MOLA) topography. Surface and subsurface reflections are apparent, the subsurface reflection representing the boundary between the base of the ice-rich SPLD materials and the predominantly lithic substrate [*Plaut et al.*, 2007a]. This interface is very apparent on the left-hand side of the radargram, although on the right-hand side it becomes discontinuous, indistinct and even absent. A pattern of continuous, bright bands alternating with lower reflectivity

bands commonly occurs between the surface and basal reflections in the radargrams [*Plaut et al.*, 2007a]. These may correspond to boundaries between major packages of layering within the deposits [*Putzig et al.*, 2007].

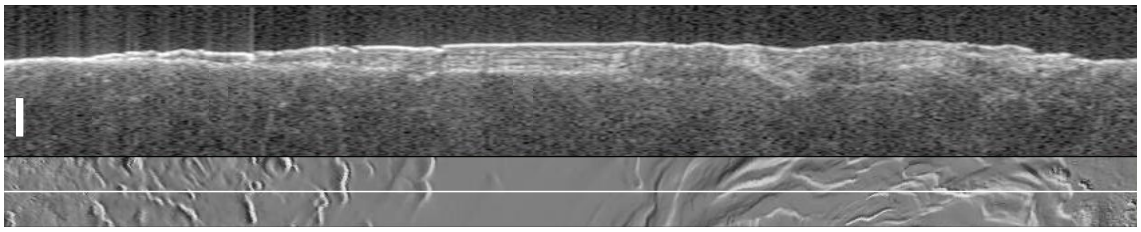

Figure 5.3. Portions of MARSIS radargrams 2753 obtained at a central frequency of 4 MHz over the south polar layered deposits. The corresponding groundtrack is shown on a shaded relief map (which has a width of 100 km) beneath the radargram. White, vertical bar represents 25 μs one-way travel time.

Where the basal reflection is strongest, the attenuation of the radio waves by the PLD is very low; if the material is assumed to be 'dirty' water ice overlying a basaltic substrate, the loss tangent ranges between 0.001 and 0.005 for the SPLD material, corresponding to water ice with a dust contamination of 0 to 10% [*Heggy et al.*, 2006b]. The low attenuation is also consistent with a very low temperature of the ice. The study of *Zhang et al.* [2008] estimated that the dielectric constant of the SPLD ranges from 3 to 5, whereas the basaltic substrate has a dielectric constant value ranging from 7.5 to 8.5.

Plaut et al. [2007a] mapped the thickness of the SPLD by subtracting the elevations of the interpolated basal topography from the high-resolution MOLA surface topography. The thickness map shows an asymmetric distribution, with the maximum measured thickness of the deposits (3.7 ± 0.4 km) occurring at the polar cap. It was estimated that the integrated volume of the entire SPLD is $1.6 \pm 0.2 \times 10^6$ km^3, translating to an equivalent global water layer thickness of 11 ± 1.4 m (assuming an SPLD composition of nearly pure ice). While a corresponding map for the NPLD has not yet been published, MARSIS observations of the base of the NPLD suggests that their volume will be similar to that of the SPLD.

5.2.2 The Dorsa Argentea Formation

The Hesperian Dorsa Argentea Formation (DAF) borders the SPLD, with its centre located at 78°S, 327°E. The DAF has a notably lower crater density than the Noachian cratered plains that characterise much of the southern Martian hemisphere, and displays enigmatic landforms such as heavily pitted materials and sinuous ridges [*Plaut et al.*, 2007b]. Figure 5.4 shows a HiRISE image of the DAF.

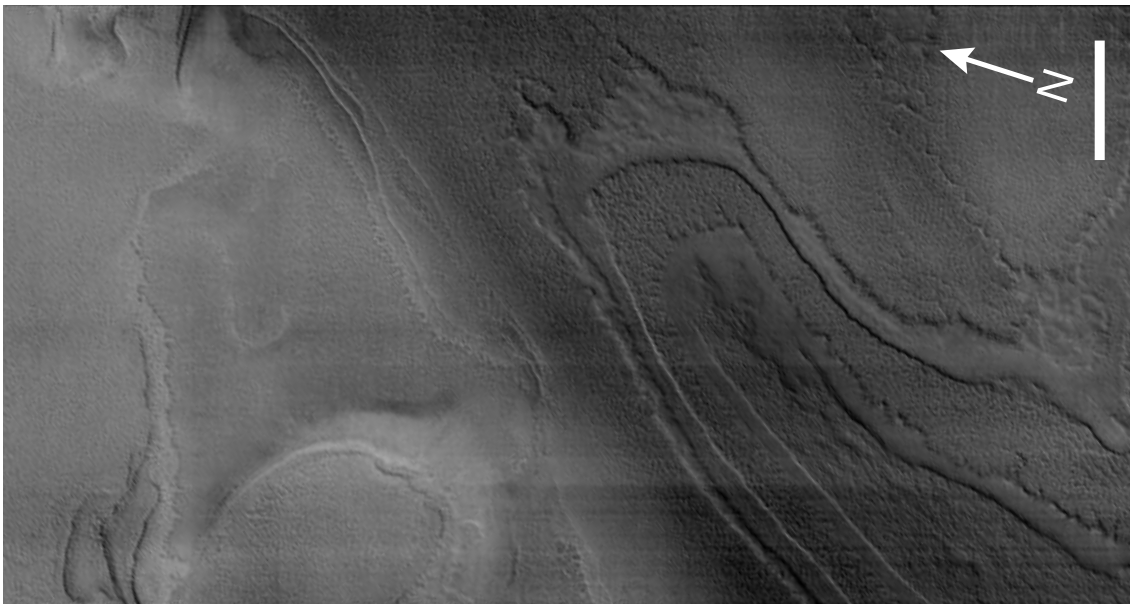

Figure 5.4. HiRISE image PSP_004670_0990 showing a sinuous ridge in the Dorsa Argentea Formation. Image is centred at 80.7°S, 54.6°E. Scale bar measures 1 km. Scene is illuminated from the bottom of the image.

Suggested origins for the DAF include volcanism, aeolian deposition [*Tanaka and Scott*, 1987; *Plaut et al.*, 1988], debris flows [*Tanaka and Kolb*, 2001], and glacial and subglacial activity [*Kargel and Strom*, 1992; *Head and Pratt*, 2001; *Milkovich et al.*, 2002; *Ghatan and Head*, 2004]. In MARSIS radargrams, interfaces are seen beneath the surface of the DAF that extend across a wide area of the south polar region (sometimes reaching as far as 1000 km from the margins of the SPLD) and which have time delays extending to ~10 μs (see Fig. 5.5) [*Plaut et al.*, 2007b]. Unlike the PLD, the DAF displays no positive relief above the surrounding terrain, meaning that there are no topography measurements which can be used to calibrate the depth to the interface. In order to estimate the depth to the interface, *Plaut et al.* [2007b] assumed that the material above the interface consisted of a mixture of ice and lithic material (i.e. basalt), based on the fact that the DAF is located in a polar region, with a relatively ice-poor

substrate beneath. The different dielectric constants of the two constituent materials mean that the velocity of the radio waves through the DAF (and hence the estimated depth to the interface) depends on the proportions of the two materials in the DAF. *Plaut et al.* [2007b] estimated the interface seen in Fig. 5.5 to be between 600 and 900 m deep, with the latter value corresponding to an ice-rich mixture. The depth of the reflector varies from a few hundred metres to more than a kilometre across the DAF. The echo strength of the interface is consistent with a high ice content, yet the exact origin of the DAF is still somewhat obscure; *Plaut et al.* [2007b] hypothesised that the present formation (including the ice) may be a sedimentary deposit from the original deposition of the DAF due to its eroded and subdued appearance.

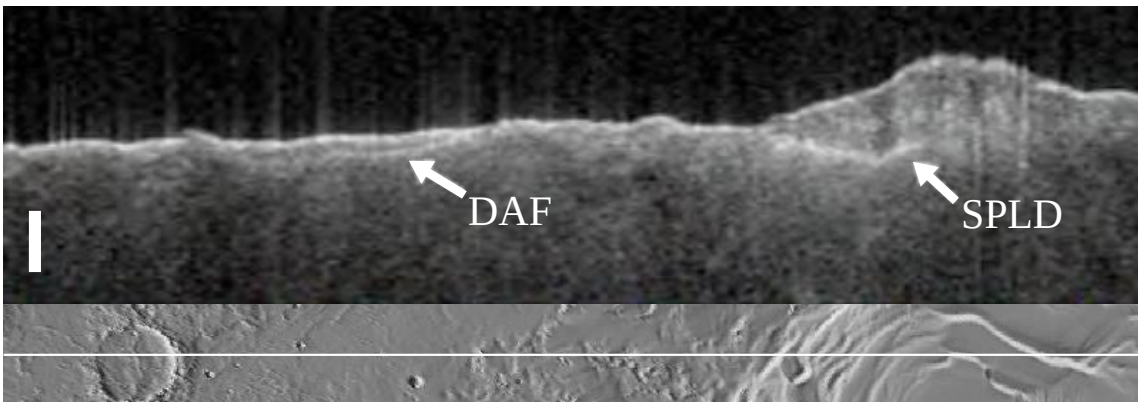

Figure 5.5. A portion of MARSIS radargram 2638, obtained at a central frequency of 4 MHz over the Dorsa Argentea Formation. The corresponding groundtrack is shown on a shaded relief map (which has a width of 100 km) beneath the radargram. North is at the right end of the radargram. White, vertical bar represents 25 μs one-way travel time.

5.2.3 The Medusae Fossae Formation

The Medusae Fossae Formation (MFF) occurs discontinuously at equatorial latitudes along the boundary of the hemispheric dichotomy from Amazonis to Elysium Planitia (~130°E to 240°E). The MFF is interpreted to comprise some of the youngest surficial deposits on Mars, unconformably overlying ancient Noachian heavily cratered highlands and young Amazonian lowlands [*Watters et al.*, 2007]. The configuration of deposits resting on flat plains makes them resemble the PLD in the sense that their thickness is the same as their topographic relief above the surrounding plains – in the case of the MFF, about 3.5 km at the greatest [*Head and Kreslavsky*, 2004]. Over large horizontal scales the deposits comprise undulating hills that appear to be relatively smooth, yet at smaller scales, systems of parallel ridges and grooves interpreted as yardangs are resolvable [*Scott and Tanaka*, 1982]. Figure 5.6 shows a THEMIS image

of such features. Remnant yardangs and outliers exist some distance from the thicker units, suggesting that the MFF deposits once covered a larger area of the northern lowlands [*Bradley et al.*, 2002; *Hynek et al.*, 2003]. Layering at various scales has been observed within the MFF deposits [*Bradley et al.*, 2002; *Hynek et al.*, 2003].

Proposed origins for the MFF include ignimbrite or volcanic ash deposits from now-buried vents [*Hynek et al.*, 2003], aeolian deposits from materials weathered early in Martian history [*Carr*, 1996], and deposits analogous to polar layered and circumpolar layered deposits formed as a consequence of polar wandering [*Schultz and Lutz*, 1988] or during periods of high obliquity [*Head and Kreslavsky*, 2004].

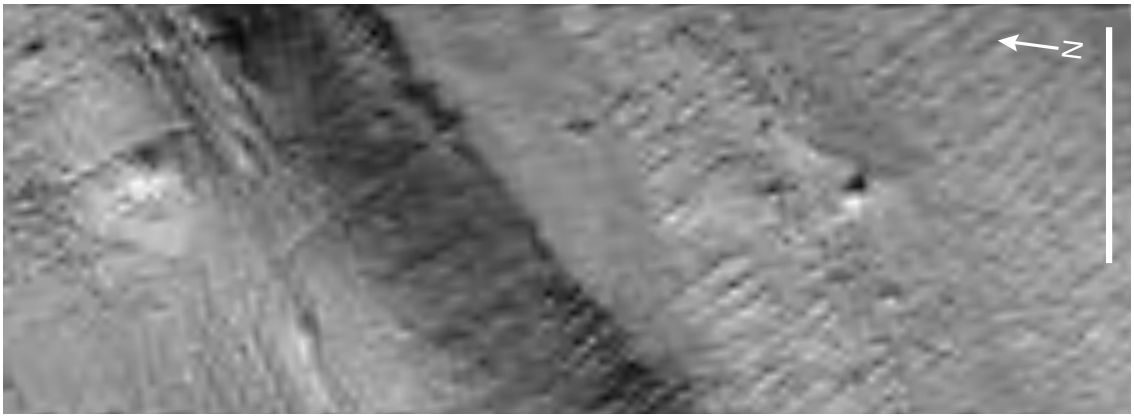

Figure 5.6. THEMIS visible image V13163010 showing Medusae Fossae Formation (MFF) material in Elysium Planitia. The MFF material appears to be in the process of being stripped away, partially exposing the lowlands plains beneath. Numerous yardangs have formed within the deflated MFF material. Scale bar measures 10 km. Scene is illuminated from the bottom of the image.

MARSIS radargrams that include the MFF show a basal interface between the MFF and the underlying substrate that reaches a time delay of a few tens of μs (see Fig. 5.7a). The time delay of the basal interface suggests that the MFF overlies a flat surface that is a continuation of the surrounding plains. The strength of the subsurface reflection varies, sometimes resembling that of the surface reflection (indicative of low attenuation of the radio waves), sometimes being much weaker. In a few instances, a discontinuous interface resulting from an internal dielectric horizon is apparent between the basal and surface reflections (see Fig. 5.7b); this may be related to the layering observed in the deposits. MARSIS data supports previous estimates of the total volume of MFF material, which range from 1.4×10^6 km^3 to 1.9×10^6 km^3 [*Hynek et al.*, 2003].

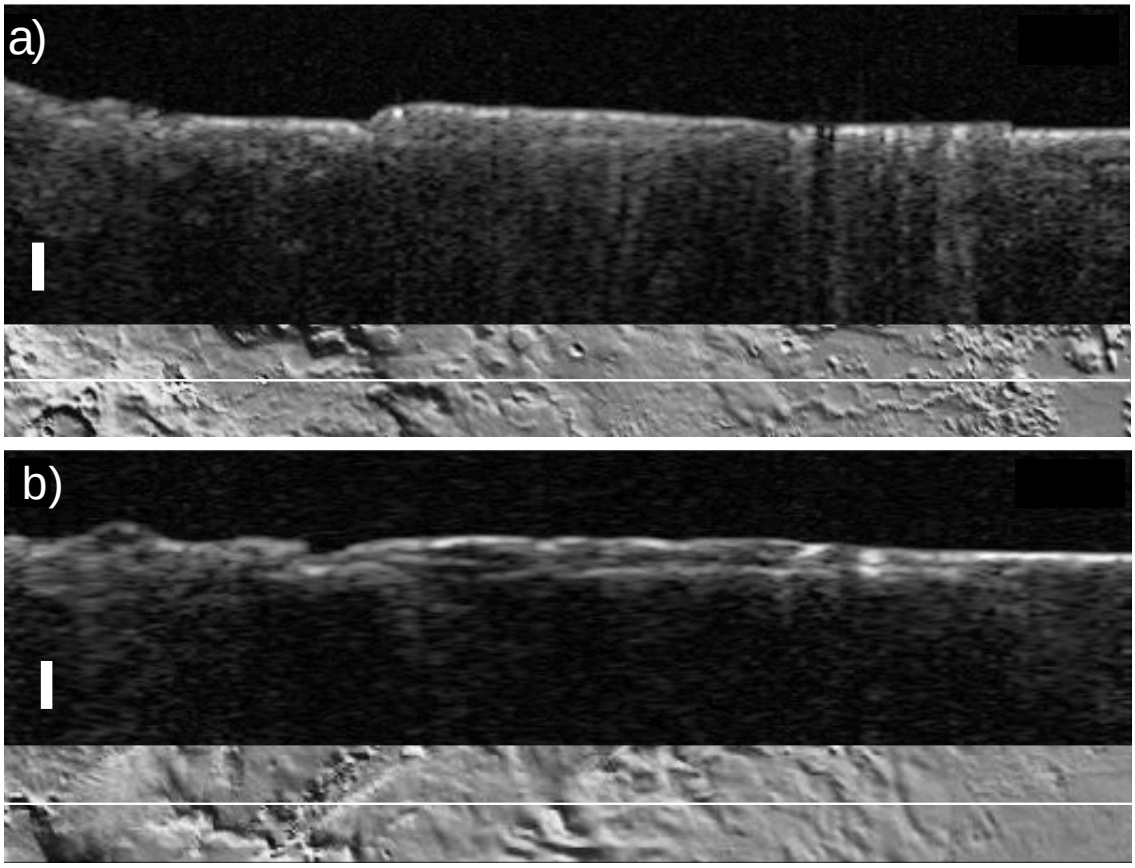

Figure 5.7. Portions of MARSIS radargrams 4011 (a), and 3868 (b), both obtained at central frequencies of 4 MHz over the MFF. The corresponding groundtracks are shown on shaded relief maps (which have widths of 100 km) beneath the radargrams. North is at the right end of the radargrams. White, vertical bars represent 25 μs one-way travel time.

The strength of the subsurface reflection and the observed time delays suggest a value of ~2.9 ± 0.4 for the dielectric constant of the MFF [*Watters et al.*, 2007]. For a centre frequency of 4 MHz, the loss tangent ranges from ~0.002 to 0.006. These values are consistent with two scenarios. The first is that the MFF material is poorly consolidated and comprised of non-ice material with low dielectric loss, e.g. ice-poor ash or an aeolian deposit. If so, it must have an unusually high porosity and a low bulk density (<1.9 kg m^{-3}) to account for the estimated value of the dielectric constant. Alternatively, the MFF may be ice-rich, with a non-ice component of higher dielectric constant. The presence of yardangs at the surface is indicative of poorly consolidated, dry material, meaning that sublimation may have removed volatiles from the putative ice-rich deposits to leave metres of dust and sand, protecting the ice-rich material underneath from sublimation. With two possible compositions of the MFF indicated by the MARSIS data, the origin of the deposits remains elusive.

5.2.4 Parabolic reflections observed in the northern lowlands

MARSIS has recorded numerous parabolic-shaped reflections at various locations spread across the northern lowlands. Examples are the multiple, complex parabolic reflections that are seen in the adjacent radargrams 1892 and 1903, obtained over Chryse Planitia (see Figs. 5.8a and 5.8b), and whose groundtracks are separated by ~50 km at this location. The reflections can spread across lateral distances totalling several hundred kilometres, and can reach time delays of ~180 μs. The ends of the parabolas in each radargram appear to touch the surface reflection, and some parabolas are much deeper-reaching than others. In addition, radargram 1903 shows a flat reflection at a time delay of ~30 μs. In ground-range projections, the parabolic reflections project into arcs with constant curvature, thereby defining circles on the surface (*Watters et al.*, 2006). The circles defined by the reflections plot in the same locations for both radargrams, indicating that they may be manifestations of buried impact structures [*Picardi et al.*, 2005], consisting of a ~220-km-diameter basin superimposed on a larger ~310-km-diameter basin. *Picardi et al.* [2005] hypothesize that the parabolic echoes are off-nadir echoes reflected from the buried walls of the basin, which initially curve away from the groundtrack and subsequently curve back towards it. The flat reflection is interpreted to represent a nadir echo of the interface between the basin fill and the substrate, with the time delay corresponding to a depth of 2 to 2.5 km, assuming a plausible range of Martian materials [*Picardi et al.*, 2005]. The high return strength of the reflection indicates a low attenuation of the basin fill (loss tangent <0.005), which may suggest that unusual, possibly ice-rich, material fills the basin [*Picardi et al.*, 2005].

A number of the parabolic reflections observed in MARSIS data across the northern plains appear to correspond to the locations of subdued quasi-circular depressions (QCDs). These features were originally identified in MOLA data and have been mapped by *Frey et al.* [2002], who interpreted them to be ancient impact basins buried by subsequent resurfacing. Indeed, the proposed 310-km-diameter buried basin seen in radargrams 1892 and 1903 over Chryse Planitia corresponds roughly to a 315-km-diameter QCD. However, many of the MARSIS buried basins have no apparent topographic expression in MOLA data, and some QCDs exist in locations that show no reflections in MARSIS data: such factors make the link between the MARSIS

reflections and QCDs more tenuous. Furthermore, the appearance of the reflections in separate radargrams that pass over the same area is inconsistent. This is demonstrated in radargrams 1892 and 1903: the flat reflection is very apparent in radargram 1903 but is entirely absent from radargram 1892. Furthermore, radargram 3819 (Fig. 5.8c), whose groundtrack is located ~45 km to the west of that of radargram 1903, and which should pass over the hypothesized buried basin, shows no sign of any parabolic reflections that were so apparent in 1892 and 1903. This absence calls into question the status of all the parabolic reflections in the northern plains as being caused by subsurface interfaces, as they all share the same morphological characteristics. The issue of what may be causing the parabolic reflections will be explored in detail in section 5.3 that concerns similar reflections seen in the Ma'adim Vallis region.

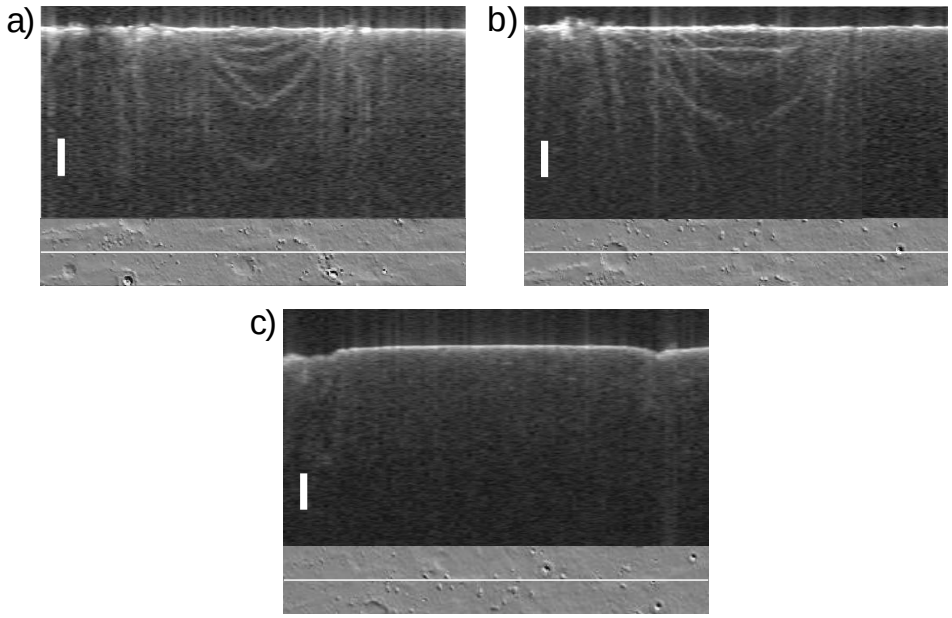

Figure 5.8. Portions of MARSIS radargrams 1892 (a), and 1903 (b), both obtained at central frequencies of 4 MHz, showing the multiple parabolic reflections (and single flat reflection) seen in the northern plains of Chryse Planitia (located at 37°N, 337°E). A portion of the 'barren' radargram from the adjacent orbit 3819 is also shown (c). The corresponding groundtracks are shown on shaded relief maps (which have widths of 100 km) beneath the radargrams. North is at the right end of the radargrams. White, vertical bars represent 50 μs one-way travel time.

5.2.5 Summary

The three geological environments where MARSIS observations have revealed subsurface interfaces are evidently characterised by significant contrasts in composition/consolidation across the boundary between the overlying deposits and the

substrate, even though the exact composition of some of the deposits (namely the DAF and MFF) remains uncertain. The substrate in each case is likely to be basaltic in composition, with a value of ε' between 7.5 and 8.5. In the case of the PLD and DAF, the overlying deposits evidently consist of a mixture of ice and basaltic dust, with a value of ε' between 3 and 5. The MFF, with a dielectric constant value of 2.5 to 3.3, may consist of either a similar dust/ice mixture, or poorly consolidated, possibly porous volcanic ash and/or aeolian material. It has been hypothesized that the parabolic reflections in the northern plains may be manifestations of off-nadir echoes from the rims of buried basins, yet the inconsistent occurrence of such reflections between MARSIS radargrams indicates that this hypothesis may be flawed. The following section examines a series of similar parabolic reflections that cluster within the Ma'adim Vallis region in an effort to determine what process may be causing such reflections.

5.3. Reflections recorded by MARSIS in the vicinity of Ma'adim Vallis[1]

5.3.1 Introduction

Ma'adim Vallis is located just to the south of the dichotomy boundary at ~180° longitude. Ma'adim Vallis is one of the most prominent valleys in the Martian highlands with a width of 8 to 15 km and a length of 900 km [*Irwin et al.*, 2002]. A system of tributaries occurs at the head of the valley, which meanders northwards, terminating in the 150 km diameter Gusev impact crater, site of operations of the Mars Exploration Rover Spirit. It has been interpreted that water and aqueous sediments ponded here after being carried through the valley inlet in the southern rim of Gusev crater [*Cabrol et al.*, 1996], and the results of the science investigations of Spirit to date have confirmed that aqueous infiltration, cementation and alteration have affected impact and volcaniclastic materials present at the site [*McCoy et al.*, 2008].

MARSIS recorded reflections over a region just to the west of Ma'adim Vallis over a period of more than two and a half years (February 2006 to October 2008). Figure 5.9

[1] Section 5.3 has been published: White, O.L., A. Safaeinili, J.J. Plaut, E.R. Stofan, S.M. Clifford, W.M. Farrell, E. Heggy, G. Picardi, and the MARSIS Science Team (2009) MARSIS radar sounder observations in the vicinity of Ma'adim Vallis, Mars. *Icarus*, **201**, pp. 460-473, doi:10.1016/j.icarus.2009.01.015.

displays eight radargrams in the Ma'adim Vallis region that show apparent subsurface reflections, as well as five nearby radargrams which do not show any apparent subsurface reflections, other than off-nadir reflections predicted by simulations. The radargrams are in a region that extends across only 3.2° of longitude (about 200 km). The radargrams are grouped according to their locations and the characteristics of their reflections (Figs. 5.9a, 5.9b, 5.9c and 5.9d, the latter featuring radargrams displaying no reflections). The form of these reflections varies considerably: reflections such as those in radargrams 4786 and 2676 (Fig. 5.9a) occur at small time delays relative to the surface, are roughly horizontal and relatively laterally inextensive. Those in radargrams 2687 (Fig. 5.9b) and 4775 (Fig. 5.9c) have steeper, parabolic morphologies, reach much greater time delays, and have greater lateral extents. Those in radargrams 4808 and 3024 (Fig. 5.9b) display almost hyperbolic morphologies, whereby the central region of the reflection dips down steeply and fades away, creating two separate 'arms'. Radargrams 6145 and 2665 (Fig. 5.9c) display reflections with high time delays, but which are tenuous and discontinuous, apparently resembling segments of parabolas. The groups in Figs. 5.9a, 5.9b and 5.9c are examined in sections 5.3.3, 5.3.4, and 5.3.5, respectively. In order to simplify the reference system for the radargrams, each radargram will be assigned a reference letter in place of the four digit MARSIS orbit number; these are shown in Table 5.1.

Figure 5.9 (following four pages). MARSIS radargrams from orbits in the Ma'adim Vallis region displaying the variety of echoes seen. Radargrams are grouped into four sections according to their locations and reflection characteristics: (a) The central radargrams 4786 (A) and 2676 (B), displaying shallow and relatively laterally inextensive reflections. (b) The westerly radargrams 4808 (C), 3024 (D) and 2687 (E), displaying reflections that reach to large time delays and show tenuous, parabolic and hyperbolic morphologies. (c) The easterly radargrams 6145 (F), 4775 (G) and 2665 (H), displaying similarly deep, parabolic and tenuous reflections. (d) Radargrams 2698 (I), 6163 (J), 4797 (K), 3002 (L) and 2991 (M), which occur in the Ma'adim Vallis region but display no reflections. Radargrams in each group are aligned at the same latitude relative to each other. Radargrams are accompanied by the orbit number, reference letter, frequency band centre and groundtrack (horizontal white line) on a shaded relief map of the surface. Locations of the reflections on the surface are shown as white groundtracks in Fig. 5.11. The widths of the shaded relief maps are 100 km. North is at the left end of the radargrams. Vertical white scale bar represents 25 μs one-way radio wave travel-time. White arrows highlight relevant reflections.

a)

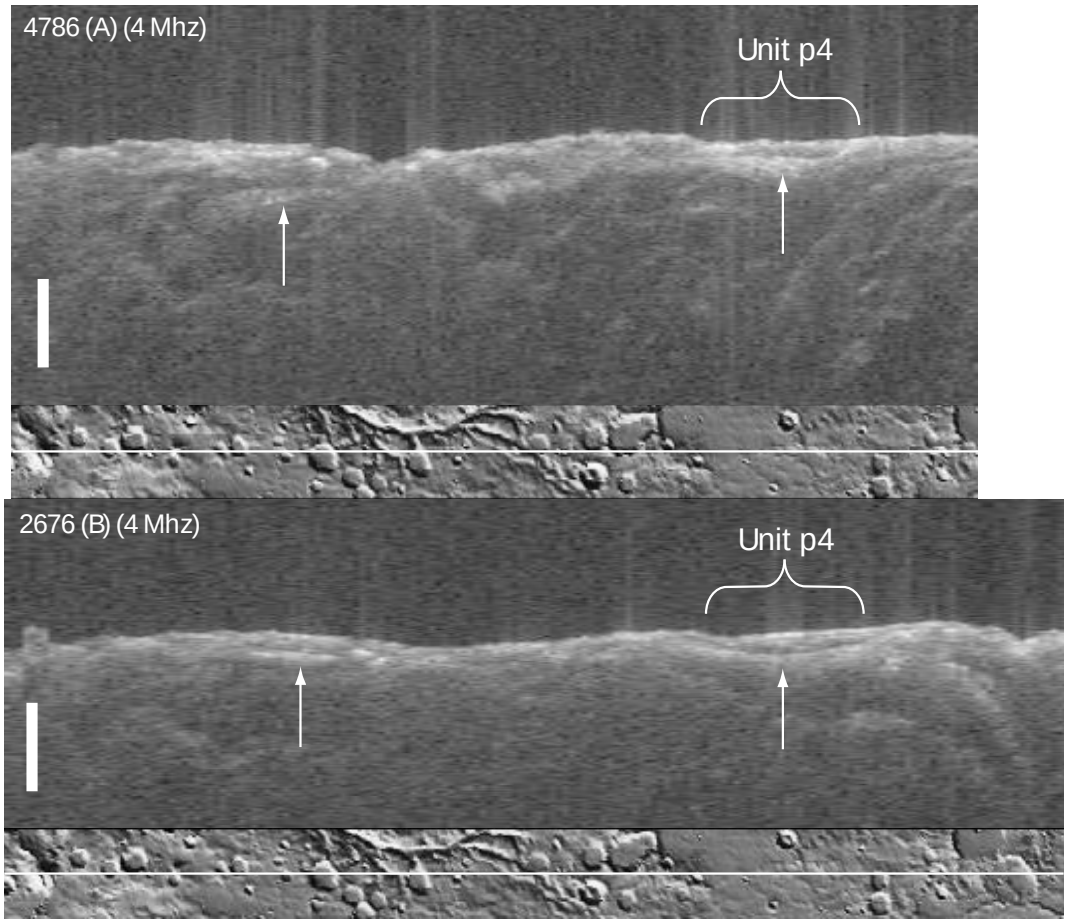

b)

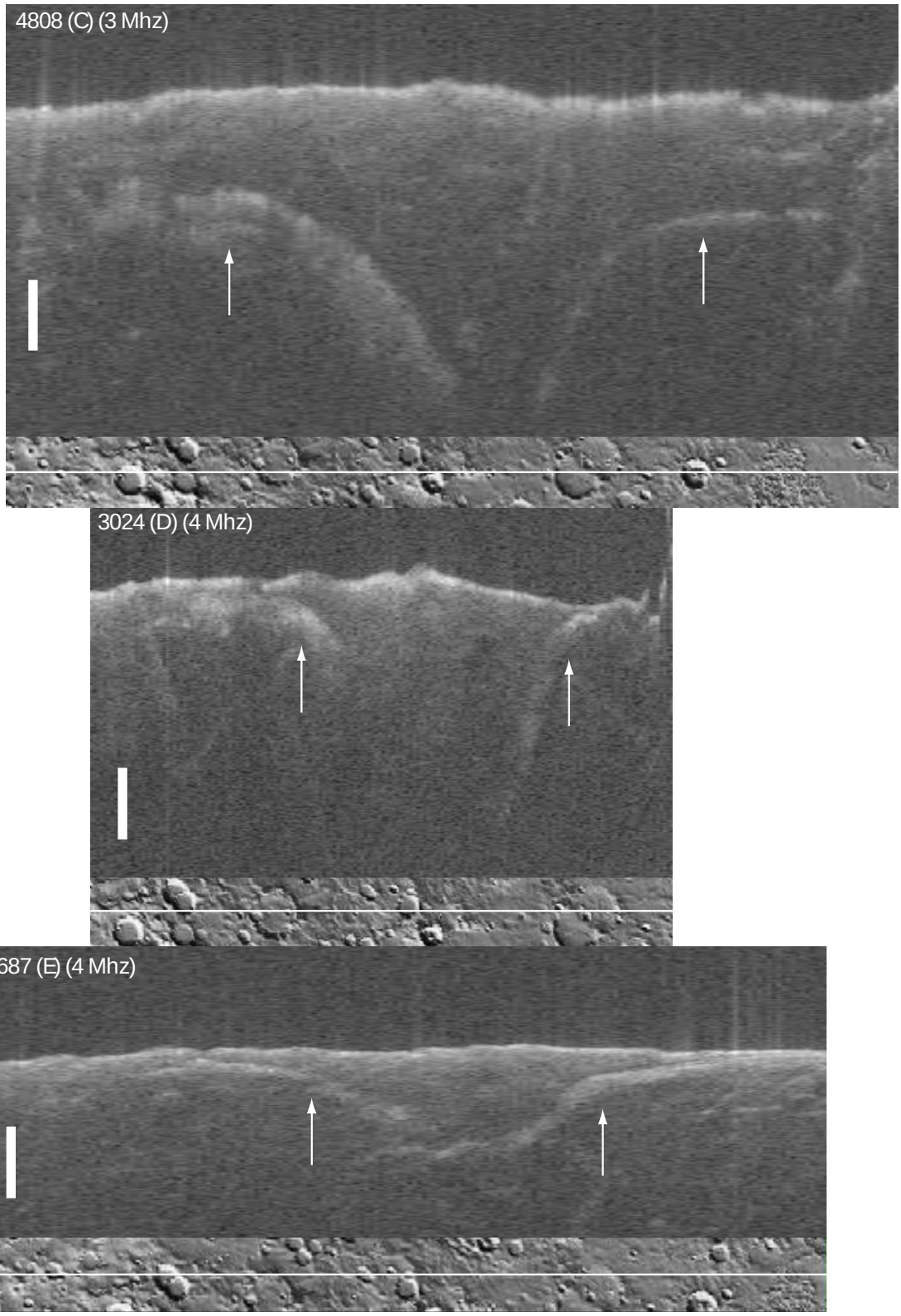

c)

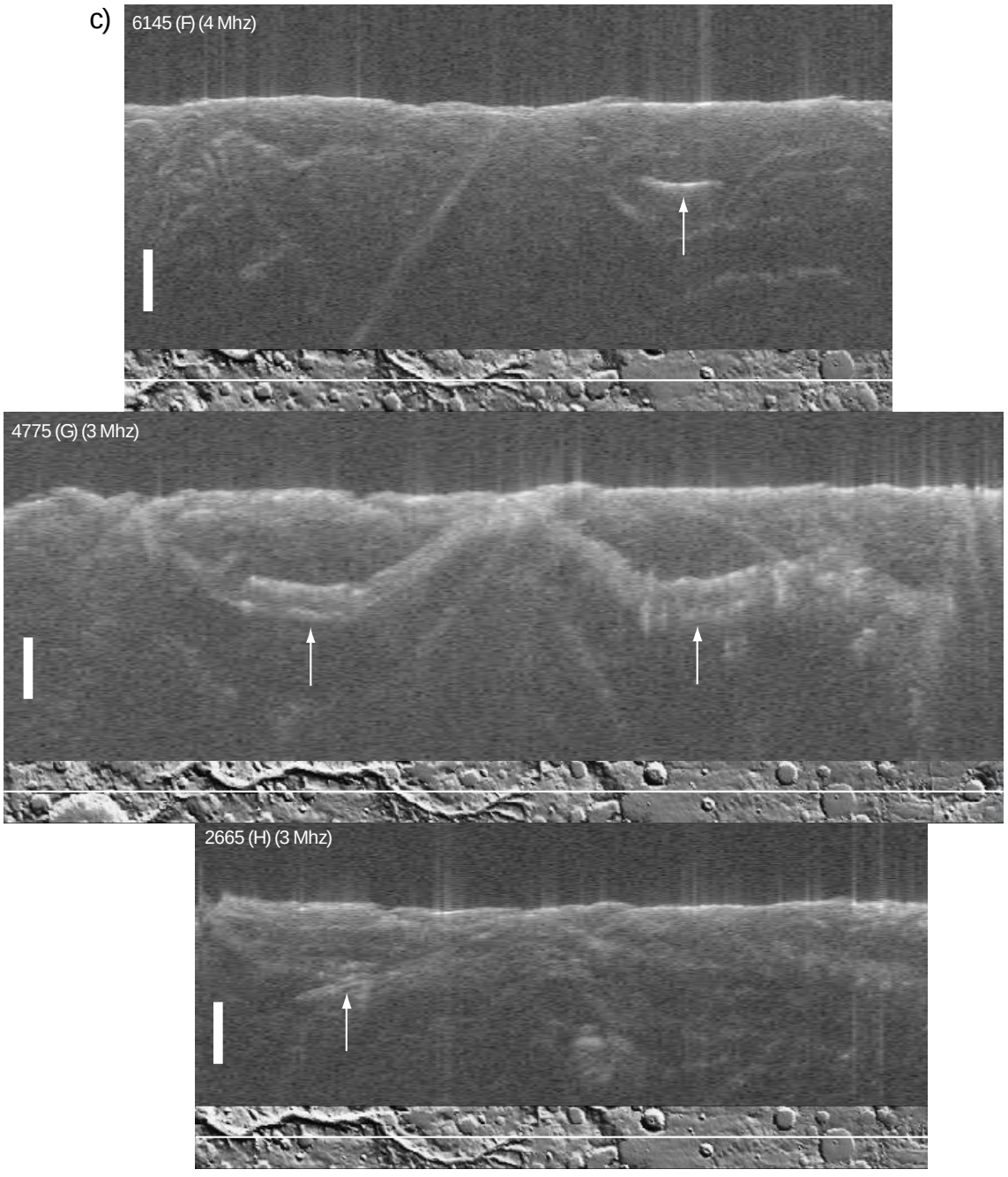

d)

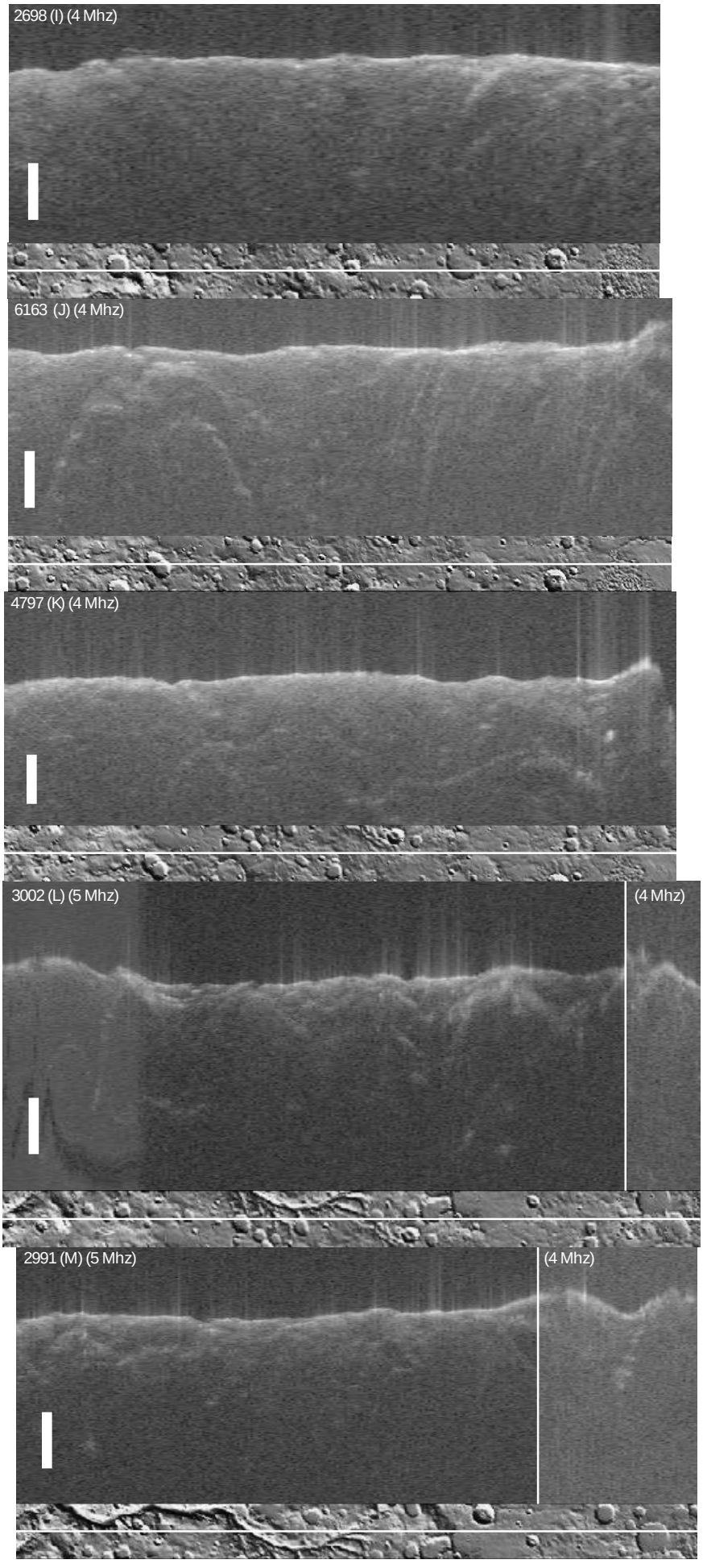
2698 (I) (4 Mhz)
6163 (J) (4 Mhz)
4797 (K) (4 Mhz)
3002 (L) (5 Mhz)
(4 Mhz)
2991 (M) (5 Mhz)
(4 Mhz)

Table 5.1. Correlation of MARSIS orbit numbers to the reference letters that will be used throughout the chapter.

MARSIS orbit no.	Radargram ref. letter
4786	A
2676	B
4808	C
3024	D
2687	E
6145	F
4775	G
2665	H
2698	I
6163	J
4797	K
3002	L
2991	M

Each radargram was obtained in two of the four frequency bands available to MARSIS (the specific frequency bands differ between radargrams): in each of the eight radargrams the reflections are apparent in both frequency bands. The morphologies of the reflections are fairly similar between the radargrams of different frequencies. The resolution of the reflections often varies for different sounding frequencies as demonstrated in Fig. 5.10 for radargram E. This may be caused by variation in the magnitude of volume scattering (radio signals with different wavelengths will be scattered by inhomogeneities of different scales) or ionospheric attenuation.

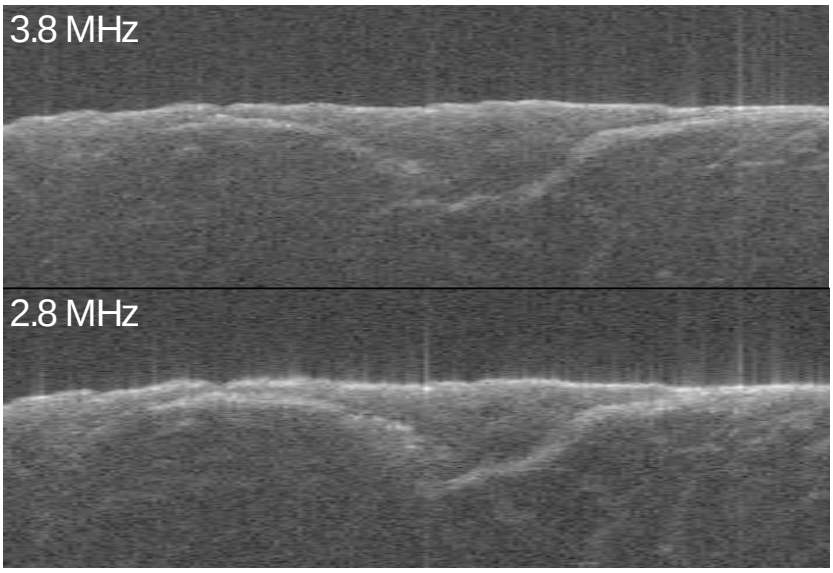

Figure 5.10. Comparison of the appearances of the E reflection as seen in radargrams obtained at centre frequencies of 2.8 MHz and 3.8 MHz.

A geological map of the Ma'adim Vallis region was created in order to assess the likelihood of individual reflections resulting from subsurface interfaces by comparing the positions of the reflections with the positions of mapped geological units. The map was produced through the study of individual Mars Orbital Camera and THEMIS images as well as MOLA altimetric data.

5.3.2 Geology of the Ma'adim Vallis region

Fig. 5.11 shows the geological map of the Ma'adim Vallis region with the locations of the MARSIS reflections indicated. Short descriptions and interpretations of the various units are included in the legend.

Of particular relevance to the present study is the mottled, dissected plains material (unit p4), which occurs in large topographic depressions south of Ma'adim Vallis, and which noticeably coincides with reflections in MARSIS radargrams A and B (Fig. 5.9a). This unit often has a mottled albedo and sometimes softens the relief of underlying features such as craters and wrinkle ridges, presumably in the areas where unit p4 is thin. The unit has been eroded in places (particularly in the basin to the west) to produce fretted, flat-topped mesa-like features, indicative of weakly consolidated material. The p4 unit is often bounded by the p2 unit, whose numerous channel networks terminate in the p4 unit. A previous estimate of the crater density in this unit suggests a late Noachian age of >3.5 to 3.7 Ga [*Irwin et al.*, 2002]. The system of overlapping and highly degraded basins that harbor the p4 unit form Eridania Planitia, previously described in *Irwin et al.* [2002; 2004] as having been occupied by lakes in the late Noachian which overflowed at the northern rim to form Ma'adim Vallis. The valley networks of unit p2 located in the surrounding highlands would have been a major source of water for these lakes. A similar configuration of lacustrine basins bordered by channeled terrain has been identified in the area surrounding Hesperia Planum [*Jones et al.*, 2007]. *Irwin et al.* [2002] noted the unusual bowl-shaped floors of these depressions, which they suggested had resulted from deposition of sediment around the margins of impact basins filled with standing water. This contrasts with flat-floored, sediment-filled basins, where fluvial rather than lacustrine regimes transport sediment far into the interior of the basins. *Irwin et al.* [2002] also noted that shoreline morphologies are evident in several locations on the rims of these basins. The location of the p4 unit corresponds reasonably well to the location of the hypothesized lake

system described in *Irwin et al.* [2002; 2004] (outlined by the thick dotted line in Fig. 5.11). Sediments of the valley floor material (unit v1) at the head of Ma'adim Vallis border the lacustrine sediments of unit p4 in Eridania Planitia, supporting the hypothesis of *Irwin et al.* [2002; 2004] that Ma'adim Vallis was formed after overflow of the lake system into an impact basin to the north during the late Noachian.

This area has been mapped previously in separate maps created during the Viking era in the late 1970s. They include that of the Aeolis Quadrangle by *Scott et al.* [1978], the south easternmost point of which is at 180°E, 30°S; the Eridania Quadrangle by *De Hon* [1977], the north easternmost point of which is at 180°E, 30°S; the Memnonia Quadrangle by *Mutch and Morris* [1979], the south westernmost point of which is at 180°E, 30°S; and the Phaethontis Quadrangle by *Howard* [1979], the north westernmost point of which is at 180°E, 30°S. These maps describe the bulk of the terrain around Ma'adim Vallis as either 'hilly and cratered material' or 'cratered plateau material', analogous to the rough plain material in Fig. 5.11. The maps also describe 'plains material' which sometimes (but not always) coincides with the ridged plains material in Fig. 5.11, particularly in the eastern half of the map. The western half of Eridania Planitia is mapped as 'plains material' in *Scott et al.* [1978] and *De Hon* [1977], although its central region is mapped as 'hilly and cratered material'. Mutch *and Morris* [1979] and *Howard* [1979] mapped the eastern parts of Eridania Planitia as 'plains material' and 'dissected plateau material', the latter being analogous to the mottled, dissected plains material in Fig. 5.11. The knobby mesa material and valley floor material in Fig. 5.11 are mapped in virtually identical locations in the earlier maps. The maps do not feature an analogy for the channeled plains material in Fig. 5.11.

Figure 5.11 (following two pages). Geological map of the Ma'adim Vallis area with the locations of the MARSIS reflections superimposed. Base map is a Viking image mosaic of sinusoidal projection, with a resolution of 220 px/degree.


15°52′29″ S
169°31′06″ E
15°48′23″ S
175°31′12″ W
35°39′59″ S
169°26′09″ E
35°40′26″ S
175°29′47″ W
I
J
K
L
M
A
B
C
D
E
F
G
H
p1
p2
p3
p4
p5
p6
c1
c2
h1
h2
v1
v2
N

DESCRIPTION OF MAP UNITS

CRATER MATERIALS

c1 FRESH IMPACT CRATER MATERIAL: Sharp, raised, complete rims. Floors bowl-shaped and lower than surrounding terrain. Central peaks and ejecta blankets often present.

c2 DEGRADED IMPACT CRATER MATERIAL: Eroded, sometimes incomplete rims. Floors flat (filled by unit p6) and at the same elevation as surrounding terrain. Slumping and terracing often seen on walls. Central peaks and ejecta blankets generally not present.

HIGHLAND MATERIALS

h1 MOUNTAINOUS MATERIAL: Forms rugged isolated massifs with high relief reaching 40 km across, mainly in the north of the mapping area. *Interpretation:* Remnants of Noachian mountain complexes.

h2 VOLCANIC MATERIAL: Symmetrical cone of Zephyria Tholus, located in NW of mapping area. Circular summit crater is flooded and prominent radial dissection has affected flanks. *Interpretation:* Stratovolcano/composite cone of uncertain age.

PLAINS MATERIALS

p1 ROUGH PLAINS MATERIAL: Hummocky, rugged terrain. Features a higher density of large (>12 km diameter), eroded impact craters than other units. Wrinkle ridges are seen occasionally. *Interpretation:* strongly brecciated Noachian crust.

p2 CHANNELED PLAINS MATERIAL: Hummocky, rugged terrain similar to unit p1, but which displays numerous small valley networks and eroded terraces and mesas. *Interpretation:* Noachian terrain that has experienced extensive alteration caused by the action of precipitation and/or groundwater sapping [*Jones et al.*, 2007].

p3 RIDGED PLAINS MATERIAL: Smooth, low-relief terrain featuring numerous sharp linear and circular wrinkle ridges. Density of large, eroded impact craters is less than that for unit p1. *Interpretation:* Flood lavas emplaced in low lying areas of the highlands, possibly during the late Noachian/early Hesperian.

p4 MOTTLED, DISSECTED PLAINS MATERIAL: Smooth, low-relief terrain, generally with a patchy albedo. Unit is eroded and dissected in places to form mesas and terraces. Unit is sometimes seen to subdue the morphology of underlying features (e.g. wrinkle ridges, impact basins, etc.). Exhibits low crater density. *Interpretation:* Lacustrine sediments deposited during the late Noachian.

p5 KNOBBY MESA MATERIAL: Chaotic terrain comprising numerous densely-packed flat-topped mesas and rounded knobs reaching 10 km across. Abrupt contact exists between the unit and surrounding plains. Exhibits low crater density. Unit generally occurs within unit p4. *Interpretation:* resistant lacustrine sediments deposited during the late Noachian?

p6 SMOOTH PLAINS: Very smooth, very lightly-cratered surfaces on the floors of degraded impact craters. *Interpretation:* crater fill material eroded from the sides of large, degraded impact craters.

VALLEY MATERIALS

v1 VALLEY FLOOR MATERIAL: Smooth, slightly pitted and lightly-cratered deposits forming the floor of Ma'adim Vallis as well as those of tributaries feeding into it and other large channels in the mapping area. *Interpretation:* sediments deposited by water flowing through valleys during the late Noachian.

v2 VALLEY TERRACE MATERIAL: Smooth, flat terraces located on the walls and in the center of Ma'adim Vallis. Terraces are sometimes lineated perpendicular to the valley wall, and often have fretted margins on the valley side. *Interpretation:* remnants of resistant geological layers partly eroded by water flowing through Ma'adim Vallis during the late Noachian.

- Geological boundary
- Crater rim
- Crater central peak
- QCD rim identified in *Frey et al.* [2002]
- Locations of reflections seen in MARSIS radargrams (reflections labelled with orbit reference letter)
- Locations of significant radargrams that do not display any reflections (radargrams labelled with orbit reference letter)
- Lake shoreline hypothesized in *Irwin et al.* [2002]

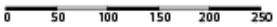

Distance (km)

CORRELATION OF MAP UNITS

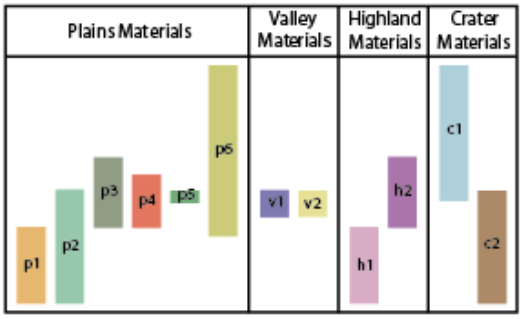

5.3.3 Radargrams 4786 (A) and 2676 (B)

Radargrams A and B (Fig. 5.9a) display shallow, horizontal reflections that are located to the east and south of Ma'adim Vallis; their groundtracks overlap almost exactly in the area where their reflections are seen. Radargram B displays two well-defined reflections (the northern one 160 km long, the southern one 275 km long). Reflections are discernible in similar locations in radargram A, positioned only a few km to the east of radargram B. The reflections in radargram B attain one-way time delays of 5.5 μs and 6.6 μs for the northern and southern reflections, respectively, whereas the time delays of the corresponding reflections in radargram A are 12.8 μs and 4.6 μs, respectively. The time delays of the southern pair of reflections are similar, yet the time delays of the northern pair differ by a factor of more than two.

The southern reflections in radargrams A and B are notable in that the locations of their groundtracks correspond well to the boundaries of unit p4 mapped in Fig. 5.11. The reflections in both radargrams commence at the northern boundary of unit p4 (at the rim of Eridania Planitia). The A reflection commences at a 'step' representing the drop in topography at the boundary between Eridania Planitia and the cratered highlands. This step is not as apparent in B. The B reflection extends ~50 km further to the north and south than the A reflection. The fact that these reflections nearly overlap and display similar, low time delays supports the interpretation that both of these reflections are caused by a subsurface interface comprising the base of deposits filling the Eridania Planitia basin. The reflections have a consistently high intensity suggestive of a pronounced dielectric contrast. However, the subsurface hypothesis does not account for the significant discrepancy in their lengths, unexpected given that they nearly overlap.

The northern reflections in the two radargrams do not appear to correspond to the surface geology when plotted on the map in Fig. 5.11, and do not seem to manifest themselves in adjacent radargrams (e.g. M and K in Fig. 5.9d). The possibility that the reflections are representative of a buried former course of Ma'adim Vallis was considered, yet detailed study of images in this vicinity revealed only cratered plains and no manifestation of any relict channels. A possible alternative is that the reflections may be off-nadir surface clutter. Figures 5.12a and 5.12b show ground-range projections of the reflections in radargrams A and B respectively, which plot where the

reflections would fall on the surface (on both sides of the spacecraft groundtrack) if they were being produced by off-nadir surface clutter. Figures 5.12c and 5.12d compare the observed radargrams with simulations that model where reflections from off-nadir reflectors would be expected in the radargrams (created by Ali Safaeinili of the Jet Propulsion Laboratory, a co-author on the *Icarus* paper). Figures 5.12a and 5.12b show that the northern projections in both radargrams are aligned well with Ma'adim Vallis, yet are often offset from the channel typically by several tens of kilometres, although the southern segments of the northern B projection do coincide well with the wall of the channel. The southern projections in both radargrams do not coincide with any topographic features. Figures 5.12c and 5.12d show that the simulations do not predict any of the reflections seen in radargrams A and B, although they do predict faint reflections originating from Ma'adim Vallis, which are seen in the observed data (highlighted by arrows).

Figure 5.12 (this and following page). (a and b) Ground-range projections of reflections (white lines) from the A (a) and B (b) radargrams superimposed on a map comprising THEMIS daytime infrared images of the Ma'adim Vallis region. Scale bar measures 150 km in both images. (c and d) Comparisons of simulations of radargrams A (c) and B (d) (above) and the observed radargrams (below). Arrows on the simulations and observed radargrams mark reflections caused by off-nadir surface clutter from Ma'adim Vallis. Scale bar represents 25 μs one-way radio wave travel-time. North is at the left of the radargrams.

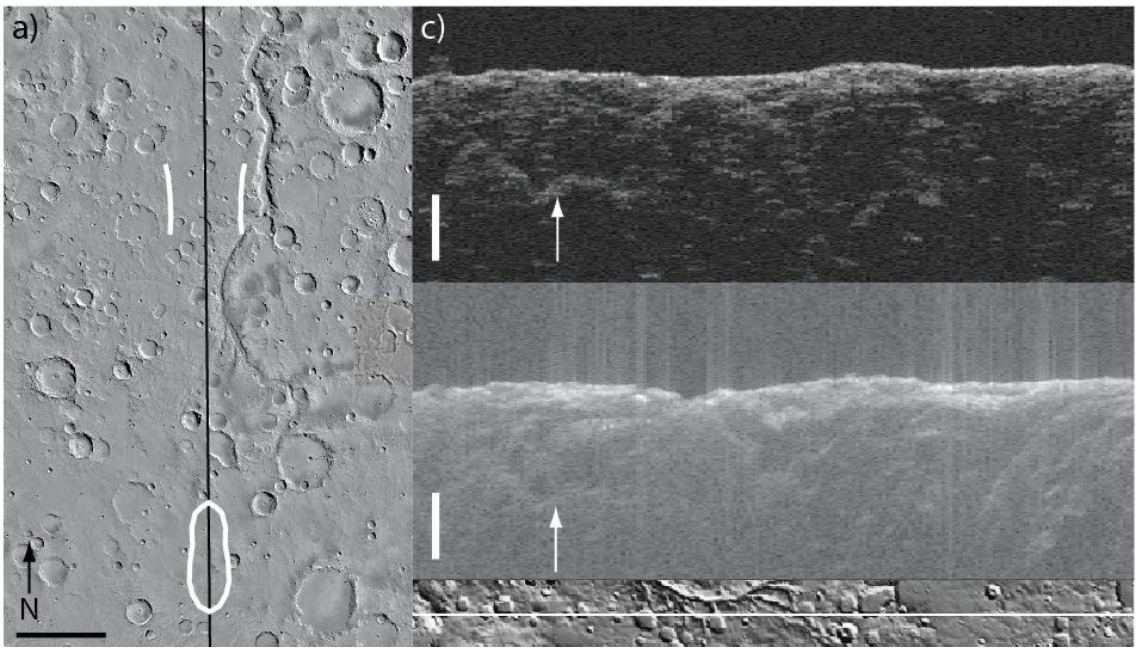

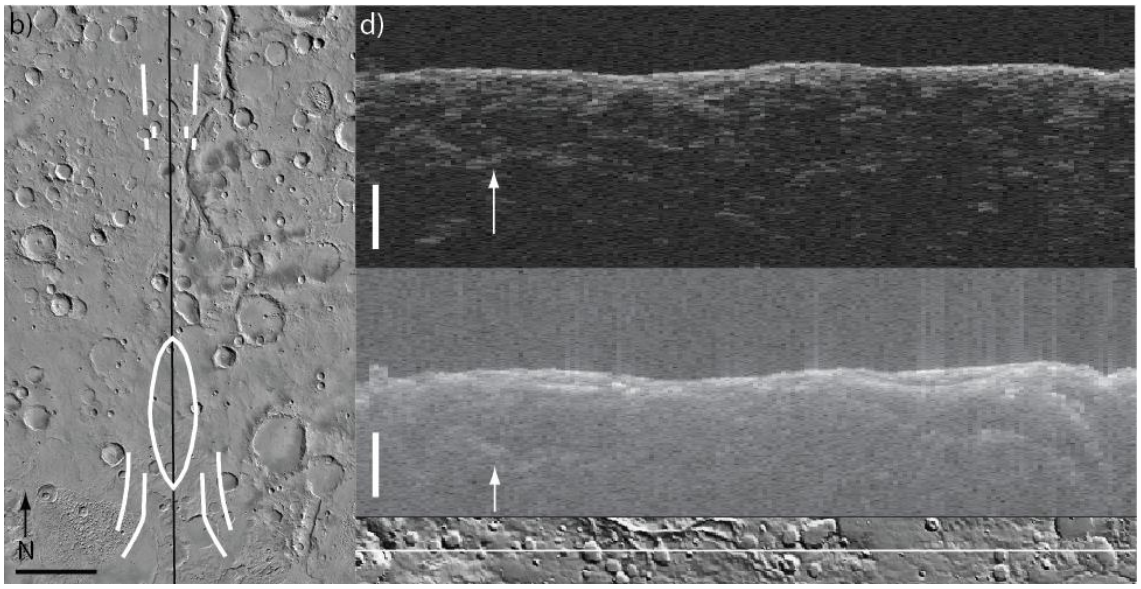

Both sets of reflections (north and south) therefore either stem from a subsurface interface or are the product of ionospheric distortion. It is possible that they have different causes. In the case of the southern reflections, a potential subsurface interface could comprise the base of the Eridania Planitia lacustrine deposits (unit p4 in Fig. 5.11). For the northern reflections, the potential subsurface interface has no apparent surface expression. However, geological materials such as ice or high porosity rock are required to explain the strong dielectric contrast implied by the high intensity reflections. Using Eq. 4.13 and assuming a value of 5 for ε_r of the surface layer (corresponding to the fluvial sediments in the second geoelectrical model of *Heggy et al.* [2003]), as well as accounting for volume scattering, the time delays of the reflections in radargram B would correspond to depths of 590 m and 710 m for the northern and southern reflections, respectively, whereas the depths of the corresponding reflections in radargram A would be 1380 m and 500 m, respectively. The lower value of ε_r associated with an icy or porous rock (in the region of 3 to 5 [*Zhang et al.*, 2008]) would result in greater inferred depths of these reflections if either or both of these properties characterized the surface layer. The strongest evidence against a subsurface origin is that the reflections are not manifested in adjacent radargrams such as K to the west and G and M to the east (Figs. 5.9c and d), unexpected given the consistently high definition of the reflections within their radargrams as well as their substantial lateral extents. The fact that the time-delay of the northern reflection differs significantly between the two radargrams, whose groundtracks overlap at this point, suggests that

ionospheric interference may have influenced the paths of the MARSIS signals differently at the times the radargrams were recorded – the potential for this occurring will be discussed in section 5.3.6.

Radargram B also displays two additional, tenuous reflections at its southern end that have larger time delays than the aforementioned reflections; these reflections are horizontal at their northern ends, yet dip as they progress to the south, and are not predicted by the simulation in Fig. 5.12d. Figure 5.12b shows that these reflections do not correspond to any off-nadir topography, in which case they may alternatively be explained by ionospheric distortion of MARSIS signals.

Radargram L (Fig. 5.9d), whose groundtrack coincides almost exactly with those of A and B, was obtained on the dayside and appears to have been affected by the increased electron density in the dayside ionosphere. As such, the surface reflection seen in this radargram is considerably blurred; possible manifestations of subsurface reflections are seen in the same locations as those seen in radargrams A and B, yet they are too distorted and tenuous to confirm as being definitely related to those in the other radargrams.

5.3.4 Radargrams 4808 (C), 3024 (D) and 2687 (E)

The reflections in radargrams C, D and E (Fig. 5.9b) are quite different from those already considered. They (along with those in radargrams F, G and H in Fig. 5.9c) tend to have much greater lateral extents, reach greater time delays, and dip at greater angles than the other relatively flat reflections. They appear to have little or no relation to the surface geomorphology.

Radargram E displays a reflection that is very long (~790 km), with shallow, gently-dipping outer margins (each 175-220 km long, reaching a one-way time delay of 9.4 μs) that dip sharply as they approach the centre. The southern half of the reflection flattens out at the centre and appears to undercut the northern reflection. The reflection has a maximum one-way time delay of 33.9 μs. Compared with the other reflections in this group, the E reflection has a consistently sharp definition.

The location of this reflection roughly corresponds to a circular region of slightly lower topography than its surroundings, one of the subtle QCDs described by *Frey et al.* [2002]. The QCD in question has a diameter of ~400 km, is bisected by Ma'adim Vallis and is interpreted to be an ancient, eroded impact basin [*Irwin et al.*, 2002]. A possible

origin for this reflection is that it represents the basal contact between the basin-fill of the QCD and the substrate. If so, the deepest part of the reflection would represent a thickness of the basin-fill of 4.5 km (assuming a value of 5 for ε_r). This would, however, contrast with the estimate of MARSIS penetration in a lithic environment obtained by *Heggy et al.* [2006a], who suggested an average penetration depth of 500 metres based on ground-penetrating radar surveys of an eroded Mars-analogue lava flow at Craters of the Moon volcanic field, Idaho. The surface layer would need to be comprised of an implausibly low-attenuation material to result in such a strong return from such a long time delay. Alternatively, rather than being a nadir reflection from the curved, buried floor of the impact basin, the reflection may be an off-nadir echo from the buried rim of the impact basin, produced via the same mechanism suggested by *Watters et al.* [2006] and *Picardi et al.* [2005] to explain the parabolic reflections seen by MARSIS in the northern plains.

Figure 5.13a shows the ground-range projection of the E reflection, indicating the extent to which the reflection and QCD basin rim overlap. The lateral extent of the reflection is actually larger than the width of the QCD along the orbit groundtrack, and the centres of the two features are offset by more than ~220 km, thus making both of the aforementioned hypotheses somewhat doubtful. Figure 5.13b compares the observed radargram with the simulation. Three reflections are predicted by the simulation: a short time-delay, laterally inextensive reflection at the north end of the radargram, a faint, long time delay reflection in the centre of the radargram, and a short time delay reflection at the southern end of the radargram that approaches the surface as it progresses southward. All of these reflections overlap with the reflection seen in the observed radargram. Figure 5.13a indicates that the ground-range projection of the northern reflection corresponds well to the wall of a 30 km-diameter crater to the west of the orbit groundtrack. The central reflection appears to correspond well to the walls of Ma'adim Vallis and an associated tributary to the east of the groundtrack. The southern reflection does not appear to coincide with any clearly visible topographic feature in Fig. 5.13a, yet the clutter may be originating from crater walls to the west of the groundtrack. The fact that each of these reflections seem to be originating from unrelated topographic features suggests that their overlap with the E reflection may be purely coincidental and that they do not originate from surface outcrops of a large, mostly buried subsurface structure observed in the E reflection.

There are, however, some observations that support the interpretation of the E reflection as a subsurface reflection. The intensity of the reflection decays as the time delay increases (regardless of frequency), which would be expected for a deepening subsurface contact as attenuation increases. The reflection also has a more blurred appearance in the 3.8 MHz radargram, compared with the 2.8 MHz radargram (apparent in Fig. 5.10), a possible indication of subsurface volume scattering. Furthermore, there is an apparent latitudinal continuity between this reflection and those in adjacent radargrams: C and D, located 40 and 30 km west of the E reflection respectively. The C and D reflections differ from E in that they are initially flat at their outer edges but steepen dramatically inward, with a gap at the centre separating them, making them resemble hyperbolas. Like E, neither of the reflections corresponds to the surface geology or off-nadir topography in any way. Figure 5.9b positions the three radargrams at their correct latitudes relative to each other, and shows that the latitudinal positions and extents of the 'arms' of the C and D reflections are broadly consistent with those of the 'arms' of the E reflection. There is an apparent consistency between the morphologies of the reflections: the fact that the C and D reflections dip down below detection at their centres may be a continuation of the effect seen in the E reflection, where the two ends flatten out and meet at the centre.

Despite the consistency that exists between them, the eccentric appearance of these reflections (particularly the tenuous C and D reflections) and the absence of similar reflections in radargrams located a few tens of kilometres to the east and west (I and K, Fig. 5.9d) weaken the hypothesis that they arise from a subsurface interface. The potential for ionospheric distortion to explain their origin will be discussed in section 5.3.6.

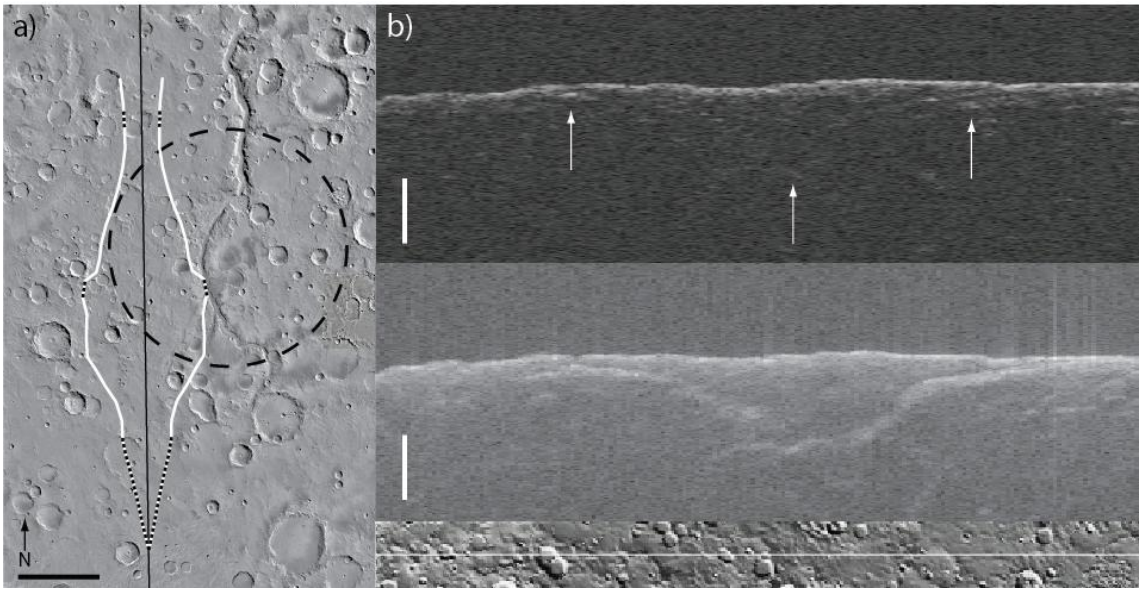

Figure 5.13. (a) Ground-range projection of reflections from the E radargram superimposed on a map comprising THEMIS daytime infrared images of the Ma'adim Vallis region. The dashed circle marks the approximate rim of a QCD identified by *Frey et al.* [2002]. The dotted segments of the reflections indicate where reflections are also seen in the simulation. Scale bar measures 150 km. (b) Comparison of a simulation of radargram E (above) and the observed radargram (below). Arrows on the simulation mark where reflections caused by off-nadir surface clutter are expected. Scale bar represents 25 μs one-way radio wave travel-time. North is at the left of the radargrams.

5.3.5 Radargrams 6145 (F), 4775 (G) and 2665 (H)

The positions of the radargrams F, G and H (Fig. 5.9c) virtually coincide with Ma'adim Vallis, and surface clutter from the channel is seen within them. Radargram G displays two reflections that constitute laterally extensive parabolic reflections (each more than 650 km across) that thicken as their time delay increases such that the time delay between the top and bottom of the reflections reaches >10 μs. The reflections reach a maximum one-way time delay below the surface reflection of 49 μs. The reflections join at their tips, and the southern tip of the southern reflection dips back downwards before it reaches the surface, terminating below the surface at a one-way time delay of 39 μs. Radargram H, located just 5 km to the east of G, does not display a parabolic reflection; instead, it shows a strong, linear reflection that dips to the north, virtually in the same location and at the same time delay as the south limb of the northern parabolic G reflection. The reflection reaches a maximum one-way time delay of 35 μs, and appears to extend to the surface (although it becomes tenuous and indistinct as it nears the surface). Another potential, but much more tenuous, reflection occurs to the south and appears to correspond to the position of the north limb of the

southern G reflection. Radargram F displays an anomaly among all the Ma'adim reflections. A single, high intensity, well-defined, 140 km long reflection exists at a one-way time delay of 31 μs, virtually the same time delay as the southern G reflection that coincides with the F reflection.

Figure 5.9c shows that there is an apparent consistency between the time-delays and latitudinal positions of the reflections in these three radargrams. This would suggest a shared origin for the reflections. However, none of them appear to correspond to the surface geology or off-nadir topography in any way. Furthermore, the continuity is undermined by the fact that radargram M (Fig. 5.9d), whose groundtrack coincides exactly with that of G, shows no apparent reflections that resemble those seen in radargrams F, G or H. Considered along with the erratic morphologies of the reflections, this strongly suggests that the F, G and H reflections are not subsurface reflections as they would be expected to be seen in all radargrams that pass over this location, supporting the hypothesis that they may arise entirely from ionospheric effects.

5.3.6 Ionospheric distortion in the Ma'adim Vallis radargrams

The influence of the ionosphere is an important factor that must be considered when interpreting MARSIS radargrams. MARSIS performs subsurface studies optimally on the nightside, since the dayside ionosphere does not allow the propagation of frequencies below 3.5 MHz (the typical peak plasma frequency of the ionosphere on the dayside [*Safaeinili et al.*, 2007]) thereby limiting penetration capabilities [*Picardi et al.*, 1998]. The waves that do reach the surface on the dayside will be both attenuated and dispersed by the ionosphere [*Safaeinili et al.*, 2007]. The dispersion is caused by the frequency dependence of the radio wave propagation speed in the ionosphere [*Budden*, 1985] and acts to 'smear out' surface and subsurface reflections. The escalating effect of this dispersion on the surface reflection as Mars Express passes from the nightside to the dayside is shown in *Safaeinili et al.* [2007].

Despite the fact that the subsurface mode of MARSIS is mainly active on the nightside, it does sometimes remain in operation a short distance into the dayside hemisphere. The possibility that the elevated daytime ionospheric plasma frequency might play a role in the production of the reflections seen in the Ma'adim Vallis region was explored by comparing the solar elevation angles for radargrams with and without reflections (shown in Table 5.2). Of the radargrams that did show reflections, all but

one were obtained on the nightside. Of the radargrams that did not show reflections, three were obtained on the nightside whereas two were obtained on the dayside, albeit at solar elevation angles of less than 10°. This indicates that no clear relationship exists between the ionospheric plasma frequency and the appearance of reflections in the radargrams: reflections were present and absent in both daytime and nighttime radargrams.

Table 5.2. Sun elevation angles during the times at which radargrams over Ma'adim Vallis were recorded. For radargrams with reflections, the elevation angles displayed are those that existed at either end of the reflection; for radargrams without reflections, the elevation angles displayed are those that existed at either end of the radargram, the limits of which are shown in Fig. 5.11 (N end is at 15°52'29"S, S end is at 35°39'59"S).

Radargram ref. letter	**Reflections seen?**	**Sun elevation at N end of reflection/radargram (°)**	**Sun elevation at S end of reflection/radargram (°)**
H	Y	-31.90	-31.19
B	Y	-30.69	-28.79
E	Y	-29.37	-28.25
D	Y	9.65	4.99
G	Y	-27.25	-17.64
A	Y	-20.31	-18.79
C	Y	-21.96	-15.96
F	Y	-8.47	-8.94
I	N	-28.06	-26.69
M	N	7.90	-0.94
L	N	7.76	0.49
K	N	-24.85	-15.87
J	N	-3.25	-6.59

The ionosphere can affect the radio waves transmitted by MARSIS in ways other than dispersion and attenuation. *Krymskii et al.* [2004] described results of the Radio Science experiment aboard Mars Global Surveyor that indicated a correlation between the variability of ionospheric parameters and crustal magnetic field direction [*Mitchell et al.*, 2001]. These observations were confirmed by the Active Ionospheric Sounding (AIS) experiment on MARSIS, which recorded the delay times to echoes of radio waves reflected off the ionosphere as a function of frequency [*Nielsen et al.*, 2007]. Two traces were often present in spectrograms of the Martian ionosphere: one corresponding to reflections from the nadir, the other originating from a localized reflector in the ionosphere. *Gurnett et al.* [2005] and *Nielsen et al.* [2007] found that the localized

reflectors are associated with regions of near-vertical crustal magnetic fields, which create steep cusps in the electron density in the ionosphere.

Safaeinili et al. [2007] mapped the near-global distribution of the total electron count in the ionosphere on the nightside. The data provide a global view of the relationship between the crustal magnetic field and the electron content in the ionosphere on the nightside. *Safaeinili et al.* [2007] reported the presence of cusp-like regions of high electron concentrations similar to those described by *Nielsen et al.* [2007], and interpreted them as being caused by the connection of solar wind to the Martian nightside ionosphere. They observed that these regions frequently occur where the crustal magnetic field has a large vertical component, consistent with the hypothesis of *Nielsen et al.* [2007].

This study suggests that the cusp-like regions of elevated electron concentration in the ionosphere may play a role in producing the reflections seen in radargrams C to H. The Ma'adim Vallis region is located in a part of Mars with elevated crustal magnetic anomalies, with the most intense magnetic crustal sources (producing maximum magnetic anomalies >100 nT at 400 km altitude) lying in the Terra Sirenum region, which has Ma'adim Vallis situated at its northern boundary [*Acuña et al.*, 1999; *Connerney et al.*, 2005]. These strong crustal magnetic anomalies have often been found to have a large vertical component [*Safaeinili et al.*, 2007]. The anomalies exist as long, E-W-aligned bands of alternating upward- and downward- pointing field lines that extend over several tens of degrees of longitude. It is therefore expected that the ionosphere in this region would have high concentrations of the cusp-like features predicted in *Nielsen et al.* [2007].

There is a possibility that the radio waves that are yielding the anomalous Ma'adim Vallis reflections are being affected by a process illustrated in Fig. 5.14. This process is adapted from a mechanism described in *Nielsen et al.* [2007], which involves the paths of off-nadir radio waves being reflected off the sides of ionospheric cusps where the electron column is pushed up over the magnetic anomaly. Figure 5.14 of this study instead proposes a situation whereby the anomalous Ma'adim reflections arise by ionospheric refraction of off-nadir waves reflected off the planet's surface rather than by reflection of the waves off the ionospheric inhomogeneity itself. The figure indicates how this could generate a parabolic or hyperbolic reflection in MARSIS data, as the refracted waves would initially have low time delays at the edge of the cusp, which

subsequently lengthen as MARSIS moves towards the centre of the cusp, and shorten as it moves away from the centre. If such ionospheric cusps were present in the Ma'adim Vallis region, the mechanism could explain the exaggerated parabolic and hyperbolic morphologies of the reflections seen in radargrams C to H, yet might not explain as well the shallower, flatter morphologies of the reflections seen in radargrams A and B. The fact that a number of the reflections are blurred may be an indication that off-nadir waves with different off-nadir angles are being refracted to varying extents by the ionospheric inhomogeneity, and therefore travelling on paths of varying lengths, resulting in varying time delays for the consequential reflections.

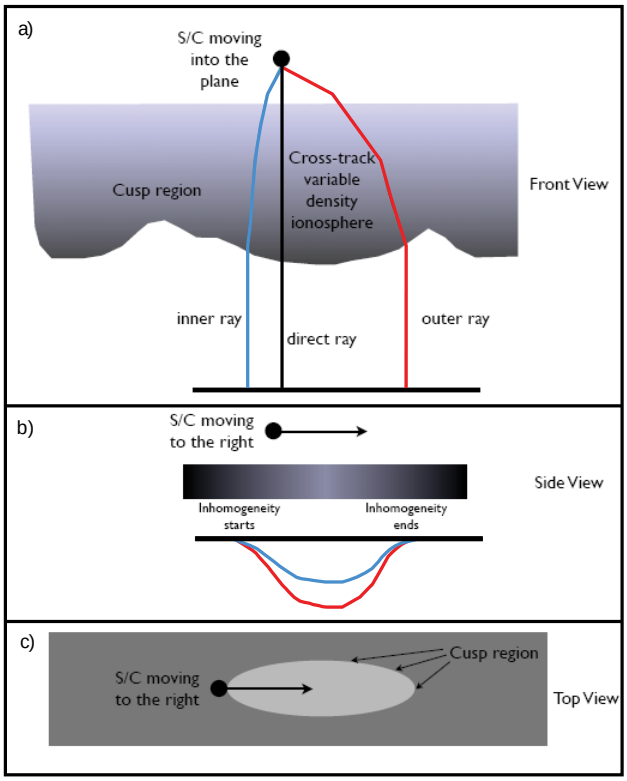

Figure 5.14. Schematic of a proposed mechanism for the production of the anomalous morphologies of the Ma'adim reflections. MARSIS radio waves of varying off-nadir angles are refracted to varying extents by ionospheric inhomogeneities, and as such travel on paths of varying distances to the surface before they are reflected back. The magnitude of the refraction varies as Mars Express progresses through the inhomogeneity. (a) Front view. (b) Side view. (c) Top view.

Figure 5.15 (following two pages). Both maps cover the same area mapped in Fig. 5.11 of this study. (a) Map of the absolute strength of the radial magnetic field, derived from a model provided by *Langlais et al.* [2004]. Bright areas are regions where the magnetic field is vertical. (b) Detail of the electron density distribution map shown in *Safaeinili et al.* [2007]. Black areas represent data gaps. TEC is Total Electron Count. The locations of MARSIS reflections (with accompanying orbit reference letters) are overlaid on both maps.

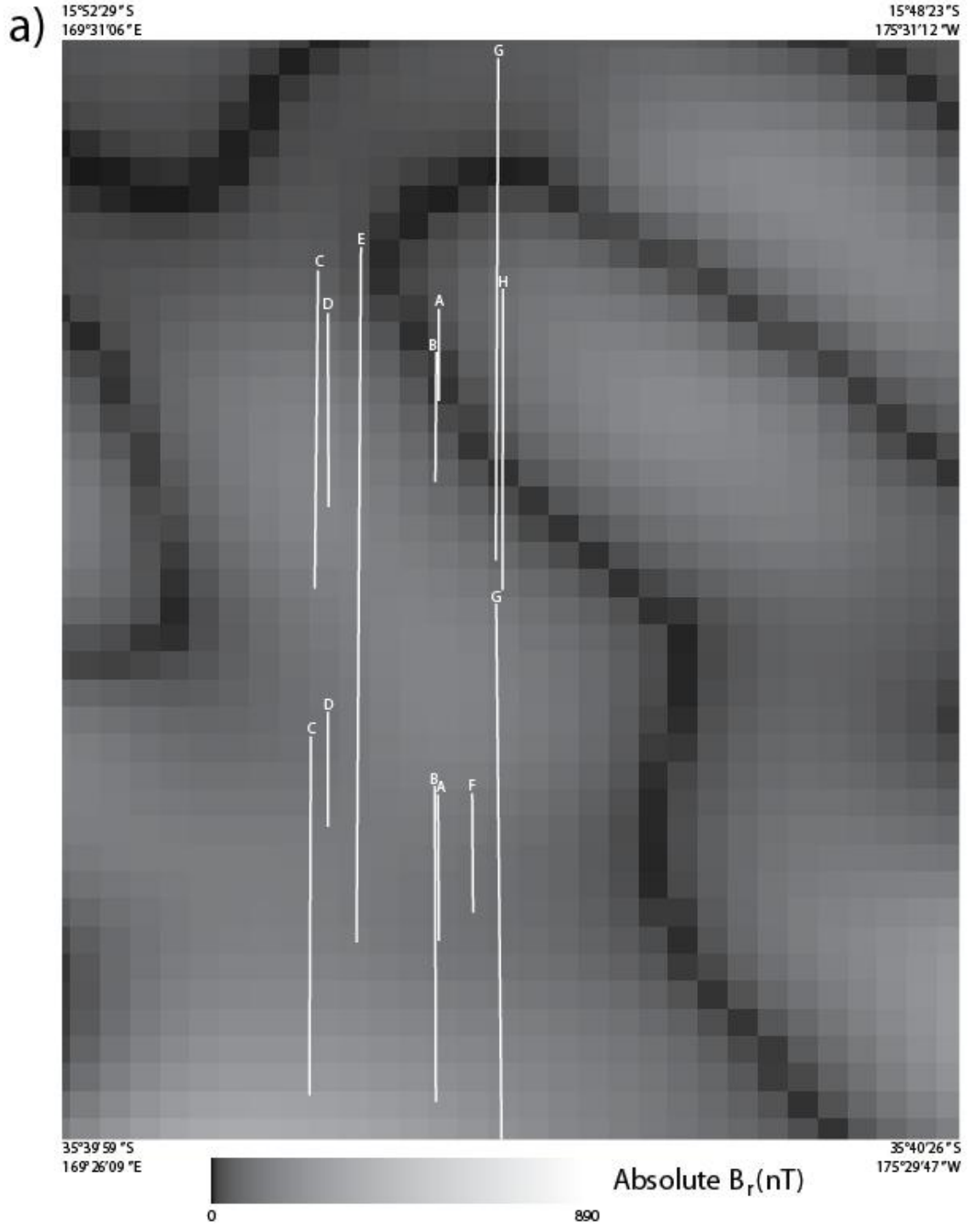
a)
15°52'29"S
169°31'06"E
15°48'23"S
175°31'12"W
35°39'59"S
169°26'09"E
35°40'26"S
175°29'47"W
G
E
C
D
A
B
H
G
D
C
B
A
F
Absolute B_r(nT)
0
890

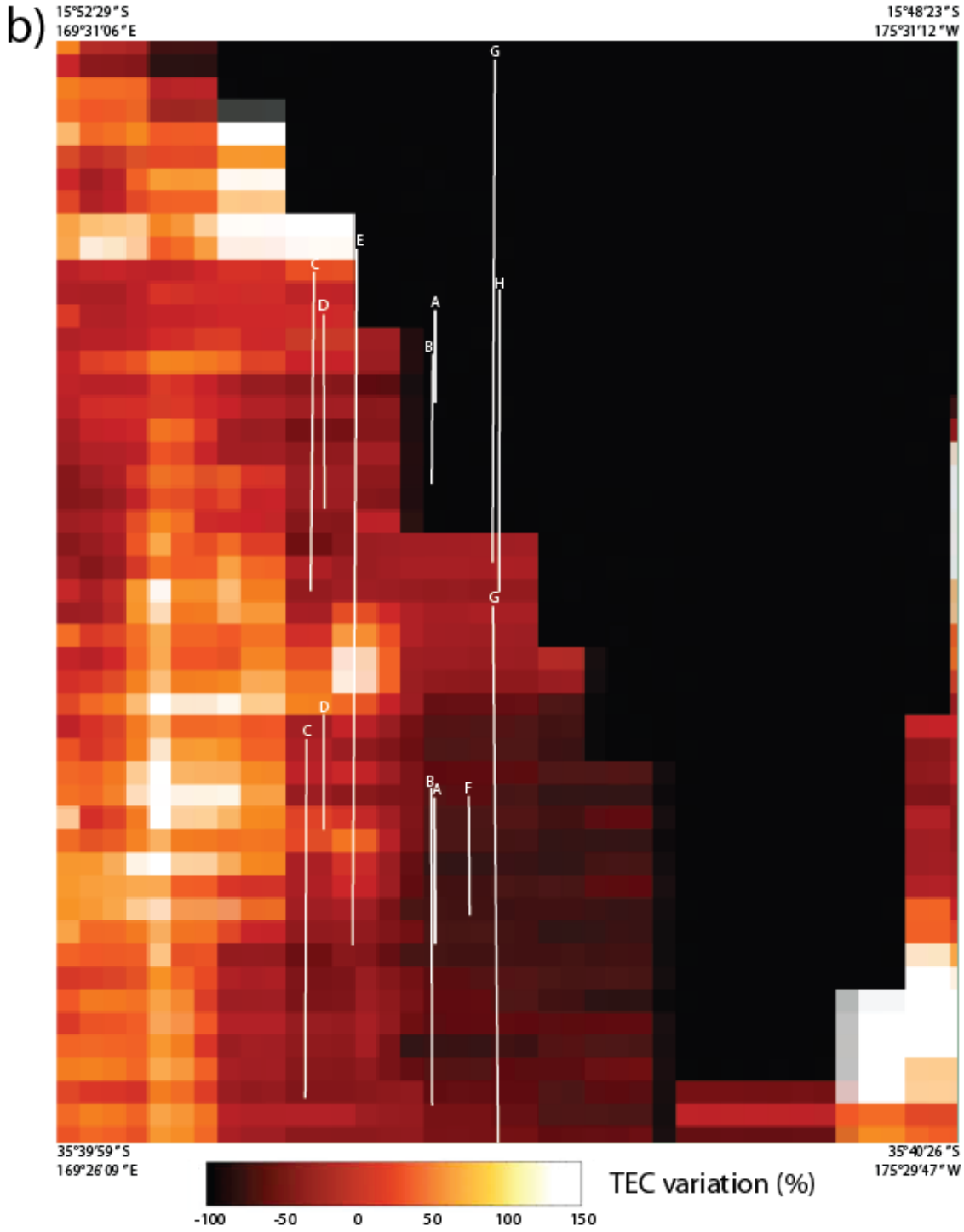
b)
15°52'29 "S
169°31'06 "E
15°48'23 "S
175°31'12 "W
G
E
C
H
D
A
B
G
D
C
B
A
F
35°39'59 "S
169°26'09 "E
35°40'26 "S
175°29'47 "W
TEC variation (%)
-100
-50
0
50
100
150

Figures 5.15a and 5.15b, respectively, superimpose the locations of the MARSIS reflections on maps of the radial component of the magnetic field and of the relative electron distribution (originally shown in *Safaeinili et al.* [2007]) whose areas correspond to the same area of the map in Fig. 5.11 of this study. Figure 5.15b shows that elevated electron counts exist in the west and south-east corner of the Ma'adim Vallis region, whereas the centre and south of the map show intermediate electron counts. Virtually the whole of the east and north sections of the map are obscured by a large data gap. The most striking correlation is that the locations of the dips in reflections C, D and E correspond well to a prominent peak in the electron density that reaches >100 km across. The large parabola in reflection E occurs directly in the centre of the feature, whereas the other two reflections exist to the west of the centre. This raises the possibility that off-nadir MARSIS signals may be being interfered with in a manner consistent with the previously described model.

No such ionospheric inhomogeneities characterize the areas where reflections A, B, F, G and H occur (although half of G and most of H are occupied by the data gap). If these reflections are assumed to result from ionospheric interference, then perhaps the electron density distribution does not remain static, thus explaining why these reflections occur in regions thought to have low ionospheric electron densities as mapped by *Safaeinili et al.* [2007]. Direct penetration of solar wind into the atmosphere (and hence ionosphere) of an unmagnetized planet is a viable form of interaction between the two [*Michel*, 1971]. Therefore, as the flux of solar wind arriving at Mars fluctuates due to changing solar activity, localized elevations in electron concentration may form and disperse at different locations in the ionosphere, perhaps amplifying the concentrations of pre-existing inhomogeneities. This would make the inhomogeneities in the ionosphere transient phenomena, along with the reflections associated with them. Indeed, this may explain why other radargrams obtained in the Ma'adim Vallis area do not display subsurface reflections of any type.

While no data exist for the solar wind pressure at Mars during the times these reflections were recorded, a proxy has been developed by *Brain et al.* [2005] which uses Mars Global Surveyor magnetometer data to extract upstream solar wind pressure for each orbit. This represents the best estimate of the solar wind pressure in the absence of any specific data. *Brain et al.* [2005] assumed that upstream solar wind pressure is directly related to magnetic pressure in the Martian interaction region where the solar

wind current encounters the ionosphere: the higher the solar wind pressure, the higher the magnitude of the subsolar magnetic field as a result of compression of the magnetic field lines. The values for subsolar field strength up to October 2006 (the point at which MGS failed) are published at http://sprg.ssl.berkeley.edu/~brain/proxies/subsolfield.html. This period incorporates the times at which radargrams B, D, E, H, I, L and M were obtained; radargrams A, C, F, G, J and K were obtained after MGS was lost. Table 5.3 shows the approximate field strength at each of the relevant times: all of the radargrams (with the exception of L) were obtained during times of intermediate field strengths (ranging from ~20 T to ~60 T), with the variation in field strength being equally distributed across radargrams with and without reflections. L was obtained during a strong peak in the field strength (80 T). In addition to the fact that it was obtained on the dayside (sun elevation of 0.49° to 7.76°), this may explain the strong interference apparent in the L radargram. Yet the overall absence of any correlation relating the occurrence of reflections and periods of high subsolar magnetic field strength reduces the potential for interference caused by solar wind supplementation of the ionosphere to be their cause. However, there remains the possibility that the magnetic field proxy is not entirely efficient in acting as a proxy for the solar wind pressure. *Brain et al.* [2005] pointed out that the proxy does assume unvarying solar wind pressure conditions over the two hour timespan of the MGS orbit. There is also the potential for an alternative scenario whereby varying solar X-ray fluxes rather than varying solar wind fluxes may be contributing to changing levels of ionization in the ionosphere, yet no X-ray flux data for Mars currently exist.

Table 5.3. Subsolar magnetic field strengths measured by the magnetometer experiment on board Mars Global Surveyor at the times of acquisition of MARSIS radargrams over the Ma'adim Vallis region.

	Radargram ref. letter	**Time of radargram acquisition (UT)**	**Subsolar magnetic field strength (T)**
Radargrams displaying reflections	H	7 Feb 2006, 21:42	~33
	B	10 Feb 2006, 23:39	~60
	E	14 Feb 2006, 01:35	~30
	D	19 May 2006, 10:26	~33
Radargrams not displaying reflections	I	17 Feb 2006, 03:31	~41
	M	10 May 2006, 04:41	~21
	L	13 May 2006, 06:33	~80

A paradox that is not adequately answered by the ionospheric distortion hypothesis is why such strong reflections should cluster in the Ma'adim Vallis region. The electron density distribution in the Ma'adim Vallis region is not unique from that in surrounding areas. Similar interference reflections would be expected in the radargrams further to the south of the Ma'adim Vallis region (35°S to 85°S), where magnetic anomalies are stronger (the strongest reaching >100 nT at 400 km altitude [*Connerney et al.*, 2005]). Such reflections are entirely absent from this southerly region, or indeed from anywhere else in the immediate surroundings. Furthermore, the parabolic reflections occurring in the northern plains exist in an area that displays a generally homogeneous ionospheric electron density, with much smaller-magnitude anomalies relative to the Ma'adim Vallis region. This might indicate that ionospheric distortion is not sufficient on its own to explain the occurrence of these reflections.

The reflections cannot realistically be considered undistorted nadir subsurface reflections primarily because of their eccentric morphologies and the very large time delays to which they extend. Even if the surface layer were comprised of an exotic, low-attenuation geological material such as ice or high-porosity rock (which is not the case based on the results of the geological mapping of the Ma'adim Vallis area), it is virtually impossible that the radio waves could penetrate to such high time delays due to volume scattering alone. Further evidence against the reflections originating from the subsurface in any way (whether distorted or undistorted) is that there are additional radargrams devoid of subsurface reflections between and near those radargrams displaying strong reflections, combined with the abrupt disappearance of the reflections in radargrams to the east and west of longitudes 177°E and 173.5°E respectively. The echo strength of the reflections is too high and the spacing between reflections (in combination with their large lateral extents) too close to explain the absence of the reflections in radargrams I to M as a consequence of varying dielectric contrasts at the interface. Thus, while no definite relationship has been detected between the appearance of the reflections and ionospheric electron content or solar activity, these facts appear to decisively undermine a subsurface origin. While there is the potential for temporal variability in the properties of the ionosphere, none should exist for the subsurface.

5.4 Summary

MARSIS has succeeded in resolving subsurface reflectors associated with the bases of three large scale surficial deposits on Mars: the Polar Layered Deposits, the Dorsa Argentea Formation, and the Medusae Fossae Formation. These observations have allowed accurate measurement of the volumes of these deposits, as well as deduction of their compositions and physical properties. Other reflections with quite different morphological and distributional characteristics are observed elsewhere around the planet, most notably spread across the northern plains and within the Ma'adim Vallis region. These reflections frequently display parabolic and laterally extensive morphologies, and are erratically distributed, often being located directly adjacent to 'barren' radargrams with no reflections present within them. The morphologies of the northern plains reflections are consistent with the theory that they represent off-nadir reflections from the rims of buried basins, yet the fact that some radargrams that pass over the inferred buried basins display no subsurface reflections whatsoever calls this into doubt.

A detailed examination of the Ma'adim Vallis reflections has been conducted, and has proposed that while a minor quantity of the reflections may be originating from subsurface interfaces (i.e. those underneath Eridania Planitia), most of them are in fact off-nadir echoes from the surface that have been refracted by high concentrations of charged particles in the ionosphere. An ionospheric electron density map created by *Safaeinili et al.* [2007] has shown that a region of elevated electron density coincides with the location of a number of the parabolic reflections. However, this hypothesis does suffer from ambiguity associated with the erratic timing of the occurrence of the reflections, and the fact that similar reflections are not seen in areas with similar electron density anomalies. Furthermore, the morphologically comparable northern plains reflections occur in areas where the electron density is generally homogeneous and presents much smaller-magnitude anomalies relative to the Ma'adim Vallis region. The Ma'adim Vallis and northern plains reflections therefore exemplify the ambiguities that can beset interpretation of MARSIS data, problems that are exacerbated by the failure of the monopole antenna.

Chapter 6
The Failure of MARSIS to Detect Aquifers and Associated Implications for the Martian Water Budget

6.1 Introduction

A notable aspect of MARSIS data to date is the absence of any deep, continuous reflectors that might indicate the interface between dry or ice-rich rock and an aquifer. Detecting such a boundary was the primary motive behind flying the MARSIS instrument, and as such their complete absence is highly significant with respect to speculations about the water inventory of the Martian subsurface, as well as speculations about the penetration capabilities of MARSIS. This chapter aims to reassess the penetration capability of MARSIS based on the estimates of previous studies, as well as on an original estimate. The aquifer detection ability of MARSIS will be reconciled with a model of the expected distribution of ice and water within the Martian crust using current best estimates for various crustal physical parameters, and from this the significance of the absence of deep reflectors with respect to constraining scenarios for water and ice in the subsurface will be assessed.

6.2 Previous estimates of the MARSIS aquifer detection depth

Previous studies that have focused on the potential penetration depth of MARSIS (specifically in its 2 MHz frequency band) have used a disparate range of methods and models to predict its capabilities, with varying results. The following text summarizes the various methods and conclusions of each study that has focused on estimating the ability of MARSIS to detect an aquifer beneath a surface layer of porous basalt mixed with ice.

***Picardi et al.* [1998] and *Picardi et al.* [2004]:** These studies assessed the penetration capabilities of MARSIS through theoretical modelling by evaluating the backscattered power from surface and subsurface layers under different surface backscatter scenarios. A scenario of ice-saturated porous crust over water-saturated porous crust was regarded as being representative of the crustal profile. *Picardi et al.* [1998] considered andesite and basalt as end-member crustal host-rock compositions, whereas *Picardi et al.* [2004] instead considered three theoretical 'main reference categories' with dielectric properties based on those of terrestrial volcanic, sedimentary

and metamorphic rocks. *Picardi et al.* [1998] considered a surface porosity of 35%, whereas *Picardi et al.* [2004] considered a range varying between 20% and 50%. For each of their hypothesized crustal scenarios, *Picardi et al.* [1998] and *Picardi et al.* [2004] modelled the associated Fresnel reflectivities (Γ) and surface backscatter coefficients (σ_0) in order to determine the maximum depth at which a detectable signal would be returned to MARSIS from the subsurface interfaces. Both studies discounted the effect of volume scattering; *Picardi et al.* [1998] regarded the megaregolith as containing an insufficient component of clasts of the size range to scatter signals at MARSIS wavelengths (62-158 m). For various MARSIS frequencies, *Picardi et al.* [1998] quantified the expected level of return from the subsurface interface compared with surface returns arriving at the same time, allowing determination of the maximum detection depth of MARSIS for different scenarios of MARSIS frequency and rms slope. The aquifer detection depth for an ice-saturated over water-saturated interface beneath a basaltic surface layer of dielectric constant 7.1 and loss tangent 0.014 reaches 4000 m at a frequency of 1.9 MHz. *Picardi et al.* [2004] estimated separate detection depths for the subsurface scenarios depending on whether the dynamic range of MARSIS or the surface clutter was the limiting factor for penetration. In the case of an interface of the same type modelled by *Picardi et al.* [1998], detection depths ranged from <1000 m to 4000 m depending on the limiting scenario and the variation in the parameters associated with each.

***Heggy et al.* [2001] and *Heggy et al.* [2003]:** The studies of *Heggy et al.* [2001] and *Heggy et al.* [2003] employ methods related to those of *Picardi et al.* [1998] and *Picardi et al.* [2004], but investigate the potential penetration depth of MARSIS more thoroughly by experimentally constructing geoelectrical profiles representative of the Martian subsurface. This was accomplished by measuring the electric permittivity and magnetic permeability of well-defined mixtures of basaltic, volcanic and sedimentary materials known to exist on Mars at porosities and temperatures appropriate for the upper crust. The backscattered radar echo arising from each profile was then simulated at the 2 MHz frequency band in order to assess the magnitude of the radar attenuation, as well as the ability of MARSIS to identify a subsurface aquifer/ice layer among surrounding geological materials. The effects of iron oxides and evaporates were considered, but the effects of volume scattering and off-nadir surface clutter were not.

Heggy et al. [2001] created a single profile representative of the general Martian subsurface, consisting of an uppermost iron oxide-rich dust layer 10 m thick, overlying volcanic layers of fractured basalt and lava flows 190 m thick, which themselves overlie sedimentary deposits 200 m thick. These are in turn underlain by a layer of permafrost 2.1 km thick, which melts at a depth of 2.5 km, yielding an aquifer. *Heggy et al.* [2001] considered the penetration depth to be a function only of the dielectric constant and magnetic permeability for a given sounder frequency. *Heggy et al.* [2001] measured the effect of sounding frequency on the real and imaginary parts (ε' and ε'') of the dielectric constant and magnetic permeability of powders (50% porosity, representing the surface dust layer) and compacted pellets (20% to 30% porosity, representing the underlying fractured basalt and lava flows) of different Martian analogue volcanic materials. These measurements were used to calculate the penetration depth as a function of frequency for various volcanic samples for a maximum MARSIS dynamic range of 60 dB. *Heggy et al.* [2001] suggested that the high values obtained for the loss tangent of the altered basaltic rock (0.1 to 0.9) due to compaction with depth, and the iron-oxide-rich surface dust layer, would both act to strongly attenuate the radar signal. The penetration depth for a permafrost mixture of 50% basalt and 50% water ice ($\varepsilon' = 6$, $\tan\delta = 0.05$) was 394 m. This does not reach the 2.5 km depth at which the top of the aquifer is hypothesized to exist in the model by a large margin and assuming that the general geoelectrical model is valid for most of Mars, *Heggy et al.* [2001] suggested that water in the Martian crust cannot be easily detected by MARSIS.

Instead of creating a single, generalized profile, *Heggy et al.* [2003] considered four geoelectrical models corresponding to specific Martian sites where recent fluvial-like features suggest the presence of near-subsurface ground ice and perhaps liquid water. These models corresponded to possible local stratigraphy, and each was referred to specific locations on Mars where the subsurface could correspond to the model, yet large uncertainties still exist about the composition and nature of the subsurface material. Three of the models corresponded to environments where subsurface aquifers may be expected: volcanic areas with high geothermal gradient, outflow channels, and impact crater ejecta in the ice-rich northern plains. The last considered sediments formed by desiccation of an ancient lake. *Heggy et al.* [2003] presented the measured values for the real and imaginary parts of the dielectric constant and magnetic permeability of the volcanic and sedimentary materials interpreted to comprise each

layer for each model. *Heggy et al.* [2003] identified the elevated geothermal gradient model as that for which a radar sounder would have the highest probability of detecting a shallow aquifer. This model features a 10 m thick dust layer overlying 50 m of eroded basalt, which overlies 100 m of porous basalt with interstitial ice, which itself overlies a layer of porous, wet basalt. A significant echo resulting from the dielectric contrast between the ground ice and aquifer was predicted by the simulation, despite the fact that the aquifer is overlain by 160 m of volcanic materials that present a reasonable attenuation factor. *Heggy et al.* [2003] acknowledged that for real data, multiple combinations of geoelectrical subsurface layers could be used to explain a given subsurface reflection, and that the interpretation of a given echo depended on a thorough interpretation of the geological context of the site.

***Farrell et al.* [2009]:** This study appeared four years after MARSIS had commenced sounding operations, with MARSIS not having recorded any subsurface reflections that undoubtedly represented a subsurface water table. *Farrell et al.* [2009] aimed to quantify the conditions of the subsurface that would allow detection of a deep aquifer, and thereby to assess the extent to which a 'null result' rules out the existence of such an aquifer. *Farrell et al.* [2009] considered radargrams obtained over the northern plains, whose surface is relatively smooth by the standards of most Martian terrains, but which still produces a significant degree of off-nadir clutter in the radargrams, manifested as a long echo 'tail' that continues after the peak surface return pulse. *Farrell et al.* [2009] hypothesized that for a subsurface water table to be detected by MARSIS, the echo signal returning from it must have been attenuated to a small-enough degree by the material overlying the aquifer such that it still exceeds the surface clutter-defined noise level. In order to assess the crustal material attenuation required to reduce the aquifer echo power to less than the clutter-defined noise power, *Farrell et al.* [2009] applied a simple crustal model consisting of an icy-basaltic surface layer of a certain thickness overlying an aquifer. Using this model, *Farrell et al.* [2009] assessed what conductivity ranges both allow and disallow aquifer detection for particular surface layer thicknesses. For a surface layer conductivity of 10^{-5} S/m (equivalent to a loss tangent of 0.008), the modelling of *Farrell et al.* [2009] implied that noise from surface clutter would eclipse the signal returning from an aquifer deeper than 2042 m. *Farrell et al.* [2009] considered the attenuation of the signal by the overlying icy-basaltic surface layer to be of a sufficient magnitude such that the lack of an observed

groundwater table detection by MARSIS does not automatically rule out the possibility of the water table's existence.

6.3 Independent estimate of the MARSIS aquifer detection depth

This study aims to independently estimate an aquifer detection depth in the basaltic terrain which characterizes most of Mars through use of the formulae described in Chapter 4; these relate the powers of signals echoed from dielectric boundaries to the dielectric properties of the respective layers and the reflection coefficients of the interfaces between them, as well as to parameters of the MARSIS sounder itself.

The method is based on the determination of the minimum reflected power to which MARSIS is susceptible given the dynamic range of MARSIS and the proportion of the transmitted signal echoed from the surface. The depth of the interface between porous, ice-filled basalt and an aquifer from which such a minimum power would be returned can then be deduced based on the dielectric properties assigned to the respective layers. The model assumes a crustal scenario whereby a surface layer comprising porous basalt with interstitial ice (ε_1 = 6, tan δ = 0.05) overlies a layer comprising porous, wet basalt (ε_2 = 36). The values of the parameters of these materials are laboratory measurements under Martian geophysical conditions taken from the study of *Heggy et al.* [2001], and are relevant to a sounder frequency of 2 MHz.

The dynamic range of the MARSIS sounder represents the ratio between the maximum and minimum powers to which the MARSIS receiver is sensitive. Being a ratio, dynamic range is measured in decibels on a logarithmic scale; a difference in dynamic range of 10 dB represents a difference of a factor of 10 between the maximum and minimum powers. When considering a radargram which displays only the reflection from the surface, the maximum power is defined by that of the surface reflection itself. The dynamic range of the sounder defines the minimum echoed signal power to which the sounder would be susceptible in the given circumstances. In this instance dynamic range is defined by the following formula:

$$L_{dB} = 10\log_{10}\left(\frac{P_s}{P_{ss}}\right) \tag{6.1}$$

where P_s is the power (in W) of the signal reflected from the surface and P_{ss} is the power of the signal reflected from the subsurface boundary. *Jordan et al.* [2009] cited a range of possible values of the dynamic range extending from 40 to 50 dB. P_s can be calculated for the modelled scenario using Eqs. 4.7 and 4.10, where G = 2.1 dB, λ = 149.9 m, H = 525,000 m, and P_t = 5 W. Using a rearrangement of Eq. 6.1, the minimum signal power echoed from the aquifer, P_{ss}, that will be detectable by MARSIS may be calculated. The two-way time delay, τ, to the top of the aquifer from which such a power would be echoed back to MARSIS may be calculated using a rearrangement of the following equation:

$$R_{ss} = \frac{R_s}{1-R_s^2}\sqrt{10^{2.74\pi f \tan\delta} \cdot \frac{P_{ss}}{P_s}} \tag{6.2}$$

where f = 2,000,000 Hz and R_{ss} may be obtained using Eq. 4.9. The depth corresponding to such a time delay may then be calculated using Eq. 4.13.

These formulae do not consider the effect of volume scattering which for most of Mars would be a significant factor considering the heterogeneous nature of the subsurface [*Heggy et al.*, 2006a]. The effect can be accounted for to some extent using the results of *Heggy et al.* [2006a], who display graphically the discrepancy between the theoretical and observed penetration depths as a result of volume scattering with changing frequency for the scoria cone at the Craters of the Moon lava field. For a frequency of 2 MHz, the observed penetration depth represented a ~28% reduction of the theoretical penetration depth. The calculated values of the maximum detection depth of an aquifer may be reduced by this amount in order to attempt to account to some degree for the effect of volume scattering on the MARSIS signals. However, it should be recalled that the Martian crust will be significantly more brecciated and fractured than the lava flow at Craters of the Moon, and that the volume scattering will be of greater significance as a result. The final value derived for the MARSIS aquifer detection depth based on the assumed crustal model, and after consideration of volume scattering, ranges from 387 m to 307 m (for dynamic ranges of 50 dB and 40 dB respectively), with a mean of 348 m. This estimate is compared with those of three of the studies discussed in section 6.2 in Table 6.1.

Table 6.1. MARSIS aquifer detection depth estimates from various studies. Electrical properties of the surface layer are similar but not identical in each case: $\varepsilon_1 = 7.1$, $\tan\delta = 0.014$ for Picardi et al. [2004]; $\varepsilon = 6$, $\tan\delta = 0.05$ for Heggy et al. [2001]; $\varepsilon = 6$, $\tan\delta = 0.008$ for Farrell et al. [2009]; $\varepsilon = 6$, $\tan\delta = 0.05$ for the present study.

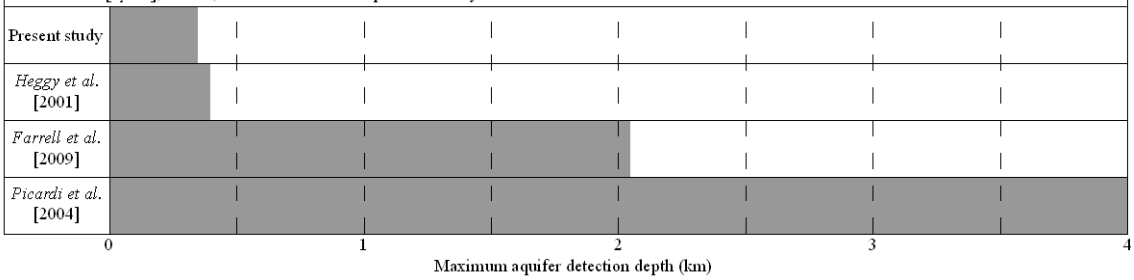

The presence of clays and iron oxide-rich minerals (e.g. hematite and magnetite) in the Martian crust will act to further attenuate radio waves transmitted by MARSIS and reduce its penetration ability, even at low concentrations [*Heggy et al.*, 2001]. The OMEGA and CRISM instruments on the respective Mars Express and Mars Reconnaissance Orbiter spacecraft have recently identified phyllosilicates on Mars, including kaolinite, chlorite, and illite/muscovite [*Poulet et al*, 2005; *Mustard et al.*, 2008]. Data from the Thermal Emission Spectrometer aboard Mars Global Surveyor showed a region interpreted as crystalline hematite, approximately 300 km in diameter, near the equator in Meridiani Planum [*Christensen et al.*, 2000]. The Mars Exploration Rover Opportunity later confirmed that abundant hematite was present in the form of spherules concentrated not only on the surface but also in the sedimentary layers encountered by the rover [*Squyres et al.*, 2004]. Although the subsurface extent of these clays and iron oxide minerals cannot confidently be mapped, it should be assumed that there is always the potential for them to be present in the subsurface to some degree.

6.4 Reconciliation of ground ice observations with absence of MARSIS reflections

The various observations that imply the existence of near-surface ground ice across large swaths of the mid- to high-latitudes on Mars have been discussed in section 1.3.4. The separate lines of evidence include the clustering at mid-latitudes of geomorphological features that appear to have undergone viscous creep [*Squyres and Carr*, 1986; *Squyres et al.*, 1992b; *Holt et al.*, 2008], Mars Odyssey neutron spectrometer measurements that indicate that hydrogen-rich deposits exist within the top metre of soil poleward of ±60° latitude [*Feldman et al.*, 2004], and the direct observation of water ice within the top metre of soil by the Phoenix lander [*Smith*, 2009] and HiRISE camera aboard the Mars Reconnaissance Orbiter [*Byrne et al.*, 2009].

While the ice layer is only directly apparent within the uppermost metre of the soil poleward of ±60° latitude, theoretical considerations suggest that the top of the layer will exist at greater depths at lower latitudes [*Farmer and Doms*, 1979].

MARSIS signals must therefore be penetrating into ice-rich ground across wide swaths of the planet, and the fact that it has been unable to detect a continuous interface at depth that would represent the water table of an aquifer implies two potential scenarios:

1) The ice layer does not extend deep enough to reach the melting isotherm, meaning that all water in the crust is stored as ice.

2) The ice layer does extend deep enough to reach the melting isotherm, but the intervening crustal material attenuates the MARSIS return signal sufficiently for it to be eclipsed by noise.

The validity of each of these potential scenarios depends on the estimate used for the MARSIS aquifer detection depth, as well as on the assumed values for various physical parameters of the crust, as these will influence the expected distribution of ice and water within the crust. While the absence in MARSIS data of any continuous subsurface reflections potentially representing a water table presents an obvious challenge to constraining the subsurface water budget of Mars, the estimate of the MARSIS aquifer detection depth derived by this study can at least be considered in conjunction with modelling of crustal water distribution in an attempt to constrain the extent to which the absence of aquifer reflections seen by MARSIS places a limit on the Martian water budget. The following section describes how the best current estimates for the relevant model parameters have been derived.

6.5 Derivation of values for Martian crustal physical properties

The most prominent study to focus on the subsurface behaviour of water on Mars is that of *Clifford* [1993], which considered the response of a water-rich Mars to climate change and to the physical and thermal evolution of its crust, based on the assumption that Mars possesses a global inventory of water sufficient to both saturate the pore volume of the cryosphere and create a groundwater system of global extent. *Clifford* [1993] noted the existence of the outflow channels, whose distribution, size and range of ages represent evidence that a significant body of groundwater has been present on Mars throughout a significant proportion of its geological history. Based on estimates

of the crustal porosity profile and thermal structure, the latitudinal and vertical distribution of both frozen and liquid water in the crust was modelled by *Clifford* [1993] based on different water inventories. However, since the study of *Clifford* [1993], new measurements and observations have caused the original estimates of some crustal physical parameters to be reassessed. The details of the derivation of relevant crustal parameters are discussed briefly below.

6.5.1 Porosity variation with depth

In order for a global groundwater system to exist on Mars, a suitably porous and permeable layer must exist in which the groundwater can reside. *Clifford* [1993] considered the porosity profile of the Martian crust to be best described by an exponential decline with depth according to Eq. 4.2, with a Martian porosity decay constant of 2.82 km. *Clifford* [1993] considered two porosity profiles: the first is based on a surface porosity of 20%, the same value used for the Moon by *Binder and Lange* [1980]. The second employs a surface porosity of 50%, which is consistent with estimates of the bulk porosity of Martian soil as analyzed by the Viking landers [*Clark et al.*, 1976]. These models yield self-compaction depths (that at which the crustal porosity falls below 1%) of ~8.5 km and ~11 km respectively. *Clifford* [1993] regarded the surface porosity of 50% to be an upper limit for Mars; this study will regard a surface porosity of 35%, a value midway between the two considered by *Clifford* [1993], to be a reasonable value for the generalized Martian surface porosity.

6.5.2 Thermal structure

The Martian cryosphere is defined as the region of the crust where the temperature remains continuously below the freezing point of water [*Fanale*, 1976]. Assuming a solute-free freezing point of 273 K, this condition is satisfied at every latitude below the diurnal skin depth, thereby defining the cryosphere's upper bound. Yet since neither the magnitude of the Martian geothermal heat flux nor the thermal conductivity of the crust are precisely known, the depth to the lower bound of the cryosphere is much less certain [*Clifford*, 1993].

The depth to the base of the cryosphere can be calculated from the steady state one-dimensional heat conduction equation:

$$z = \kappa \frac{T_{mp} - T_{ms}}{Q_g} \tag{6.3}$$

where κ is the thermal conductivity of the crust, T_{mp} is the melting temperature of the ground ice, T_{ms} is the mean annual surface temperature, and Q_g is the geothermal heat flux [*Fanale*, 1976]. T_{ms} is the only variable that is currently known to any accuracy (ranging from 154 K at the poles to 218 K at the equator). The other three variables have associated uncertainties of 20-50% [*Clifford*, 1993]. *Clifford* [1993] attempted to constrain the ranges for each of these variables; more recent observations and measurements have altered the original estimates of certain parameters since the study of *Clifford* [1993].

Thermal Conductivity: *Clifford and Fanale* [1985] highlighted four principal factors that affect the thermal conductivity of terrestrial permafrost: bulk density, degree of pore saturation, particle size, and temperature. The effects of bulk density and pore saturation on the thermal conductivity of permafrost are well understood, but the effects of particle size and temperature are less well known. Because a direct measurement of the bulk thermal conductivity of the Martian megaregolith is lacking, *Clifford* [1993] inferred a likely range of values using laboratory measurements of the thermal conductivity of samples of frozen soil and basalt from several previous studies, which were conducted at temperatures between 253 and 273 K [*Clifford et al.*, 2009]. *Clifford* [1993] concluded that the spatially variable thermal conductivity of the Martian cryosphere likely fell within the range of 1-3 W m^{-1} K^{-1}, with a probable mean value of 2 W m^{-1} K^{-1}. However, *Clifford et al.* [2009] considered the temperatures at which these measurements were conducted to be higher than those that would be expected in the Martian cryosphere, and instead proposed a column-averaged, though latitudinally variable, thermal conductivity closer to 3 W m^{-1} K^{-1}. As a compromise, this study will regard a thermal conductivity of 2.5 W m^{-1} K^{-1} to be a reasonable bulk value for the Martian cryosphere.

Melting temperature: The melting temperature of ground ice can be depressed beneath 273 K by pressure and solute effects, although the effect of pressure is minimal, whereas that of dissolved salts is comparatively large. Therefore, at locations where the cryosphere is in direct contact with groundwater, the presence of dissolved salts may

significantly reduce the thickness of frozen ground. The existence of various salts in the Martian regolith has been supported by numerous datasets, both remote and in-situ. Results from the inorganic chemical analysis experiments on board both Viking Landers led to NaCl, $MgCl_2$ and $CaCl_2$ being regarded as the most likely candidates for regolith salts, with eutectic melting temperatures of 252 K, 238 K and 218 K respectively [*Clark and Van Hart*, 1981]. Chlorine salts have also been identified in soil by the Phoenix lander, and include Mg^{2+}, Na^{+}, K^{+}, Cl^{-} and ClO_4^{-} [*Kounaves et al.*, 2009]. However, other recent acquisition of compositional data, notably by the OMEGA instrument aboard Mars Express [*Langevin et al.*, 2005; *Gendrin et al.*, 2005] and the Opportunity Mars Exploration Rover [*Tosca et al.*, 2008], has revealed that sulphur may be more abundant on the planet than previously thought, especially in the form of Mg-, Ca- and Fe-sulphates [*Langevin et al.*, 2005; *Gendrin et al.*, 2005]. This is significant as the chemical and thermodynamic stabilities of $CaCl_2$ and $MgCl_2$ (which are among the strongest melting temperature depressors) under Martian ambient conditions have been doubted, particularly in the presence of abundant sulphates [*Clark and Van Hart*, 1981]. Sulphates themselves are ineffective depressors of melting temperatures (by ~5 K) [*Clark and Van Hart*, 1981]. This would leave NaCl as the most likely chloride to be found within the crust that would significantly depress the melting temperature of brines (by 21 K). Therefore, although the melting temperature of Martian brines will vary with changing chemistry across Mars, a value roughly in the region of 252 K (that for a brine based solely on NaCl) is deemed to be plausible, but the value will probably be slightly lower due to the presence of other chloride and/or sulphate salts in the brine.

Geothermal heat flux: A wide range of estimates exist for the Martian geothermal heat flux. *Solomon and Head* [1990] noted that if Mars were to lose heat at the same rate per unit mass as the Earth, it should have a mean global heat flux of ~31 mW m^{-2}, a value that agrees fairly well with the independently derived estimates of *Fanale* [1976] (30 mW m^{-2}), *Toksöz and Hsui* [1978] (35 mW m^{-2}), *Turcotte et al.* [1979] (33.5 mW m^{-2}) and *Stevenson et al.* [1983] (28.0 to 32.4 mW m^{-2}). Yet other published estimates have been both considerably higher and lower: thermal modelling by *Toksöz et al.* [1978], *Davies and Arvidson* [1981] and *Schubert and Spohn* [1990] suggest a current heat flux as high as 40-45 mW m^{-2}, whereas *Solomon and Head* [1990] estimated values as low as 15-25 mW m^{-2}, based on rheological estimates of lithospheric thickness and mantle heat production inferred from the composition of the SNC meteorites. More

recently, the study of *Phillips et al.* [2008] noted that data from the MARSIS and SHARAD orbiting radar sounders indicated that the mass loads of the north and south PLDs deflected their underlying substrates minimally (maximum deflection of ~200-250 m). *Grott* [2008] noted that such a negligible deflection would imply a very thick Martian lithosphere (~300 km) and a geothermal heat flux much less than 20 mW m^{-2}. Such a low value cannot be reconciled with theoretical considerations of the planet's thermal evolution based on the abundance of radioactive elements as determined from SNC meteorites [*Wänke and Dreibus*, 1994] and on the expected relationship between planetary heat flux and radius [*Grott*, 2008]. The issue of the geothermal heat flux is therefore unresolved, and direct evidence in the form of drilling and in situ temperature logging is needed to reach a conclusive answer. If the evidence for a higher heat flow than that implied by the MARSIS data is considered, then a globally averaged value of 25 mW m^{-2} may be regarded as a reasonable value for the present day heat flow.

6.6 Modelling the Martian cryosphere and groundwater distribution

The values regarded by this study to be reasonable estimates for geothermal heat flow (Q_g = 25 mW m^{-2}), crustal thermal conductivity (k = 2.5 W m^{-1} K^{-1}) and ground ice melting temperature (T_{mp} = 252 K) were entered into Eq. 6.3, and depths to the base of the cryosphere were calculated for each mean annual surface temperature value at particular latitudes, as described in Table 4 of *Clifford* [1993]. This yielded a depth to the base of the cryosphere varying from 3.2 km at the equator to 9.6 km at the poles (see Table 6.2), an increase reflecting the corresponding poleward decline in mean annual surface temperature. In addition, the surface porosity value of 35% was entered into Eq. 4.2, resulting in a self-compaction depth of 9950 m.

The determination of the self-compaction and melting isotherm depths leads to the question of how much groundwater could potentially be stored in the remainder of the porous megaregolith beneath the melting isotherm. This value depends on the water inventory present within the Martian crust. *Clifford* [1993] noted that the primary thermodynamic sink for subsurface water on Mars is the cryosphere – if the total amount of water present is less than the pore volume of the cryosphere then all the water will be stored within the cryosphere as ice [*Soderblom and Wenner*, 1978]. However, if the amount of water present were sufficient to saturate the pore volume of the

cryosphere with ice, then any remaining water will drain beneath the melting isotherm and saturate the lowermost porous regions of the crust [*Clifford*, 1981].

Table 6.2. Latitudinal variation of cryospheric thickness as determined using updated values for the various parameters in the thermal model of Clifford [1993] (Eq. 6.3).

Latitude (°)	Mean annual surface temperature (K)	Depth to base of cryosphere (km)
90	154	9.6
80	157	9.3
70	167	8.3
60	179	7.1
50	193	5.7
40	206	4.4
30	211	3.9
20	215	3.5
10	216.5	3.35
0	218	3.2
-10	216.5	3.35
-20	215	3.5
-30	211	3.9
-40	206	4.4
-50	193	5.7
-60	179	7.1
-70	167	8.3
-80	157	9.3
-90	154	9.6

Mars is not a perfect sphere, with a surface of considerable heterogeneity and topographic relief. Assuming that the relation of porosity to depth as described in Eq. 4.2 is applicable to the entire planet, the depth of self-compaction will mirror the gross variation of the surface topography, defining an irregular, impermeable lower bound for the occurrence of groundwater. Such a uniform porosity profile and depth of self-compaction across the whole planet is very unlikely, but must be assumed given that present data do not allow the variation in these parameters to be characterized. Groundwater percolating downwards through the porous zone of the crust will fill the lowest portions first, with these portions lying beneath the surface areas with the lowest topography.

The cryospheric model is depicted in Fig. 6.1, which shows a pole-to-pole cross section of the crust where the surface elevation has been averaged as a function of latitude, with the self-compaction depth existing at a constant depth of 9950 m beneath it. The cross section illustrates the potential stratigraphic relationships between surface topography, ground ice, and groundwater, for liquid groundwater inventories whose

volumes correspond to GELs of 10 m and 100 m in depth. For a groundwater system in hydrostatic equilibrium, the water table conforms to a surface of constant gravitational potential, whereas the distribution of ground ice is controlled by the local surface temperature and magnitude of the geothermal gradient. Aquifers would most likely be detected beneath low-lying areas such as the northern plains and the Hellas basin, where the porous megaregolith would be expected to extend to its deepest levels, assuming a uniform porosity profile.

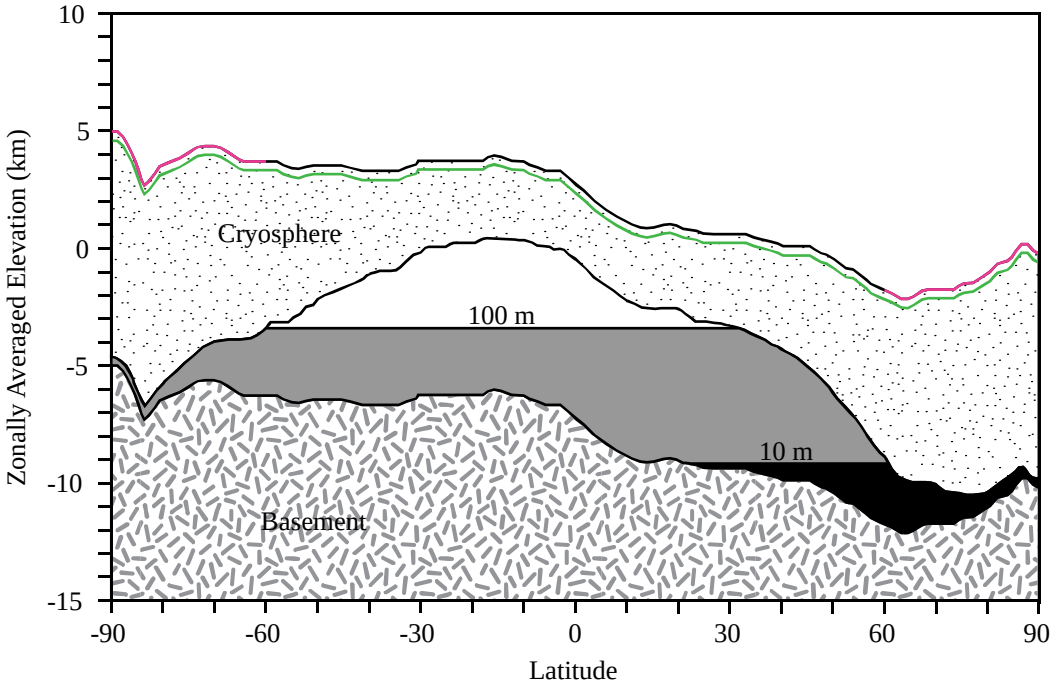

Figure 6.1. Pole-to-pole cross-section of the Martian crust illustrating the potential relationship between topography, ground ice, and groundwater. Profile has been created using the model of *Clifford* [1993] and employs the various thermal and porosity parameters as described in section 6.5. Surface elevations are averaged as a function of latitude based on the USGS Mars Digital Terrain Model. Levels to which a global aquifer system would rise are shown for groundwater GELs of 10 m (in black) and 100 m (in grey); the levels assume that the groundwater is in hydrostatic equilibrium, that the local porosity profile of the crust is given everywhere by Eq. 4.2, and that the self-compaction depth mirrors the gross variation of surface topography at a constant depth of 10 km beneath the surface. Green line represents the maximum MARSIS aquifer detection depth of 348 m at a sounding frequency of 2 MHz as estimated by this study. Purple lines that overlap with the surface profile at latitudes poleward of ±60° represent the latitude range across which the Mars Odyssey Neutron Spectrometer has detected hydrogen-rich deposits ranging between ~20% and 100% water-equivalent by mass.

Superimposed on the profile is the mean MARSIS aquifer detection depth of 348 m as estimated by this study. It can be seen that at no point anywhere along the profile does the penetration depth extend to the base of the cryosphere, which is 3.2 km deep at its shallowest. If the generalized model of *Clifford* [1993] is regarded to be valid, signals transmitted by MARSIS would therefore not return an identifiable echo from an

aquifer to the sounder from any location on Mars. Yet the absence of MARSIS reflections also indicates that there are evidently no locations on Mars where anomalously shallow aquifers are present; such shallow aquifers would be permitted to exist in localized areas where anomalous values for one or more thermal parameters allowed shallow melting (e.g. a volcanic zone that features an anomalously high heat flux, or a local concentration of a volatile or combination of volatiles that greatly depresses the melting temperature of ice). The shallow ice layers that are apparent across much of the high latitudes are either everywhere frozen to at least a depth of ~350 m beneath the surface, or simply do not extend to more than that depth.

6.7 Summary

MARSIS has failed to detect any continuous, deep subsurface reflections that might be representative of the water table of an aquifer, the main purpose for which it was designed. By deriving an original estimate of the aquifer detection depth of MARSIS and updating the model of the Martian cryosphere and porous megaregolith used by *Clifford* [1993], this study has attempted to determine the extent to which the absence of MARSIS reflections may have helped to constrain the depth of a large-scale aquifer system as proposed by *Clifford* [1993], and therefore place constraints on the Martian water budget.

Reconciliation of current estimates for crustal physical parameters with the estimate for the MARSIS aquifer detection suggests that MARSIS signals will not be able to return an interpretable echo back to the sounder from an aquifer that exists below the base of the cryosphere at any location on the planet. This assertion is based on the generalized model for the global cryospheric thickness proposed by *Clifford* [1993], and does not consider localized areas where anomalous variations in the thermal properties of the crust might allow aquifers to form at particularly shallow depths. MARSIS has essentially succeeded in ruling out the presence of any anomalously shallow aquifers that exist within ~350 m of the surface, which is only marginally helpful with regard to constraining Martian subsurface groundwater inventories. Results from the Phoenix, Odyssey and MRO missions have shown that ground ice located just beneath the surface evidently does exist across large swaths of the high northern and southern latitudes, yet the absence of MARSIS reflections means that it remains unknown as to whether this layer melts at depth or expires before it reaches the base of the cryosphere.

With respect to constraining the quantity and location of subsurface water and ice on Mars, the results of the MARSIS investigation are limited. It follows that MARSIS has not succeeded in showing where, how and to what extent water and ice may have influenced volcanic processes in Mars' history, both ancient and recent.

Chapter 7
Fieldwork Investigations of Icelandic Rootless Cone Groups and Implications for the Formation Conditions and Modification Histories of Martian Rootless Cones

7.1 Introduction

Current knowledge regarding the formation of rootless cones on Earth and Mars, and their relevance to the central premise of this thesis, has been discussed in Chapter 1, and the methodology of ground penetrating radar has been described in Chapter 4. This chapter describes the localities in Iceland where the fieldwork was performed, the progress of the surveys, and their results. The results are used to determine the formation and modification histories of the Icelandic cones and how these relate to the environments in which they are situated, and to assess the implications for the evolution of Martian cones based on observations of their morphologies and environmental settings.

7.2 Field localities

The Álftaver district in south-central Iceland includes a field of rootless cones that formed on the Eldgjá flow of 933-34 AD [*Larsen*, 2000; *Thordarson et al.*, 2001], which was emplaced on the Mýrdalssandur jökulhlaup flood plain through which the Skalm river flows. The jökulhlaups originated from Mýrdalsjökull glacier, 30 km to the west, which overlies Katla caldera. Figure 7.1a shows an aerial photograph of the study area at Álftaver with the locations of the four cones surveyed highlighted. Cones 1, 2 and 3 were located within a small group of cones at the locality of Útsýnisskifa, whereas cone 4 was located ~3 km to the west. The cones are shown in Figs. 7.2a-d, and their coordinates and dimensions are listed in Table 7.1 (note that the diameters and heights refer to the topography of the cones at the surface and do not consider buried structure apparent in the radar profiles). The cones in the Útsýnisskifa group displayed morphologies typical of those seen at Álftaver: small craters and steep 'witches' hat' profiles. Cone 4 was located in a field of cones characterised by larger craters and more convex flanks. Vegetation was sparse at the Útsýnisskifa locality, comprising a light to moderate covering of moss on the surface, but the more westerly cone field displayed a consistent covering of grass. Bordering the south margin of the cone field, there exists

an area occupied by craggy mounds consisting of decimetre-sized clasts to blocks reaching several metres wide that are separated by interstitial sand-sized ash (Fig. 7.2e).

Mývatn in northeast Iceland includes a field of rootless cones that exist around the shores of the lake, and within the lake itself, where they form small islands. The cones formed on the Younger Laxá flow that was emplaced into the lake ~1800-2300 years ago (considerably earlier than the Eldgjá flow), and originated from the Threngslaborgir-Lúdentsborgir fissure zone located 5 km to the east of the shore of Mývatn [*Thorarinsson*, 1953]. Cone 5, the example Mývatn cone that was surveyed during the 2007 expedition, is shown in Fig. 7.2f, and its location, situated 800 m from the northwest shore of Mývatn, is shown in Fig. 7.1b. Mývatn cones display morphologies similar to that of cone 4 at Álftaver, having large crater/cone diameter ratios. The cones are spaced at similar intervals to those at Álftaver, yet more frequently overlap with each other. The terrain at Mývatn is mostly covered by thick, heath vegetation.

Figure 7.1 (below and following page). (a) Aerial photograph of the field locality in the Álftaver rootless cone group, with the four surveyed cones highlighted in white. White 'X' marks where alluvial sediments from the banks of the river Skalm were collected. On land, lighter areas are vegetated whereas darker areas are covered in volcanic ash, whether as fall deposits or river bank deposits. Image source: Landmælingar Íslands. (b) Satellite image of Mývatn, with the location of cone 5 highlighted by a white 'X'. Dark areas are water. Image source: GoogleEarth.

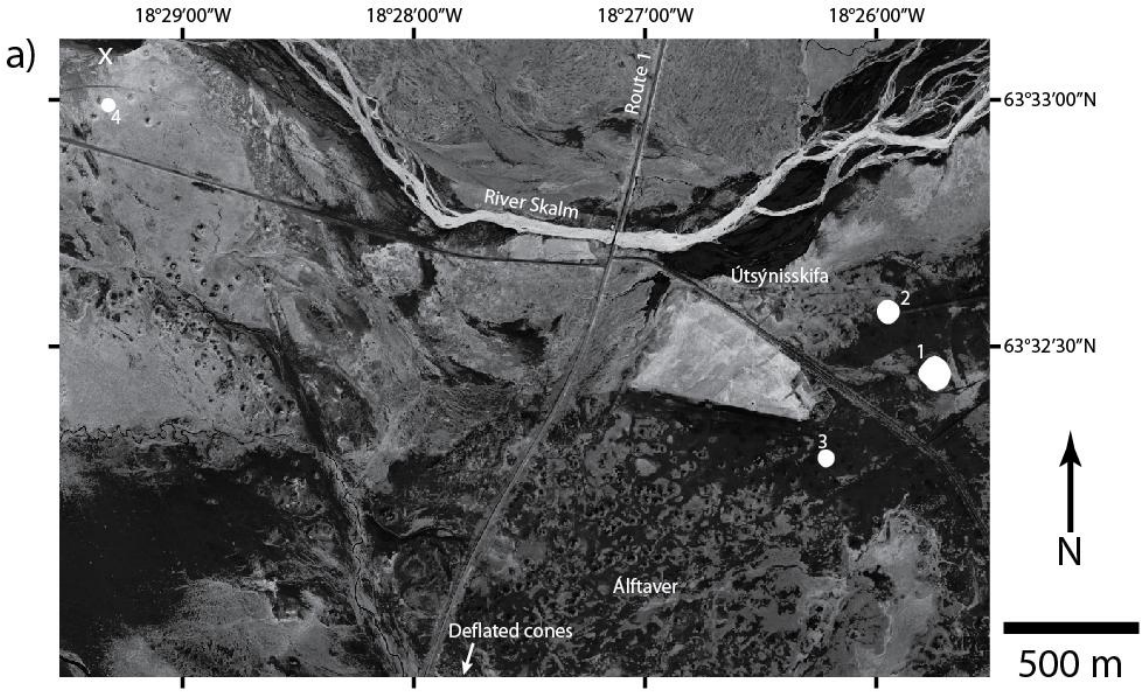

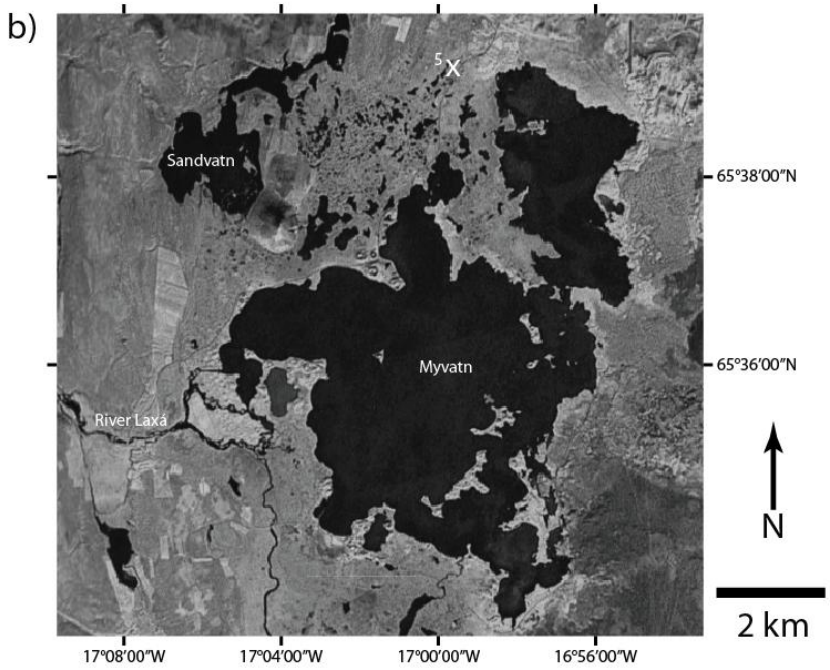

Figure 7.2 (below and following page). Views of field localities at Álftaver and Mývatn. (a) Cone 1, diameter 123 m. (b) Cone 2, diameter 84 m. The gently sloping outer apron occupies the foreground. (c) Cone 3, diameter 61 m. The gently sloping outer apron occupies the foreground. (d) Cone 4, diameter 48 m. (e) Severely deflated class C cones existing in the south-western region of Álftaver. Mounds in the middle ground are tens of metres across and several metres high. (f) Cone 5, diameter 47 m. (g) Dense concentration of sub-cm to several cm-sized scoria and spatter clasts on the lower flanks of cone B. Pen for scale. (h) View comparing the profiles of cones 1 and 2. (i) A cone, proximal to cone 4, that has half-collapsed as a result of erosion by a tributary of the River Skalm, exposing the interior structure. Cone is ~8 m high. (j) A deflated cone existing in the central Álftaver region whose morphology is intermediate between those in Figs. 7.2a-c and Fig. 7.2e. Mýrdalsjökull, the nearest portion of which is 20 km distant, is seen in the background. Sheep for scale. (k) View of cones in the western region of Álftaver. Dashed white lines highlight the boundaries of dark, tapering jökulhlaup deposits occurring in the lee of rootless cones. Length of the left-hand deposit is ~90 m.

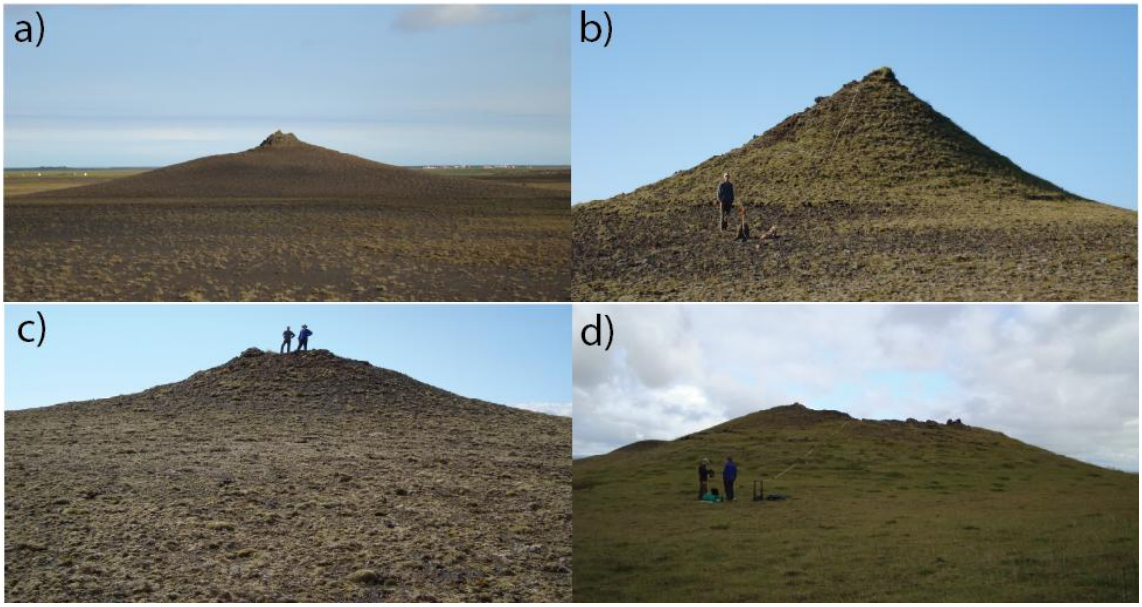

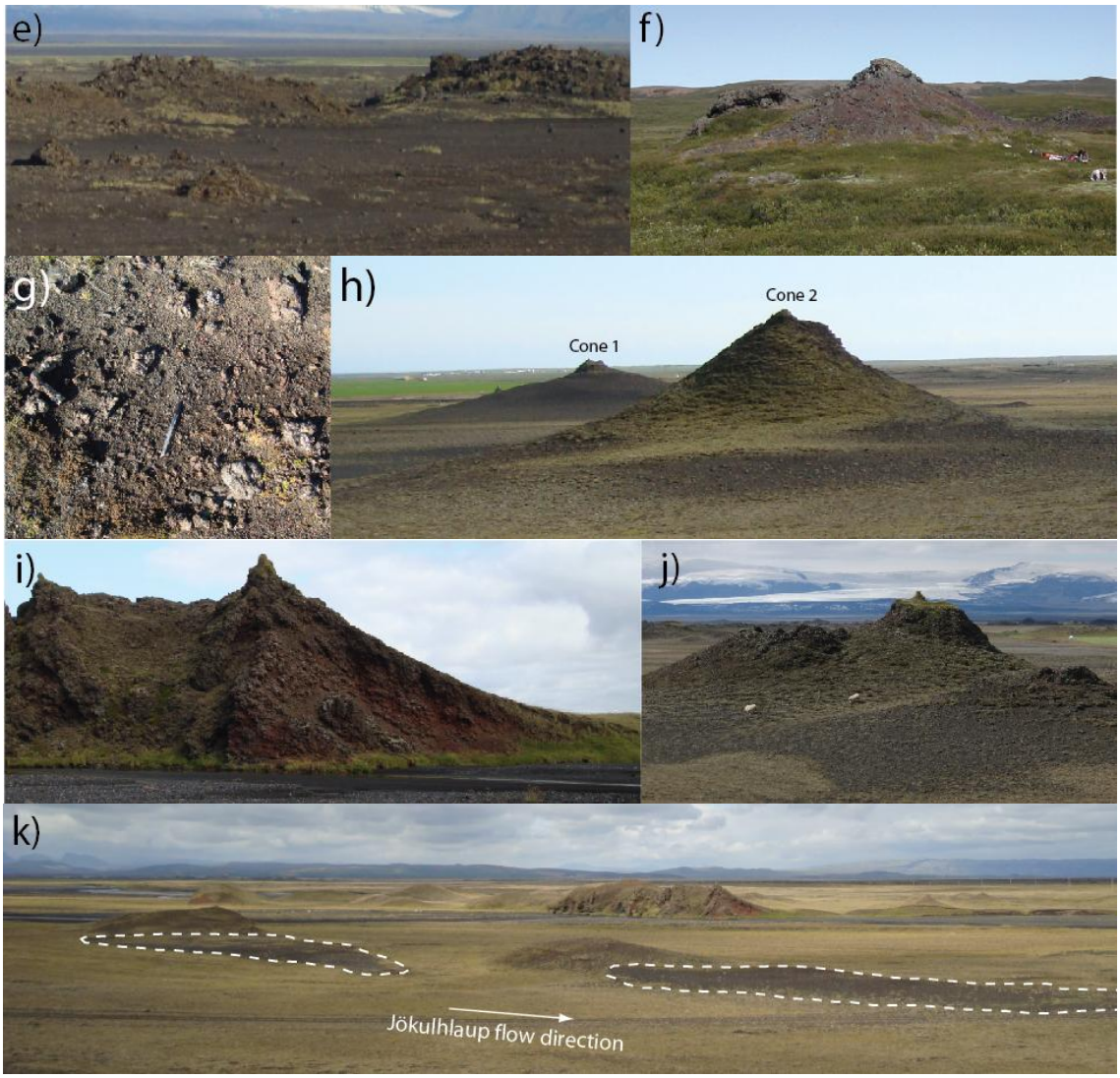

Table 7.1. Coordinates and statistics of cones 1-4 at Álftaver and cone 5 at Mývatn.

Cone No.	Latitude	Longitude	Cone Diameter (m)	Cone Height (m)	Crater Diameter (m)	Crater/Cone ratio	Central cone slope (°)	Outer apron slope (°)
1	63°32'27"N	18°25'42"W	123	10.4	3.2	0.03	45	11
2	63°32'36"N	18°25'54"W	84	10.7	5.7	0.07	35	13
3	63°32'17"N	18°26'11"W	61	5.4	5.6	0.09	19	11
4	63°33'02"N	18°29'18"W	48	5.0	17.1	0.36	20	-
5	65°39'09"N	16°59'40"W	47	6.4	10.8	0.23	22.5	-

7.3 Survey and analysis details

The GPR surveys were performed using a Sensors & Software, pulseEKKO PE100 instrument, with 200 MHz antennas and a 1000 volt transmitter. The antennas were deployed in a perpendicular-broadside configuration (antennas parallel and oriented perpendicular to the survey line), separated by 50 cm and were moved in 10 cm increments along the survey line. Settings of the GPR for the Álftaver cone field surveys were as follows: the time window was set at 350 ns, the number of stacks at 32,

the AGC at a maximum value of 200, and the sampling interval at 800 ps. The same settings applied to the Mývatn cone field surveys, except that the time window was set at 250 ns, the number of stacks at 64, and the antennas were moved in 20 cm increments. The GPR penetrated to a depth of 9 metres.

Survey line orientations were selected such that the lines were everywhere several tens of metres from other cones, in order to try to minimise interference from the deposits of different cones. The GPR data were recorded in the field on a laptop computer with output in real time, and once meaningful reflections had ceased to be returned, it was deemed appropriate to terminate the survey. At Álftaver, once the radar survey was complete, a topographic survey was performed along the GPR survey line using a Sokkia Set 5 total station in order to fit the radar profile to the topography. In addition to allowing topographic calibration of the GPR data, this allowed accurate measurement of the diameters and heights of the cones. At Mývatn the topography was measured using a dumpy level.

In addition to the cone surveys, eight common midpoint (CMP) surveys were also performed on relatively flat terrain on the lower slopes of the cones: seven surveys were performed at Álftaver, one at Mývatn. These involved positioning the two antennas 20 cm on either side of the midpoint of the survey line and moving them further apart in 20 cm increments until they reached 20 m apart, at which point the survey was terminated. This produced a graph of antenna separation plotted against EM pulse travel time, with the ground wave represented by a steeply dipping line on the graph. The gradient of this line represents the velocity of the EM pulse in the ground at the surface in the field locality.

Following the surveys, the raw GPR data was entered into the EKKO_View Deluxe™ GPR processing and display program and subsequently corrected for the topography and the measured ground wave and subsurface velocities. The migration processing technique [*Ulriksen*, 1982] was also applied to the data using pulseEKKO 2D F-K migration.

Upon completion of the radar surveys at Álftaver, pits located at points along the survey lines were dug into the flanks of the cones in an effort to ‘ground-truth’ the radar profiles by comparing the actual rock facies encountered with the facies apparent in the profiles, as well as to collect rock samples for later analysis.

The grain-size distribution of samples collected in the pits was determined using an automated sieve-shaker that sorted the grains into sieves of different coarseness. The samples were first dried overnight in a drying oven to eliminate any water from them that would influence the mass and consolidation of the samples. The grain-size distribution of the samples can be used as an aid to stratigraphic profiling to infer whether certain layers encountered in a particular pit also outcrop in pits dug elsewhere on the cone flanks by comparing the grain-size distributions of layers between pits. The grain-size distribution of a particular tephra layer is also a property that is diagnostic of the explosiveness of the lava-water interaction during formation of the facies – finer grain sizes should be indicative of more violent interaction that fragments the lava into smaller pieces.

7.4 Results

One complete traverse of each cone at Álftaver was accomplished with the GPR, with the exception of cone 1, where two surveys were performed across the cone at right angles to each other. At cones 1 and 2, the steep, rocky outcrops of agglutinate spatter at the cone summits prevented the passage of the survey all the way across, so two separate GPR surveys were performed on opposite flanks. The survey of the Mývatn cone extended up only one flank of the cone and could not progress over the deep and steep-sided crater. The seven common mid-point surveys performed on the cones at Álftaver yielded a mean groundwave velocity of 0.095 m/ns, whereas the one performed at Mývatn yielded a velocity of 0.110 m/ns, with an associated error of ±0.006 m/ns at each site. *Reynolds* [1997] cites a velocity of 0.106 m/ns for radio waves through wet basalt, a value that resembles the measured ones. Comparing these values is justified by the fact that the basaltic tephra encountered in the pits was moist, although the top few tens of centimetres were desiccated.

Figure 7.3 displays the fully processed and annotated radar profiles for all the cones described in this paper. The inferred extents of various structural components of the cone are indicated for each cone, based on the radar facies observed and their correlation to the surface geology. Given that the frequency of the antenna is 200 MHz with a pulse period of 5 ns, the pulse wavelength will be 0.475 m at Álftaver and 0.55 m at Mývatn (±0.03 m at each site). The vertical resolution of the radar profile can be

taken as being one quarter of the wavelength [*Reynolds*, 1997], meaning that the vertical resolution is 0.119 m at Álftaver and 0.138 m at Mývatn (±0.0075 m at each site).

The interpretation of the GPR profiles is based on identification of discrete radar facies, which are defined as mappable, three-dimensional sedimentary units comprised of reflections whose parameters differ from those of adjacent units [*Jol and Bristow*, 2003]. The radar facies seen in the cones are described and interpreted in Table 7.2 – note that the radar facies displayed in the table are ideal examples. Different radar facies may sometimes appear to grade into each other; this gradation is indicated by dotted lines marking boundaries in the radar profiles in Fig. 7.3. Based on the configurations of different radar facies seen in the GPR data and observations of the morphologies of the cones, three distinct morphological cone classes were established to exist at Álftaver and Mývatn. Schematics of the different classes are shown in Fig. 7.4. The three morphological classes exist in fairly clearly defined zones within Álftaver and cones of different morphologies do not generally coexist. Class A cones are located within the central and eastern regions of the cone group, class B cones are located within the western regions of the group, and class C cones are located within the southern regions of the group. Class B cones are virtually ubiquitous at Mývatn. The characteristics of each class are described in the following sections, with reference to the surveyed cones.

Figure 7.3 (following two pages). Annotated radar profiles of cones 1-4 surveyed at Álftaver and cone 5 surveyed at Mývatn. The various radar facies are described and interpreted in Table 7.2. Where the boundaries between facies are indistinct, interpolated boundaries are represented by dotted lines. Dashed lines highlight the profiles of the rocky summit regions of cones 1 and 2 which the GPR survey could not traverse. Location and depths of pits dug into the cone flanks are shown as red lines. (a) N-S-aligned survey across cone 1. (b) W-E-aligned survey across cone 1. (c) N-S-aligned survey across cone 2. (d) NE-SW-aligned survey across cone 3. (e) S-N-aligned survey across cone 4. (f) W-E-aligned survey across cone 5.

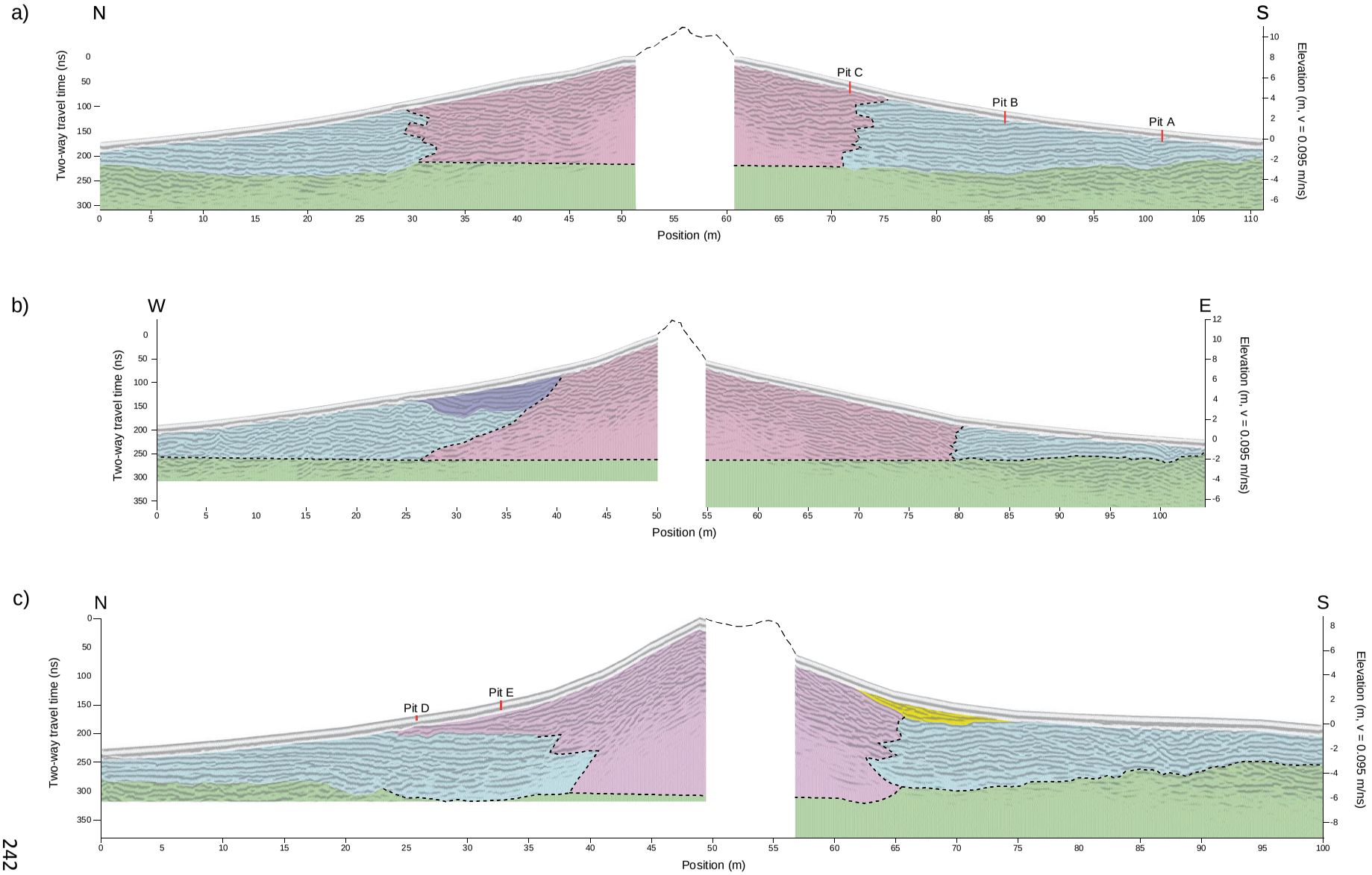
a)
N
S
Pit C
Pit B
Pit A
Two-way travel time (ns)
Elevation (m, v = 0.095 m/ns)
Position (m)
b)
W
E
Two-way travel time (ns)
Elevation (m, v = 0.095 m/ns)
Position (m)
c)
N
S
Pit D
Pit E
Two-way travel time (ns)
Elevation (m, v = 0.095 m/ns)
Position (m)

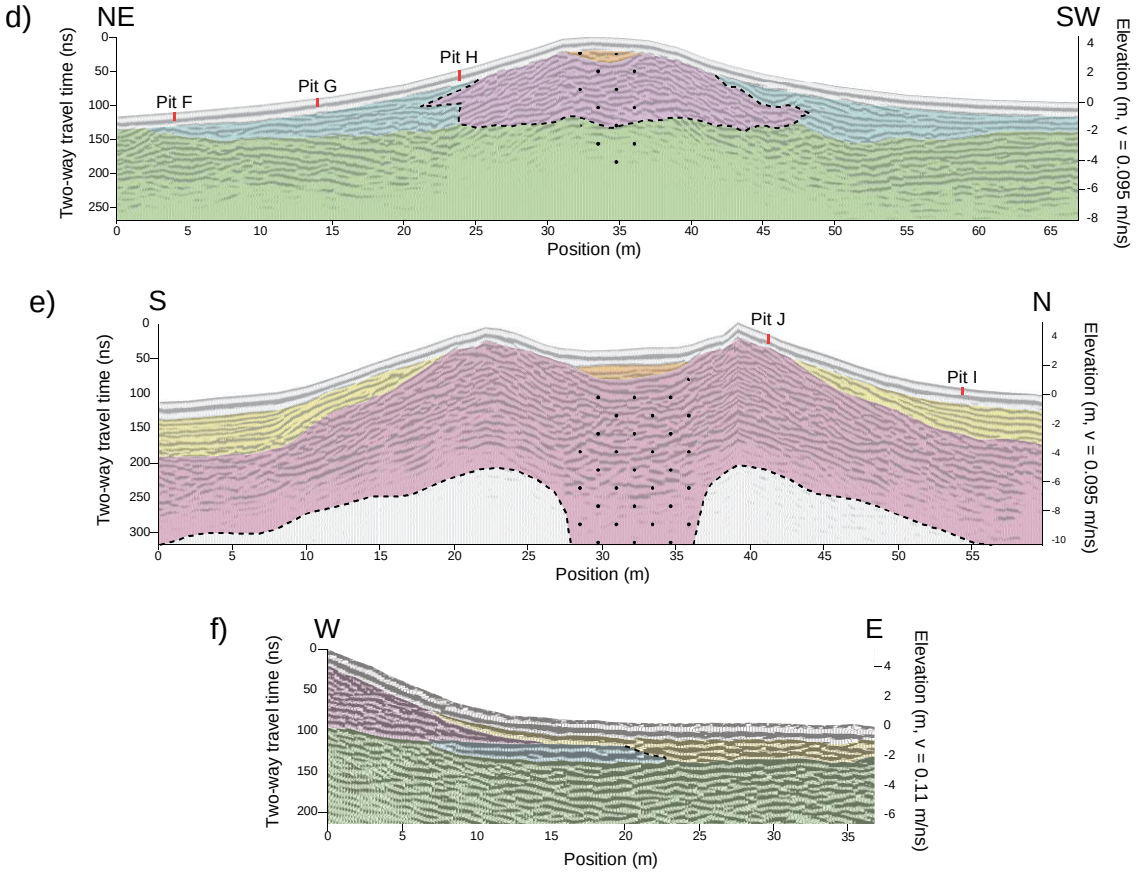

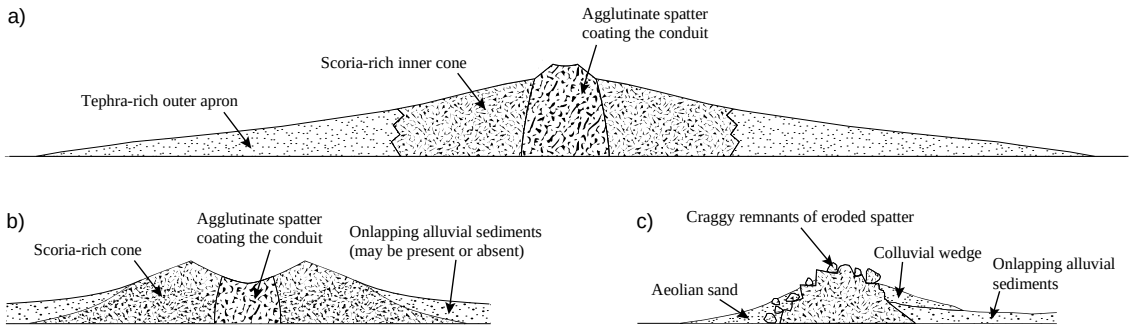

Figure 7.4. Schematics of the three morphological classes of rootless cones identified at Álftaver and Mývatn, drawn to the same scale. (a) Class A, which incorporates surveyed cones 1, 2 and 3. (b) Class B, which incorporates surveyed cones 4 and 5. (c) Class C.

Table 7.2. Appearances, descriptions and interpretations of radar facies identified within the radar profiles.

No.	Appearance	Description	Interpretation	Colour
1		Reflections generally dip away from the center of the cone. Reflections are undulating, discontinuous and frequently truncate each other.	Facies represents dipping layers of spatter/scoria-rich material that comprises the body of the steep, inner cone. Frequent truncation of reflections is indicative of heterogeneity and a high proportion of coarse-grained material.	
2		Successions of horizontal, continuous reflections that infrequently truncate each other. Reflections sometimes curve upwards and taper off as they approach the centre of the cone.	Facies represents ash-rich material that comprises the gently sloping, outer apron of the cone. Uninterrupted nature of reflections indicates homogeneity and a paucity of coarse-grained material in the facies.	
3	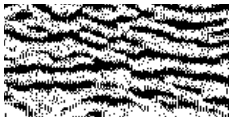	Successions of horizontal, undulating, generally discontinuous reflections that often truncate each other.	Facies represents the lava flow that underlies all the cones. Undulating, discontinuous nature of the reflections indicates heterogeneity within the flow.	
4		Successions of horizontal, often discontinuous, undulating, coarse reflections that extend beneath the central crater and curve upwards on either side, grading into the finer reflections that characterize facies 1 of the cone flanks.	Facies represents spatter filling the conduit that leads upwards to the central crater. Gradation of this facies into the surrounding facies 1 indicates little heterogeneity between the two.	
5		Successions of horizontal, continuous reflections that exist in the central crater of the cone. Reflections are truncated by the reflections of facies 1 that lies underneath.	Facies represents colluvium (erosional debris) and possibly other wind-blown debris that has collected within the central crater of the cone.	
6		Successions of continuous reflections that curve upwards and taper off as they approach the center of the cone. Reflections do not truncate each other, but they are truncated by or onlap onto the cone flanks beneath.	Facies represents onlapping alluvial deposits or erosional talus, which coat the flanks of the cone and taper upslope. Continuous nature of reflections indicates a paucity of coarse-grained material in the facies.	
7		Successions of continuous reflections that curve upwards and taper off as they approach the center of the cone. Reflections do not truncate each other, but they are truncated by the cone flanks that surround them.	Facies is confined to the north flank of cone A, and while similar in appearance to facies 6, its configuration (surrounded by rather than resting on the cone flank) suggests that it may represent slumped flank material.	

Pits were dug at different points along the survey lines for each cone at Álftaver: three pits for cones 1 (on the N-S-aligned line) and 3, and two pits for cones 2 and 4. Figure 7.5 shows graphic logs for each pit. Table 7.3 collates the median grain sizes and associated standard deviations for each of the 17 sampled layers, as well as for a sample of alluvial sand collected from the banks of the River Skalm. The deepest pit dug had a depth of 80 cm, which only partly extends below the region on the radar profiles that is 'masked' by the air and ground waves, which generally eclipse the top ~50 cm of the subsurface. Consequently, most of the stratigraphy observed in the pits could not be directly related to the radar profiles.

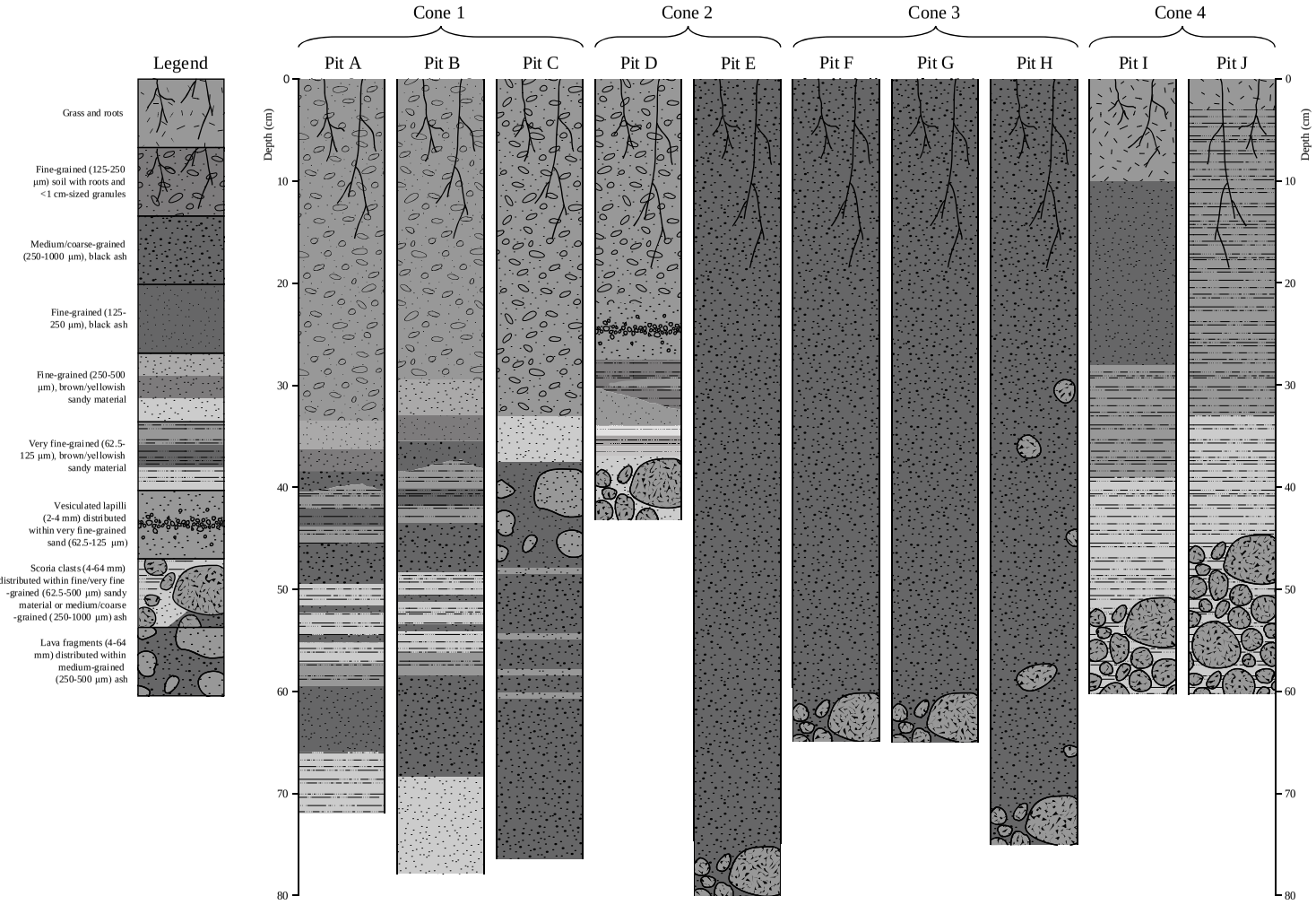

Figure 7.5. Stratigraphic columns derived from pits dug into the flanks of the four cones survyed at Álftaver. Locations of columns are shown as red lines on the radar profiles in Fig. 7.3. Geological facies and their associated grain sizes are described in the legend. Grain size descriptions use the Udden-Wentworth classification scheme [*Wentworth*, 1922]. Clast sizes shown in legend are drawn to scale.

Table 7.3. Median grain sizes and standard deviations of individual layers encountered in the pits dug into the cones at Álftaver. Smaller standard deviations are indicative of more poorly sorted layers. Layers in bold are ash layers interpreted to originate from exterior sources; layers in italics are ash layers interpreted to be intrinsic to the cones.

Cone No.	Pit	Layer depth (cm)	Median grain size (μm)	% of sample mass within 1 standard deviation from the mean grain size
1	A	**40**	**313**	**12.58**
		65	**248**	**12.97**
		78	107	15.12
	B	**60**	**346**	**11.49**
		75	188	14.36
	C	40	38,688 and 189	9.59
		60	*623*	*7.91*
2	D	15	229	8.06
		25	3381 and 68	15.04
		28	73	20.83
	E	*35*	*438*	*7.78*
3	F	*30*	*444*	*9.19*
	G	*30*	*362*	*8.22*
	H	*30*	*350*	*9.28*
4	I	**15**	**227**	**15.26**
		40	96	9.71
	J	60	40,888 and 69	16.67
River sand sample			**304**	**9.94**

7.4.1 Class A cones

Cones 1, 2 and 3 at Álftaver exist within this class (Figs. 7.2a-c). The morphologies of class A cones are characterized by broad, gently sloping (<8°) outer flanks which comprise most of the diameter of the cone. The flanks often become steeper towards the centre of the cone (<25°), and the cone may be capped by a steep summit outcrop of rheomorphic spatter that harbors a central crater. The summit spatter outcrop was found to be steeper and craggier on the south flank compared with the north flank for all three class A cones surveyed. The surface of the flanks is covered by a high density of centimetre- to decimetre-sized, coarse, angular, dark scoria clasts which increase in abundance and often become redder nearer the summit (Fig. 7.2g).

Some variety is observed between the profiles of the three cones. Cone 1 features gently sloping outer flanks that extend nearly to the summit of the cone, at which point they are interrupted by the steep summit spatter outcrop. The outer flanks of cone 2 do not extend as far up the sides of the steep, central spatter cone, and the difference in gradient between the slopes of the central cone and outer flanks is smaller for cone 2 (22°) compared with cone 1 (34°) – the profiles can be compared directly in Fig. 7.2h.

Cone 3 presented a more subdued profile than the other two cones; a steep summit outcrop is virtually absent, with a shallow crater bounded by coarse rheomorphic spatter at its rim existing in its place.

Two perpendicularly-aligned radar surveys were performed across cone 1 (Figs. 7.3a and b), and one each was performed across cone 2 (Fig. 7.3c) and cone 3 (Fig. 7.3d). The radar profiles of class A cones display horizontal, continuous reflections representing radar facies 2 existing within the outer, gently sloping portions of the cone deposits. Steeper, more discontinuous reflections characteristic of radar facies 1 occupy the inner cone, and the transition between the two radar facies can range from being ambiguous (e.g. Fig. 7.3b) to well-defined (e.g Fig. 7.3c). The distance from the cone centre at which the transition between the two radar facies occurs can be very variable, even within the same cone as shown in Figs. 7.3a and b. The boundary between these two cone radar facies and the underlying radar facies 3 can range from being easily identifiable (e.g. Fig. 7.3d) to virtually invisible (e.g. Fig. 7.3b). The horizontal reflections of radar facies 2 are almost always truncated by the air/ground waves.

The upper western flank of cone 1 (seen in Fig. 7.3b) displays a distinct zone of radar facies 7 reflections, which appear to sag downwards. The boundaries that separate radar facies 7 and radar facies 2 from radar facies 1 join smoothly, indicating that radar facies 7 may represent a slumped section of radar facies 2. On the south flank of cone 2, at the base of the steep, central cone, onlapping reflections representative of radar facies 6 exist, and which truncate any reflections that encounter them. Cone 3, the only class A cone to be surveyed across its whole diameter, displays radar facies 5 reflections filling its shallow summit crater, beneath which extend radar facies 4 reflections representative of spatter filling the central conduit.

Pits dug into class A cones contain stratigraphies that fall into two categories: the diverse, intricately layered stratigraphies seen in pits A, B and D, and the much more homogeneous, ash-dominated stratigraphies seen in pits C, E, F, G and H. In nearly all cases, large (several cm-sized) clasts are absent in the near-subsurface, in contrast to the prevalence of coarse scoria clasts that litter the surface of the flanks.

Pits A and B, dug into the lower flanks of cone 1, display a layer of brown soil overlying a diverse sequence of alternating light and dark layers that show identical stratigraphy between the pits. The darker, black layers are comprised of approximately spherical, coarse to fine-grained ash particles with a rough surface texture and dull

luster. The lighter, brown layers display fine to very fine grain sizes, and were found to include organic matter in the form of short (<1 mm) root-like strands, indicating that these layers are soil horizons.

Pit D, dug into the lower flanks of cone 2, comprises a topmost layer of brown soil similar to that seen in pits A and B, but the soil overlies a diverse sequence of layers that displays a different stratigraphy to the layers seen in pits A and B. A layer of vesiculated, light-coloured lapilli distributed within finer grained material overlies a sequence of very fine sands ranging from black through brown to white. These are themselves underlain by a layer of closely-packed, coarse scoria clasts (generally a few cm across) with little interstitial material.

The remaining pits (C, E, F, G and H) displayed much more homogeneous stratigraphies than the aforementioned three. Pit C was dug into the reddish upper flanks of cone 1, and features a layer of brown soil analogous to that in pits A and B overlying a layer of coarse-grained black ash. The upper part of the ash layer displays numerous angular, compacted, low porosity, relatively unmodified lava fragments.

Pits E, F, G and H displayed stratigraphies comprising medium-grained black ash extending throughout the entire depth of the pits, with a layer of closely-packed, coarse scoria clasts existing beneath.

7.4.2 Class B cones

Cones 4 (at Álftaver) and 5 (at Mývatn) exist within this class (Figs. 7.2d and f). The morphologies of Class B cones are characterized by steeply dipping (25° to 30°) flanks leading to the rim of a wide and deep summit crater that occupies a much higher proportion of the diameter of the cone than the craters in class A cones. Cone 5 actually displays two distinct craters, one occupying the southern half and one the northern half. Figure 7.2f shows the southern crater, whose south rim has been eroded. What appears to be an outer carapace of consolidated spatter can be seen on the west rim of the south crater, on the left in Fig. 7.2f – the carapace overhangs what is presumably less well-consolidated scoria beneath it. The lower flanks of both cones are covered by onlapping deposits, which smooth the break in slope of the flanks with the surrounding flat terrain. The flanks of cone 4 are covered by a continuous layer of thick grass up to the crater rim, but those of cone 5 are largely exposed and consist of angular, rubbly, red scoria,

with coarse rheomorphic spatter capping the summit of the crater – fine-grained tephra is not visible anywhere at the surface at either cone.

The profile of cone 4 was subdued enough for the GPR survey to pass all the way across it, but the sides of the central crater of cone 5 were too steep and craggy to move the GPR across, and the survey only passed across one flank of the cone. The radar profiles of class B cones indicate that the bodies of the cones are characterized almost exclusively by radar facies 1 material. In the profile of cone 4, this radar facies apparently extends beneath the maximum depth to which the GPR can penetrate, so its lowermost bound as seen in the profile has been marked with a dotted line. The flanks of the cone appear to flatten out on the north and south sides of the cone – there is no apparent radar facies transition that defines the continuation of the sloping flank underground. For cone 5, the boundary between radar facies 1 and the underlying lava flow (radar facies 3) is resolvable.

Radar facies 5 fills the crater of cone 4, with the horizontal, slightly downsagging reflections characteristic of the central conduit (radar facies 4) extending beneath it. For both cones, radar facies 6 is apparent onlapping onto the flanks, almost reaching the rim of the crater in cone 4, but reaching only part of the way up in cone 5. Radar facies 2 is not apparent anywhere in the profile of cone 4, but can be tenuously identified lying beneath radar facies 1 for cone 5. A notable difference between the configurations of radar facies 1 and 2 in cone 5 with respect to the Álftaver class A cones is that the reflections of radar facies 2 appear to entirely underlie those of radar facies 1, rather than horizontally grade into them. It is risky to base the diagnosis of a separate radar facies on just a few reflections, and this interpretation cannot be conclusively verified without ground truthing.

The radar profiles of cones 4 and 5 may be compared with the cross-section of a half-collapsed cone located 400 m to the northwest of cone 4, shown in Fig. 7.2i. The cone displays morphology analogous to that of cone 4, and shows a deep, bowl-shaped central crater from which any previously existing crater-fill material has been emptied. Both the walls of the central crater and the surface of the east flank (on the right of Fig. 7.2i) show an apparently consolidated outer carapace of consolidated spatter: the ‘Schweiss-Schlacken’ described by *Thorarinsson* [1951]. The carapace on the east flank appears to have been more resistant to erosion than the red, scoriaceous material below, which it overhangs in a few places, similar to the configuration seen in cone 5.

The scoriaceous material has a rubbly, heterogeneous consistency and is analogous to radar facies 1. What appears to be soil/ash onlapping onto the lower flanks exists at the far right of Fig. 7.2i – these deposits are presumably analogous to radar facies 6.

Two pits were dug into the north flank of cone 4. Pit J displays dark brown overlying light brown, muddy layers of very fine grain size, which themselves overlie a layer of close-packed, lapilli-sized scoria clasts. Pit I shows a similar configuration, except that a layer of black, fine-grained ash particles overlies the dark brown layer of very fine-grained particles.

7.4.3 Class C cones

Class C cones (Fig. 7.2e) exist on the southern fringes of the Álftaver cone field, and take the form of highly eroded mounds comprising angular stones and boulders reaching a few metres across, separated by a high proportion of interstitial ash. No morphology associated with the cones in the previous two categories is preserved in this category, and class C cones probably represent erosional remnants of the other two cone categories. The morphologies of class A cones located to the north of the class C cones appear to grade into the class C category; Fig. 7.2j shows a cone whose preservation state is apparently midway between the two classes.

7.5 Interpretation

7.5.1 Pit stratigraphies

Pits A and B in cone 1 are notable in that they appear to display identical stratigraphy consisting of alternating soil and ash layers. This suggests that these layers have been deposited at an inclination matching the slope of the cone flank, i.e. that these layers are mantling the surface of the cone. This is in apparent contrast to the horizontally oriented reflections of facies 2 that characterize the outer flanks of the cone, and which are truncated by the air/ground waves. The air/ground waves may therefore be masking a thin mantling layer that comprises an alternating sequence of Katla ash layers and interstitial soil horizons, deposited on the flanks of the cone after its formation in 934 AD. The tephrochronology in this area has been characterized previously [*Larsen*, 2000; *Óladóttir et al.*, 2005; *Óladóttir et al.*, 2008]. *Óladóttir et al.* [2008] display a stratigraphic column showing the tephrochronology of the area east of

Katla caldera (incorporating Álftaver) spanning the last 8400 years. The historical section corresponding to deposits younger than the Eldgjá eruption is based on the results of logging at Hrífunes (~10 km north of Álftaver), Ytri-Dalbaer (~35 km northeast of Álftaver) and Tjaldgilsháls (~40 km north of Álftaver). These deposits attain a total thickness of 125 cm (pits A and B are <80 cm deep) and incorporate numerous discrete ash layers from both Katla and other volcanic systems, in addition to the soil intervals that separate them. The thicker ash layers all originate from Katla whereas thinner ones originate from either Katla or volcanic systems further afield. Pits A and B both display two consistent black ash layers, one centered at 46 cm depth, the other at 63 cm depth, which are 4.5 cm and 8 cm thick respectively, and which are separated by 10 cm. Based on comparison of the stratigraphy seen in pits A and B with the tephra log seen in *Óladóttir et al.* [2008], it is proposed that the lower and upper layers are analogous to the 1262 and 1416 AD layers respectively; these layers are the only thick (i.e. >5 cm) tephra layers deposited after the Eldgjá eruption that are separated by this distance. As shall be discussed in section 7.5.2, the later stratigraphy containing the 1625 and 1755 AD tephra layers is regarded to have been removed through erosion.

The stratigraphy seen in pit D of cone 2 does not resemble the alternating ash-soil sequence recorded in pits A and B or in the stratigraphic column of *Óladóttir et al.* [2008]. No visible organic material was present in any of the samples collected from pit D, and there were apparently no soil intervals present in its stratigraphy. The sequence of individual beds displaying varying grain sizes and colours is indicative of fine-grained ash deposits of varying composition and formation conditions – the lapilli would have formed under less violent explosive conditions compared with the finer ash particles present beneath it.

The considerable variety of compositions and grain sizes seen in the tephra layers exposed in pits A, B and D, combined with the facts that their stratigraphies are not consistent with the description of the outer apron deposits as described by *Fagents and Thordarson* [2007], nor with the horizontally oriented reflections that comprise the outer apron in the radar profile, suggests that the observed layers are indeed later mantling deposits unassociated with formation of the cone. The fact that the stratigraphy seen in pit D is different from those seen in pits A and B suggests that a different sequence in the tephra record is being sampled. The appearance of the black

ash grains is consistent with the description of hydrovolcanic ash by *Palais et al.* [1988] as being 'commonly equant, blocky glass shards with few vesicles' – their dull luster would have originated from magma-water interaction at Katla caldera (which is overlain by Mýrdalsjökull glacier).

The stratigraphies seen in the remaining class A cone pits are relatively homogeneous, consisting primarily of black ash with occasional scoria clasts distributed among it. This would suggest that these pits are penetrating into the intrinsic cone deposits, which would be less compositionally diverse relative to the products of caldera eruptions. The lack of alteration apparent in the coarse lava clasts distributed within the ash in pit C suggests that these represent clasts from the lava flow on which the cone formed that were erupted late in the formation of the cone when little water was available to drive explosions, meaning that the clasts were fractured but otherwise remained essentially unmodified. The concentration of scoria and spatter clasts on the surfaces of class A cones, and the apparent total absence of them from the shallow subsurface, suggests that the surface clasts have probably been eroded from the steep, central scoria cones and deposited around the lower flanks. The concentration of the clasts would be heightened by wind deflation of the cones, which would act to remove ash from their surfaces, but would not succeed in removing the larger scoria clasts, which would be left as a residual deposit.

The distribution of particular stratigraphies between class A cones provides an indication of the extents to which each cone has been modified. Pits A, B and D, which exist on the lower flanks of cones 1 and 2, show stratigraphies interpreted to represent later tephra and soil layers deposited on top of the cones, whereas pits C, E, F, G and H on the upper flanks of cones 1 and 2, and all along the flanks of cone 3, display stratigraphies interpreted to represent tephra intrinsic to the cones themselves. This distribution of near-surface stratigraphies would indicate that cone 3 and the upper flanks of cones 1 and 2 have experienced erosion to the extent that any mantling tephra and soil layers have been stripped off, whereas the lower flanks of cones 1 and 2 have retained their mantling deposits. Cones 1 and 2, therefore, would appear to have suffered less modification by erosion than cone 3.

Pits I and J in cone 4 display stratigraphies that are dominated mostly by a muddy, fine-grained lithology, although both display closely-packed scoria at their bases. This lithology is quite different from the generally ash-dominated ones seen in the class A

cone pits, and when considered with the thick vegetation that occurs on the class B cones, suggests that this area has experienced the action of water more frequently throughout its history than where the class A cones exist to the east. The black, fine-grained ash present in pit I is very similar to a sample of black, alluvial sediments collected from the banks of the River Skalm, 180 m to the north of cone 4. The river sediments have a median grain size of 304 μm compared with 227 μm for the cone ash, and a standard deviation of 9.9% from the mean grain size compared with 9.7%. These similarities indicate that the ash present in pit I and the river sediments likely originated from the same source, i.e. it was deposited by jökulhlaups originating from Katla caldera beneath Mýrdalsjökull to the west. The ash seen in pit I was presumably deposited by the last jökulhlaups to cover Álftaver, during the Katla eruption of 1918 [*Larsen and Ásbjörnsson*, 1995]. The ash layer is not present in pit J higher up the cone, meaning it has presumably tapered out and eventually disappeared as it extends up the cone flank.

The identification of ash layers that are interpreted to originate from exterior sources (ashfalls for cones 1 and 2 and jökulhlaups for cone 3) is supported by the fact that these layers display ash of universally finer grain size, and which is also more poorly sorted, than that from layers interpreted to be intrinsic to the cones (see Table 7.3). The foreign ash has a mean grain size of 288 μm relative to 443 μm for the intrinsic ash, and a mean standard deviation of 8.48% from the mean grain size relative to 11.43%, based on five ash samples each for both types. The finer grain sizes may result from a greater explosiveness characterizing the lava-ice interaction during eruptions of Katla beneath Mýrdalsjökull relative to the rootless cone eruptions, and/or from the preferential transport of finer material to further distances from Katla relative to coarser material.

7.5.2 Cone morphologies

The fundamental morphological difference between class A and class B cones is that class A cones display gently sloping outer flanks generally leading to a relatively small, steep summit spatter outcrop that has a small crater, whereas class B cones display steep flanks leading to a wide summit crater. This difference in exterior morphology is reflected in the radar profiles by the presence of radar facies 2 within the outer flanks of class A cones, and the (general) absence of radar facies 2 in class B cones. As shown in Table 7.2, the continuous, horizontal nature of radar facies 2 reflections is interpreted to

represent material that is fine grained and homogeneous (i.e. ash), with few large point reflectors such as scoria clasts. The undulating, discontinuous, truncated nature of radar facies 1 reflections is interpreted to represent coarser, more heterogeneous material analogous to welded scoria and spatter clasts, with little interstitial ash. The fine grainsize and poor consolidation of the ash that comprises radar facies 2 is interpreted to be more easily eroded than the coaser grained scoria and spatter that comprises radar facies 1.

It is reasonable to suggest that class B cones would originally have featured ash aprons surrounding their central cones if consideration is given to their formation conditions relative to those of class A cones. *Fagents et al.* [2002] described a generalized interpretation of how cone morphology should vary with the explosive intensity of the lava-water interactions: as explosive intensity increases, cone morphology evolves from narrow, steep-sided, spatter-rich, craterless, hornito-like edifices to wide, less steep-sided, scoria- and lapilli-rich cones with wide craters. This progression of morphologies with explosive intensity would suggest that the class B cones at Álftaver formed under more explosive conditions than class A cones. This morphological distinction would apparently contradict the petrology observed in the different cone classes; finer clast sizes are also a consequence of increasing explosiveness between the lava and ice [*Fagents et al.*, 2002], and fine-grained material appears to be absent from class B cones. The highly explosive conditions of formation of class B cones as indicated by their large crater/cone ratios would imply that they originally displayed large aprons of fine-grained ash, rivalling those of the present class A cones in volume; the volume ratio of radar facies 2 material to radar facies 1 material in cone 1, evidently the best-preserved of the cones, is currently ~5:2. Only cone 5 shows any hint that a minor amount of outer apron material may have remained around some of the class B cones.

If class B cones did originally feature wide aprons comprised of ash-sized material around their steep central scoria cones, the present general absence of facies 2 material from class B cones would suggest that these cones have experienced more extensive removal of material since formation than class A cones; as will be discussed in section 7.5.3, class B cones exist in an environment that is likely to have experienced more intense erosion and modification processes compared with that in which class A cones exist. Yet the original morphologies of class B cones would not have been identical to

class A cones; the crater/cone diameter ratio remains larger for the class B cones than that for the crater and steep, central cone of the class A cones. This suggests that the present morphological differences between class A and class B cones are not entirely the result of differential modification after formation, and that differential formation conditions and processes are important as well, which will be discussed in section 7.5.3.

Class A cones are therefore interpreted to be better preserved than class B cones, yet the morphological variations between class A cones, as well as evidence from the radar profiles, suggest that these cones also display varying preservation states. The progression of morphologies from cone 1 through cone 2 to cone 3 is characterized by increasingly eroded outer aprons, and in the case of cone 3 a considerably more eroded and smoothened central scoria cone. The truncation of the horizontal reflections of facies 2 by the air and ground waves complement the morphological evidence for the removal of material from the outer aprons of these cones – if the apron had not been eroded at all, the reflections would taper out as they approached the edge of the deposits. Figure 7.6 shows schematics of how the radar profile would have appeared for the newly-formed cone 1, how removal of outer apron material has created the present truncated appearance of the facies 2 reflections, and how the profile may appear in future if the summit spatter outcrop is worn down to the extent that the cone resembles the present cone 3.

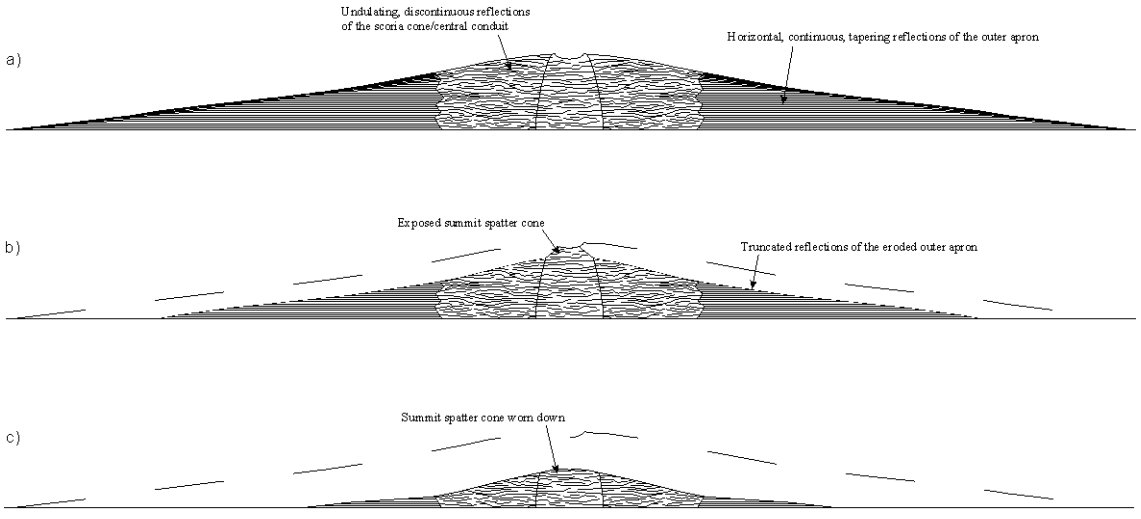

Figure 7.6. Schematics of the interpreted evolution of the cone 1 radar profile. (a) A hypothesized profile of the newly-formed cone, with the facies 2 reflections tapering towards the edges of the outer apron. (b) Current profile of cone 1, showing the emergence of the resistant, steep-sided summit spatter outcrop, and the truncation of the facies 2 reflections as the outer apron is eroded back. (c) A hypothesized future profile, whereby the summit spatter cone has become worn down, smoothing the profile of the cone such that is resembles the present-day cone 3.

Class C cones represent the most advanced erosional stage of any cone group in Álftaver, and barely even resemble conical edifices. There is an apparent gradation from class A cones to class C cones – the succession of cone morphologies seen in Figs. 7.2a, b, j and e represents a sequence from high to low states of preservation. The large blocks that constitute the cones are interpreted to be the remnants of what would have been the steep, scoriaceous central cones that are seen in class A cones – if outer aprons existed for class C cones, no trace of them remains, having been washed away by jökulhlaups or removed by the wind. The mounds do appear to feature a high proportion of black, sand-sized ash that permeates the interstitial spaces between the blocks. This ash, like that which covers the outwash plains of Mýrdalssandur, would have been deposited by jökulhlaups from Mýrdalsjökull [*Larsen and Ásbjörnsson*, 1995] or would have been blown onto the residual cones, yet there is a possibility that some of it may comprise ash intrinsic to the cones themselves.

7.5.3 Interpretation of results with respect to formation conditions and erosional histories

Observations of the cone morphologies, radar profiles and pit stratigraphies at Álftaver and Mývatn have led to interpretations of the formation conditions and erosional histories of the cones both between and within different classes. When the locations of the different cone classes are considered, both within and between different cone fields, the interpreted formation conditions and erosional histories of each class can be correlated to the environmental conditions expected to exist at each locality.

Based on the different crater/cone diameter ratios presented by cone classes A and B, it has been hypothesized that class B cones would have formed under more explosive lava-water interaction conditions compared with class A cones. The efficiency of interaction is related to the supply of lava to the explosion site, the geometry of the internal lava feeder pathways, and the accessibility of substrate water [*Wohletz*, 1983; 1986; *Mattox and Mangan*, 1997]. The former two factors cannot be easily constrained by the fieldwork of the present study, although it can be established that cones with class B morphologies appear to exist in areas that are likely to have particularly high water contents in the substrate, i.e. low elevation terrain near to the water table on a

jökulhlaup outwash plain for the Álftaver cones [*Larsen and Ásbjörnsson*, 1995], and a lacustrine environment for the Mývatn cones [*Thorarinsson*, 1953].

At Álftaver, class A cones are observed to cluster within the central and northeastern parts of the field, class B cones occur within the northwestern parts of the field, and class C cones exist within the southern parts. Álftaver is part of the Mýrdalssandur jökulhlaup outwash plain [*Larsen and Ásbjörnsson*, 1995], with the jökulhlaup flow paths concentrating to the southwest of Álftaver, and along the low topography presented by the River Skalm [*Larsen*, 2000; *Duller et al.*, 2008]. The western and southern areas are also the most exposed to prevailing westerly and southerly winds blowing onshore from the Atlantic Ocean; deflation of fine grained ash from around the cones by the wind will also have made a significant contribution to the erosional modification of the cones in these areas. The fact that the more poorly-preserved class B and C cones are concentrated within the western and southern areas of the field is therefore unsurprising given that these two classes, particularly the class C cones, are situated most directly within the paths of approaching jökulhlaups and prevailing winds. Class A cones have also experienced some deflation, as is evident from the steep, craggy south flanks of their scoriaceous cones; however, the dense concentration of large scoria clasts on their lower flanks (Fig. 7.2g) will have effectively shielded the underlying ash from further deflation, aiding the preservation of class A cones.

Class B cones show numerous morphological characteristics indicative of considerable modification by jökulhlaups, including the absence of any tephra aprons, the presence of onlapping deposits coating their flanks that reach 3 metres thick, and the occasional presence of southeastward-pointing, tapering lobes of alluvial deposits extending from the bases of the cones, which can reach 100 m long (Fig. 7.2k). Class A cones, however, are generally either situated away from the main paths of the jökulhlaups, or are shielded from their direct impact by the presence of the class B cones to the east, which would act to mitigate some of the force of the jökulhlaups. Class B cones exist in an area that has a noticeably thicker vegetational cover and a greater prevalence of small streams than that in which the class A cones reside, suggesting that this area is nearer to the water table; lower-lying ground will be affected to a greater extent by jökulhlaup flooding compared with higher ground.

At Mývatn, virtually all the cones fall into class B, and cluster particularly around the southern and western shores of the lake, in addition to existing within it. With the

absence of jökulhlaups, the erosional environment at Mývatn is less intense than that at Álftaver, yet the Mývatn cones are approximately twice the age of the Álftaver cones. A potential source of cone erosion is the periodic flooding of Mývatn. *Rist* [1979] noted that floods from the small plains in the vicinity of Mývatn may be expected in late winter or early spring, when porous ground may be made impervious by the freezing of interstitial water, and all fissures and depressions are filled with ice or water. Repeated inundation of the cones over hundreds of years, combined with freeze-thaw weathering, would contribute significantly to local slope degradation of the cones, and formation of colluvium that is consistent with the evidence from the GPR profiles.

7.6 Comparison with Martian rootless cones

Numerous fields of structures interpreted to be rootless cones have been identified on Mars, mostly in the northern plains [*Fagents et al.*, 2002]. Impact crater-frequency relationships indicate that the surfaces upon which the cones sit may be no older than 10 Ma [*Lanagan et al.*, 2001], making them considerably older than their terrestrial counterparts, but extremely young by Martian standards. Virtually all of the Martian cones display morphologies apparently analogous to those of the class B cones seen at Álftaver and Mývatn. Based on surveys of Martian and Icelandic cones, *Fagents et al.* [2002] established that the Martian crater/cone diameter ratios generally match those of the Mývatn cones, which are class B cones. The spatial distribution of Martian cones has been quantified by *Bruno et al.* [2004] and varies considerably between fields, from widely spaced single cones or small clusters (Fig. 7.7a) to densely packed, multiple overlapping cones (Fig. 7.7b).

A prominent aspect of morphological variation between Martian cones is that cones in some fields display low-relief aprons around their bases whereas in other fields these aprons are either rare or non-existent. Fig. 7.7a shows a cone field in central Amazonis Planitia, most of whose cones display such aprons, which act to subdue the relief of the terrain beneath. Details of such cones in this area are shown in Figs. 7.7c and d, whereas Figs. 7.7e and f show details of similar cones located within western Amazonis Planitia. In contrast, the cone fields in Fig. 7.7b (located in southern Amazonis Planitia) and 7.7g (located within Isidis Planitia) appear to show no aprons. *Fagents et al.* [2002] noted that the 'smooth, thin, flat-lying haloes' may be analogous to the aprons of 'fine pyroclastic material associated with some Icelandic cones'. This study concurs with

such an interpretation, and suggests that the presence or absence of the apron material, in addition to other morphological characteristics, provides an indication of the preservation state of the cones.

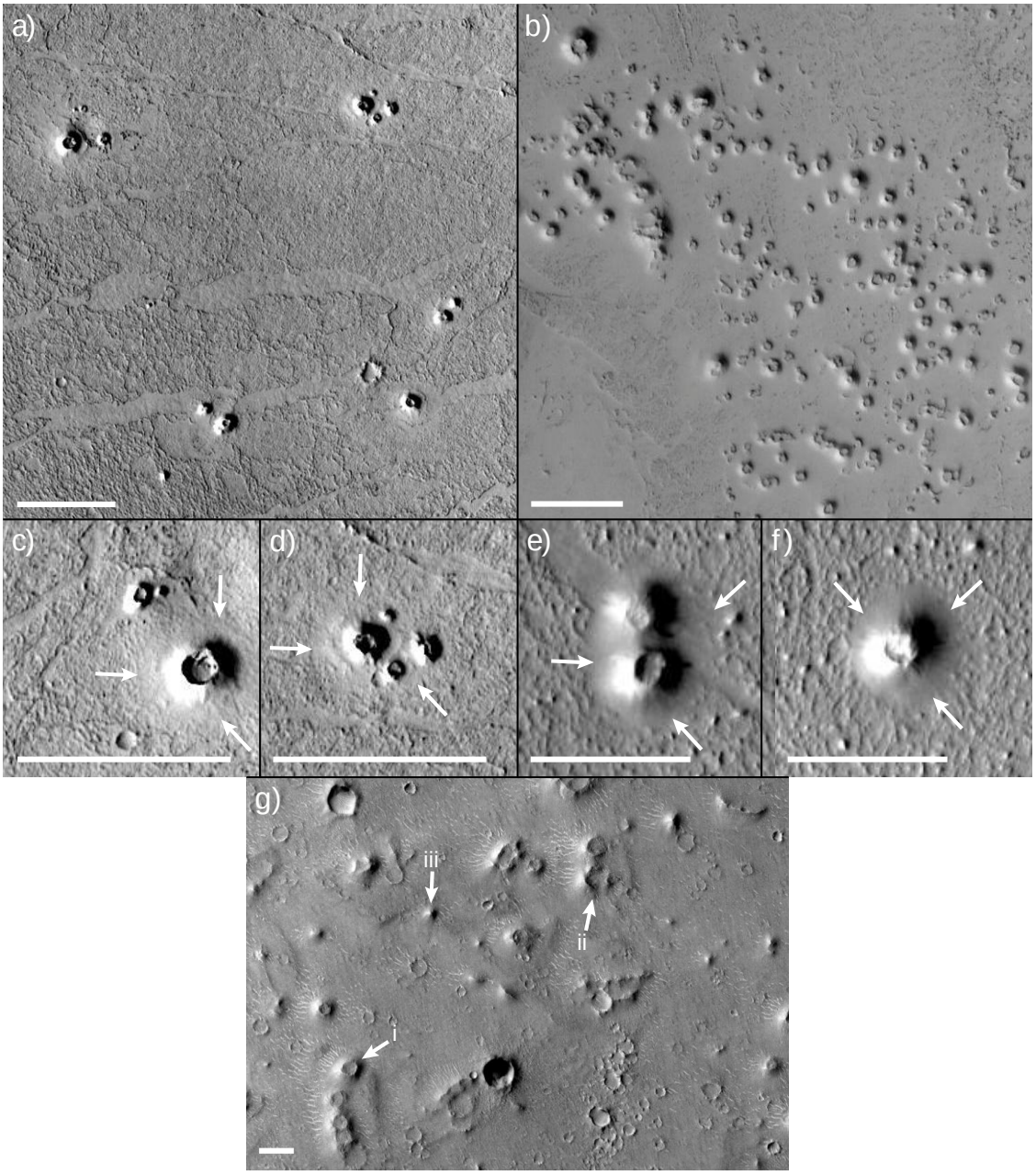

Figure 7.7. MOC (Mars Global Surveyor) and CTX (Mars Reconnaissance Orbiter) images of Martian rootless cone fields and individual cones. (a) Portion of MOC image M0303958 of a cone field near 24.8°N, 171.4°W (central Amazonis Planitia). (b) Portion of MOC image M0801962 of a cone field near 26.0°N, 189.7°W (western Amazonis Planitia). (c & d) Portions of MOC image M0303958, showing individual cones near 24.8°N, 171.4°W (southern Amazonis Planitia). White arrows highlight margins of low-relief outer aprons. (e & f) Portions of MOC image M0307175, showing individual cones near 12.8°N, 162.9°W (southern Amazonis Planitia). White arrows highlight margins of low-relief outer aprons. (g) Portion of CTX image P02_001701_1899_XI_09N274W of a cone field near 10°N, 274.2°W (Isidis Planitia). Scale bars represent 500 m in all images. Illumination is from the left and north is up in all images.

A correlation can be identified at these four localities between the presence of the aprons around the cones and the extent to which the surrounding terrain and the cones themselves appear to have been modified. Those seen in Figs. 7.7a, c, d, e and f display more sharply-defined bases, deeper craters and better-preserved flanks than those in Figs. 7.7b and g, and the terrains on which they are situated show sharp relief and relatively few small (<500 m) impact craters. The cones in Fig. 7.7b, in addition to other topographic features in the image, appear to be draped by a mantling deposit (likely wind-blown dust) that subdues their relief, and a small proportion of the cones appear to lack flanks on one or more sides, indicative of mass wasting. The small impact crater frequency of the terrain on which the cones are situated is relatively low. The cones in Fig. 7.7g exist on terrain that shows widespread mantling material, which manifests itself in the form of numerous high albedo transverse aeolian ridges (TARs) [*Balme and Bourke*, 2005], and the cones show somewhat lower relief as a likely result. The terrain also displays a much higher small impact crater frequency than the three other sites. There is evidently a progression of cone preservation states at this site: the best-preserved (cone i in Fig. 7.7g) largely retain their flanks and summit craters; those that have been moderately eroded (cone ii) display collapsed flanks, but their conical appearance is still identifiable; the most eroded cones display only faint curved remnants of the original flanks, or in the case of cone iii, exist only as small knobs.

The observations that Martian rootless cones that lack outer aprons frequently display signs of erosion, and tend to occur at sites that display a mantling deposit and/or a high frequency of small impact craters, imply that these cones have been modified to a greater extent than those that have retained their aprons. If the outer aprons are indeed comprised of fine-grained and poorly consolidated material, then they will be the part of the cones that are most vulnerable to erosion. The terrain in Fig. 7.7g has accumulated a high small impact crater frequency and is covered by an aeolian mantling deposit, both indicative of an age of the terrain that is greater than those of the three other cone sites: many of the cone aprons have likely been eroded away since cone formation, whether by impacts or wind action, and the remnants that have remained have likely been covered by the mantling material. The presence of TARs supports aeolian reworking as a likely process for apron erosion, and there is the possibility that the ash that has been eroded from the cones may itself comprise a proportion of the mantling material. The terrain in Fig. 7.7b shows a low small impact crater frequency, suggesting

a relatively young age, but also shows a mantling deposit covering the topography: any aprons surrounding the cones here may be relatively intact but their low relief has caused them to be obscured by the aeolian material covering them. The separate terrains in Figs. 7.7a, c, d, e and f display low small impact crater frequencies, implying a young age, and high topographic relief, implying the absence of a mantling deposit; as a result, both of these terrains display rootless cones with sharply-defined features and generally intact and visible outer aprons.

These observations stand as evidence that cone modification processes are active on Mars as well as Earth, although on Mars the processes are much slower and, in the absence of a recent water cycle, consist predominantly of wind erosion, mantling by aeolian material, mass wasting and impact cratering. The correlation of Martian cone morphologies with their erosional/modification environment has implications for the modification experienced by the Icelandic cones of this type. The Martian cones almost exclusively display morphologies and crater/cone diameter ratios like those of the class B cones seen at Álftaver and Mývatn, yet outer aprons are sometimes apparent around the Martian cones, whereas they are never observed around the Icelandic cones. If the Icelandic cones formed analogously to the Martian ones, then this observation acts as additional evidence that the Icelandic class B cones should have originally been surrounded by such aprons, which have since been removed and/or obscured by the very active terrestrial erosional/modification processes. There remains the tentative but inconclusive evidence for a remnant of such an apron around cone 5 in its radar profile – in this sense, this cone may be analogous to the better preserved cones seen in Fig. 7.7g, whose aprons have probably been mostly eroded away as well as covered by later deposits.

No Martian cones have yet been identified whose morphologies resemble those of class A cones, although the knobs seen in Fig. 7.7g could in some cases represent the remnant steep, central, craterless cones of such edifices. However, without a definite morphological progression from well-preserved to poorly-preserved class A cones on Mars, this is impossible to verify. An explanation for why class A cones are not seen may lie with the atmospheric pressure and gravity conditions of Mars. The Martian atmospheric pressure is considerably lower than Earth's, which acts to promote explosive activity by enhancing the energy released due to gas expansion [*Wilson and Head*, 1983, 1994; *Fagents and Wilson*, 1996; *Greeley et al.*, 2000; *Fagents et al.*,

2002]. The low gravitational acceleration will act to lengthen clast ejection distances. Combination of these effects would therefore act to create wider craters for the Martian cones. The smaller crater/cone diameter ratios of class A cones relative to class B cones are interpreted to indicate less explosive formation conditions. The formation conditions of class A cones may therefore be characterised by an intensity of explosiveness that is below the threshold allowed by the Martian atmospheric and gravitational conditions.

7.7 Summary

The GPR surveys performed across the rootless cones at Álftaver and Mývatn, in conjunction with the shallow stratigraphic columns on their flanks, have shown that GPR constitutes an efficient, non-destructive method of characterising the interior structures of these features. In this sense, this study complements previous occasions where GPR has successfully been used to study terrestrial Mars-analogue volcanic structures [*Heggy et al.*, 2006b; 2006c].

These surveys have promoted a better understanding of how the current morphologies of cones at different locations in Iceland have been influenced by the lava-water interaction conditions at the time of formation as well as by later modification processes. Surveys and observations of five cones in the Álftaver and Mývatn districts have identified three discrete morphological classes of rootless cone. Consideration of the near-surface stratigraphies of the cones as revealed by pit-digging, as well as the locations of the different cone classes within and between cone fields, has shown that this morphological diversity is largely the result of the different erosional and modification environments interpreted to exist at the different localities. Erosion by wind and flowing water (jökulhlaups) preferentially removes ash from around the cones. This reduces the apparent cone diameter and increases the ratio of cone height to diameter. The removal of ash aprons from around the cones increases the slope on the flanks of the cones, exposes the consolidated spatter to increased weathering, leading to slope failure resulting in further degradation of cones and the transformation of A and B type cones to type C cones.

The results indicate that the variation in cone morphology with intensity of lava-water interaction during formation, as presented in *Fagents et al.* [2002], is essentially correct, but that the interpretation is applicable only to the inner scoria cone, and

neglects to consider the outer aprons of fine-grained ash that surround the steep, central cones. These are particularly susceptible to being eroded away and/or obscured by overlying deposits since formation.

The morphologies of the Icelandic cones have been compared with structures seen on Mars that are interpreted to be rootless cones. As with their terrestrial counterparts, the morphologies of the Martian cones indicate that they show a range of preservation states that can be correlated to their interpreted erosional environments. Most notably, outer aprons appear to exist around Martian cones that have suffered less erosion and modification, an observation that matches what is seen in Iceland. The fact that the well-preserved Martian class B cones are surrounded by outer aprons implies that the newly-formed Icelandic class B cones would also likely have had such aprons associated with them.

Chapter 8
Conclusions

8.1 Introduction

This chapter summarises the conclusions of the previous chapters, and highlights their significance in addressing the primary theme of the thesis, specifically how environmental conditions on the terrestrial planets influence volcanic processes, which has been investigated from a variety of different aspects that use different research methods. In addition, recommendations for future research and improvements to the research methods employed throughout the thesis are discussed.

8.2 Environmental controls on intermediate volcano morphology on Mars and Venus

8.2.1 Conclusions

The main research topic in this thesis has involved compilation of a catalogue of all intermediate-sized volcanoes on Venus and Mars. This has been accomplished in order to acquire an accurate and comprehensive database of volcanic features which may be used to investigate what determines the distribution of certain volcano morphologies, both within and between planets. The survey of intermediate volcanic landforms on Venus and Mars performed for this study has succeeded in identifying many previously unrecognized features, and in compiling extensive quantitative and qualitative morphological data for each feature catalogued. Based on the results, the analysis has singled out three subject areas that are considered to benefit most from the new data, which include the evolution of intermediate cone-type volcanoes into large volcanoes on Venus, the morphologies of low-relief shields on Mars and Venus, and the morphologies of steep-sided domes on Venus.

Particular attention has been focused on reassessing the significance of neutral buoyancy as a factor in controlling edifice morphology, which has been promoted as a strong influence by previous studies (e.g. *Head and Wilson* [1992]; *Keddie and Head* [1992; 1994b]; *Grosfils and Head* [1995]; *Ristau et al.* [1998]), but which has been disputed by others (e.g. *Krause and Grosfils* [1999]; *Stofan et al.* [2001]). Neutral buoyancy theory, as proposed by *Head and Wilson* [1992], is not consistently supported by the findings of this study. Some aspects of neutral buoyancy theory are supported in

various instances. The marked dichotomy in the morphologies of low-relief shield calderas on Venus and Mars (equidimensional collapse caldera versus fissure, respectively) is interpreted to indicate that magma reservoir depths beneath these shields are much shallower on Venus than on Mars; this is consistent with the neutral buoyancy hypothesis that the different atmospheric pressures on Venus and Mars should result in varying volatile exsolution in erupting lavas, and therefore very different crustal density profiles, on the two planets [*Head and Wilson*, 1992; *Wilson and Head*, 1994]. In addition to low-relief shields, various morphological traits of intermediate cone-type and large volcanoes, which are interpreted to represent different evolutionary stages of the same volcano type, also appear to support the hypothesis of neutral buoyancy theory. The increasing diameters of the summit calderas of Venusian cone-type volcanoes and the increasing contributions to the edifice volumes from flank flows with increasing volcano size are regarded to imply a laterally expanding magma chamber with increasingly widely distributed magma pathways to the surface. In addition, the almost ubiquitous occurrence of sheet flows at intermediate volcanoes and the increased occurrence of sheet and fan flows forming steep central edifices at large volcanoes are interpreted to represent an increase in the magma reservoir depth with increasing edifice height. This is based on the argument that eruption volumes will be lower at the summits of large volcanoes than at their flanks or the summits of intermediate volcanoes as a result of the decreasing driving pressure available to transport magma to the summit with increasing edifice height; in addition, the steepening slope conditions with edifice growth reduce the ability of the flows to spread sideways. These effects are consistent with the hypothesis of neutral buoyancy theory that the magma reservoir should ascend very slowly with edifice growth on Venus, and will consequentially be greatly enlarged and widened through ascent of magma from the mantle source.

However, other observations appear to be less consistent with the predictions of neutral buoyancy theory. The consistent occurrence of summit collapse calderas across the edifice diameter and summit elevation range of intermediate and large cone-type volcanoes indicates that shallow magma storage is not necessarily confined to smaller volcanoes, or volcanoes with summit elevations above 2.5 km above MPR, as was proposed by *Head and Wilson* [1992]. In addition, while the diameters of the summit collapse calderas of intermediate and large cone-type volcanoes tend to increase with increasing edifice size and summit elevation above MPR, there is considerable scatter

within the data that is interpreted to represent the influence of environmental factors other than neutral buoyancy on the relationship between caldera size and edifice size/summit elevation.

The issue of the extent to which neutral buoyancy affects volcano morphology is therefore complicated by the fact that different morphological relationships, particularly for Venusian volcanoes, offer conflicting interpretations of the magma storage configuration; this study has hypothesized that different morphological features may be sensitive to different aspects of the intrusive systems of these edifices. The primary magma reservoirs of the volcanoes may grow laterally and deepen as the volcanoes increase in height, resulting in the expanding caldera size, but with smaller pockets of melt rising to shallower levels within the edifice and stalling to create discrete collapse zones. If this is the case, then movement of magma that is not predicted by neutral buoyancy theory is evidently a common occurrence among Venusian volcanoes, meaning that other environmental factors are influencing the movement and storage of magma. *Hughes et al.* [1990] and *Stofan et al.* [2001] hypothesized that the stress field, in addition to neutral buoyancy, will influence the movement of magma within an edifice, a viewpoint which this study supports. It has been determined that around 50% of all intermediate cone-type volcanoes exist within terrain described as 'fractured plains', with 13% of the volcanoes appearing to directly influence the configuration of surrounding regional fracturing.

The effect of magma volatile concentration on neutral buoyancy has also been addressed through comparison of low-relief shield morphologies on Venus and Mars, the only volcano category to occur in appreciable quantities on both planets. The existence of certain shields with very similar fissure-like caldera morphologies on both planets, the Martian members of have been interpreted to form through fire fountain activity [*Wilson et al.*, 2009], has led to the interpretation that if the Venusian members are also formed by fire fountain activity, the magma forming them must have displayed a very high volatile content in order for there to have been sufficiently explosive volatile exsolution to sustain fire fountain activity. This type of Venusian shield is very rare, and tends to exist at high altitudes, where the lower atmospheric pressure should aid volatile exsolution. This rareness reflects the few instances where the necessary combination of altitude (usually above 500 m above MPR) and magma volatile content (2-4 wt %) that allows such activity to take place is attained, whereas on Mars the low

atmospheric pressure means that low volatile concentrations are sufficient to allow fire fountain activity. The fact that the Venusian shields initially display fissure vents is interpreted to mean that they represent the few instances where the magma supplying shields on that planet originates from a deep source, potentially a mantle plume, rather than a shallow magma reservoir. The observation that many of these Venusian shields appear to have later developed collapse calderas is interpreted to represent a decrease over time in the volatile concentration of the magmas supplying them, with the consequent development of a shallow neutral buoyancy zone and associated magma reservoir.

The study of domes on Venus, which display more morphological subcategories than any other volcano type, has focused on the aspect ratios and caldera sizes of the domes, and the extent to which their flanks have collapsed, and has established links between these. The range of aspect ratios displayed by the domes is related to differences in effusion rate and lava viscosity (and associated yield strength [*Best*, 2003]), and domes that display lower aspect ratios (i.e. lower diameter to height ratios) have been found to display collapsed flanks more frequently than those with higher aspect ratios. This is interpreted to result from oversteepening of the flanks, although the overlap in height and aspect ratio for many steep-sided and modified domes indicates that other factors also influence flank collapse. The occurrence of large collapse calderas and summit downsags has been found to be closely linked to the occurrence of collapsed flanks. This study interprets the calderas and downsags to form as a result of magma withdrawal during dome emplacement, caused by the restricting pressure exerted by the weight of the dome and the yield strength of the thickening crust exceeding the upward pressure of the rising magma. The formation of a large caldera or a summit downsag is interpreted to depend on the rate of withdrawal of magma and the rheology of the dome at the time of withdrawal. The stresses inflicted on domes by magma withdrawal and the formation of large calderas and summit downsags, in addition to dome aspect ratio, are regarded as being influential in causing flank collapse.

This study has also identified steep-sided domes that occur at the summits of intermediate and large cone-type volcanoes on Venus as representing a compositionally discrete category from domes that exist within the plains, and which also provide an indication of magma residence times within the parent volcanoes. In contrast to most plains domes, which display smooth surfaces, low heights and large aspect ratios,

summit domes tend to display rougher and more fractured surfaces, greater heights and smaller aspect ratios that are regarded to be indicative of a more evolved lava composition. The steeper flanks of summit domes, when combined with the fact that they exist within an unstable volcanic environment, contributes to them displaying collapsed flanks more frequently than plains domes. The presence of summit domes across intermediate and large cone-type volcanoes of a very wide range of diameters indicates that the domes represent the final lavas erupted during one of several eruption phases that characterize the lives of the volcanoes, especially since many domes have either collapsed and/or been embayed by later lavas emitted by the parent volcano. The fact that such domes exist at volcanoes of a wide range of sizes indicates that many such eruption cycles characterize the lives of these volcanoes, which would appear to support the assertion of *Stofan et al.* [2001] that magma residence times within the reservoir are short.

8.2.2 Future paths of volcanological research on Venus and Mars

The survey performed for this thesis has succeeded in identifying and comprehensively describing many volcanic features within the intermediate size range on Mars and Venus. This study, like virtually all studies that have focused on the topic of Venusian volcano morphology since the early 1990s, has used Magellan data, which have proven to be instrumental in contributing to our present interpretation of the processes that have shaped the surface of Venus. However, there are several issues regarding volcanism on Venus that remain unresolved, and there are significant omissions in the currently available dataset that will need to be filled if research into Venusian surface processes is to progress. Perhaps the most pressing outstanding issue is whether volcanism is still active on Venus; with respect to the theme of the present study, observation of active eruptions on Venus would allow eruption style and its effect on edifice morphology to be directly characterized, without having to resort to inferring eruption style based on present morphology. Answering this question will require a more intensive and varied reconnaissance of the surface of Venus than has currently been achieved. The mapping of 90% of the Venusian surface at microwave frequency at ~100 m/pixel by Magellan is unlikely to be improved upon significantly in the near future by an orbital mapping mission, yet mapping of the surface only at microwave frequency at a resolution of ~100 m/pixel does not allow all physical properties of the

surface to be determined. The altimetric mapping of Venus at a vertical resolution greater than 50 m, and a lateral resolution of ~10 km [*Saunders et al.*, 1990], could be improved upon if a parabolic high-gain antenna with a diameter significantly greater than that of Magellan's (3.7 m [*Ford*, 1993]) was used. A laser altimeter of the sort used on Mars Global Surveyor would not be appropriate for mapping the topography of Venus at fine detail given the opaqueness of the Venusian atmosphere.

Some success in imaging the surface of Venus at infrared wavelengths from orbit has been achieved by the Visual and Infrared Thermal Imaging Spectrometer onboard the European Space Agency spacecraft Venus Express [*Drossart et al.*, 2007], and recent research [*Smrekar et al.*, 2010] has even interpreted the data to reveal that ongoing volcanism is occurring on Venus. The instrument has provided a map of thermal emission for much of the southern hemisphere of Venus' surface in the atmospheric 'window' at 1.02 μm [*Lecacheux et al.*, 1993]. The data have been used to identify variations in the thermal emissivity of the surface at three of the nine broad topographic rises on Venus that have been interpreted to be analogous to Hawai'ian hot spot volcanism [*McGill et al.*, 1981; *Phillips and Malin*, 1984; *Stofan et al.*, 1995]. *Smrekar et al.* [2010] have identified compositional differences in lava flows at these three hot spots based on these variations in thermal emissivity. *Smrekar et al.* [2010] interpreted these anomalies to represent a lack of surface weathering, and estimated the flows to likely be 250,000 years old or less, indicating that Venus is actively resurfacing.

Ideally, the evidence presented by *Smrekar et al.* [2010] would need to be supplemented by further evidence from a different dataset in order to confirm ongoing volcanic activity at Venus. Imagery of the surface in visible wavelengths is desirable, yet such a feat is only possible if the camera is operating beneath the high-altitude clouds that cloak the entirety of the planet. A proposed method is to deploy balloons into the Venusian atmosphere that would obtain continuous high-resolution visible and near-infrared imagery as they float above the surface over a matter of weeks [*Baines et al.*, 2009; *Bullock et al.*, 2009]; the success of the twin Soviet Vega balloons in 1985 [*Kremnev et al.*, 1986; *Sagdeev et al.*, 1986] has shown that this method is practically feasible, although only very small fractions of the surface would be imaged by each balloon over its lifetime, and they would not be able to provide continuous coverage of a particular location. A further option involves targeting landers at specific locations on

the surface where recent flows are thought to exist [*Basilevsky et al.*, 2007]. The landers would perform in-situ geochemical and geothermal analyses in order to refine estimates of flow ages, and obtain imagery of the surrounding terrain in order to provide a clearer impression of flow textures. However, the examples of the Soviet Venera [*Florensky et al.*, 1977; 1982] and Vega [*Blamont and Sagdeev*, 1984; *Surkov et al.*, 1985] landers have shown that the logistics of landing spacecraft on Venus are very difficult given the extreme surface pressure and conditions, with the necessary technology for such missions still in its relative infancy; the Venera and Vega probes were operational on the surface for not much more than an hour each. At present, there are no definite plans by any space agency to send a mission to Venus that is based in the atmosphere or on the surface, although the architecture and operations for such missions are being anticipated (e.g. *Basilevsky et al.* [2007]; *Baines et al.* [2009]; *Bullock et al.* [2009]). For the foreseeable future, continuous monitoring of the Venusian surface will likely only be possible using ground-based radar observations (e.g. the Goldstone Solar System Radar [*Rumsey et al.*, 1974; *Jurgens et al.*, 1980; 1988a; 1988b; *Plaut and Arvidson*, 1992]).

In contrast to Venus, imagery of the surface of Mars is currently available that reaches resolutions of less than a metre. The HiRISE camera onboard the Mars Reconnaissance Orbiter has enabled some small portions of Mars to be imaged at such a scale [*McEwen et al.*, 2007], allowing intricate, small-scale morphological features of some volcanoes to be characterized at a scale almost familiar to terrestrial field geologists (e.g. *Brent et al.* [2007]; *Mouginis-Mark and Rowland* [2008]). *Mouginis-Mark and Rowland* [2008] described the applications of such observations with regard to investigating the stratigraphy of the top kilometre of Mars at sub-metre spatial resolution at locations such as the walls of graben, canyons and impact graters; when applied to volcanoes, this allows refinement of estimates of long-term magma production rates and typical volumes of lava erupted per event based on observations of lava flow thicknesses. Of perhaps even greater significance with respect to characterizing volcano morphologies at a fine scale will be the ~1000 stereopairs that will be returned by the HiRISE camera [*Kirk et al.*, 2007]; consisting of two images of a site of interest that have been obtained at different incidence angles, these stereopairs may be used to create digital topographic models that will provide an unprecedented three-dimensional view of the Martian surface at metre scale. Fresh volcanic features

such as those observed in Athabasca Valles have been highlighted as a high-priority target of observation by the HiRISE team [*Kirk et al.*, 2007]. When applied to these volcanic features, such models would allow highly accurate determination of edifice heights, flank slopes and vent depths, as well as the surface textures of the shields, which would lead to refined estimates of parameters such as flow rheologies and eruption rates.

As with Magellan radar observations at Venus, HiRISE is regarded by this study to essentially represent the apex of visible-wavelength observations of Mars from orbit, although throughout the lifetime of Mars Reconnaissance Orbiter HiRISE will obtain imagery of only a minor portion of the surface of Mars; *McEwen et al.* [2007] estimated that HiRISE would cover ~1% of the Martian surface during its first two years of operation. Nevertheless, the combined datasets of the three currently active spacecraft in orbit around Mars (Mars Express, Mars Odyssey and Mars Reconnaissance Orbiter), as well as those of the expired Mars Global Surveyor, should be able to fuel research into past volcanism on Mars for several years to come.

Based on the available imagery of Mars, it had generally been concluded at the end of the 20th century that eruptive activity is at least nonexistent or at most very rare and insubstantial on Mars in the present era (e.g. *McCauley et al.* [1972]; *Masursky* [1973]; *Carr* [1973]). However, the study of *Neukum et al.* [2004] identified calderas on five major Martian volcanoes that were interpreted to have undergone repeated activation and resurfacing during the last 20% of Martian history, with phases of activity as young as two million years, and suggested that the volcanoes are potentially still active today. *Neukum et al.* [2004] noted that several different collapse episodes with widely differing ages were often detectable in the calderas, and considered this to be in agreement with the theoretical analysis of *Wilson et al.* [2001], which suggested that magma reservoirs must cool and solidify between caldera collapse events, indicating that magma supply to major shield volcanoes on Mars must have been episodic rather than continuous. In addition, the detection of methane 'hotspots' in the atmosphere in the past decade has stimulated discussion as to whether this methane is originating from lingering volcanic activity or biological activity [*Formisano et al.*, 2004; *Krasnopolsky et al.*, 2004; *Mumma et al.*, 2004; 2009]; methane is stable in the Martian atmosphere for 250 to 300 years before it is oxidised [*Wong et al.*, 2003]. The 'Mars Trace Gas Mission' [*Smith et al.*, 2009], currently planned for launch in 2016 as a joint NASA-ESA mission, will

contain instruments whose objectives will be to accurately characterize the spatial and temporal variability of the methane concentrations, and to identify whether the methane is of geological or biological origin.

8.3 Interpretation of MARSIS reflections and implications for aquifer detection

8.3.1 Conclusions

The original intention of studying MARSIS radargrams was to identify the distribution of aquifers and ice layers within the Martian crust as a new means of assessing the extent to which magma-water interaction has influenced the volcanic history of Mars. As of June 2010, the MARSIS radar sounder [*Jordan et al.*, 2009] has been operational for five years, yet in that time has not succeeded in recording any subsurface reflections outside of the polar layered deposits that may plausibly be caused by the electrical discontinuity resulting from any combination of dry rock, ice-rich rock or an aquifer. This study has reviewed the literature examining the locations on Mars where definite subsurface reflections have been recorded, specifically the Polar Layered Deposits [*Plaut et al.*, 2007a], the Dorsa Argentea Formation [*Plaut et al.*, 2007b], and the Medusae Fossae Formation [*Watters et al.*, 2007]. Based on the strengths of the returned signals from these basal reflectors, previous studies have succeeded in refining estimates of the compositions and physical properties of these various deposits. In the cases of the Polar Layered Deposits and Dorsa Argentea Formation, the contrast in electrical properties results from the compositional difference between the ice-rich surface deposits and basaltic underlying bedrock [*Plaut et al.*, 2007a; 2007b]. In the case of the Medusae Fossae Formation, the contrast may potentially result from the surface deposit comprising an ice-rich material or a porous, ice-poor material [*Watters et al.*, 2007].

These are the only three extensive geological deposits on Mars where the respective electrical properties of the stratigraphic layers and the resolution abilities of MARSIS are such that identifiable subsurface reflections are resolved. This study has undertaken an investigation of a series of anomalous reflections within the vicinity of Ma'adim Vallis, the only other location on Mars where numerous, apparently subsurface reflections are grouped into a localized area. The origin of these reflections is ambiguous based on the fact that their locations do not appear to correspond to mapped

geological units in the way that the other three suites of reflections do. The study was performed with the intention of determining whether these reflections have arisen as a result of heterogeneities in the subsurface (which may be related to the presence of an aquifer or ice layer), or through some other cause.

The examination of the Ma'adim Vallis reflections has found that they frequently display parabolic and laterally extensive morphologies, and are erratically distributed, often being located directly adjacent to 'barren' radargrams with no reflections present within them. The investigation has concluded that a minor quantity of the reflections may be originating from subsurface interfaces (i.e. those underneath Eridania Planitia), in which case the reflections are caused by the electrical discontinuity between the bedrock and basin-filling material. However, most of them are regarded to be off-nadir echoes from the surface that have been refracted by high concentrations of charged particles in the ionosphere. This interpretation stems from an ionospheric electron density map, created by *Safaeinili et al.* [2007] using MARSIS data, which shows that a region of elevated electron density coincides with the location of a number of the parabolic reflections. However, this mechanism cannot explain the erratic timing of the occurrence of the reflections, and the fact that similar reflections are not seen in areas with similar electron density anomalies. The Ma'adim Vallis reflections exemplify the ambiguities that can beset interpretation of MARSIS data, yet the reflections are not considered to derive from an electrical discontinuity resulting from the presence of an aquifer or ice layer. This is based on their eccentric morphologies and the fact that they extend to time delays beyond which MARSIS would be able to resolve such dielectric boundaries.

The failure of MARSIS to detect an aquifer contains implications for the inventory, state and distribution of subsurface water on Mars, as well as for estimates of the performance capabilities of MARSIS. This study has derived an original estimate of the maximum depth for which MARSIS should be able to detect an aquifer, and has compared the result with those of previous studies with the same aim. In addition, this study has used updated parameters for the model developed by *Clifford* [1993], which predicts the extent of the Martian cryosphere and porous megaregolith. By reconciling the newly-derived detection estimate with the updated cryospheric model, the significance of the absence of MARSIS reflections for constraining the depth of a large-scale aquifer system may be evaluated.

Based on calculations of the decay of the MARSIS signal with depth, a maximum aquifer detection depth of ~350 m has been derived. When compared with the updated cryosphere model, it has been noted that this detection limit does not reach beneath the base of the cryosphere at any latitude, and therefore that MARSIS signals should not be expected to return an interpretable echo back to the sounder from an aquifer existing below the base of the cryosphere at any location on the planet. However, the generalized model of *Clifford* [1993] does not consider localized areas where anomalous variations in the thermal properties of the crust might allow aquifers to form at particularly shallow depths. Despite the confirmation of the presence of near-surface ice across much of the high latitudes of Mars through independent methods by the Phoenix [*Smith,* 2009], Odyssey [*Feldman et al.,* 2004] and Mars Reconnaissance Orbiter [*Byrne et al.,* 2009] missions, the absence of MARSIS reflections means that it remains unknown as to whether this layer melts beneath a depth of ~350 m or expires before it reaches the base of the cryosphere. It follows that MARSIS has not succeeded in showing where, how and to what extent water and ice may have influenced volcanic processes in Mars' history, both ancient and recent.

8.3.2 Recommendations for future work

The failure of MARSIS to resolve any subsurface reflections that may be interpreted as being caused by aquifers or ice layers has been attributed largely to the shallow maximum detection depth of ~350 m as estimated by this study, rather than the absence of such water bodies on Mars. Other studies that have addressed the issue of the MARSIS aquifer detection depth, specifically *Heggy et al.* [2001] and *Heggy et al.* [2003], have arrived at similarly low MARSIS detection estimates. In addition, it has been noted that the presence of clays and iron oxide-rich minerals in the Martian crust will act to further attenuate radio waves transmitted by MARSIS, even at low concentrations [*Heggy et al.,* 2001]. MARSIS transmits radio signals at frequencies that were thought to achieve the most suitable balance between resolution and penetration depth for detecting deep crustal water bodies, meaning that if MARSIS has failed to detect any such bodies, then it is unlikely that any future orbiting radar sounder will succeed either.

The SHARAD radar sounder aboard Mars Reconnaissance Orbiter has been operating since November 2006 at the higher frequency of 20 MHz, with a

correspondingly lower penetration depth than MARSIS. The instrument has successfully imaged the interiors of the polar layered deposits [*Milkovich et al.*, 2007; *Putzig et al.*, 2007] and Medusae Fossae Formation [*Carter et al.*, 2009] on a finer scale than MARSIS, and has also resolved the bases of buried glaciers in the southern mid-latitudes [*Holt et al.*, 2008] and the bases of Amazonian ice-rich and pristine volcanic deposits in the northern plains [*Stillman and Grimm*, 2009]. However, *Stillman and Grimm* [2009] noted that SHARAD signals outside these exceptional geological units appear to have experienced more attenuation than expected [*Stillman and Grimm*, 2009], as has been the case with MARSIS.

The attempt to constrain the volume, phase, and distribution of water within the Martian crust using sounding radar has therefore not been successful, with the consequence that no new deductions can be made using MARSIS data regarding the extent to which subsurface ice or water has interacted with volcanism in the past. Our knowledge of the history of Martian volcano-ice interactions therefore currently rests with the morphological evidence revealed by spacecraft imagery, described in section 1.2.2.4. Alternative methods will have to be pursued in order to locate aquifers on Mars, and they will likely be based on the surface rather than in orbit.

Terrestrial ground-based methods for water detection include ground resistivity measurement and magnetic resonance. The resistivity method exploits the fact that groundwater is ionically conductive as a result of the various dissolved salts it contains, and enables electric currents to flow in the ground [*Bernard*, 2003]. Measuring the ground resistivity may therefore allow the presence of water to be identified, depending on the resistivity of the water and the porosity of the rock; a low ground resistivity may correspond either to a high porosity or a low water resistivity, introducing an element of uncertainty with respect to interpreting resistivity anomalies. This method requires two electrodes to transmit a current through the ground, and another two to measure the potential created on the surface by the circulation of the current. In terrestrial surveys, the four electrodes are generally laid out along a linear survey line. Increasing the length of the survey line will increase the depth of investigation. For a Wenner alpha array [*Edwards*, 1977], whereby the two current-transmitting electrodes are positioned at the ends of the survey line with the potential-measuring electrodes placed at constant spacings between them, the survey line would need to be 17.3 km long in order to map

the resistivity to a depth of 3 km [*Loke*, 1999]. In order to map to a depth of 5 km, the survey line would need to be 28.9 km long.

The magnetic resonance method involves exciting the hydrogen protons of the water molecules with a magnetic field, produced by a current at the proton precession frequency, that passes through a loop laid out on the ground [*Bernard*, 2003]. The proton precession frequency is determined by the ambient magnetic field. The amplitude of the magnetic field produced in return by the protons in the same loop is proportional to the water content, whereas the time constant of the amplitude decay is linked to the permeability of the formation in which the aquifer resides. The depth of detection is roughly equal to the diameter of the loop, meaning that a loop circumference of 9.4 km is required to achieve a maximum investigation depth of 3 km, and a circumference of 15.7 km to achieve a depth of 5 km [*www.geoinstruments.com.au/pdf/numis-tutorial.pdf*].

The resistivity method is sensitive only to liquid water, and uncertainty exists in the interpretation of anomalies; the magnetic resonance method permits a direct, definite detection of water, yet cannot distinguish liquid water and ice, and must be performed at a location on Mars where the crust displays a remanent magnetic field (in order for the hydrogen protons to display a precession frequency). These methods therefore both have their benefits and disadvantages, and both could feasibly be performed automatically on Mars, with rovers laying out the necessary survey lines; as of May 2010, the Mars Exploration Rover Opportunity has travelled more than 20 km since January 2004 [*marsrovers.nasa.gov/home/*]. However, there are no current plans to include such experiments on any future lander missions to Mars. Ultimately, the most reliable method of identifying the presence of Martian aquifers would be to drill cores into the subsurface on the order of several hundred metres to kilometres in depth. However, such operations would be too labour-intensive and complex for automated missions, and would ideally require manned supervision in order to succeed.

8.4 Icelandic rootless cone groups and implications for Martian rootless cone histories

8.4.1 Conclusions

The study of Mars-analogue rootless cones in Iceland is separate from that focusing on intermediate volcanoes on Mars and Venus, yet despite the very different scales of the features under scrutiny, the nature of the investigation is consistent with the objectives of the thesis. The aims of this study have been to assess the extent to which formation conditions and subsequent erosion/modification have influenced the current morphologies of Icelandic cones. Through comparison of cone morphologies on both planets, the fieldwork performed in Iceland has been used to make inferences regarding the histories of analogous cones seen on Mars.

Surveys have been performed on four cones in the Álftaver cone group in south Iceland and one cone in the Mývatn cone group in north Iceland. In an attempt to relate the interior structures of the cones to their exterior morphologies, the surveys have employed ground-penetrating radar, topographic surveying, geomorphological observation, and petrological analysis of samples obtained from pits dug into the cone flanks. Three discrete morphological classes of rootless cone have been identified at the two localities. Consideration of the different modification environments experienced by cones both within and between cone fields has led to the conclusion that such disparities are largely responsible for the differences between the three morphological classes. However, differences in the availability of water at the eruption sites during formation of the cones have also affected their present morphologies.

Class A cones, which display larger cone/crater ratios than class B cones, are interpreted to have formed in locations where the magma-water ratio was less favourable to explosive eruption. This is despite the fact that class A cones display more extensive fine-grained ash deposits, which are interpreted to result from intensely explosive eruptive conditions, relative to class B cones. This has been explained by the observation that class B cones are located in areas that are interpreted to have experienced more intense erosional and depositional modification than class A cones. This is based on the presence of thick jökulhlaup deposits covering the flanks of class B cones at Álftaver, and the existence of ash deposits on the flanks of class A cones that are interpreted to originate from exterior sources (potentially Katla caldera). At the

southern boundary of Álftaver, wind and jökulhlaup erosion have combined to create the strongest weathering conditions, reducing both class A and class B cones to class C cones, which comprise irregular blocky remnants separated by interstitial ash.

A similar range of preservation states has been observed to characterize rootless cones on Mars. Most of the Martian cones display cone/crater ratios similar to those of class B cones. The most visible morphological disparity between different cone types is either the presence or absence of an outer apron surrounding the central steep cone, which is evidently related to the extent to which the surrounding terrain and the cones themselves have been modified. Cones that display the aprons tend to feature more sharply-defined bases, deeper craters and better-preserved flanks, and are situated within terrain that shows sharp relief and relatively few small impact craters, compared with those that do not. Given the absence of aqueous processes on present day Mars, modification processes are essentially confined to mass wasting, mantling by wind-blown dust, and impact cratering.

The correlation of Martian cone morphologies with their modification environment is also regarded as containing implications for the modification experienced by Icelandic rootless cones. Martian cones with class B-type cone/crater ratios sometimes display outer aprons around their central cones, whereas Icelandic class B cones have not been observed to do this. If the formation processes of the cones on the two planets are analogous, then the Icelandic class B cones should have originally been surrounded by such aprons, which have since been removed and/or obscured by the very active terrestrial modification processes. The observed absence of class A cones on Mars may be a consequence of the Martian atmospheric and gravitational conditions, and potentially thicker Martian lava flows, promoting more explosive eruption conditions relative to those on Earth.

8.4.2 Recommendations for future work

The GPR surveys performed at the rootless cones fields at Álftaver and Mývatn have shown that GPR constitutes an efficient, non-destructive method of characterising the interior structures of these features. However, the surveys could have been improved in various ways, which would have reduced uncertainty in the interpretation of the data.

The pits dug into the flanks of the cones did not reach more than a metre in depth, which frustrated attempts to correlate the observed stratigraphy with the radar profiles, as the air and ground waves of the radar profiles eclipse the top metre or so of the subsurface. Digging deeper pits into the flanks would therefore have been desirable. However, digging deeper than a metre would require the pit to be widened considerably as well as deepened, and in some cases the presence of a layer of coarse scoria can significantly inhibit progress. This would serve to lengthen the timescale of the fieldwork, but is the only realistic option that allows comparison between stratigraphy and radar profile. Deeper stratigraphy may be observed if, once a pit has been dug as far as is deemed necessary and safe, a coring tube is hammered into the base of the pit and extracted; when used in conjunction, pit-digging and coring may allow a few metres of stratigraphy beneath the topmost metre to be observed.

Given the fairly constrained timescale allocated to the fieldwork (three full days at Álftaver), certain cones were selected for surveying that were regarded to be ideal representatives of their cone class. While this allowed definition of the different cone classes, as well as resolution of structural variations within the classes, a more accurate impression of how the cone structures vary across the field would have been obtained had surveys been performed across cones in a wider range of localities than the two that were studied. This would in turn have allowed a finer-scale characterization of how the varying modification conditions across the field affect the morphologies and structures of cones in different parts. Furthermore, there are several other rootless cone fields known to exist across Iceland [*Fagents et al.*, 2002]. While the cone fields of Álftaver and Mývatn were chosen as fieldwork sites because of their accessibility and general suitability for GPR surveying, the investigation of how formation conditions and modification processes affect cone morphology would benefit from applying the same fieldwork methods to these localities as well.

The study of Martian rootless cones should be aided by high-resolution imagery returned by cameras aboard Mars Reconnaissance Orbiter. Figure 7.7g shows an example of a rootless cone field imaged by the Context Imager camera, which attains a pixel resolution of 6 m [*Malin et al.*, 2007]. The HiRISE camera, which attains a pixel resolution of less than a metre [*McEwen et al.*, 2007], would allow the finer details of the cones, such as the extents of their outer aprons, to be even more accurately defined. There is also the potential for the topography of the cones, which has so far been poorly

characterized based on MOLA data, to be resolved on the scale of HiRISE imagery using stereo techniques [*Kirk et al.*, 2007; *Li et al.*, 2008]. However, the method would require a particular cone field to be imaged twice at different incidence angles. Observations such as these would constitute a valuable test of the extent to which the Martian cone morphologies resemble those of terrestrial cones.

Appendix I

This appendix contains Figs. App.1 to App.10, which display graphically various statistics relating to the morphologies of the Venusian and Martian intermediate volcanoes that have been catalogued for this study. The statistics displayed in each graph are commented on in section 2.4.

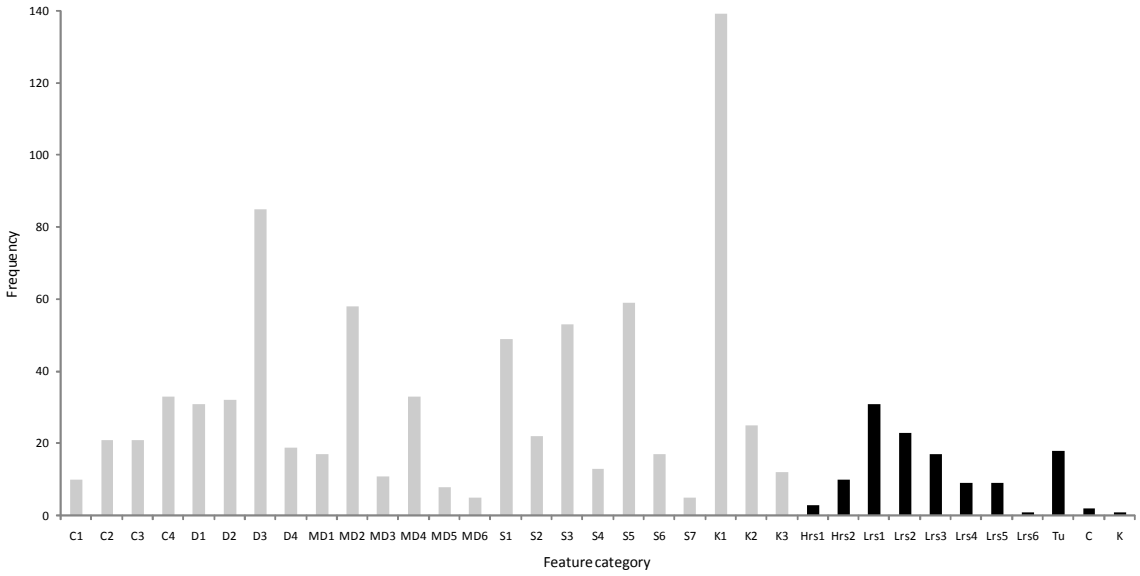

Figure App.1. The frequencies of each morphological subcategory. Venusian categories are shown in grey, Martian categories are shown in black.

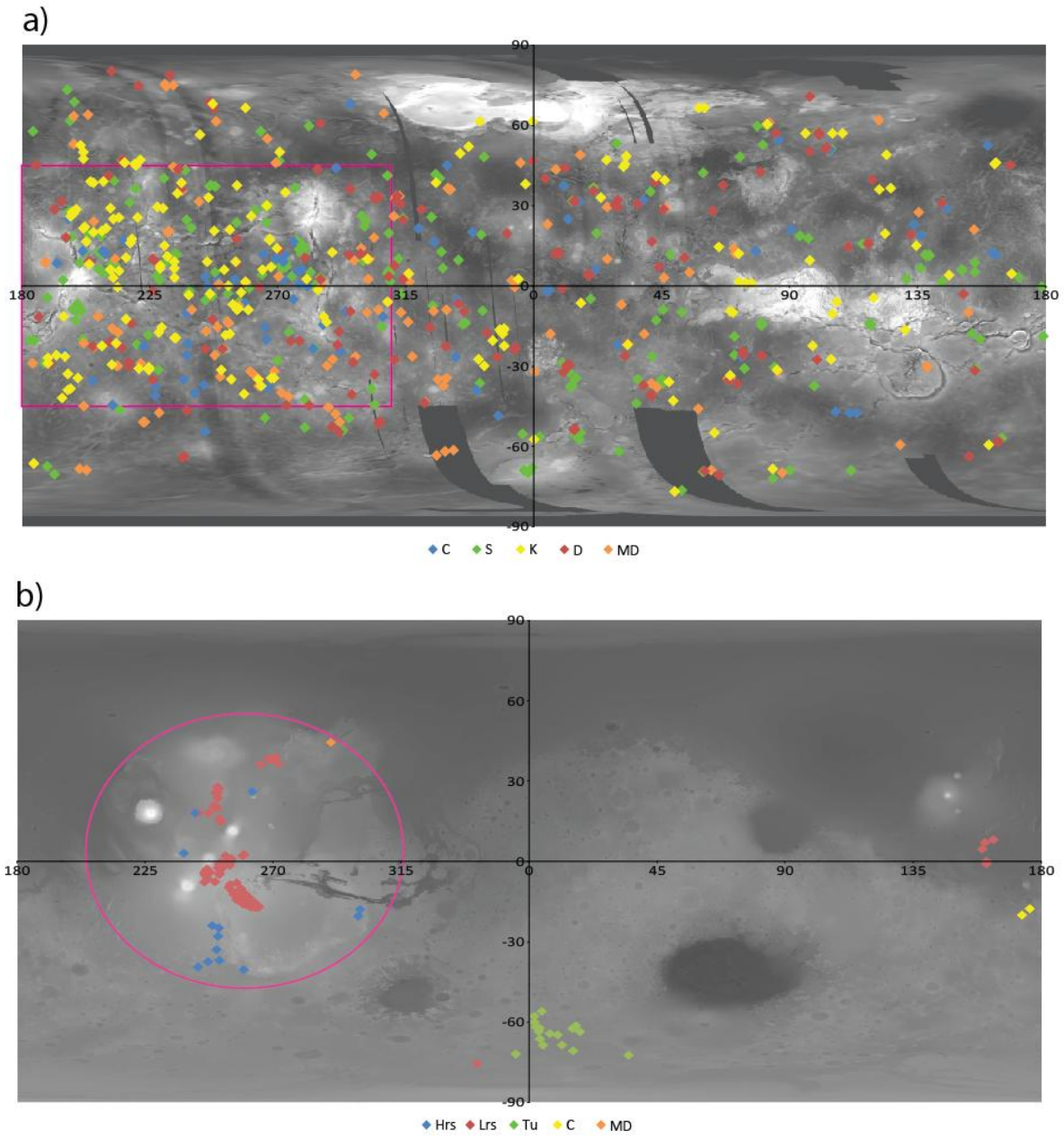

Figure App.2. Maps showing the distributions of the major morphological categories across Venus and Mars. (a) Venus base map is a GTDR, simple cylindrical projection with a resolution of 24 px/deg. Rectangle outlined in purple represents the boundary of the BAT region (45°N to 45°S, 180°E to 310°E). (b) Mars base map is a MOLA, simple cylindrical projection with a resolution of 16 px/deg. Purple ellipse highlights the approximate boundary of the Tharsis region.

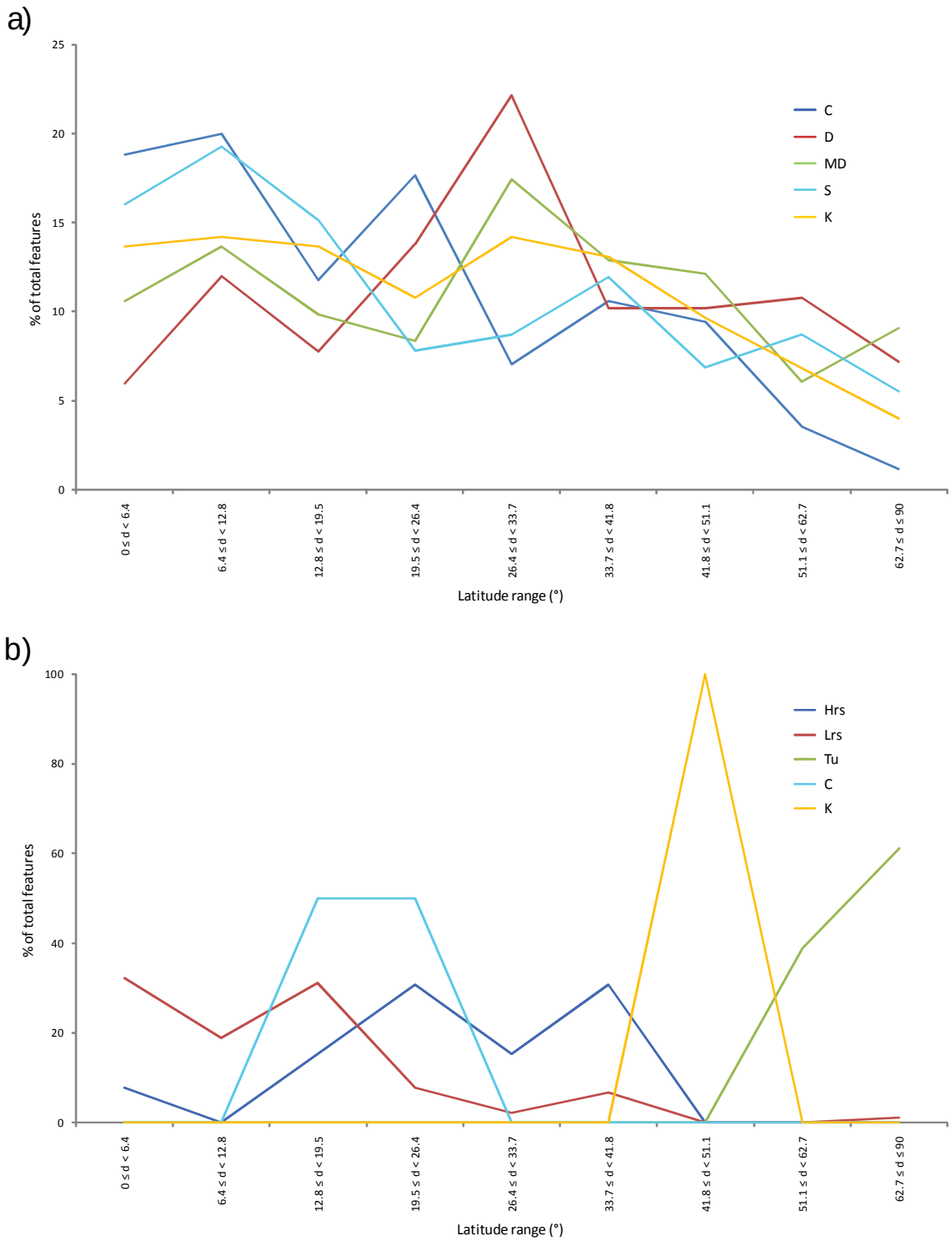

Figure App.3. The latitudinal distributions of the major morphological classes on Venus (a) and Mars (b).

a)

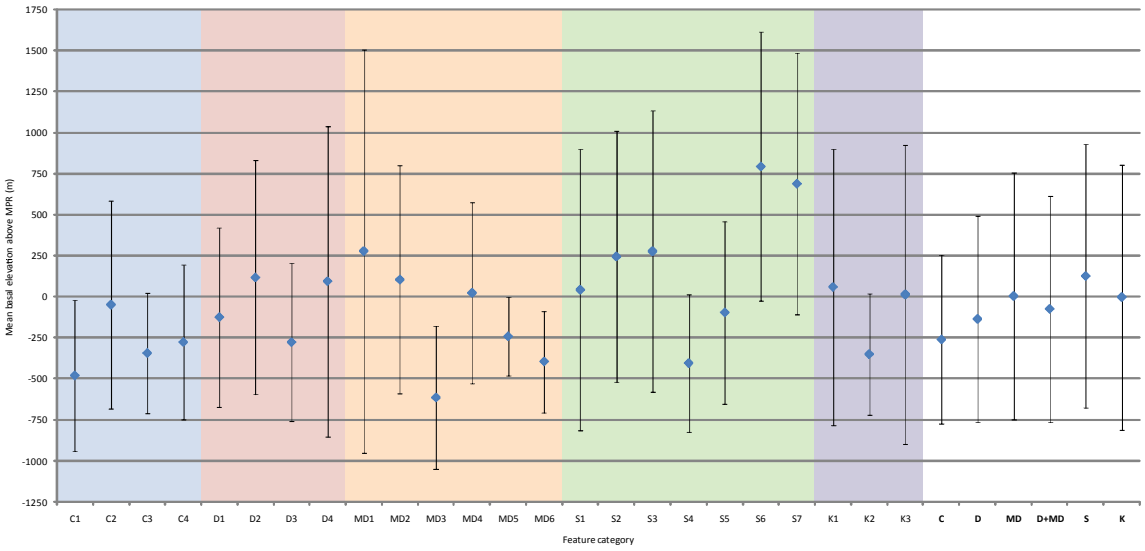

b)

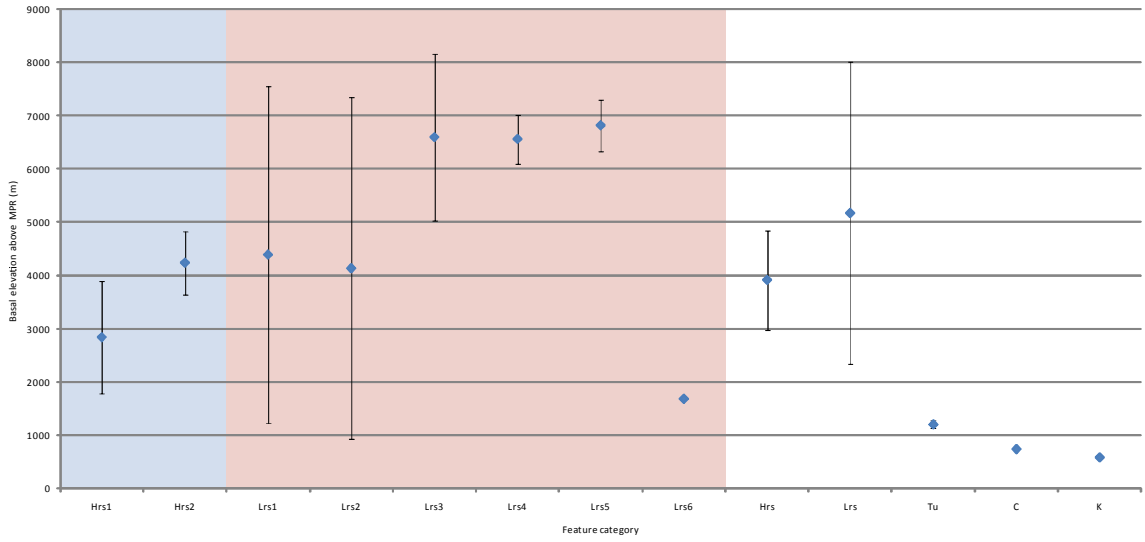

Figure App.4. The mean elevations of all morphological subcategories as well major categories on Venus (a) and Mars (b). Groups of related subcategories are highlighted by backdrops of different colours. Each value for the mean elevation has an associated standard deviation, indicated by error bars.

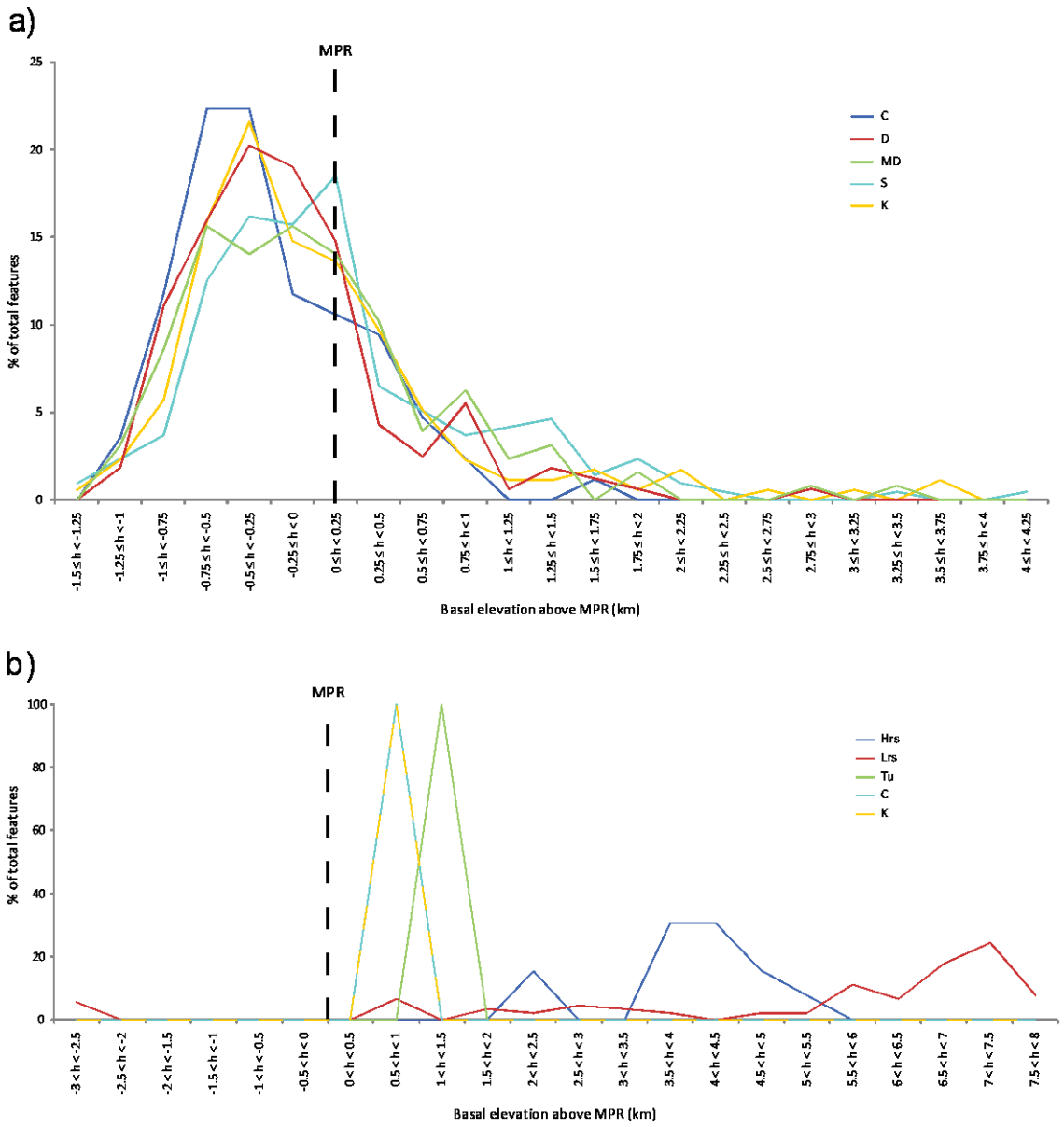

Figure App.5. The altitudinal distribution of the major morphological classes on Venus (a) and Mars (b). Mean planetary radius is highlighted by the dashed line on both charts. Note that for the Martian chart the cone and caldera lines overlap exactly.

a)

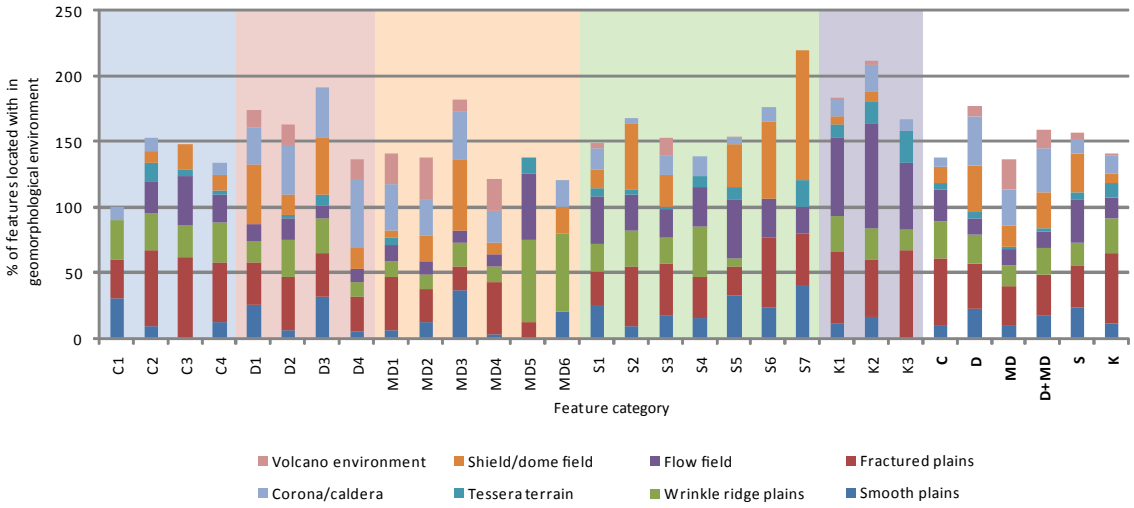

b)

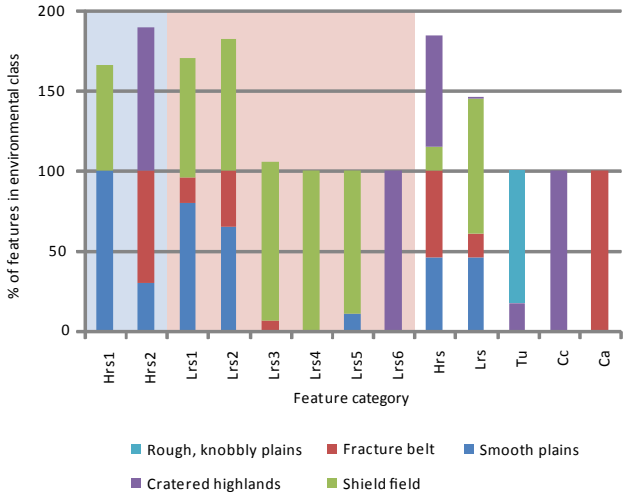

Figure App.6. Stacked column charts showing the percentages of each morphological subcategory and major category existing within each geological setting on Venus (a) and Mars (b). Because features can be located within more than one environment type the total percentages for each feature category add up to at least 100%.

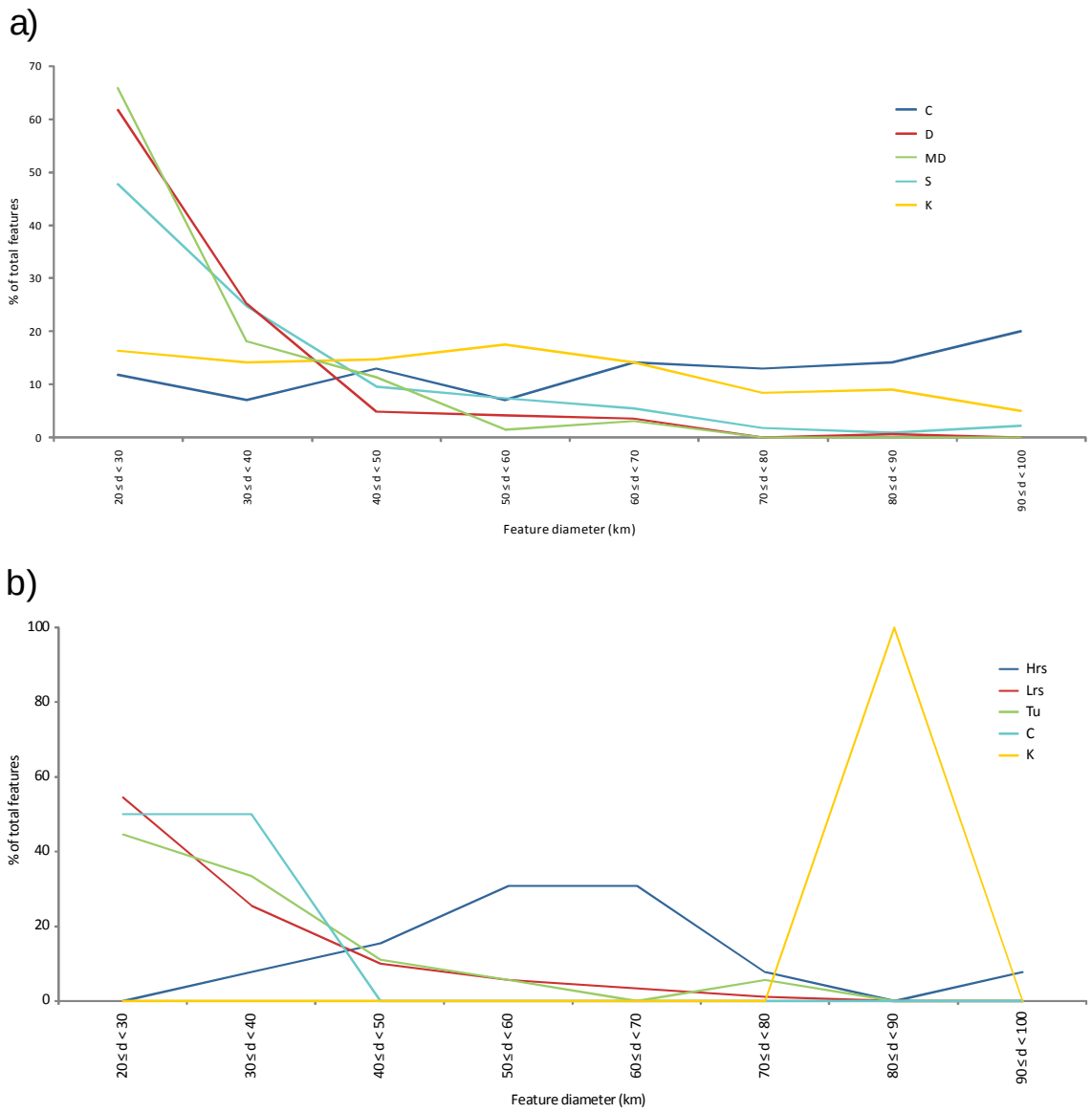

Figure App.7. The diameter distributions of the major morphological classes on Venus (a) and Mars (b).

a)

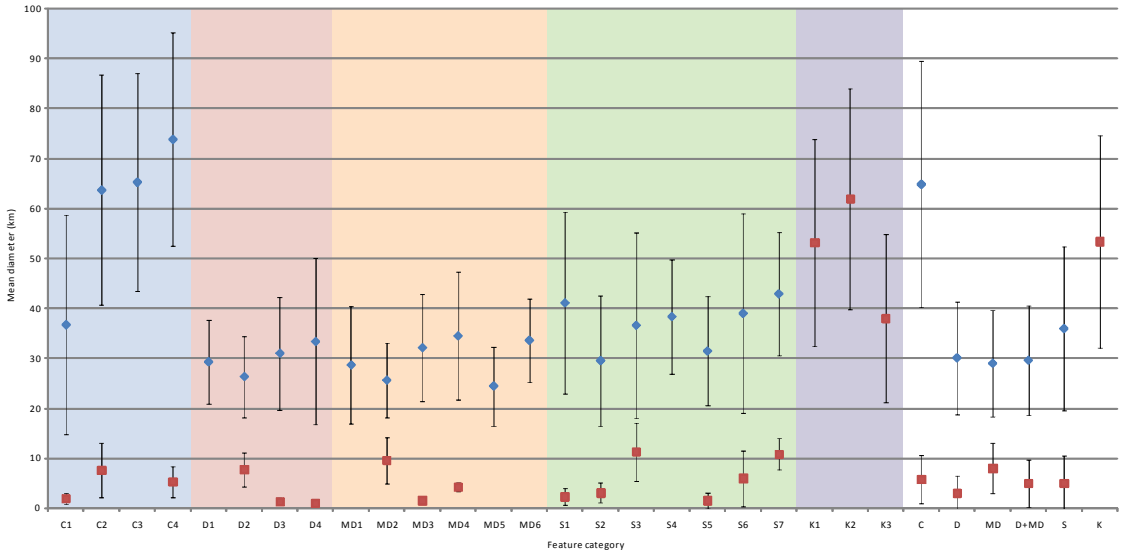

b)

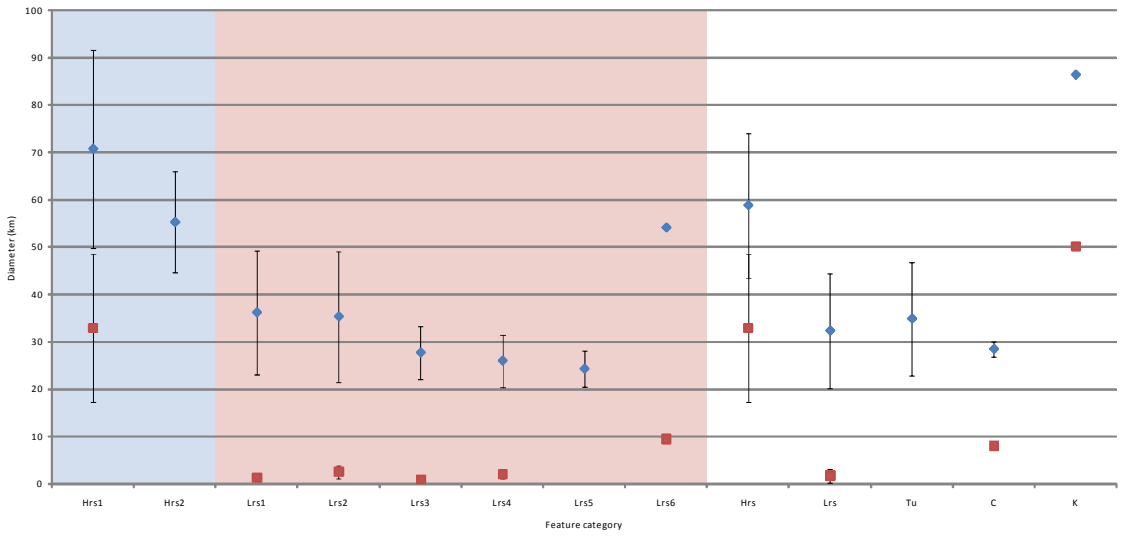

Figure App.8. The mean diameters of the edifices (in blue) and calderas (in red) of all morphological subcategories as well major categories on Venus (a) and Mars (b). Groups of related subcategories are highlighted by backdrops of different colours. Each value for the mean diameter has an associated standard deviation, indicated by error bars.

a)

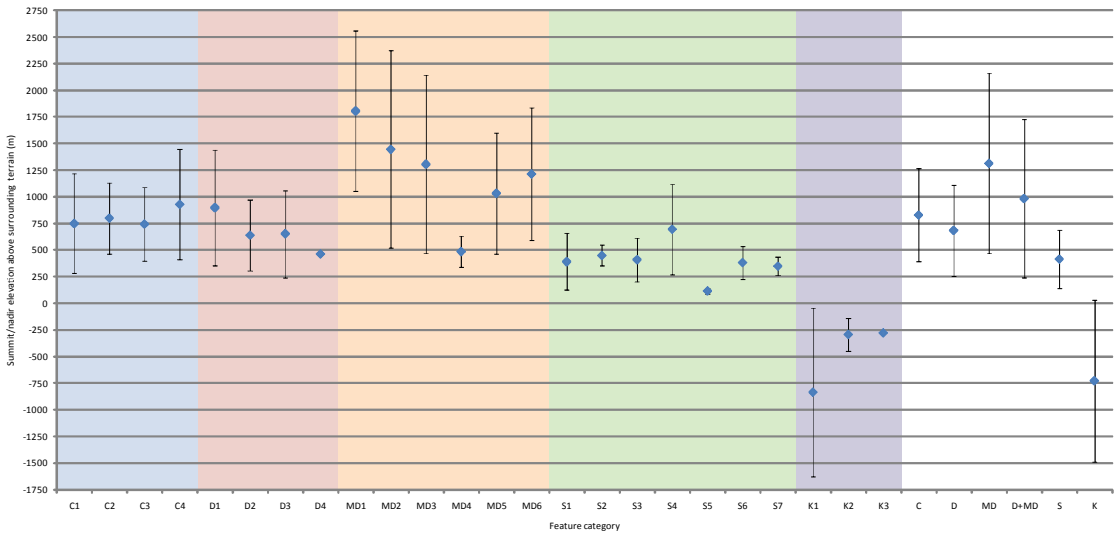

b)

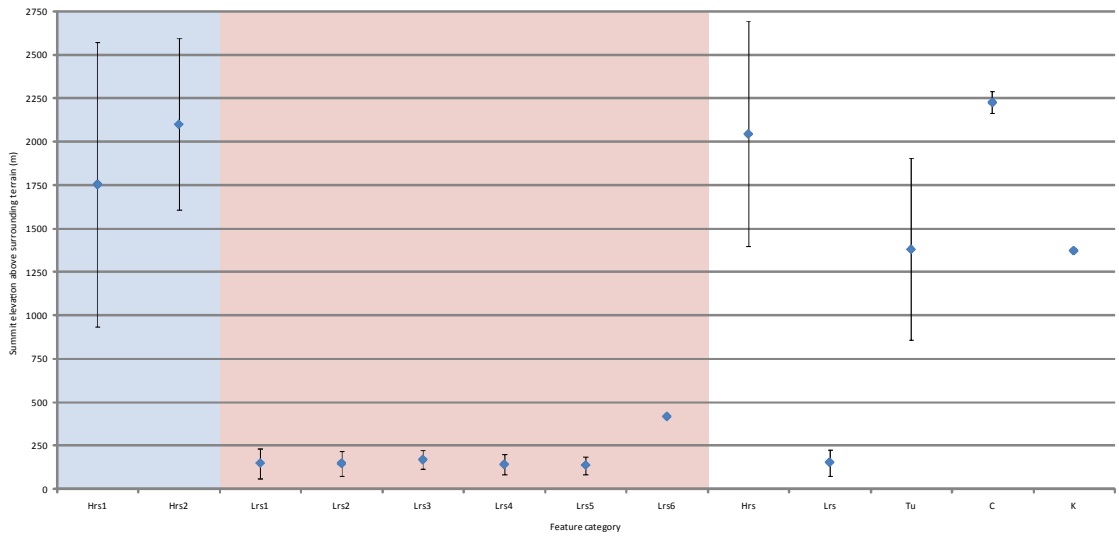

Figure App.9. The mean heights of all morphological subcategories as well major categories on Venus (a) and Mars (b). Groups of related subcategories are highlighted by backdrops of different colours. Each value for the mean height has an associated standard deviation, indicated by error bars.

a)

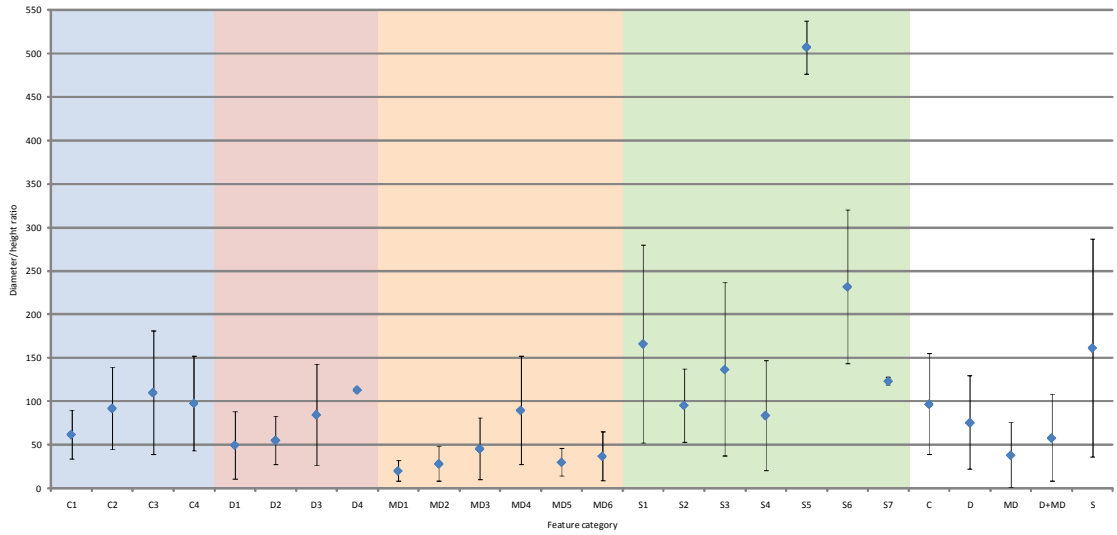

b)

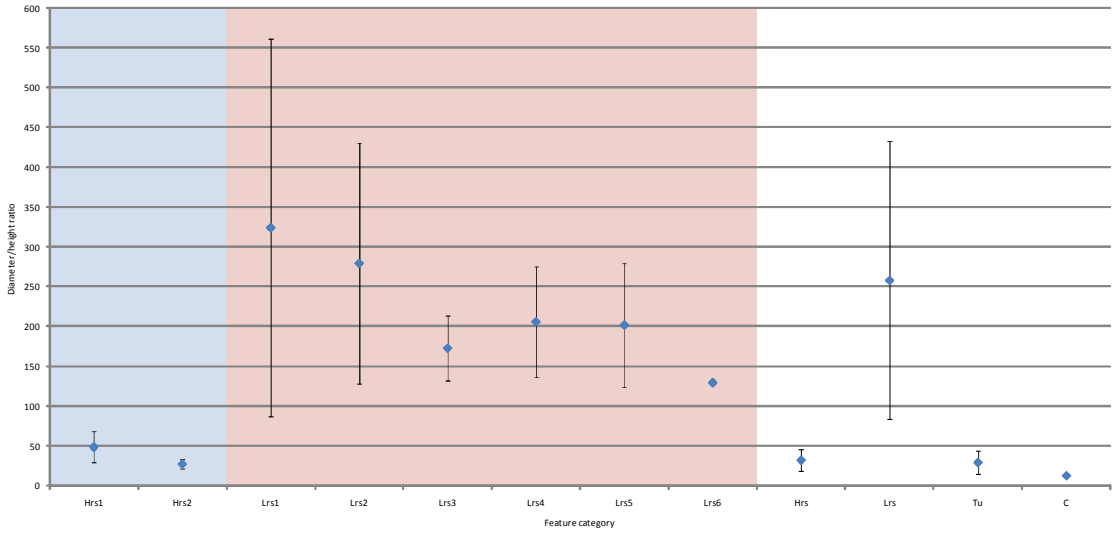

Figure App.10. The mean aspect ratios of all morphological subcategories as well major categories on Venus (a) and Mars (b). Groups of related subcategories are highlighted by backdrops of different colours. Each value for the mean height has an associated standard deviation, indicated by error bars.

References

Acuña, M.H., and 12 colleagues (1999) Global distribution of crustal magnetization discovered by the Mars Global Surveyor MAG/ER experiment. *Science*, **284**, 790-793.

Atreya, S.K., and J.E. Blamont (1990) Stability of the Martian atmosphere: Possible role of heterogeneous chemistry. *Geophys. Res. Lett.*, **17**, pp. 287-290.

Baines, K.H., S.K. Atreya, D. Crisp, J.L. Hall, V.V. Kerzhanovich, S.S. Limaye, and K. Zahnle (2009) In-situ exploration of Venus by balloon – science objectives and mission architecture. *Lunar Planet. Sci. Conf. XL*, Abstract #1238.

Baker, V.R. (1982) *The Channels of Mars*. Univ. of Texas Press, Austin.

Baker, V.R., R.G. Strom, V.C. Gulick, J.S. Kargel, G. Komatsu, and V.S. Kale (1991) Ancient oceans, ice sheets and the hydrological cycle on Mars. *Nature*, **352**, pp. 589-594.

Baker, V.R., M.H. Carr, V.C. Gulick, C. Williams, and M.S. Marley (1992) Channels and valley networks. From *Mars*, pp. 493-522, edited by H.H. Kieffer, B.M. Jakosky, C.W. Snyder, and M.S. Matthews, Univ. of Arizona Press, Tucson.

Balme, M.R., and M.C. Bourke (2005) Preliminary results of a new study of transverse aeolian ridges (TARs) on Mars. *Lunar Planet. Sci. Conf. XXXVI*, Abstract #1892.

Baratoux, D., P. Pinet, M.J. Toplis, N. Mangold, R. Greeley, and A.R. Baptista (2009) Shape, rheology and emplacement times of small martian shield volcanoes. *J. Volcan. Geoth. Res.*, **185**, pp. 47-68.

Barnett, D.N., F. Nimmo, and D. McKenzie (2002) Flexure of Venusian lithosphere measured from residual topography and gravity. *J. Geophys. Res.*, **107**(E2), 10.1029/2000JE001398.

Barsukov, V.L., and 29 colleagues (1986) The geology and geomorphology of the Venus surface as revealed by the radar images obtained by Veneras 15 and 16. *J. Geophys. Res.*, **91**, pp. D378-D398.

Basilevsky, A.T., M.A. Ivanov, J.W. Head, M. Aittola, and J. Raitala (2007) Landing on Venus: past and future. *Planet. Space Sci.*, **55**, pp. 2097-2112.

Beget, J.E., and J. Kienle (1992) Cyclic formation of debris avalanches at Mount St. Augustine volcano. *Nature*, **356**, pp. 701-704.

van Bemmelen, R.W. (1949) *The geology of Indonesia and adjacent archipelago*. The Hague: Government Printing Office.

Bernard, J. (2003) Short note on the principles of geophysical methods for groundwater investigations. Practical guide published online at www.heritagegeophysics.com/papers/ Groundwater_n_Geophysics.pdf

Best, M.G. (2003) *Igneous and metamorphic petrology*, 729 pp., Wiley-Blackwell.

Biccari, D., G. Picardi, R. Seu, A. Coradini, and R. Orosei (2001) The Mars High Resolution Advanced Radar for 2005 Space Mission. *Conference on the Geophysical Detection of Subsurface Water on Mars*, Abstract #7029.

Binder, A.B., and M.A. Lange (1980) On the thermal history, thermal state, and related tectonism of a moon of fission origin. *J. Geophys. Res.*, **85**, pp. 3194-3028.

Blake, S. (1981) Volcanism and the dynamics of open magma chambers. *Nature*, **289**, pp. 783-785.

Blamont, J., and R.Z. Sagdeev (1984) The VEGA mission. *Naturwissenschaften*, **71**, pp. 295-302.

Bleacher, J.E., and R. Greeley (2008) Relating volcano morphometry to the developmental progression of Hawaiian shield volcanoes through slope and hypsometric analyses of SRTM data. *J. Geophys. Res.*, **113**, B09208, doi:10.1029/2006JB004661.

Booth, M.C., and H.H. Kieffer (1978) Carbonate formation in Marslike environments. *J. Geophys. Res.*, **83**, pp. 1089-1815.

Bradley, B.A., S.E.H. Sakimoto, H. Frey, and J.R. Zimbelman (2002) Medusae Fossae Formation: new perspectives from Mars Global Surveyor. *J. Geophys. Res.*, **107**, 5058, doi:10.1029/2001JE001537.

Brain, D.A., J.S. Halekas, R. Lillis, D.L. Mitchell, R.P. Lin, and D.H. Crider (2005) Variability of the altitude of the Martian sheath. *Geophys. Res. Lett.*, **32** (L18203), doi:10.1029/2005GL023126.

Brent, G.W., J.R. Zimbelman, J.E. Bleacher, D.A. Williams, and M.E. Trumble (2007) Geologic mapping of Ascraeus Mons volcano, Mars at 1:1M scale: an analysis of the geomorphology and formation of Ascraeus Chasmata. *Geological Society of America, Abstracts with Programs*, **39**, No. 6, p. 590.

Brian, A.W. (2001) A study of large volcanoes and their geological settings on Venus. Thesis submitted for the degree of Doctor of Philosophy of the University of London.

Brian, A.W., S.E. Smrekar, and E.R. Stofan (2004) An admittance survey of large volcanoes on Venus: implications of volcano growth. *Lunar Planet. Sci. XXXV*, Abstract #1318.

Bridges, N.T. (1997) Ambient effects on basalt and rhyolite lavas under Venusian, subaerial, and subaqueous conditions. *J. Geophys. Res.*, **102**, No. E4, pp. 9243-9255.

Brown, C.D., and R.E. Grimm (1999) Recent tectonic and lithospheric thermal evolution of Venus. *Icarus*, **139**, pp. 40-48.

Bruno, B.C., S.A. Fagents, T. Thordarson, S.M. Baloga, and E. Pilger (2004) Clustering within rootless cone groups on Iceland and Mars: effect of nonrandom processes. *J. Geophys. Res.*, **109** (E07009), doi:10.1029/2004JE002273.

Budden, K.G. (1985) *The Propagation of Radio Waves*, Cambridge Univ. Press, New York.

Bullock, M.A., and 29 colleagues (2009) A Venus flagship mission: report of the Venus science and technology definition team. *Lunar Planet. Sci. Conf. XL*, Abstract #2410.

Bulmer, M.H., and J.E. Guest (1996) Modified volcanic domes and associated debris aprons on Venus. From *Volcano Instability on the Earth and Other Planets*, Geological Society Special Publication No. 110, pp. 349-371.

Byrne, S., 15 other colleagues, and the HiRISE, CTX and CRISM teams (2009) Excavation of subsurface ice on Mars by new impact craters. *Lunar Planet. Sci. XL*, Abstract #1831.

Cabrol, N.A., and E.A. Grin (1999) Distribution, classification and ages of Martian impact crater lakes. *Icarus*, **142**, pp. 160-172.

Cabrol, N.A., E.A. Grin and G. Dawidowicz (1996) Ma'adim Vallis revisited through new topographic data: evidence for an ancient intravalley lake. *Icarus*, **123**, pp. 269-283.

Campbell, B.A., and P.G. Rogers (1994) Bell Regio, Venus: integration of remote sensing data and terrestrial analogs for geologic analysis. *J. Geophys. Res.*, **99** (E10), pp. 21,153-21,171.

Campbell, B.A., L. Glaze, and P.G. Rogers (1998) Pyroclastic deposits on Venus: remote-sensing evidence and modes of formation. *Lunar Planet. Sci. XXIX*, Abstract #1810.

Carr, M.H. (1973) Volcanism on Mars (Martian volcanic and tectonic features from Mariner 9 photography, comparing evolutionary phases with lunar and terrestrial morphology). *J. Geophys. Res.*, **78**, pp. 4049-4062.

Carr, M.H. (1974) Tectonism and volcanism of the Tharsis region of Mars. *J. Geophys. Res.*, **79**, pp. 3943-3949.

Carr, M.H. (1984) Mars, in *The Geology of the Terrestrial Planets*, ed. M.H. Carr, pp. 207-219, NASA SP-469.

Carr, M.H. (1986) Mars: a water rich planet? *Icarus*, **67**, pp. 187-216.

Carr, M.H. (1996) *Water on Mars*, Oxford University Press.

Carr, M.H., and G.G. Schaber (1977) Martian permafrost features. *J. Geophys. Res.*, **82**, pp. 4039-4054.

Carr, M.H., and G.D. Clow (1981) Martian channels and valleys: their characteristics, distribution and age. *Icarus*, **48**, pp. 91-117.

Carr, M.H., and 12 colleagues (1976) Preliminary results from the Viking orbiter imaging experiment. *Science*, **193**, pp. 766-776.

Carr, M.H., K.R. Blasius, R. Greeley, J.E. Guest, and J.E. Murray (1977) Observations on some Martian volcanic features as viewed from the Viking orbiters. *J. Geophys. Res.*, **82**, pp. 3985-4015.

Carter, L.M., and eleven colleagues (2009) Shallow radar (SHARAD) sounding observations of the Medusae Fossae Formation, Mars. *Icarus*, **199**, pp. 295-302.

Cas, R.A.F., and J.V. Wright (1987) *Volcanic Successions*, publ. Allen and Unwin, Winchester, Mass.

Chadwick, W.W., and K.A. Howard (1991) The pattern of circumferential and radial eruptive fissures on the volcanoes of Fernandina and Isabela islands, Galapagos. *Bull. Volcanol.*, **55**, pp. 259-275.

Chapman, M.G. (1994) Evidence, age, and thickness of a frozen paleolake in Utopia Planitia, Mars. *Icarus*, **109**, pp. 393-406.

Christensen, P.R., B.M. Jakosky, H.H. Kieffer, M.C. Malin, H.Y. McSween, K. Nealson, G.L. Mehall, S.H. Silverman, S. Ferry, M. Caplinger, and M. Ravine (2004) The

Thermal Emission Imaging System (THEMIS) for the Mars 2001 Odyssey Mission. *Space Sci. Rev.*, **110**, pp. 85-130.

Clark, B.C. and D.C. Van Hart (1981) The salts of Mars. *Icarus*, **45**, pp. 370-378.

Clark, B.C., A.K. Baird, H.J. Rose, P. Toulmin, K. Keil, A.J. Castro, W.C. Kelliher, C.D. Rowe, and P.H. Evans (1976) Inorganic analysis of Martian surface samples at the Viking landing sites. *Science*, **194**, pp. 1283-1288.

Clifford, S.M. (1981) A model for the climatic behaviour of water on Mars. Paper presented to the Third Int. Colloq. on Mars, *LPI Contrib. 441*, pp. 44-45, Lunar and Planetary Inst., Houston, Tex.

Clifford, S.M. (1993) A model for the hydrologic and climatic behaviour of water on Mars. *J. Geophys. Res.*, **98**, pp. 10,973-11,016.

Clifford, S.M. and F.P. Fanale (1985) The thermal conductivity of the Martian crust. *Lunar Planet. Sci. XVI*, pp. 144-145.

Clifford, S.M., and D. Hillel (1983) The stability of ground ice in the equatorial region of Mars. *J. Geophys. Res.*, **84**, pp. 8115-8130.

Clifford, S.M., and T.J. Parker (2001) The evolution of the martian hydrosphere: implications for the fate of a primordial ocean and the current state of the northern plains. *Icarus*, **154**, pp. 40-79.

Clifford, S.M., E. Heggy, J. Boisson, P. McGovern, and M.D. Max (2009) The occurrence and depth of subpermafrost groundwater on present-day Mars: implications of revised estimates of crustal heat flow, thermal conductivity, and freezing point depression. *Lunar Planet. Sci. XL*, Abstract #2557.

Connerney, J.E.P., M.H. Acuña, N.F. Ness, G. Kletetschka, D.L. Mitchell, R.P. Lin and H. Reme (2005) Tectonic implications of Mars crustal magnetism. *Proc. Natl. Acad. Sci. USA*, **102**, no. 42, 14970-14975.

Coradini, M., and E. Flamini (1979) A thermodynamical study of the Martian permafrost. *J. Geophys. Res.*, **88**, pp. 2456-2474.

Costard, F.M. (1988) Thickness of sedimentary deposits at the mouth of outflow channels. *Lunar Planet. Sci. XIX*, pp. 211-212 (Abstract).

Costard, F.M. (1989) Asymmetric distribution of volatiles on Mars. *Lunar Planet. Sci. XX*, pp. 187-188 (Abstract).

Crown, D.A., and R. Greeley (1993) Volcanic geology of Hadriaca Patera and the eastern Hellas region of Mars. *J. Geophys. Res.*, **98**, pp. 3431-3451.

Crumpler, L.S., and J.C. Aubele (1978) Structural evolution of Arsia Mons, Pavonis Mons, and Ascraeus Mons: Tharsis region of Mars. *Icarus*, **34**, pp. 496-511.

Crumpler, L.S., and J.C. Aubele (2000) Volcanism on Venus. From *Encyclopedia of Volcanoes*, pp. 727-770, edited by H. Sigurdsson, B. Houghton, S.R. McNutt, H. Rymer, and J. Stix, Academic Press.

Crumpler, L.S., J.C. Aubele, J.W. Head, R.S. Saunders, and the Magellan Science Team (1991) Global distribution of volcanic features on Venus. *Geol. Soc. Am. Abstr. Programs*, **23**, A400.

Crumpler, L.S., J.C. Aubele, D.A. Senske, S.T. Keddie, K.P. Magee, and J.W. Head (1997) Volcanoes and centers of volcanism on Venus. From *Venus II: Geology, Geophysics, Atmosphere, and Solar Wind Environment*, pp. 697-756, edited by S.W. Bougher, D.M. Hunten, and R.J. Philips, Univ. of Arizona Press, Tucson.

Daag, A.S., M.T. Dolan, E.P. Laguerta, G.P. Meeker, C.G. Newhall, J.S. Pallister, and R.U. Solidum (1996) Growth of a postclimactic lava dome at Mount Pinatubo, July-October 1992. From *Fire and Mud: Eruptions and Lahars of Mount Pinatubo, Philippines*, ed. C.G. Newhall and R.S. Punongbayan, University of Washington Press.

Davies, G.F. and R.E. Arvidson (1981) Martian thermal history, core segregation, and tectonics. *Icarus*, **45**, pp. 339-346.

Davis, J.C. (1986) Statistics and Data Analysis in Geology, 1st edition, pub. Wiley, Chichester, New York.

De Hon, R.A. (1977) Geologic Map of the Eridania Quadrangle of Mars. *U.S. Geol. Survey. Invest. Ser. Map, I-1008 (MC-29).*

Delamere, W.A., and 15 colleagues (2009) Color imaging of Mars by the High Resolution Imaging Science Experiment (HiRISE). *Icarus*, **205**, pp. 38-52.

Delaney, P.T., and D.D. Pollard (1982) Solidification of basaltic magma during flow in a dike. *Am. J. Sci.*, **282**, pp. 856-885.

Dohm, J.M., and K.L. Tanaka (1999) Geology of the Thaumasia Region, Mars: plateau development, valley origins, and magmatic evolution. *Planet. Space Sci.*, **47**, pp. 411-431.

Donahue, T.M., and R.R. Hodges (1992) Past and present water budget of Venus. *J. Geophys. Res.*, **97**, pp. 6083-6091.

Donahue, T.M., and C.T. Russell (1997) The Venus atmosphere and ionosphere and their interaction with the solar wind: an overview. From *Venus II: Geology, Geophysics, Atmosphere, and Solar Wind Environment*, pp. 3-32, edited by S.W. Bougher et al., Univ. Of Ariz. Press, Tucson.

Donahue, T.M., J.H. Hoffman, R.R. Hodges, and A.J. Watson (1982) Venus was wet: a measurement of the ratio of deuterium to hydrogen. *Science*, **216**, pp. 630-633.

Drossart, P., and 43 colleagues (2007) Scientific goals for the observation of Venus by VIRTIS on ESA/Venus express mission. *Planet. Space Sci.*, **55**, pp. 1653-1672.

Duller, R.A., N.P. Mountneys, A.J. Russell, and N.C. Cassidy (2008) Architectural analysis of a jökulhlaup deposit, southern Iceland: sedimentary evidence for supercritical flow. *Sedimentology*, **55**, pp. 939-964.

Duncan, A.M., and J.E. Guest (1982) Mount Etna: variations in its internal plumbing. *Geophys. Surv.*, **5**, pp. 213-227.

Edwards, L.S. (1977) A modified pseudosection for resistivity and induced-polarization. *Geophysics*, **42**, pp. 1020-1036.

Einarsson, T. (1966) Physical aspects of sub-glacial eruptions. *Jokull*, **16**, pp. 167-174.

Fagents, S.A., and T. Thordarson (2007) Rootless volcanic cones in Iceland and on Mars, in *The Geology of Mars: Evidence from Earth-based Analogs*, edited by M. Chapman, pp. 151-177, Cambridge University Press.

Fagents, S.A., and L. Wilson (1996) Numerical modelling of ejecta dispersal around the sites of volcanic explosions of Mars. *Icarus*, **123**, pp. 284-295.

Fagents, S.A., P. Lanagan, and R. Greeley (2002) Rootless cones on Mars: a consequence of lava-ground ice interaction. From *Volcano-Ice Interaction on Earth and Mars*, ed. J.L. Smellie and M.G. Chapman, Geological Society Special Publication no.202, pp. 295-317.

Fanale, F.P. (1976) Martian volatiles: their degassing history and geochemical fate. *Icarus*, **28**, pp. 179-202.

Fanale, F.P., J.R. Salvail, W.B. Banerdt, and R.S. Saunders (1982) Mars: The regolith-atmosphere-cap system and climate change. *Icarus*, **50**, pp. 381-407.

Fanale, F.P., J.R. Salvail, A.P. Zent, and S.E. Postawko (1986) Global distribution and migration of subsurface ice on Mars. *Icarus*, **67**, pp. 1-18.

Fanale, F.P., S.E. Postawko, J.B. Pollack, M.H. Carr, and R.O. Pepin (1992) Mars: epochal climate change and volatile history. From *Mars*, pp. 1135-1179, edited by H.H. Kieffer, B.M. Jakosky, C.W. Snyder, and M.S. Matthews, Univ. of Arizona Press, Tucson.

Farmer, C.B., and P.E. Doms (1979) Global and seasonal variation of water vapour on Mars and the implications for permafrost. *J. Geophys. Res.*, **84**, pp. 2881-2888.

Farmer, C.B., D.W. Davies and D.P. La Porte (1976) Mars: northern summer ice cap – water vapour observations from Viking 2. *Science*, **194**, pp. 1339-1341.

Farrell, W.M., J.J. Plaut, S.A. Cummer, D.A. Gurnett, G. Picardi, T.R. Watters, and A. Safaeinili (2009) Is the Martian water table hidden from view? *Geophys. Res. Lett*., **36** (L15206), doi:10.1029/2009GL038945.

Fedotov, S.A. (1978) Ascent of basic magmas in the crust and the mechanism of basaltic fissure eruptions. *Int. Geol. Rev.*, **20**, pp. 33-48.

Feldman, W.C., and 14 colleagues (2004) Global distribution of near-surface hydrogen on Mars. *J. Geophys. Res.*, **109**, E09006, doi:10.1029/2003JE002160.

Fink, J.H. (1993) The emplacement of silicic lava flows and associated hazards. From *Active Lavas*, pp. 5-24, edited by C.R.J. Kilburn and G. Luongo, Univ. College London Press, London.

Fink, J.H., and S.W. Anderson (2000) Lava domes and coulees. From *Encyclopedia of Volcanoes*, pp. 307-319, edited by H. Sigurdsson, B. Houghton, S.R. McNutt, H. Rymer, and J. Stix, Academic Press.

Fink, J.H., and S.W. Kieffer (1993) Estimate of pyroclastic flow velocities resulting from explosive decompression of lava domes. *Nature*, **363**, pp. 612-615.

Fink, J.H., N.T. Bridges, and R.E. Grimm (1993) Shapes of Venusian "pancake" domes imply episodic emplacement and silicic composition. *Geophys. Res. Lett.*, **20**, pp. 261-264.

Fisher, R.V. (1961) Proposed classification of volcaniclastic sediments and rocks. *Geol. Soc. Amer. Bull., 72*, 1409-1414.

Fisher, R.V., H.X. Glicken, and R.P. Hoblitt (1987) Mount St. Helens deposits in South Coldwater Creek, Washington. *J. Geophys. Res.*, **92**, pp. 10,267-10,283.

Fiske, R.S., and W.T. Kinoshita (1969) Inflation of Kilauea volcano prior to its 1967-1968 eruption. *Science*, **165**, pp. 341-349.

Florensky, C.P., L.B. Ronca, A.T. Basilevsky, G.A. Burba, O.V. Nikolaeva, A.A. Pronin, A.M. Trakhtman, V.P. Volkov, and V.V. Zazetsky (1977) The surface of Venus as revealed by Soviet Venera 9 and 10. *Geol. Soc. Am. Bull.*, **88**, pp. 1537-1545.

Florensky, C.P., A.T. Basilevsky, V.P. Kryuchkov, R.O. Kuzmin, A.A. Pronin, O.V. Nikolaeva, I.M. Chernaya, A.S. Selivanov, M.K. Naraeva, and Y.S. Tyuflin (1982) An analysis of the panoramic pictures of the landing sites of Venera 13 and Venera 14. *Pisma Astron. Zh.*, **8**, p. 429.

Folch, A., and J. Marti (2004) Geometrical and mechanical constraints on the formation of ring-fault calderas. *Earth Planet. Sci. Lett.*, **221** (1-4), pp. 215-225.

Ford, J.P. (1993) Magellan: The Mission and the System, in *Guide to Magellan Image Interpretation*, pp. 1-5, edited by J.P. Ford, J.J. Plaut, C.M. Weitz, T.G. Farr, D.A. Senske, E.R. Stofan, G. Michaels, and T.J. Parker, JPL Publication 93-24.

Ford, J.P., and J.J. Plaut (1993) Magellan Image Data, in *Guide to Magellan Image Interpretation*, pp. 7-18, edited by J.P. Ford, J.J. Plaut, C.M. Weitz, T.G. Farr, D.A. Senske, E.R. Stofan, G. Michaels, and T.J. Parker, JPL Publication 93-24.

Forget, F., R.M. Haberle, F. Montmessin, B. Levrard, and J.W. Head (2006) Formation of glaciers on Mars by atmospheric precipitation at high obliquity. *Science*, **311**, pp. 368-371.

Formisano, V., S. Atreya, T. Encrenaz, N. Ignatiev, and M. Giuranna (2004) Detection of methane in the atmosphere of Mars. *Science*, **306**, pp. 1758-1761.

Fox, J.L., and A. Dalgarno (1983) Nitrogen escape from Mars. *J. Geophys. Res.*, **88**, pp. 9027-9032.

Francis, P.W., and G. Waadge (1983) The Olympus Mons aureole: Formation by gravitational spreading. *J. Geophys. Res.*, **88**, pp. 8333-8344.

Francis, P.W., M.J. Roobol, G.P.L. Walker, P.R. Cobbold, and M. Coward (1974) The San Pedro and San Pablo volcanoes of northern Chile and their hot avalanche deposits. *Geologische Rundschau*, **63**, pp. 357-388.

Frenkel, M.Y., and Y.V. Zabalueva (1983) The solidification of effusive melts on Venus and Earth. *Geochem. Int.*, **20**, pp. 43-47.

Frey, H.V., and M. Jarosewich (1982) Subkilometer martian volcanoes: properties and possible terrestrial analogs. *J. Geophys. Res.*, **87**, pp. 9867-9879.

Frey, H.V., B.L. Lowry, and S.A. Chase (1979) Pseudocraters on Mars. *J. Geophys. Res.*, **84**, pp. 8075-8086.

Frey, H.V., J.H. Roark, K.M. Shockey, E.L. Frey and S.E.H. Sakimoto (2002) Ancient Lowlands on Mars. *Geophys. Res. Lett*., **29**, doi:10.1029/2001GL013832.

Fröhlich, G., B. Zimanowski, and V. Lorenz (1993) Explosive thermal interactions between molten lava and water. *Experimental Thermal and Fluid Science*, **7**, pp. 319-32.

Garvin, J.B., S.E.H. Sakimoto, J.J. Frawley, C.C. Schnetzler, and H.M. Wright (2000) Topographic evidence for geologically recent near-polar volcanism on Mars. *Icarus*, **145**, pp. 648-652.

Gault, D.E., and R. Greeley (1978) Exploratory experiments of impact craters formed in viscous-liquid targets: analogs for Martian rampart craters? *Icarus*, **33**, pp. 483-513.

Gendrin, A., N. Mangold, J.-P. Bibring, Y. Langevin, B. Gondet, F. Poulet, G. Bonello, C. Quantin, J. Mustard, R. Arvidson, and S. LeMouélic (2005) Sulfates in Martian layered terrains: the OMEGA/Mars Express view, *Science*, **307**, pp. 1587-1591.

Gerlach, T. M. (1986) Exsolution of H_2O, CO_2 and S during eruptive episodes at Kilauea volcano, Hawaii, *J. Geophys. Res.*, **91**(B12), pp. 12,177–12,185.

Ghatan, G.J., and J.W. Head (2002) Candidate subglacial volcanoes in the south polar region of Mars: morphology, morphometry, and eruption conditions. *J. Geophys. Res.*, **107**, doi:10.1029/2001JE001519.

Ghatan, G.J., and J.W. Head (2004) Regional drainage of meltwater beneath a Hesperian-aged south circumpolar ice sheet on Mars. *J. Geophys. Res.*, **109**, E07006, doi:10.1029/2003JE002196.

Gorshkov, G.S. (1959) Gigantic eruption of the volcano Bezymianny. *Bull. Volcan.*, **20**, pp. 77-112.

Greeley, R. (1982) The Snake River Plain, Idaho: representative of a new category of volcanism. *J. Geophys. Res.*, **87**, No. B4, pp. 2705-2712.

Greeley, R., and D.A. Crown (1990) Volcanic geology of Tyrrhena Patera, Mars. *J. Geophys. Res.*, **95**, pp. 7133-7149.

Greeley, R., and P. Spudis (1981) Volcanism on Mars. *Rev. Geophys. Space Phys.*, **19**, pp. 13-41.

Greeley, R., and B. Schneid (1991) Magma generation on Mars: amounts, rates and comparisons with Earth, Moon and Venus. *Science*, **254**, pp. 996-998.

Greeley, R., and S.A. Fagents (2001) Icelandic pseudocraters as analogs to some volcanic cones on Mars. *J. Geophys. Res.*, **106**(E9), 20527, doi:10.1029/2000JE001378.

Greeley, R., N. Lancaster, S. Lee, and P. Thomas (1992a) Martian aeolian processes, sediments and features. From *Mars*, pp. 730-766, edited by H.H. Kieffer, B.M. Jakosky, C.W. Snyder, and M.S. Matthews, Univ. of Arizona Press, Tucson.

Greeley, R., R.E. Arvidson, C. Elachi, M.A. Geringer, J.J. Plaut, R.S. Saunders, G. Schubert, E.R. Stofan, E.J.P. Thouvenot, S.D. Wall, and C.M. Weitz (1992b) Aeolian features on Venus: preliminary Magellan results. *J. Geophys. Res.*, **97**, pp. 13,319-13,345.

Greeley, R., N.T. Bridges, D.A. Crown, L. Crumpler, S.A. Fagents, P.J. Mouginis-Mark, and J.R. Zimbelman (2000) Volcanism on the red planet: Mars, in *Environmental Effects on Volcanic Eruptions: From Deep Oceans to Deep Space*, edited by J.R. Zimbelman and T.K.P. Gregg, pp. 75-112, Kluwer Academic/Plenum Press, New York.

Gregg, T.K.P., and S.N. Williams (1996) Explosive mafic volcanoes on Mars and Earth: deep magma sources and rapid rise rate. *Icarus*, **122**, pp. 397-405.

Griffiths, R.W., and J.H. Fink (1992) The morphology of lava flows in planetary environments: predictions from analog experiments. *J. Geophys. Res.*, **97**, pp. 19,739-19,748.

Grindrod, P.M., F. Nimmo, E.R. Stofan, and J.E. Guest (2005) Strain at radially fractured centers on Venus. *J. Geophys. Res.*, **110** (E12002), doi:10.1029/2005JE002416.

Grosfils, E.B., and J.W. Head (1994) Emplacement of a radiating dike swarm in western Vinmara Planitia, Venus; Interpretation of the regional stress field orientation and subsurface magma configuration. *Earth, Moon and Planets*, **66**, pp. 153-171.

Grosfils, E.B., and J.W. Head (1995) Radiating dike swarms on Venus: evidence for emplacement at zones of neutral buoyancy. *Planet. Space Sci.*, **43**, No. 12, pp. 1555-1557.

Grott, M. (2008) Is Mars geodynamically dead? *Science*, **320**, pp. 1171-1172.

Guest, J.E. (1982) Styles of eruption and flows morphology on Mt. Etna. In *Mount Etna Volcano: A Review of Recent Earth Science Studies*, ed. R. Romano, pp. 49-67, Mem. Societa Geologica Italiana XXIII.

Guest, J.E., and A.M. Duncan (1981) Internal plumbing of Mount Etna. *Nature*, **290**, pp. 584-586.

Guest, J.E., D.K. Chester, and A.M. Duncan (1984) The Valle Del Bove, Mount Etna: its origin and relation to the stratigrahpy and structure of the volcano. *J. Volcan. Geoth. Res.*, **21**, pp. 1-23.

Guest, J.E., J.W. Hughes, and A.M. Duncan (1987) *Lava Flow-Field Morphology – A Case Study from Mount Etna, Sicily*, pp. 69-71, LPI Technical Report 88-05.

Guest, J.E., M.H. Bulmer, J. Aubele, K. Beratan, R. Greeley, J.W. Head, G. Michaels, C. Weitz, and C. Wiles (1992) Small volcanic edifices and volcanism in the plains of Venus. *J. Geophys. Res.*, **97**, pp. 15,949-15,966.

Guinness, E.A., R.E. Arvidson, M.A. Dale-Bannister, R.B. Singer, and E.A. Bruckenthal (1987) On the spectral reflectance properties of materials exposed at the Viking landing sites. *J. Geophys. Res.*, **92**, No. B4, pp. E575-E587.

Gulick, V.C., and V.R. Baker (1990) Origin and evolution of valleys on Martian volcanoes. *J. Geophys. Res.*, **95**, pp. 14,325-14,344.

Gurnett, D.A., D.L. Kirchner, R.L. Huff, D.D. Morgan, A.M. Persoon, T.F. Averkamp, F. Duru, E. Nielsen, A. Safaeinili, J.J. Plaut, and G. Picardi (2005) Radar soundings of the ionosphere of Mars. *Science*, **310**, pp. 1929-1933.

Harrison, K.P., and R.E. Grimm (2005) Groundwater-controlled valley networks and the decline of surface runoff on early Mars. *J. Geophys. Res.*, **110** (E12S16), doi:10.1029/2005JE002455.

Hartmann, W.K., and G. Neukum (2001) Cratering chronology and evolution of Mars. *Space Science Reviews*, **95**, pp. 167-196.

Head, J.W., and M. Kreslavsky (2004) Medusae Fossae Formation: ice-rich airborne dust deposited during periods of high obliquity? *Lunar Planet. Sci. XXXV*, Abstract #1635.

Head, J.W., and D.R. Marchant (2003) Cold-based mountain glaciers on Mars: Western Arsia Mons. *Geology*, **31**, pp. 641-644.

Head, J.W., and S. Pratt (2001) Extensive Hesperian-aged south polar ice sheet on Mars: evidence for massive melting and retreat, and lateral flow and ponding of meltwater. *J. Geophys. Res.*, **106**, pp. 12,275-12,299.

Head, J.W., and S.C. Solomon (1981) Tectonic evolution of the terrestrial planets. *Science*, **213**, pp. 62-76.

Head, J.W., and L. Wilson (1986) Volcanic processes and landforms on Venus: theory, predictions, and observations. *J. Geophys. Res.*, **91**, pp. 9407-9446.

Head, J.W., and L. Wilson (1987) Lava fountain heights at Pu'u 'O'o, Kilauea, Hawaii: indicators of amount and variations of exsolved magma volatiles. *J. Geophys. Res.*, **92**, pp. 13,715-13,719.

Head, J.W., and L. Wilson (1989) Basaltic pyroclastic eruptions: influence of gas-release patterns and volume fluxes on fountain structure, and the formation of cinder cones, spatter cones, rootless flows, lava ponds and lava flows. *J. Volcanol. Geotherm. Res.*, **37**, pp. 261–271.

Head, J.W., and L. Wilson (1992) Magma reservoirs and neutral buoyancy zones on Venus: implications for the formation and evolution of volcanic landforms. *J. Geophys. Res.*, **97**, pp. 3877-3903.

Head, J.W., and L. Wilson (2002) Mars: a review and synthesis of general environments and geological settings of magma-H_2O interactions. From *Volcano-Ice Interaction on Earth and Mars*, ed. J.L. Smellie and M.G. Chapman, Geological Society Special Publication No. 202, pp. 27-57.

Head, J.W., and L. Wilson (2003) Deep submarine pyroclastic eruptions: theory and predicted landforms and deposits. *J. Volcanol. Geotherm. Res.*, **121**, pp. 155–193.

Head, J.W., L.S. Crumpler, J.C. Aubele, J.E. Guest, and R.S. Saunders (1992) Venus volcanism; Classification of volcanic features and structures, associations, and global distribution from Magellan data. *J. Geophys. Res.*, **97**, pp. 13,153-13,197.

Head, J.W., M.A. Kreslavsky, H. Hiesinger, M.A. Ivanov, S. Pratt, N. Seibert, D.E. Smith, and M.T. Zuber (1998) Oceans in the past history of Mars: tests for their presence using

Mars Orbiter Laser Altimeter (MOLA) data. *Geophys. Res. Lett.*, **25**(24), pp. 4401-4404.

Head, J.W., H. Hiesinger, M.A. Ivanov, M.A. Kreslavsky, S. Pratt, and B.J. Thomson (1999) Possible ancient oceans on Mars: evidence from Mars Orbiter Laser Altimeter data. *Science*, **286**, pp. 2134-2137.

Head, J.W., J.F. Mustard, M.A. Kreslavsky, R.A. Milliken, and D.R. Marchant (2003) Recent ice ages on Mars. *Nature*, **426**, pp. 797-802.

Heggy, E., P. Paillou, G. Ruffié, J.M. Malézieux, F. Costard and G. Grandjean (2001) On water detection in the Martian subsurface using sounding radar. *Icarus*, **154**, pp. 244-257.

Heggy, E., P. Paillou, F. Costard, N. Mangold, G. Ruffié, F. Demontoux, G. Grandjean, and J.M. Malézieux (2003) Local geoelectrical models of the Martian subsurface for shallow groundwater detection using sounding radars. *J. Geophys. Res.*, **108**(E4), 8030, doi:10.1029/2002JE001871.

Heggy, E., S.M. Clifford, R.E. Grimm, C.L. Dinwiddie, D.Y. Wyrick, and B.E. Hill (2006a) Ground-penetrating radar sounding in mafic lava flows: assessing attenuation and scattering losses in Mars-analog volcanic terrains. *J. Geophys. Res.*, **111**, E06S04, doi:10.1029/2005JE002589.

Heggy, E., S.M. Clifford, A. Younsi, J.L. Miane, R. Carley, and R.V. Morris (2006b) On the dielectric properties of dust and ice-dust mixtures: experimental characterization of the Martian Polar Layered Deposits analog materials. *4th International Conference on Mars Polar Science and Exploration*, Abstract #8105.

Heggy, E., S.M. Clifford, R.E. Grimm, C.L. Dinwiddie, J.A. Stamatakos, and S.H. Gonzalez (2006c). Low-frequency radar sounding investigations of the North Amargosa Desert, Nevada: a potential analog of conductive subsurface environments on Mars. *J. Geophys. Res.*, **111**, E06S03, doi:10.1029/2005JE002523.

Heiken, G. and K. Wohletz (1987) Tephra deposits associated with silicic dome and lava flows. From *The Emplacement of Silicic Domes and Lava Flows*, ed. J.H. Fink, Geological Society of America Special Paper, **212**, pp. 55-76.

Hodges, C.A., and H.J. Moore (1994) *Atlas of Volcanic Landforms on Mars*, US Geological Survey Professional Paper 1534.

Holt, J.W., and 11 colleagues (2008) Radar sounding evidence for buried glaciers in the southern mid-latitudes of Mars. *Science*, **322**, pp. 1235-1238.

Howard, J.H. (1979) Geologic Map of the Phaethontis Quadrangle of Mars. *U.S. Geol. Survey. Invest. Ser. Map, I-1145 (MC-24).*

Hughes, J.W., J.E. Guest, and A.M. Duncan (1990) Changing styles of effusive eruption on Mount Etna since AD 1600. From *Magma Transport and Storage*, pp. 385-406, edited by M.P. Ryan, publ. Wiley, New York.

Hulme, G. (1982) A review of lava flow processes related to the formation of lunar sinuous rilles. *Geophys. Surv.*, **5**, pp. 245-279.

Hunten, D.M., T.M. Donahue, J.F. Kasting, and J.C.G. Walker (1989) Escape of atmospheres and loss of water. From *Origin and Evolution of Planetary and Satellite Atmospheres*, pp. 386-422, edited by S.K. Atreya, J.B. Pollack, and M.S. Matthews, publ. Tucson, Univ. Of Arizona Press.

Hynek, B.M., R.J. Phillips, and R.E. Arvidson (2003) Explosive volcanism in the Tharsis region: global evidence in the Martian geologic record. *J. Geophys. Res.*, **108**(E9), doi:10.1029/2003JE002062.

Ingersoll, A.P. (1969) The runaway greenhouse: a history of water on Venus. *J. Atmos. Sci.*, **26**, pp. 1191-1198.

Irwin, R.P., T.A. Maxwell, A.D. Howard, R.A. Craddock, and D.W. Leverington (2002) A Large Paleolake Basin at the Head of Ma'adim Vallis, Mars. *Science*, **296**, pp. 2209-2212.

Irwin, R.P., A.D. Howard, and T.A. Maxwell (2004) Geomorphology of Ma'adim Vallis, Mars, and associated paleolake basins. *J. Geophys. Res.*, **109**, E12009, doi:10.1029/2004JE002287.

Ivanov, B.A. (2001) Mars/Moon cratering rate ratio estimates. *Space Science Reviews*, **95**, pp. 89-106.

Ivanov, B.A., and J.W. Head (2001) Chryse Planitia, Mars: topographic configuration, outflow channel continuity and sequence, and tests for hypothesized bodies of water using Mars Orbiter Laser Altimeter (MOLA) data. *J. Geophys. Res.*, **106**, pp. 3275-3296.

Ives, R.L. (1940) Rock glaciers in the Colorado Front Range. *Bull. Geol. Soc. Amer.*, **51**, pp. 1271-1294.

Jaggar, T.A. (1947) Origin and development of craters. *Geol. Soc. Am., Mem.*, **21**, 508 pp.

Jakosky, B.M., and C.B. Farmer (1982) The seasonal and global behavior of water vapor in the Mars atmosphere - Complete global results of the Viking atmospheric water detector experiment. *J. Geophys. Res.*, **87**, pp. 2999-3019.

James, P.B., H.H. Kieffer, and D.A. Paige (1992) The seasonal cycle of carbon dioxide on Mars. From *Mars*, pp. 934-968, edited by H.H. Kieffer, B.M. Jakosky, C.W. Snyder, and M.S. Matthews, Univ. of Arizona Press, Tucson.

Jol, H.M., and C.S. Bristow (2003) GPR in sediments: advice on data collection, basic processing and interpretation, a good practice guide. From *Ground Penetrating Radar in Sediments,* pp. 9-27, edited by Bristow C.S. and Jol H.M., Geological Society Special Publication no.211.

Jones, A.P. and K.T. Pickering (2003) Evidence for aqueous fluid-sediment transport and erosional processes on Venus. *J. Geol. Soc.*, **160**, pp. 319-327.

Jones, T.K., T.K.P. Gregg, and D.A. Crown (2007) A quantitative investigation of fluvial activity in the Hesperia Planum region, Mars. *Lunar Planet. Sci. XXXVIII*, Abstract #2156.

Jordan, R., and 18 colleagues (2009) The Mars Express MARSIS sounder instrument. *Planet. Space Sci.*, **57**, Issues 14-15, pp. 1975-1986.

Jurgens, R.F., R.M. Goldstein, H.R. Rumsey, and R.R. Green (1980) Images of Venus by three-station interferometry: 1977 results. *J. Geophys. Res.*, **85**, pp. 8282-8294.

Jurgens, R.F., M.A. Slade, L. Robinett, S. Brokl, G.S. Downs, C. Franck, G.A. Morris, K. Farazian, and R.P. Chan (1988a) High resolution images of Venus from ground-based molar. *Geophys. Res. Lett.*, **15**, pp. 577-580.

Jurgens, R.F., M.A. Slade, and R.S. Saunders (1988b) Evidence for highly reflective materials on the surface and subsurface of Venus. *Science*, **240**, pp. 1021-1023.

Kahn, R. (1985) The evolution of CO_2 on Mars. *Icarus*, **62**, pp. 175-190.

Kargel, J.S. (2004) *Mars: A Warmer, Wetter Planet*, Praxis Publishing Ltd.

Kargel, J.S., and R.G. Strom (1992) Ancient glaciation on Mars. *Geology*, **20**, pp. 3-7.

Kasting, J.F. (1988) Runaway and moist greenhouse atmospheres and the evolution of Earth and Venus. *Icarus*, **74**, pp. 472-494.

Keddie, S.T., and J.W. Head (1992) Large shield volcanoes on Venus: the effect of neutral buoyancy zone development on evolution and altitude distribution. *Lunar and Planetary Inst., Papers Presented to the International Colloquium on Venus*, pp. 56-57.

Keddie, S.T., and J.W. Head (1994a) Sapas Mons, Venus: evolution of a large shield volcano. *Earth, Moon and Planets*, **65**, pp. 129-190.

Keddie, S.T., and J.W. Head (1994b) Height and altitude distribution of large volcanoes on Venus. *Planet. Space Sci.*, **42**, No. 6, pp. 455-462.

Keddie, S.T., and J.W. Head (1995) Formation and evolution of volcanic edifices on the Dione Regio rise, Venus. *J. Geophys. Res.*, **100**, pp. 11,729-11,754.

Kiefer, W.S., and E.K. Potter (2000) Gravity anomalies at Venus shield volcanoes: implications for lithospheric thickness. *Lunar Planet. Sci. XXXI*, Abstract #1924.

Kieffer, H.H., T.Z. Martin, A.R. Peterfreund, B.M. Jakosky, E.D. Miner, and F.D. Palluconi (1977) Thermal and albedo mapping of Mars during the Viking primary mission. *J. Geophys. Res.*, **82**, pp. 4249-4291.

Kieffer, H.H. (1990) H_2O Grain Size and the Amount of Dust in Mars' Residual North Polar Cap. *J. Geophys. Res.*, **95**, pp. 1481-1493.

Kieffer, H.H., and Zent A.P. (1992) Quasi-periodic climate change on Mars. From *Mars*, pp. 1180-1218, edited by H.H. Kieffer, B.M. Jakosky, C.W. Snyder, and M.S. Matthews, Univ. of Arizona Press, Tucson.

Kieffer, H.H., B.M. Jakosky, and C.W. Snyder (1992) The Planet Mars: From Antiquity to the Present. From *Mars*, pp. 1-33, edited by H.H. Kieffer, B.M. Jakosky, C.W. Snyder, and M.S. Matthews, Univ. of Arizona Press, Tucson.

Kilburn, C.R.J. (1993) Lava crusts, aa flow lengthening and the pahoehoe-aa transition. From *Active Lavas*, pp. 263-280, edited by C.R.J. Kilburn and G. Luongo, Univ. College London Press, London.

Kirk, R.L., E. Howington-Kraus, M.R. Rosiek, D. Cook, J. Anderson, K. Becker, B.A. Archinal, L. Keszthelyi, R. King, A.S. McEwen, and the HiRISE Team (2007) Ultrahigh resolution topographic mapping of Mars with HiRISE stereo images: methods and first results. *Seventh International Conference on Mars*, Pasadena, CA, Abstract #3391.

Klein, F.W., R.Y. Koyanagi, J.S. Nakata, and W.R. Tanigawa (1987) The seismicity of Kilauea's magma system. *U.S. Geol. Surv. Prof. Pap.*, **1350**, pp. 1019-1185.

Klingelhöfer, G., and 18 colleagues (2004) Jarosite and Hematite at Meridiani Planum from Opportunity's Mössbauer Spectrometer. *Science*, **306**, pp. 1740-1745.

Kounaves, S.P., D. Catling, B.C. Clark, L. DeFlores, K. Gospodinova, M.H. Hecht, J. Kapit, D.W. Ming, R.C. Quinn and the Phoenix Science Team (2009) Aqueous carbonate chemistry of the Martian soil at the Phoenix landing site. *Lunar Planet. Sci. XL*, Abstract #2489.

Koyanagi, R.Y., D.A. Swanson, and E.T. Endo (1972) Distribution of earthquakes related to mobility of the south flank of Kilauea volcano, Hawaii. *U.S. Geol. Surv. Prof. Pap.*, 800-D, pp. 89-97.

Krasnopolsky, V.A., J.P. Maillard, and T.C. Owen (2004) Detection of methane in the martian atmosphere: evidence for life? *Icarus*, **172**, pp. 537-547.

Krause, M.O., and E.B. Grosfils (1999) The altitude distribution of uncategorized intermediate volcanoes on Venus. *Lunar Planet. Sci. XXX*, Abstract #1685.

Kremnev, R.S., and 12 colleagues (1986) VEGA Balloon System and Instrumentation. *Science*, **231**, pp. 1408-1411.

Krymskii, A.M., N.F. Ness, D.H. Crider, T.K. Breus, M.H. Acuña, and D.P. Hinson (2004) Solar wind interaction with the ionosphere/atmosphere and crustal magnetic fields at Mars: Mars Global Surveyor Magnetometer/Electron Reflectometer, radio science and accelerometer data. *J. Geophys. Res.*, **109**, A11306, doi:10.1029/2004JA010420.

Kuzmin, R.O. (1978) The peculiarities of the Martian cryolithosphere. *Problems of Cryolithology*, **7**, pp. 7-27.

Kuzmin, R.O., N.N. Bobina, E.V. Zabalueva, and V.P. Shashkina (1988) Structure inhomogeneities of the Martian cryolithosphere. *Solar System Res.*, **22**, pp. 195-212.

Kuzmin, R.O., N.N. Bobina, E.V. Zabalueva, and V.P. Shashkina (1989) Martian cryolithosphere: structure and relative ice content. *Intl. Geol. Congress*.

Kuznetz, L.H. and D.C. Gan (2002) On the existence and stability of liquid water on the surface of Mars today. *Astrobiology*, **2**, No.2, pp. 183-195.

Lanagan, P.D., A.S. McEwen, L.P. Keszthelyi, and T. Thordarson (2001) Rootless cones on Mars indicating the presence of shallow equatorial ground ice in recent times. *Geophys. Res. Lett.*, **28**(12), pp. 2365-2367.

Langevin, Y., F. Poulet, J.-P. Bibring, B. Gondet (2005) Sulfates in the North Polar region of Mars detected by OMEGA/Mars Express. *Science*, **307**, pp. 1584-1586.

Langlais, B., M.E. Purucker, and M. Mandea (2003) Crustal magnetic field of Mars. *J. Geophys. Res.*, **108**, doi:10.1029/2004JE002048.

Lara, L.E. (2009) The 2008 eruption of the Chaitén Volcano, Chile: a preliminary report. *Andean Geology*, **36** (1), pp. 125-129.

Larsen, G. (2000) Holocene eruptions within the Katla volcanic system, south Iceland: characteristics and environmental impact. *Jökull*, **49**, pp. 28-46.

Larsen, G., and S. Ásbjörnsson (1995) Volume of tephra and rock debris deposited by the 1918 jökulhlaups on western Mýrdalssandur, South Iceland. *Abstracts, International Symposium on Glacial Erosion and Sedimentation, 20–25 August, 67,* International Glaciological Society: Reykjavík.

Leberl, F.W., J.K. Thomas, and K.E. Maurice (1992) Initial results from the Magellan stereo experiment. *J. Geophys. Res.*, **97**, pp. 13,675-13,689.

Lecacheux, J., P. Drossart, P. Laques, F. Deladerriere, and F. Colas (1993) Detection of the surface of Venus at 1.0 micrometer from ground-based observations. *Planet. Space Sci.*, **41**, pp. 543-549.

Lewis, J.S. (1970) Venus: atmospheric and lithospheric composition. *Earth Planet. Sci. Lett.*, **10**, p. 73.

Li, R., K. Di, J. Hwangbo, and Y. Chen (2008) Rigorous photogrammetric processing of HiRISE stereo images and topographic mapping at Mars Exploration Rover landing sites. *Lunar Planet. Sci. XXXIX*, Abstract #1864.

Lofgren, G., et al. (1981) Volatiles in planetary basalts: Hydrogen, carbon and sulphur gas species, in *Basaltic Volcanism on the Terrestrial Planets*, pp. 385-398, publ. Pergamon, New York.

Loke, M.H. (1999) Electrical imaging surveys for environmental and engineering studies. Practical guide published online at www.heritagegeophysics.com/images/lokenote.pdf

Lopes, R.C., J.E. Guest, and C.J. Wilson (1980) Origin of the Olympus Mons aureole and perimeter scarp. *The Moon and the Planets*, **22**, pp. 221-234.

López, I., J. Lillo, and V.L. Hansen (2008) Regional fracture patterns around volcanoes: Possible evidence for volcanic spreading on Venus. *Icarus*, **195**, pp. 523-536.

Lucchitta, B.K. (1981) Mars and Earth: comparison of cold-climate features. *Icarus*, **45**, pp. 264-303.

Macdonald, G.A. (1972) *Volcanoes*. Prentice-Hall, Englewood Cliffs, NJ, 510 pp.

Magee, K.P., and J.W. Head (2001) Large flow fields on Venus: implications for plumes, rift associations, and resurfacing. From *Mantle Plumes: Their Identification Through Time*, Geological Society of America Special Paper No.352, ed. R.E. Ernst and K.L. Buchan.

Malin, M.C. (1980) Lengths of Hawaiian lava flows. *Geology*, **8**, pp. 306-308.

Malin, M.C., G.E. Danielson, A.P. Ingersoll, H. Masursky, J. Veverka, M.A. Ravine, and T.A. Soulanille (1992) Mars Observer Camera. *J. Geophys. Res.*, **97**, No. E5, pp. 7699-7718.

Malin, M.C., and 13 colleagues (2007) Context Camera Investigation on board the Mars Reconnaissance Orbiter. *J. Geophys. Res.*, **112**, E05S04, doi:10.1029/2006JE002808.

Marsh, B.D. (1984) On the mechanics of caldera resurgence. *J. Geophys. Res.*, **89**, pp. 8245-8251.

Masursky, H. (1973) An overview of geological results from Mariner 9. *J. Geophys. Res.*, **78**, pp. 4009-4030.

Masursky, H., J.M. Boyce, A.L. Dial, G.G. Schaber, and M.E. Strobell (1977) Classification and time of formation of Martian channels based on Viking data. *J. Geophys. Res.*, **82**, pp. 4016-4038.

Masursky, H., E. Eliason, P.G. Ford, G.E. McGill, G.H. Pettengill, G.G. Schaber, and G. Schubert (1980) Pioneer Venus radar results: geology from images and altimetry. *J. Geophys. Res.*, **85**, pp. 8232-8260.

Mathews, W.H. (1947) 'Tuyas', flat-topped volcanoes in Northern British Columbia. *Amer. Jour. Sci.*, **245**, pp. 560-570.

Mattox, T.N., and M.T. Mangan (1997) Littoral hydrovolcanic explosions: a case study of lava-seawater interaction at Kilauea Volcano. *J. Volcanol. Geotherm. Res.*, **75**, pp. 1-17.

Maxwell, T.A., F. El-Baz, and S.H. Ward (1975) Distribution, morphology and origin of ridges and arches in Mare Serenitatis. *Geol. Soc. Amer. Bull.*, **86**, pp. 1273-1278.

McBirney, A.R. and H. Williams (1969) Geology and petrology of the Galapagos Islands. *Geol. Soc. Am. Mem.*, **118**, 197 pp.

McCauley, J.F., M.H. Carr, J.A. Cutts, W.K. Hartmann, H. Masursky, D.J. Milton, R.P. Sharp, and D.E. Wilhelms (1972) Preliminary Mariner 9 report on the geology of Mars. *Icarus*, **17**, pp. 289-327.

McCoy, T.J., and 18 colleagues (2008) Structure, stratigraphy, and origin of Husband Hill, Columbia Hills, Gusev Crater, Mars. *J. Geophys. Res.*, **113**, E06S03, doi:10.1029/2007JE003041.

McElroy, M.B. (1972) Mars: An evolving atmosphere. *Science*, **175**, pp. 443-445.

McElroy, M.B., T.Y. Kong, and Y.L. Yung (1977) Photochemistry and evolution of Mars' atmosphere: A Viking perspective. *J. Geophys. Res.*, **82**, pp. 4379-4388.

McEwen, A., and 14 colleagues (2007) Mars Reconnaissance Orbiter's High Resolution Imaging Science Experiment (HiRISE). *J. Geophys. Res.*, **112**, E05S02, doi:10.1029/2005JE002605.

McGill, G.E., S.J. Steenstrup, C. Barton, and P.G. Ford (1981) Continental rifting and the origin of Beta-Regio, Venus. *Geophys. Res. Lett.*, **8**, pp. 737-740.

McGovern, P.J., and S.C. Solomon (1990) State of stress and eruption characteristics of Martian volcanoes. *Lunar Planet. Sci. XXI*, pp. 765-766.

McGovern, P.J., and S.C. Solomon (1997) Filling of flexural moats around large volcanoes on Venus: implications for volcanic stratigraphy and global magmatic flux. *J. Geophys. Res.*, **102**, pp. 16,303-16,318.

McGovern, P.J., and S.C. Solomon (1998) Growth of large volcanoes on Venus: mechanical models and implications for structural evolution. *J. Geophys. Res.*, **103**, pp. 11,071-11,101.

McKenzie, D., P.G. Ford, F. Liu, and G.H. Pettengill (1992) Pancake-like domes on Venus. *J. Geophys. Res.*, **97**, pp. 15,967-15,976.

Mellon, M.T., B.M. Jakosky, and S.E. Postawko (1997) The persistence of equatorial ground ice on Mars. *J. Geophys. Res.*, **102** (E8), pp. 19,357-19,369.

Melosh, H.J., and A.M. Vickery (1989) Impact erosion of the primordial Martian atmosphere. *Nature*, **338**, pp. 487-489.

Michel, F.C. (1971) Solar wind interaction with planetary atmospheres. *Rev. Geophys. Space Phys.*, **9**, 427.

Milkovich, S.M., J.W. Head and S. Pratt (2002) Meltback of Hesperian-aged ice-rich deposits near the south pole of Mars: evidence for drainage channels and lakes. *J. Geophys. Res.*, **107**, 5043, doi:10.1029/2001JE001802.

Milkovich, S.M., J.J. Plaut, R.J. Phillips, G. Picardi, and R. Seu (2007) MARSIS and SHARAD radar reflections within Promethei Lingula, South Polar Layered Deposits, Mars. *Eos Trans. AGU*, **88**(52), Fall Meet. Suppl., Abstract P11B-0545.

Miller, T.P. (1994) Dome growth and destruction during the 1989-90 eruption of Redoubt Volcano. *J. Volcan. Geoth. Res.*, **62**, pp. 197-212.

Milton, D.J. (1973) Water and processes of degradation in the Martian landscape. *J. Geophys. Res.*, **78**, pp. 4037-4047.

Mitchell, D.L., R.P. Lin, C. Mazelle, H. Réme, P.A. Cloutier, J.E.P. Connerney, M.H. Acuña, N.F. Ness (2001) Probing Mars' crustal magnetic field and ionosphere with the MGS Electron Reflectometer. *J. Geophys. Res.*, **106**(E10), pp. 23,419-23,427.

Moore, H.J., R.S. Saunders, J.J. Plaut, and T.J. Parker (1992) Magellan stereo images and Venusian geology. *Lunar and Planetary Inst., Papers Presented to the International Colloquium on Venus*, pp. 71-72.

Mouginis-Mark, P.J. (1985) Volcano/ground ice interactions in Elysium Planitia, Mars. *Icarus*, **71**, pp. 268-286.

Mouginis-Mark, P.J. (1994) Morphology of Venus calderas: Sif and Maat Montes. *Lunar Planet. Sci. XXV*, pp. 949-950.

Mouginis-Mark, P.J., and S.K. Rowland (2001) The geomorphology of planetary calderas. *Geomorphology*, **37**, pp. 201-223.

Mouginis-Mark, P.J., and S.K. Rowland (2001) Lava flows at Arsia Mons, Mars: insights from a graben imaged by HiRISE. *Icarus*, **198**, pp. 27-36.

Mouginis-Mark, P.J., L. Wilson, and J.R. Zimbelman (1988) Polygenic eruptions on Alba Patera, Mars. *Bull. Volcanol.*, **50**, pp. 361-379.

Mouginis-Mark, P.J., L. Wilson, and M.T. Zuber (1992) The physical volcanology of Mars. From *Mars*, pp. 424-452, edited by H.H. Kieffer, B.M. Jakosky, C.W. Snyder, and M.S. Matthews, Univ. of Arizona Press, Tucson.

Müller, N., J. Helbert, G.L. Hashimoto, C.C.C Tsang, S. Erard, G. Piccioni, and P. Drossart (2008) Venus surface thermal emission at 1 μm in VIRTIS imaging observations: evidence for variation of crust and mantle differentiation conditions. *J. Geophys. Res.*, **113**, E00B17, doi:10.1029/2008JE003118.

Mumma, M.J., R.E. Novak, M.A. DiSanti, B.P. Bonev, and N. Dello Russo (2004) Detection and mapping of methane and water on Mars. *Bull. Amer. Astr. Soc.*, **36**, p. 1127.

Mumma, M.J., G.L. Villanueva, R.E. Novak, T. Hewagama, B.P. Bonev, M.A. DiSanti, A.M. Mandell, and M.D. Smith (2009) Strong release of methane on Mars in northern summer 2003. *Science*, **323**, pp. 1041-1045.

Mustard, J.F., and 35 colleagues (2008) Hydrated silicate minerals on Mars observed by the Mars Reconnaissance Orbiter CRISM instrument. *Nature*, **454**, pp. 305-309.

Mutch, T.A., and E.C. Morris (1979) Geologic Map of the Memnonia Quadrangle of Mars. *U.S. Geol. Survey. Invest. Ser. Map, I-1137 (MC-16).*

Mutch, T.A., R.E. Arvidson, J.W. Head, K.L. Jones, and R.S. Saunders (1976) *The Geology of Mars*, Princeton Univ. Press, Princeton.

Mysen, B.O. (1977) The solubility of H_2O and CO_2 under predicted magma genesis conditions and some petrological and geophysical implications. *Rev. Geophys. Space Phys.*, **15**, pp. 351-361.

Nakada, S., and T. Fujii (1993) Preliminary report on the activity at Unzen Volcano (Japan), November 1990-November 1991: dacite lava domes and pyroclastic flows. *J. Volcan. Geoth. Res.*, **54**, pp. 319-333.

Naumann, T., and D. Geist (2000) Physical volcanology and structural development of Cerro Azul volcano, Isabela Island, Galapagos: Implications for the development of Galapagos-style shield volcanoes. *Bull. Volcanol.*, **61**, pp. 497-514.

Neukum, G., and D.U. Wise (1976) Mars: a standard crater curve and possible new time scale. *Science*, **194**, pp. 1381-1387.

Neukum, G., R. Jaumann, H. Hoffmann, E. Hauber, J.W. Head, A.T. Basilevsky, B.A. Ivanov, S.C. Werner, S. van Gasselt, J.B. Murray, and the HRSC Co-Investigator Team

(2004) Recent and episodic volcanic and glacial activity on Mars revealed by the High Resolution Stereo Camera. *Nature*, **432**, pp. 971-979.

Nielsen, E., X.-D. Wang, D.A. Gurnett, D.L. Kirchner, R. Huff, R. Orosei, A. Safaeinili, J.J. Plaut, and G. Picardi (2007) Vertical sheets of dense plasma in the topside Martian ionosphere. *J. Geophys. Res.*, **112**, E02003, doi:10.1029/2006JE002723.

Óladóttir, B.A., G. Larsen, T. Thordarson, and O. Sigmarsson (2005) The Katla volcano S-Iceland: Holocene tephra stratigraphy and eruption frequency. *Jökull*, **55**, pp. 53-74.

Óladóttir, B.A., O. Sigmarsson, G. Larsen, and T. Thordarson (2008) Katla volcano, Iceland: magma composition, dynamics and eruption frequency as recorded by Holocene tephra layers. *Bull. Volcanol.*, **70**, 475-493.

Ono, T., and H. Oya (2000) Lunar Radar Sounder (LRS) experiment on-board the SELENE spacecraft. *Earth, Planets and Space*, **52**, pp. 629-637.

Ono, T., A. Kumamoto, H. Nakagawa, Y. Yamaguchi, S. Oshigami, A. Yamaji, T. Kobayashi, Y. Kasahara, and H. Oya (2009) Lunar Radar Sounder observations of subsurface layers under the nearside maria of the Moon. *Science*, **323**, pp. 909-912.

Owen, T., J.P. Maillard, C. de Burgh, and B.L. Lutz (1988) Deuterium on Mars: The abundance of HDO and the value of D/H. *Science*, **240**, pp. 1767-1770.

Paige, D.A., and A.P. Ingersoll (1985) Annual heat balance of Martian polar caps: Viking observations. *Science*, **228**, pp. 1160-1168.

Palais, J.M., P.R. Kyle, W.C. McIntosh, and D. Seward (1988) Magmatic and phreatomagmatic volcanic activity at Mt. Takahe, West Antarctica, based on tephra layers in the Byrd ice core and field observations at Mt. Takahe. *J. Volcanol. Geotherm. Res.*, **35**, pp. 295-317.

Parfitt, E.A., and J.W. Head (1993) Buffered and unbuffered dike emplacement on Earth and Venus: implications for magma reservoir size, depth and rate of magma replenishment. *Earth, Moon and Planets*, **61**, pp. 249-281.

Parfitt, E.A., L. Wilson, and C.A. Neal (1995) Factors influencing the height of Hawaiian lava fountains: implications for the use of fountain height as an indicator of magma gas content. *Bull. Volcanol.*, **57**, pp. 440-450.

Parker, T.J., R.S. Saunders, and D.M. Schneeberger (1989) Transitional morphology in the west Deuteronilus Mensae region of Mars: implications for modification of the lowland/upland boundary. *Icarus*, **82**, pp. 111-145.

Parker, T.J., D.S. Gorsline, R.S. Saunders, D.C. Pieri, and D.M. Schneeberger (1993) Coastal geomorphology of the Martian northern plains. *J. Geophys. Res.*, **98**, pp. 11,061-11,078.

Pavri, B., J.W. Head, K.B. Klose, and L. Wilson (1992) Steep-sided domes on Venus: characteristics, geologic setting, and eruption conditions from Magellan data. *J. Geophys. Res.*, **97**, pp. 13,445-13,478.

Pechmann J.C. (1980) The origin of polygonal troughs on the northern plains of Mars. *Icarus*, **42**, pp. 185-210.

Peeples, W.J., W.R. Sill, T.W. May, S.H. Ward, R.J. Phillips, R.L. Jordan, E.A. Abbott, and T.J. Killpack (1978) Orbital radar evidence for lunar subsurface layering in Maria Serenitatis and Crisium. *J. Geophys. Res.*, **83**, pp. 3459-3468.

Perron, J.T., J.X. Mitrovica, M. Manga, I. Matsuyama, and M.A. Richards (2007) Evidence for an ancient martian ocean in the topography of deformed shorelines. *Nature*, **447**, pp. 840-843.

Pettengill, G.H., E. Eliason, P.G. Ford, G.B. Loriot, H. Masursky, and G.E. McGill (1980) Pioneer Venus radar results: altimetry and surface properties. *J. Geophys. Res.*, **85**, pp. 8261-8270.

Phillips, R.J., and M.C. Malin (1984) Tectonics of Venus. *Ann. Rev. Earth Planetary Sci.*, **12**, pp. 411-443.

Phillips, R.J., and 14 colleagues (1973a) Apollo lunar sounder experiment. *NASA Spec. Publ. No. 330*, 22-1-22-26.

Phillips, R.J., and 13 colleagues (1973b) The Apollo 17 lunar sounder. *Geochim. Cosmochim. Acta*, **3**, Suppl. 4, pp. 2821-2831.

Phillips, R.J. and 12 colleagues (2008) The geodynamical end game for Mars: sounding radar constraints on the present thermal state. *Lunar Planet. Sci. XXXIX*, Abstract #1493.

Picardi, G., J.J. Plaut, W.T.K Johnson and L. Borgarelli (1998) Mars Express Subsurface Sounding Radar/Altimeter Scientific and Technical Plan. Infocom Technical Report N188-23/2/1998.

Picardi, G. and 12 colleagues (2004) Performance and surface scattering models for the Mars Advanced Radar for Subsurface and Ionospheric Sounding (MARSIS). *Planet. Space Sci.*, **52**, pp. 149-156.

Picardi, G. and 33 colleagues (2005) Radar soundings of the subsurface of Mars. *Science*, **310**, pp. 1925-1928.

Pinkerton, H., and L. Wilson (1994) Factors controlling the lengths of channel-fed lava flows. *Bull. Volcanol.*, **56**, pp. 108-120.

Plaut, J.J. (1993) Stereo Imaging, in *Guide to Magellan Image Interpretation*, pp. 33-43, edited by J.P. Ford, J.J. Plaut, C.M. Weitz, T.G. Farr, D.A. Senske, E.R. Stofan, G. Michaels, and T.J. Parker, JPL Publication 93-24.

Plaut, J.J., and R.E. Arvidson (1992) Comparison of Goldstone and Magellan radar data in the equatorial plains of Venus. *J. Geophys. Res.*, **97**, pp. 16,279-16,291.

Plaut, J.J., R. Kahn, E.A. Guinness and R.E. Arvidson (1988) Accumulation of sedimentary debris in the south polar region of Mars and implications for climate history. *Icarus*, **75**, pp. 357-377.

Plaut, J.J. and 23 colleagues (2007a) Subsurface radar sounding of the south Polar Layered Deposits of Mars. *Science*, **316**, pp. 92-95.

Plaut, J.J., A. Ivanov, A. Safaeinili, S.M. Milkovich, G. Picardi, R. Seu, and R. Phillips (2007b) Radar sounding of subsurface layers in the south polar plains of Mars: correlation with the Dorsa Argentea Formation. *Lunar Planet. Sci. XXXVIII*, Abstract #2144.

Plescia, J.B., and R.S. Saunders (1979) The chronology of the martian volcanoes. *Proc. Lunar Planet. Sci. Conf. 10th*, pp. 2841-2859.

Pollack, J.B., and D.C. Black (1979) Implications of the gas compositional measurements of Venus for the origin of planetary atmospheres. *Science*, **205**, pp. 56-59.

Pollack, J.B., J.F. Kasting, S.M. Richardson, and K. Poliakoff (1987) The case for a wet, warm climate on early Mars. *Icarus*, **71**, pp. 203-224.

Porcello, L.J., R.L. Jordan, J.S. Zelenka, G.F. Adams, R.J. Phillips, W.E. Brown Jr., S.H. Ward, and P.L. Jackson (1974) The Apollo Lunar Sounder Radar System. *Proceedings of the IEEE*, **62**, pp. 769-783.

Poulet, F., J.-P Bibring, J.F. Mustard, A. Gendrin, N. Mangold, Y. Langevin, R.E. Arvidson, B. Gondet, C. Gomez, & the OMEGA Team (2005) Phyllosilicates on Mars and implications for early martian climate. *Nature*, **438**, pp. 623-627.

Pronin, A.A., and E.R. Stofan (1990) Coronae on Venus: morphology and distribution. *Icarus*, **87**, pp. 452-474.

Putzig, N.E., and 17 colleagues (2007) Internal structure of the North Polar Layered Deposits from radar sounding. *Eos Trans. AGU*, **88**(52), Fall Meet. Suppl., Abstract P11B-0544.

Ramo, S., J.R. Whinnery, and T. van Duzer (1994) *Fields and Waves in Communication Electronics, 3rd ed.*, Wiley, New York.

Rampey, M.L., K.A. Milam, H.Y. McSween, J.E. Moersch, and P.R. Christensen (2007) Identity and emplacement of domical structures in the western Arcadia Planitia, Mars. *J. Geophys. Res.*, **112**, E06011, doi:10.1029/2006JE002750.

Reynolds, J.M. (1997) Ground Penetrating Radar, in *An Introduction to Applied and Environmental Geophysics*, Wiley, New York.

Rieder, R., and 14 colleagues (2004) Chemistry of rocks and soils at Meridiani Planum from the alpha particle X-ray spectrometer. *Science*, **306**, pp. 1746-1749.

Rist, S. (1979) The hydrology of River Laxá. *Oikos*, **32**, pp. 271-280.

Ristau, S., J. Sammons, M. Gilmore, S. Kozak, E. Grosfils, and L. Reinen (1998) Distribution of intermediate volcanoes on Venus as a function of altitude. *Lunar Planet. Sci. XXIX*, Abstract #1110.

Rogers, P.G., and M.T. Zuber (1998) Tectonic evolution of Bell Regio, Venus: regional stress, lithospheric flexure, and edifice stresses. *J. Geophys. Res.*, **103**(E7), pp. 16,841–16,853.

Rubin, A.M., and D.D. Pollard (1987) Origins of blade-like dikes in volcanic rift zones. From *Volcanism in Hawaii*, pp. 1395-1446, ed. R.W. Decker, T.L. Wright, and P.H. Stauffer, *U.S. Geol. Surv. Prof. Pap. 1350*.

Rumsey, H.C., G.A. Morns, R.R. Green, and R.M. Goldstein (1974) A radar altitude and brightness image of a portion of Venus. *Icarus*, **23**, pp. 1-7.

Ryan, M.P. (1987) Elasticity and contractancy of Hawaiian olivine tholeiite and its role in the stability and structural evolution of subcaldera magma reservoirs and rift systems.

From *Volcanism in Hawaii*, pp. 1395-1446, ed. R.W. Decker, T.L. Wright, and P.H. Stauffer, *U.S. Geol. Surv. Prof. Pap. 1350*.

Ryan, M.P., J.Y.K. Blevins, A.T. Okamura, and R.Y. Koyanagi (1983) Magma reservoir subsidence mechanics: theoretical summary and application to Kilauea volcano. *J. Geophys. Res.*, **88**, pp. 4147-4181.

Rzhiga, O.N. (1987) Venera-15 and -16 spacecraft: images and maps of Venus. *Adv. Space Res.*, **7**, No. 12, pp. 269-278.

Safaeinili, A., W. Kofman, J. Mouginot, Y. Gim, A. Herique, A.B. Ivanov, J.J. Plaut and G. Picardi (2007) Estimation of the total electron content of the Martian ionosphere using radar sounder surface echoes. *Geophys. Res. Lett.*, **34**, L23204, doi:10.1029/2007GL032154.

Sagan, C., O.B. Toon, and P.J. Gierasch (1973) Climate change on Mars. *Science*, **181**, pp. 1045-1049.

Sagdeev, R.Z., V.M. Linkin, J.E. Blamont, and R.A. Preston (1986) The VEGA Venus Balloon Experiment. *Science*, **231**, pp. 1407-1408.

Sakimoto, S.E.H. (2002) Plains volcanism on Mars: topographic data on shield and flow distributions and abundances, with new quantitative comparisons to the Snake River Plain volcanic province. *2002 Denver Annual Meeting*, paper No. 77-2.

Santiago, D.L., A. Colaprete, R.M. Haberle, L.C. Sloan, and E.I. Asphaug (2005) Outflow channels influencing Martian climate; global circulation model simulations with emplaced water. *Lunar Planet. Sci. Conf. XXXVI*, Abstract #1787.

Sato, H., T. Fujii, and S. Nakada (1992) Crumbling of dacite dome lava and generation of pyroclastic flows at Unzen volcano. *Nature*, **360**, pp. 664-666.

Saunders, R.S., G.H. Pettengill, R.E. Arvidson, W.L. Sjogren, W.T.K. Johnson, and L. Pieri (1990) The Magellan Venus radar mapping mission. *J. Geophys. Res.*, **95**, pp. 8339-8355.

Schaber, G.G. (1982) Syrtis Major: a low-relief volcanic shield. *J. Geophys. Res.*, **87**, pp. 9852-9866.

Schaber, G.G. (1991) Volcanology on Venus as inferred from the morphometry of large shields. *Proc. Lunar. Planet. Sci.*, **21**, pp. 3-11.

Schubert, G., and T. Spohn (1990) Thermal history of Mars and the sulfur content of its core. *J. Geophys. Res.*, **95**, pp. 14095-14104.

Schultz, P.H., and A.B. Lutz (1988) Polar Wandering of Mars. *Icarus*, **73**, pp. 91-141.

Scott, D.H., and K.L. Tanaka (1982) Ignimbrites of Amazonis Planitia region of Mars. *J. Geophys. Res.*, **87**, pp. 1179-1190.

Scott, D.H., E.C. Morris and M.N. West (1978) Geologic Map of the Aeolis Quadrangle of Mars. *U.S. Geol. Survey. Invest. Ser. Map, I-1111 (MC-23).*

Scott, D.H., M.G. Chapman, J.W. Rice, and J.M. Dohm (1992) New evidence of lacustrine basins on Mars: Amazonis and Utopia Planitia. *Proc. Lunar. Planet. Sci.*, **22**, pp. 53-62.

Segura, T.L., O.B. Toon, A. Colaprete, and K. Zahnle (2002) Environmental effects of large impacts on Mars. *Science*, **298**, pp. 1977-1980.

Senske, D.A., and E.R. Stofan (1993) Geologic Mapping on Venus, in *Guide to Magellan Image Interpretation*, pp. 135-140, edited by J.P. Ford, J.J. Plaut, C.M. Weitz, T.G. Farr, D.A. Senske, E.R. Stofan, G. Michaels, and T.J. Parker, JPL Publication 93-24.

Senske, D.A., G.G. Schaber, and E.R. Stofan (1992) Regional topographic rises on Venus: geology of western Eistla Regio and comparison to Beta Regio and Atla Regio. *J. Geophys. Res.*, **97**, No. E8, pp. 13,395-13,420.

Seu, R., and 11 colleagues (2007) SHARAD sounding radar on the Mars Reconnaissance Orbiter. *J. Geophys. Res.*, **112**, E05S04, doi:10.1029/2006JE002745.

Sharp, R.P. (1973) Mars: fretted and chaotic terrain. *J. Geophys. Res.*, **78**, pp. 4073-4083.

Sharp, R.P., and M.C. Malin (1975) Channels on Mars. *Geol. Soc. Amer. Bull.*, **86**, pp. 593-609.

Siebert, L. (1984) Large volcanic debris avalanches: characteristics of source areas, deposits, and associated eruptions. *J. Volcan. Geoth. Res.*, **22**, pp. 163-197.

Simkin, T. (1972) Origin of some flat-topped volcanoes and guyots. *Geol. Soc. Am. Mem.*, **132**, pp. 183-193.

Simkin, T., and K.A. Howard (1970) Caldera collapse in the Galapagos Islands. *Science*, **169**, pp. 429-437.

Singer, R.B. (1982) Spectral Evidence for the Mineralogy of High-Albedo Soils and Dust on Mars. *J. Geophys. Res.*, **87**, pp. 10,159-10,168.

Smellie, J.L. (2000) Subglacial eruptions. From *Encyclopedia of Volcanoes*, pp. 403-418, edited by H. Sigurdsson, Academic Press, San Diego.

Smellie, J.L., and I.P. Skilling (1994) Products of subglacial volcanic eruptions under different ice thickness: two examples from Antarctica. *Sedimentary Geology*, **91**, pp. 115-129.

Smith, D.E., and 23 colleagues (2001) Mars Orbiter Laser Altimeter: experiment summary after the first year of global mapping on Mars. *J. Geophys. Res.*, **106**, pp. 23,689-23,722.

Smith, E.I. (1973) Mono Craters, California: a new interpretation of the eruptive sequence. *Geol. Soc. Am. Bull.*, **84**, pp. 2685-2690.

Smith, P.H. (2009). Water at the Phoenix landing site. *Lunar Planet. Sci. Conf. XL*, Abstract #1329.

Smoluchowski, R. (1968) Mars: retention of ice. *Science*, **159**, pp. 1348-1350.

Smrekar, S.E., E.R. Stofan, N. Mueller, A. Treiman, L. Elkins-Tanton, J. Helbert, G. Piccioni, and P. Drossart (2010) Recent hotspot volcanism on Venus from VIRTIS emissivity data. *Science*, **328**, pp. 605-608.

Snyder, C.W., and V.I. Moroz (1992) Spacecraft exploration of Mars. From *Mars*, pp. 71-119, edited by H.H. Kieffer, B.M. Jakosky, C.W. Snyder, and M.S. Matthews, Univ. of Arizona Press, Tucson.

Soderblom, L.A. (1977) Historical variations in the density and distribution of impacting debris in the inner solar system: evidence from planetary imaging. From *Impact and Explosion Cratering*, pp. 629-633, edited by D.J. Roddy, R.O. Pepin, and R.B. Merrill, Pergamon, N.Y.

Soderblom, L.A., and D.B. Wenner (1978) Possible fossil H_2O liquid-ice interface in the Martian crust. *Icarus*, **34**, 622-637.

Solomon, S.C., and J.W. Head (1990) Heterogeneities in the thickness of the elastic lithosphere of Mars: constraints on heat flow and internal dynamics. *J. Geophys. Res.*, **95**, pp. 11,073-11,083.

Sparks, R.S.J. (1978) The dynamics of bubble formation and growth in magmas: a review and analysis. *J. Volcanol. Geotherm. Res.*, **3**, pp. 1-37.

Squyres, S.W. (1978) Martian fretted terrain: flow of erosional debris. *Icarus*, **34**, pp. 600-613.

Squyres, S.W. (1979) The distribution of lobate debris aprons and similar flows on Mars. *J. Geophys. Res.*, **84**, pp. 8087-8096.

Squyres, S.W. (1989) Urey prize lecture: Water on Mars. *Icarus*, **79**, pp. 229-288.

Squyres, S.W., and M.H. Carr (1986) Geomorphic evidence for the distribution of ground ice on Mars. *Science*, **231**, pp. 249-252.

Squyres, S.W., D.E. Wilhelms, and A.C. Moosman (1987) Large-scale volcano-ground ice interaction on Mars. *Icarus*, **70**, pp. 385-408.

Squyres, S.W., D.M. Janes, G. Baer, D.L. Bindschadler, G. Schubert, V.L. Sharpton, and E.R. Stofan (1992a) The morphology and evolution of coronae on Venus. *J. Geophys. Res.*, **97**, pp. 13,611-13,634.

Squyres, S.W., S.M. Clifford, R.O. Kuzmin, J.R. Zimbelman, and F.M. Costard (1992b) Ice in the Martian regolith. From *Mars*, pp. 523-554, edited by H.H. Kieffer, B.M. Jakosky, C.W. Snyder, and M.S. Matthews, Univ. of Arizona Press, Tucson.

Squyres, S.W., and 49 colleagues (2004) The Opportunity rover's Athena science investigation at Meridiani planum, Mars. *Science*, **306**, pp. 1698-1703.

Stevenson, D.J., T. Spohn, and G. Schubert (1983) Magnetism and the thermal evolution of the terrestrial planets. *Icarus*, **54**, pp. 466-489.

Stillman, D., and R.E. Grimm (2009) SHARAD penetrates only the youngest geological units on Mars. *Eos Trans. AGU*, **90**(52), Fall Meet. Suppl., Abstract #P13B-1276.

Stofan, E.R., and J.W. Head (1990) Coronae of Mnemosyne Regio: morphology and origin. *Icarus*, **83**, pp. 216-243.

Stofan, E.R., V.L. Sharpton, G. Schubert, G. Baer, D.L. Bindschadler, D.M. James, and S.W. Squyres (1992) Global distribution and characteristics of coronae and related features on Venus: implications for origin and relation to mantle processes. *J. Geophys. Res.*, **97**, E8, pp. 13,347-13,378.

Stofan, E.R., S.E. Smrekar, D.L. Bindschadler, and D.A. Senske (1995) Large topographic rises on Venus: implications for mantle upwelling. *J. Geophys. Res.*, **100**, pp. 23,317-23,327.

Stofan, E.R., S.W. Anderson, D.A. Crown, and J.J. Plaut (2000) Emplacement and composition of steep-sided domes on Venus. *J. Geophys. Res.*, **105**, pp. 26,757-26,771.

Stofan, E.R., J.E. Guest, and D.L. Copp (2001) Development of large volcanoes on Venus: constraints from Sif, Gula and Kunapipi Montes. *Icarus*, **152**, pp. 75-95.

Strom, R.G., S.K. Croft, and N.G. Barlow (1992) The Martian impact cratering record. From *Mars*, pp. 383-423, edited by H.H. Kieffer, B.M. Jakosky, C.W. Snyder, and M.S. Matthews, Univ. of Arizona Press, Tucson.

Strong, D.F., and C. Jaquot (1971) The Karthala caldera, Grand Comore. *Bull. Volcanol.*, **34**, pp. 663-680.

Surkov, Y.A., L.P. Moskaleva, O.P. Shcheglov, A.D. Dudin, V.P. Kharyukova, O.S. Manvelyan, G.G. Smirnov, V.L. Gimadov, S.S. Kurochkin, and V.N. Rasputnyj (1985) Method, instrumentation and results of a determination of the Venus rock composition by the Vega 2 lander. *Astron. Vestn.*, **19**, No. 4, pp. 275-288.

Swanson, D.A., D. Dzurisin, R.T. Holcomb, E.Y. Iwatsubo, W.W. Chadwick Jr., T.J. Casadevall, J.W. Ewert, C.C. Heliker (1987) Growth of the lava dome at Mount St Helens, Washington. From *The Emplacement of Silicic Domes and Lava Flows*, ed. J.H. Fink, Geological Society of America Special Paper, **212**, pp. 1-16.

Tanaka, K.L. (1985) Ice-lubricated gravity spreading of the Olympus Mons aureole deposits. *Icarus*, **62**, pp. 191-206.

Tanaka, K.L., and M.G. Chapman (1990) The relation of catastrophic flooding of Mangala Valles, Mars, to faulting of Memnonia Fossae and Tharsis volcanism. *J. Geophys. Res.*, **95**, pp. 14,315-14,323.

Tanaka, K.L., and E.J. Kolb (2001) Geologic history of the polar regions of Mars based on Mars Global Surveyor data, I. Noachian and Hesperian Periods. *Icarus*, **154**, pp. 3-21.

Tanaka, K.L., and D.H. Scott (1987) Geologic map of the polar regions of Mars, scale 1:15,000,000. *US Geol. Surv. Misc. Invest. Ser. Map I-1802-C.*

Tanaka, K.L., D.H. Scott, and R. Greeley (1992) Global Stratigraphy. From *Mars*, pp. 345-382, edited by H.H. Kieffer, B.M. Jakosky, C.W. Snyder, and M.S. Matthews, Univ. of Arizona Press, Tucson.

Tanaka, K.L., J.S. Kargel, D.J. MacKinnon, T.M. Hare, and N. Hoffman (2002) Catastrophic erosion of Hellas basin rim induced by magmatic intrusion into volatile-rich rocks. *Geophys. Res. Lett.*, **29**, No. 8, doi:10.1029/2001GL013885.

Taylor, S.R., and I.H. Campbell (1983) No water, no granites: no oceans, no continents. *Geophys. Res. Lett.*, **10**, pp. 1061-1064.

Thomas, P., S. Squyres, K. Herkenhoff, A. Howard, and B. Murray (1992) Polar deposits of Mars. From *Mars*, pp. 767-795, edited by H.H. Kieffer, B.M. Jakosky, C.W. Snyder, and M.S. Matthews, Univ. of Arizona Press, Tucson.

Thompson, W.F. (1962) Preliminary notes on the nature and distribution of rock glaciers relative to true glaciers and other effects of the climate on the ground in North America. In *Symp. at Obergurgl*, Int. Assoc. Sci. Hydrol. Publ. No. 58, pp. 212-219, publ. Intl. Assoc. for Sci. Hydrology, Obergurgl.

Thorarinsson, S. (1951) Laxargljufur and Laxarhraun. A tephrochronological study, *Geografiska Annaler, H1-2*, pp. 1-89.

Thorarinsson S. (1953) The crater groups in Iceland. *Bull. Vol. Ser. 2*, **14**, pp. 3-44.

Thordarson, T., and A. Höskuldsson (2002) *Iceland. Classic Geology in Europe, 3.* Harpenden, UK: Terra Publishing.

Thordarson, T., M.M. Morrissey, G. Larsen, and H. Cyrusson (1992) Origins of rootless cone complexes in S. Iceland, in *The 20th Nordic Geological Winter Meeting*, edited by A. Geirsdóttir, H. Norddahl and H. Helgadóttir, Icelandic Geological Society, Reykjavik.

Thordarson, T., D.J. Miller, G. Larsen, S. Self, and H. Sigurdsson (2001) New estimates of sulfur degassing and atmospheric mass-loading by the 934 AD Eldgjá eruption, Iceland. *J. Volcan. Geoth. Res.*, **108**, pp. 33-54.

Thornhill, G.D. (1993) Theoretical modelling of eruption plumes on Venus. *J. Volcan. Geoth. Res.*, **98**(E5), pp. 9107-9111.

Thorpe, T.E. (1975) The Viking Orbiter Cameras' Potential for Photometric Measurement. *Icarus*, **27**, pp. 229-239.

Toksöz, M.N. and A.T. Hsui (1978) Thermal history and evolution of Mars. *Icarus*, **34**, pp. 537-547. *Earth, Moon and Planets*, **18**, pp. 281-320.

Toksöz, M.N., A.T. Hsui, and D.H. Johnson (1978) Thermal evolution of the terrestrial planets. *Icarus*, **34**, pp. 537-547.

Tosca, N.J., A.H. Knoll, and S.M. McLennan (2008) Water activity and the challenge for life on early Mars. *Science*, **320**, No. 5880, pp. 1204-1207.

Turcotte, D.L., F.A. Cook, and R.J. Willemann (1979) Parameterized convection within the Moon and the terrestrial planets. *Lunar Planet. Sci. X*, pp. 2375-2392.

Ui, T. (1983) Volcanic dry avalanche deposits – identification and comparison with nonvolcanic debris stream deposits. *J. Volcan. Geoth. Res.*, **18**, pp. 135-150.

Ulriksen, C.P.F. (1982) Application of impulse radar to civil engineering. PhD thesis, Lund Institute of Technology, Sweden. Published by Geophysical Survey Systems Inc.

Voight, B., H. Glicken, R.J. Janda, and P.M. Douglass (1981) Catastrophic rockslide avalanche on May 18. From *The 1980 Eruption of Mount St. Helens, Washington*, ed. P.W. Lipman and D.R. Mullineaux, US Geological Survey Professional paper, **1250**, pp. 347-378.

Wadge, G. (1977) The storage and release of magma on Mount Etna. *J. Volcan. Geoth. Res.*, **2**, pp. 361-384.

Wahrhaftig, C., and A. Cox (1959) Rock glaciers in the Alaska range. *Bull. Geol. Soc. Amer.*, **70**, pp. 383-436.

Walker, G.P.L. (1973) Lengths of lava flows. *Phil. Trans. R. Soc. London*, **A274**, pp. 107-118.

Walker, G.P.L. (1988) Three Hawaiian calderas: an origin through loading by shallow intrusion? *J. Geophys. Res.*, **93**, pp. 14,733-14,784.

Walker, G.P.L., and L.A. McBroome (1983) Mount St. Helens 1980 and Mount Pelée 1902 – flow or surge? *Geology*, **11**, pp. 571-574.

Walker, J.C.G. (1986) Impact erosion of planetary atmospheres. *Icarus*, **68**, pp. 87-98.

Walker, J.C.G., K.K. Turekian, and D.M. Hunten (1970) An estimate of the present-day deep-mantle degassing rate from data on the atmosphere of Venus. *J. Geophys. Res.*, **75**, pp. 3558-3561.

Wänke, H. and G. Dreibus (1994) Chemistry and accretion history of Mars. *Philos. Trans. R. Soc. London Ser. A*, **349**, pp. 285-293.

Warner, N., S. Gupta, J.-R. Kim, S.-Y. Lin, and J.-P. Muller (2010) Hesperian equatorial thermokarst lakes in Ares Vallis as evidence for transient warm conditions on Mars. *Geology*, **38**, pp. 71-74.

Washburn, A.L. (1973) *Periglacial Processes and Environments*. Published by Edward Arnold Ltd., London.

Watson, A.J., T.M. Donahue, and J.C.G. Walker (1981) The dynamics of a rapidly escaping atmosphere: Applications to the evolution of Earth and Venus. *Icarus*, **48**, pp. 150-166.

Watters, T.R., C.J. Leuschen, J.J. Plaut, G. Picardi, A. Safaeinili, S.M. Clifford, W.M. Farrell, A.B. Ivanov, R.J. Phillips and E.R. Stofan (2006) MARSIS radar sounder evidence of buried basins in the northern lowlands of Mars. *Nature*, **444**, pp. 905-908.

Watters, T.R. and 12 colleagues (2007) Radar sounding of the Medusae Fossae Formation Mars: equatorial ice or dry, low-density deposits? *Science*, **318**, pp. 1125-1128.

Watts, R.B., R.A. Herd, R.S.J. Sparks, and S.R.Young (2002) Growth patterns and emplacement of the andesitic lava dome at Soufrière Hills Volcano, Montserrat. From *The Eruption of Soufrière Hills Volcano, Montserrat, from 1995 to 1999*, pp. 115-152, edited by Druitt, T.H. and Kokelaar, B.P., Geological Society Memoirs No. 21.

Webb, B.M., J.W. Head, B.E. Kortz, and S. Pratt (2001) Syria Planum, Mars: a major volcanic construct in the early history of Tharsis. *Lunar and Planetary Science*, **32**, No. 1145.

White, S.E. (1976) Rock glaciers and block fields, review and new data. *Quat. Res.*, **6**, pp. 77-97.

Williams, H. (1932) *The History and Character of Volcanic Domes*. University of California Berkeley, Bulletin of the Department of Geological Science, **21**.

Wilson, L., and J.W. Head (1981) Ascent and eruption of basaltic magma on Earth and Moon. *J. Geophys. Res.*, **86**, pp. 2971-3001.

Wilson, L., and J.W. Head (1983) A comparison of volcanic eruption processes on Earth, Moon, Mars, Io and Venus. *Nature*, **302**, 5910, pp. 663-669.

Wilson, L., and J.W. Head (1990) Factors controlling the structures of magma chambers in basaltic volcanoes. *Lunar Planet. Sci. Conf. XXI*, pp. 1343-1344.

Wilson, L., and J.W. Head (1994) Mars: review and analysis of volcanic eruption theory and relationships to observed landforms. *Rev. of Geophys.*, **32**, No. 3, pp. 221-263.

Wilson, L., and J.W. Head (1997) Factors controlling the depths and sizes of magma reservoirs in Martian volcanoes. *Lunar Planet. Sci. Conf. XXVIII*, Abstract #1284.

Wilson, L., and J.W. Head (2002a) Heat transfer and melting in subglacial basaltic volcanic eruptions: implications for volcanic deposit morphology and meltwater volumes. From *Volcano-Ice Interaction on Earth and Mars*, ed. J.L. Smellie and M.G. Chapman, Geological Society Special Publication no.202, pp. 5-26.

Wilson, L., and J.W. Head (2002b) Tharsis-radial graben systems as the surface manifestation of plume-related dike intrusion complexes: Models and implications. *J. Geophys. Res.*, **107**, No. E8, doi:10.1029/2001JE001593.

Wilson, L., and J.W. Head (2007) Explosive volcanic eruptions on Mars: Tephra and accretionary lapilli formation, dispersal and recognition in the geologic record. *J. Volcanol. Geotherm. Res.*, **163**, pp. 83-97.

Wilson, L., E.D. Scott, and J.W. Head (2001) Evidence for episodicity in the magma supply to the large Tharsis volcanoes. *J. Geophys. Res.*, **106**, No. E1, pp. 1423-1433.

Wilson, L., P.J. Mouginis-Mark, S. Tyson, J. Mackown, and H. Garbeil (2009) Fissure eruptions in Tharsis, Mars: implications for eruption conditions and magma sources. *J. Volcan. Geoth. Res.*, **185**, pp. 28-46.

Wohletz, K.H. (1983) Mechanisms of hydrovolcanic pyroclast formation: grain-size, scanning electron microscopy, and experimental studies. *J. Volcanol. Geotherm. Res.*, **17**, pp. 31-63.

Wohletz, K.H. (1986) Explosive magma-water interactions: thermodynamics, explosion mechanisms, and field studies. *Bull. Volcan.*, **48**, No.5, pp. 245-264.

Wohletz, K.H., and R.G. McQueen (1984) Experimental studies of hydromagmatic volcanism, in *Explosive Volcanism: Inception, Evolution, and Hazards*, pp. 158-69, Washington, DC: National Academy of Sciences.

Wong, A.-S., S.K. Atreya, and T. Encrenaz (2003) Chemical markers of possible hot spots on Mars. *J. Geophys. Res.*, **108**, No. E4, doi:10.1029/2002JE002003.

Wood, C.A. (1979) Venusian volcanism: environmental effects on style and landforms. NASA Tech. Memo, TM-80339, pp. 244-246.

Wood, C.A. (1984) Calderas: a planetary perspective. *J. Geophys. Res.*, **89**, No. B10, pp. 8391-8406.

Yung, Y.L., and J.P. Pinto (1978) Primitive atmosphere and implications for the formation of channels on Mars. *Nature*, **288**, pp. 735-738.

Yung, H.L, J.S. Wen, J.P. Pinto, M. Allen, K. Pierce, and S. Panlom (1988) HDO in the Martian atmosphere: implications for the abundance of crustal water. *Icarus*, **76**, pp. 146-159.

Zhang, Z., T. Hagfors, E. Nielsen, G. Picardi, A. Mesdea and J.J. Plaut (2008) Dielectric properties of the Martian south polar layered deposits: MARSIS data inversion using Bayesian inference and genetic algorithm. *J. Geophys. Res.*, **113**, E05004, doi:10.1029/2007JE002941.

Zimanowski, B., G. Fröhlich, and V. Lorenz (1991) Quantitative experiments on phreatomagmatic explosions. *J. Volcanol. Geotherm. Res.*, **48**, pp. 341-58.

Zimbelman, J.R., and K.S. Edgett (1992) The Tharsis Montes, Mars: comparison of volcanic and modified landforms. *Proc. Lunar Planet. Sci.*, **22**, pp. 31-44.

Zimbelman, J.R., and T.K.P. Gregg (2000) Volcanic diversity throughout the Solar System. From *Environmental Effects on Volcanic Eruptions: From Deep Oceans to Deep Space*, pp. 1-8, edited by J.R. Zimbelman and T.K.P. Gregg, Kluwer Academic/Plenum Publishers, New York.

Zuber, M.T., D.E. Smith, S.C. Solomon, D.O. Muhleman, J.W. Head, J.B. Garvin, J.B. Abshire, and J.L. Bufton (1992) The Mars Observer Laser Altimeter Investigation. *J. Geophys. Res.*, **97**, No. E5, pp. 7781-7797.